EQUILIBRIUM AND DYNAMICS OF COLLISIONLESS CURRENT SHEETS

Michael George Harrison

A Thesis Submitted for the Degree of PhD
at the
University of St. Andrews

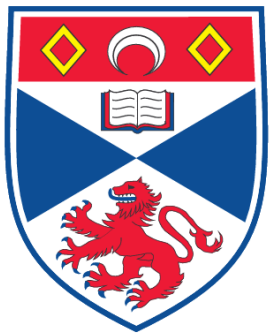

2009

Equilibrium and Dynamics of Collisionless Current Sheets

Michael George Harrison

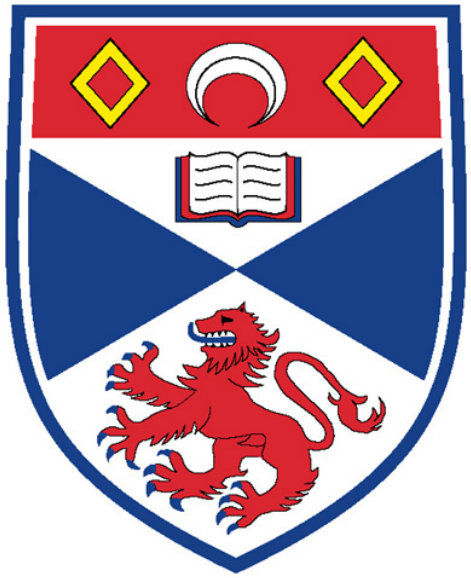

Thesis submitted for the degree of Doctor of Philosophy
of the University of St Andrews

May 2, 2009

Abstract

In this thesis examples of translationally invariant one-dimensional (1D) Vlasov-Maxwell (VM) equilibria are investigated. The 1D VM equilibrium equations are equivalent to the motion of a pseudoparticle in a conservative pseudopotential, with the pseudopotential being proportional to one of the diagonal components of the plasma pressure tensor. A necessary condition on the pseudopotential (plasma pressure) to allow for force-free 1D VM equilibria is formulated. It is shown that linear force-free 1D VM solutions correspond to the case where the pseudopotential is an attractive central potential. The pseudopotential for the force-free Harris sheet is found and a Fourier transform method is used to find the corresponding distribution function. The solution is extended to include a family of equilibria that describe the transition between the Harris sheet and the force-free Harris sheet. These equilibria are used in 2.5D particle-in-cell simulations of magnetic reconnection. The structure of the diffusion region is compared for simulations starting from anti-parallel magnetic field configurations with different strengths of guide field and self-consistent linear and non-linear force-free magnetic fields. It is shown that gradients of off-diagonal components of the electron pressure tensor are the dominant terms that give rise to the reconnection electric field. The typical scale length of the electron pressure tensor components in the weak guide field case is of the order of the electron bounce widths in a field reversal. In the strong guide field case the scale length reduces to the electron Larmor radius in the guide magnetic field.

Declaration

I, Michael George Harrison, hereby certify that this thesis, which is approximately 70,000 words in length, has been written by me, that it is the record of work carried out by me and that it has not been submitted in any previous application for a higher degree.

I was admitted as a research student in October 2005 and as a candidate for the degree of Doctor of Philosophy in October 2006; the higher study for which this is a record was carried out in the University of St Andrews between 2005 and 2009.
date: 01/05/2009 signature of candidate:

I hereby certify that the candidate has fulfilled the conditions of the Resolution and Regulations appropriate for the degree of Doctor of Philosophy in the University of St Andrews and that the candidate is qualified to submit this thesis in application for that degree.
date: 01/05/2009 signature of supervisor:

In submitting this thesis to the University of St Andrews we understand that we are giving permission for it to be made available for use in accordance with the regulations of the University Library for the time being in force, subject to any copyright vested in the work not being affected thereby. We also understand that the title and the abstract will be published, and that a copy of the work may be made and supplied to any bona fide library or research worker, that my thesis will be electronically accessible for personal or research use unless exempt by award of an embargo as requested below, and that the library has the right to migrate my thesis into new electronic forms as required to ensure continued access to the thesis. We have obtained any third-party copyright permissions that may be required in order to allow such access and migration, or have requested the appropriate embargo below.

The following is an agreed request by candidate and supervisor regarding the electronic publication of this thesis:

Access to Printed copy and electronic publication of thesis through the University of St Andrews.

date: 01/05/2009 signature of candidate: signature of supervisor:

Acknowledgements

Thanks to:

- My supervisor, Thomas Neukirch.
- Michael Hesse.
- My parents for all their support.

Finally, I would like to acknowledge the financial assistance from the Science and Technology Facilities Council(STFC).

Contents

Chapter 1

Introduction

1.1 Motivation

A plasma is any state of matter which contains enough free charged particles for electromagnetic forces to dominate its behaviour. In many areas of astrophysics the physics of plasmas play a crucial role. In astrophysics the physics of plasmas are important in understanding the interaction of the solar wind with the Earth's magnetosphere, the dynamics of the Sun and stars and many other astrophysical bodies. In fact the majority of the matter in the universe can be described as plasma. In the laboratory the physics of plasmas also plays a vital role in controlled thermonuclear fusion, in which the nuclei of deuterium and tritium are heated to tens of millions of degrees, under which conditions they exist in a plasma state.

Magnetic activity processes in the coronae of the Sun and of other stars belong to the most fascinating phenomena in plasma astrophysics. Astrophysical plasmas usually satisfy the conditions of ideal magnetohydrodynamics (MHD), but nevertheless non-ideal processes such as, for example, magnetic reconnection are known to play an important role in most coronal activity processes.

It is well-known that one way of overcoming this apparent contradiction is the formation of strongly localized regions of strong electric current, i.e. magnetic current sheets. In these regions ideal MHD can break down, allowing for non-ideal processes such as magnetic reconnection to occur. Although these non-ideal processes occur only on very small length scales, they still have a global effect in the release of stored magnetic energy.

To understand the physics behind these non-ideal processes better, kinetic theory instead of MHD has to be used and because the time and length scales on which these processes occur are usually much shorter than typical collision times and mean free paths, it is appropriate to use collisionless theory.

Plasma equilibria are suitable starting points for investigating these processes. For collisionless plasmas, the most relevant equilibria are self-consistent solutions of the Vlasov-Maxwell (VM) equations (e.g. Krall and Trivelpiece 1973; Schindler 2007).

1.2 Plasma Models

1.2.1 Kinetic Models

The most basic description of a plasma can be given by a statistical treatment based on the kinetic theory of matter. Following the description of Boyd and Sanderson (2003) this model assumes that there is a single particle distribution function $f_s(\mathbf{r}, \mathbf{v}, t)$ for each particle species which satisfies the kinetic equation

$$\frac{\partial f_s}{\partial t} + \mathbf{v} \cdot \frac{\partial f_s}{\partial \mathbf{r}} + \frac{q_s}{m_s} (\mathbf{E} + \mathbf{v} \times \mathbf{B}) \cdot \frac{\partial f_s}{\partial \mathbf{v}} = \left(\frac{\partial f_s}{\partial t} \right)_c , \tag{1.1}$$

where q_s and m_s are the charge and mass of each species respectively and $f_s(\mathbf{r}, \mathbf{v}, t) d^3r d^3v$ is the probability of finding a particle within the phase space volume $d^3r d^3v$ centred at $(\mathbf{r}, \mathbf{v})$. All observable properties are then found by taking moments of the distribution function, where the distribution function is normalised such that the number density and bulk velocities are given by,

$$n_s(\mathbf{r}, t) = \int_{-\infty}^{\infty} f_s d^3v, \tag{1.2}$$

$$\mathbf{u}_s(\mathbf{r}, t) = \frac{1}{n_s} \int_{-\infty}^{\infty} \mathbf{v} f_s d^3v. \tag{1.3}$$

The charge density and current density are then given by summing over each particle species,

$$\sigma = \sum_s q_s n_s, \tag{1.4}$$

$$\mathbf{j} = \sum_s q_s n_s \mathbf{u}_s. \tag{1.5}$$

Coupled to these equations are the full set of Maxwell's equations,

$$\nabla \cdot \mathbf{E} = \frac{\sigma}{\epsilon_0}, \tag{1.6}$$

$$\nabla \times \mathbf{E} = -\frac{\partial \mathbf{B}}{\partial t}, \tag{1.7}$$

$$\nabla \times \mathbf{B} = \frac{1}{c^2} \frac{\partial \mathbf{E}}{\partial t} + \mu_0 \mathbf{j}, \tag{1.8}$$

$$\nabla \cdot \mathbf{B} = 0. \tag{1.9}$$

Therefore the electric and magnetic fields in Eq. (1.1) are self-consistent as they depend on f_s via the source terms σ and $\mathbf{j}$. The term on the right hand side of Eq. (1.1) is referred to as the collision term and describes particle-particle interactions. Therefore, if the mathematical expression for the collision term is known then Eq. (1.1) describes the evolution of the distribution function f_s. In many astrophysical plasmas it is often a reasonable assumption to neglect collisions altogether. A collisionless plasma can be assumed as long as the mean free path of each particle species is much greater than the length scale over which the macroscopic fields vary or alternatively the collision frequency is much less than the typical frequency which characterises the time rate of change of the macroscopic fields. As described by Schindler (2007), 'typically the collision terms arise from Coulomb collisions between the charged particles. They are based on electric fluctuations in the Debye sphere, a sphere with the Debye length,

$$\lambda_D = \left(\frac{\epsilon_0 k_B T_e}{e^2 n_e}\right)^{\frac{1}{2}} = \frac{1}{\omega_{pe}}\left(\frac{k_B T_e}{m_e}\right)^{\frac{1}{2}}, \tag{1.10}$$

as its radius'. Here n_e is the electron number density and T_e is the electron temperature. The electron plasma frequency, here denoted by ω_{pe} is

$$\omega_{pe} = \left(\frac{e^2 n_e}{\epsilon_0 m_e}\right)^{\frac{1}{2}}. \tag{1.11}$$

The typical Coulomb collision terms scale as $\ln(\Lambda_p)/\Lambda_p$, where

$$\Lambda_p = \frac{4\pi}{3}\lambda_D^3 n_e \tag{1.12}$$

is the plasma parameter, which equals the number of electrons in a Debye sphere (Schindler 2007; Boyd and Sanderson 2003). It can therefore be seen that more particles in a Debye sphere causes less collective fluctuations.

	Photosphere	Corona
Number Density n $[m^{-3}]$	8×10^{22}	1×10^{15}
Temperature T $[K]$	6×10^{3}	2×10^{6}
Magnetic Field Strength B $[T]$	2×10^{-1}	1×10^{-2}
Length L $[m]$	1×10^{6}	3×10^{7}
Debye Length λ_D $[m]$	2×10^{-8}	3×10^{-3}
Plasma Parameter	2	1×10^{8}

Table 1.1: Typical values of various plasma quantities are shown for the solar photosphere and corona where the photospheric values correspond to a sunspot and the coronal values an active region (Schindler 2007). The table also includes the value of the Debye length calculated on the basis of these characteristic values.

The plasma parameter scales as $T_e^{3/2}/n_e^{1/2}$ and therefore for high temperatures and low densities,

this describes the regime of collisionless plasmas. Typical values of various plasma quantities are shown in Table 1.1 (Schindler 2007) for the solar photosphere and corona where the photospheric values correspond to a sunspot and the coronal values to an active region. Whereas the photosphere is clearly influenced by collisions, the solar corona is approximately collisionless for the small length scales associated with the non-ideal processes that are of interest, such as, for example magnetic reconnection. For a collisionless plasma the collision term can be completely neglected and the kinetic equation is

$$\frac{\partial f_s}{\partial t} + \mathbf{v} \cdot \frac{\partial f_s}{\partial \mathbf{r}} + \frac{q_s}{m_s} \left(\mathbf{E} + \mathbf{v} \times \mathbf{B} \right) \cdot \frac{\partial f_s}{\partial \mathbf{v}} = 0, \tag{1.13}$$

and is known as the Vlasov equation which states that the distribution function is constant along particle trajectories. The characteristic equations of the Vlasov equation are just the equations of motion of a particle moving in an electromagnetic field,

$$\frac{d\mathbf{r}}{dt} = \mathbf{v}, \tag{1.14}$$

$$\frac{d\mathbf{v}}{dt} = \frac{q_s}{m_s} \left[\mathbf{E} + \mathbf{v} \times \mathbf{B} \right], \tag{1.15}$$

and hence particle trajectories are just the characteristic curves of the Vlasov equation. Collisionless plasma models usually must solve for the evolution of the plasma numerically. Examples of methods for doing this include particle in cell codes (PIC) and Vlasov codes.

1.2.2 A Fluid Description

Fluid descriptions describe the behaviour of the plasma and its interaction with the magnetic field in terms of observables which depend only on space and time. These observables are found by multiplying the kinetic equation, Eq. (1.1) by various powers of velocity $\psi(\mathbf{v})$ and integrating over velocity space. This process produces equations for quantities that depend only on $(\mathbf{r}, t)$. The powers of $\mathbf{v}$ are chosen to represent density ($\psi = 1$), momentum ($\psi = m_s \mathbf{v}$) and energy ($\psi = 1/2 m_s v^2$). In general multiplying Eq. (1.1) by powers of velocity $\psi(\mathbf{v})$ and integrating over velocity space gives the general moment equation,

$$\frac{\partial}{\partial t} \left(n_s \left\langle \psi(\mathbf{v}) \right\rangle_s \right) + \frac{\partial}{\partial \mathbf{r}} \cdot \left(n_s \left\langle \psi(\mathbf{v}) \mathbf{v} \right\rangle_s \right) - \frac{n_s q_s}{m_s} \mathbf{E} \cdot \left\langle \frac{\partial \psi(\mathbf{v})}{\partial \mathbf{v}} \right\rangle_s$$
$$- \frac{n_s q_s}{m_s} \left\langle (\mathbf{v} \times \mathbf{B}) \cdot \frac{\partial \psi(\mathbf{v})}{\partial \mathbf{v}} \right\rangle_s = \int_{-\infty}^{\infty} \psi(\mathbf{v}) \left(\frac{\partial f_s}{\partial t} \right)_c d^3 v, \tag{1.16}$$

where

$$\langle \psi(\mathbf{v}) \rangle = \frac{1}{n_s} \int \psi(\mathbf{v}) f_s d^3 v. \tag{1.17}$$

Firstly it must be noted that with each higher power of $\mathbf{v}$ the resulting moment equation will contain the quantity that refers to the next higher order moment. In this way the Eq. (1.16) gives an infinite set of equations. Therefore a method of truncation must always be chosen to reduce the number of quantities to a manageable number. This is known as the closure condition. Some important physical quantities that result from taking the first and second order moments are the pressure tensor which is defined as,

$$P_{ij,s} = m_s \int_{-\infty}^{\infty} (v_i - u_{i,s})(v_j - u_{j,s}) f_s d^3v = m_s n_s \left\langle w_{i,s} w_{j,s} \right\rangle , \tag{1.18}$$

and the heat flux tensor,

$$Q_{ijk,s} = m_s \int_{-\infty}^{\infty} (v_i - u_{i,s})(v_j - u_{j,s})(v_k - u_{k,s}) f_s d^3v = m_s n_s \left\langle w_{i,s} w_{j,s} w_{k,s} \right\rangle , \tag{1.19}$$

where the deviation from the average velocity $w_{i,s}$ is defined as,

$$w_{i,s} = v_i - u_{i,s}. \tag{1.20}$$

Evaluating the zero order moment ($\psi = 1$), 1st order moment ($\psi = m_s \mathbf{v}$) and second order moment ($\psi = 1/2 m_s v^2$) and making the assumption that the pressure tensor is isotropic where,

$$P_{ij,s} = \begin{cases} 0 & i \neq j \\ P_{11,s} = P_{22,s} = P_{33,s} = \frac{1}{3} P_{ii,s} = P_s & i = j \end{cases} \tag{1.21}$$

and assuming that heat flux tensor components can be ignored then this gives the fluid equations (e.g. Schindler 2007):

$$\frac{\partial \rho_s}{\partial t} + \nabla \cdot (\rho_s \mathbf{u_s}) = 0, \tag{1.22}$$

$$\rho_s \frac{\partial \mathbf{u_s}}{\partial t} + \rho_s \mathbf{u_s} \cdot \nabla \mathbf{u_s} = -\nabla P_s + \mathbf{j_s} \times \mathbf{B} + \sigma_s \mathbf{E} + \mathbf{M_{cs}}, \tag{1.23}$$

$$\frac{\partial P_s}{\partial t} + \mathbf{u_s} \cdot \nabla P_s + \frac{5}{3} P_s \nabla \cdot \mathbf{u_s} + N_{cs} = 0, \tag{1.24}$$

$$\sum_s \sigma_s = 0, \tag{1.25}$$

$$\nabla \times \mathbf{E} = -\frac{\partial \mathbf{B}}{\partial t}, \tag{1.26}$$

$$\nabla \cdot \mathbf{B} = 0, \tag{1.27}$$

$$\nabla \times \mathbf{B} = \mu_0 \sum_s \mathbf{j_s}, \tag{1.28}$$

where it has also been assumed that the plasma satisfies quasineutrality and $\rho_s = m_s n_s$ is the mass density of each particle species. In Eqs. (1.23) and (1.24) $\mathbf{M_{cs}}$ and N_{cs} refer to the contributions to the momentum equation and to the energy equation from the collision term. These

terms therefore represent the exchange of momentum and energy due to collisions. It is assumed that collisions take place only between neighbouring particles such that energy and momentum within the volume element d^3r is conserved during a collision. This is achieved by assuming the scale size of the volume element is much larger than the mean free path. It is important to note that in Eqs. 1.23 and 1.24 the assumption of isotropic pressure may not be a valid assumption for studies of the dynamics of collisionless plasmas. In collisionless reconnection for example, the off-diagonal terms of the electron pressure tensor are very important in understanding the physics of the diffusion region (e.g. Hesse et al. 1999, 2004; Ricci et al. 2004a; Pritchett 2001).

Finally it is possible to construct a single fluid set of equations which removes all reference to the individual particle species. Summing the fluid equations for each species and defining,

$$\rho = \rho_i + \rho_e, \tag{1.29}$$
$$P = P_e + P_i, \tag{1.30}$$
$$\mathbf{u} = \frac{(\rho_i \mathbf{u_i} + \rho_e \mathbf{u_e})}{\rho} \tag{1.31}$$
$$\mathbf{M_{ce}} + \mathbf{M_{ci}} = \mathbf{0}, \tag{1.32}$$
$$N_{ce} + N_{ci} = 0, \tag{1.33}$$

the resistive MHD equations are (e.g. Schindler 2007),

$$\frac{\partial \rho}{\partial t} + \nabla \cdot (\rho \mathbf{u}) = 0, \tag{1.34}$$
$$\rho \frac{\partial \mathbf{u}}{\partial t} + \rho \mathbf{u} \cdot \nabla \mathbf{u} = -\nabla P + \mathbf{j} \times \mathbf{B}, \tag{1.35}$$
$$\mathbf{E} + \mathbf{u} \times \mathbf{B} = \eta \mathbf{j}, \tag{1.36}$$
$$\left(\frac{\partial}{\partial t} + \mathbf{u} \cdot \nabla\right)\left(\frac{P}{\rho^\gamma}\right) = \frac{\gamma - 1}{\rho^\gamma} \eta j^2, \tag{1.37}$$
$$\nabla \times \mathbf{E} = -\frac{\partial \mathbf{B}}{\partial t}, \tag{1.38}$$
$$\nabla \cdot \mathbf{B} = 0, \tag{1.39}$$
$$\nabla \times \mathbf{B} = \mu_0 \mathbf{j}. \tag{1.40}$$

Equation (1.36) is called the resistive Ohm's law. The term $\eta \mathbf{j}$ arises from the collision term $\mathbf{M_{ce}}$ in the two fluid momentum equation where it is assumed that $\mathbf{M_{ce}}$ is proportional to the relative drift between the electrons and the ions which is equivalent to the current density. The η term denotes resistivity. Therefore, it is important to remember that in the framework of resistive MHD the resistive term on the RHS of Ohm's law requires the existence of the collision term in the kinetic equation.

Ideal MHD gives an equivalent set of equations except that the resistive term in Ohm's law is neglected. In ideal MHD the field lines are frozen into the plasma. Many astrophysical plasmas

on large scales satisfy the conditions of ideal MHD.

Fluid models are applied widely in the physics of space plasmas and laboratory plasmas (e.g. tokamaks). It is always important to assess the validity of a fluid model. First of all the fluid model assumes that the characteristic scale lengths must be a lot larger than the mean free path. Second, the assumption of an isotropic pressure tensor assumes that the collision time is a lot less than the typical time scales of the plasma such that the any anisotropies are quickly smoothed out over a few collision times and therefore the local distribution function is that of a Maxwellian distribution function. In fact in many space plasmas of interest, especially when considering activity processes that occur on small length scales and fast timescales the plasma can be described as collisionless i.e. the mean free path is much larger than the typical length scale and the collision time is a lot larger than the typical time scale.

1.3 Magnetic Reconnection

As already mentioned astrophysical plasmas in general satisfy the conditions of ideal MHD. Non-ideal processes though, for example in the corona of the Sun, play a vital role in activity processes. This apparent contradiction can be overcome by the formation of strongly localised regions of strong electric current, i.e. magnetic current sheets. In these regions ideal MHD can break down allowing for non-ideal processes to occur. Although these non-ideal processes occur on very small length scales, they will still have a global effect in the release of stored magnetic energy. Perhaps the most important of these non-ideal processes is magnetic reconnection. Magnetic reconnection is thought to play a role in solar flares, coronal mass ejections and coronal heating in the solar corona (e.g. Priest and Forbes 2000). It also plays a major role in the interaction of the solar wind and the magnetosphere, transferring energy from the solar wind into the magnetosphere (e.g. Schindler 2007). In general the magnetic field is frozen into the plasma and satisfies the frozen in contraint,

$$\mathbf{E} + \mathbf{u} \times \mathbf{B} = \mathbf{0}. \tag{1.41}$$

If the RHS of Eq. (1.41) is non-zero then the magnetic field is no longer frozen into the field and magnetic reconnection can occur. Magnetic reconnection leads to a reconfiguration of the magnetic field to a lower energy state. Energy conservation means that magnetic energy is converted to thermal, non-thermal and kinetic energy with particles being accelerated to super-Alfvénic speeds where the Alfvén speed in a magnetic field B_0 with a density ρ_0 is defined as,

$$v_A = \frac{B_0}{(\mu_0 \rho_0)^{\frac{1}{2}}}. \tag{1.42}$$

An important question is by what mechanism is the frozen in flux constraint broken? If you multiply the electron kinetic equation, Eq. (1.1) by $m_e\mathbf{v_e}$ and integrate over all of velocity space then the generalised Ohm's law is (Schindler 2007),

$$\mathbf{E}+\mathbf{u}\times\mathbf{B}=-\frac{1}{en_e}\nabla\cdot\mathbf{P_e}+\frac{\mathbf{j}\times\mathbf{B}}{en_e}-\frac{m_e}{e}\left(\frac{\partial\mathbf{u_e}}{\partial t}+\mathbf{u_e}\cdot\nabla\mathbf{u_e}\right)+\eta\mathbf{j}, \tag{1.43}$$

where quasineutrality has been assumed ($n_e=n_i$), $m_e\ll m_i$ and,

$$\mathbf{j} = en_i\mathbf{u_i}-en_e\mathbf{u_e}, \tag{1.44}$$

$$\mathbf{u} = \frac{m_i\mathbf{u_i}+m_e\mathbf{u_e}}{m_i+m_e}. \tag{1.45}$$

The $\eta\mathbf{j}$ term is the contribution from the collision term on the RHS of Eq. (1.1). The terms on the RHS are the pressure term where the full pressure tensor is included, the Hall term, the electron inertia term and the resistive term.

In resistive MHD only the resistive term on the RHS of Eq. (1.43) is considered. The two most famous MHD models of reconnection are Sweet-Parker reconnection (Sweet 1958a,b; Parker 1957, 1963) and Petschek reconnection (Petschek 1964). A detailed description of these two models is given in Priest and Forbes (2000).

Copyrighted Image

Figure 1.1: A figure illustrating the Sweet-Parker configuration (Priest and Forbes 2000).

In the Sweet-Parker model a steady state is assumed. An extended region of size $2L\times 2l$ is assumed which is called the diffusion region. Magnetic flux enters the diffusion region from the top and bottom and is ejected at the Alfvén speed from the sides of the diffusion region. An illustration of the Sweet-Parker configuration is shown in Figure 1.1. The reconnection rate which is defined as the rate at which magnetic flux can be brought into the diffusion region i.e. the inflow

speed v_i, where the subscript i denotes inflow, is given by,

$$v_i = \frac{v_{Ai}}{R_{mi}^{1/2}}, \tag{1.46}$$

where $v_{Ai} = B_i/\sqrt{\mu_0 \rho}$ is the inflow Alfvén speed and $R_i = \mu_0 L v_{Ai}/\eta$ is the inflow magnetic Reynold's number based on the inflow Alfvén speed. In general $R_i \gg 1$ and the reconnection rate is of the order of $10^{-3} - 10^{-6}$ of the Alfvén speed which is much too slow to describe a solar flare.

Petschek (Petschek 1964) considered a configuration with a small Sweet-Parker regime which acts as a source for four slow mode shocks. Petschek showed that the reconnection rate is now much larger than the Sweet-Parker model. He estimated an upper limit for the non-dimensional reconnection rate M_A ($M_A = v_i/v_{Ai}$) where,

$$M_A \approx \frac{\pi}{8 \ln R_i}, \tag{1.47}$$

which is significantly faster than the Sweet-Parker reconnection rate. Neither of these models are an exact solution of the MHD equations, but they do give a significant amount of insight into the fundamental properties of reconnection. They do not though give any details of the structure of the diffusion region.

Copyrighted Image

Figure 1.2: A figure illustrating the magnetic field configuration of a tearing mode (Biskamp 2000).

The resistive tearing mode is a resistive MHD instability and is important because the magnetic field can change its topology leading to the release of stored magnetic energy. The classical paper on the resistive tearing mode is by Furth et al. (1963). The analysis of the tearing mode in general starts from a Harris current sheet (Harris 1962) which consists of an anti-parallel magnetic field configuration with a pressure gradient across the current sheet. The linearised full set of resistive MHD equations are solved. A small perturbation is added to the magnetic field. The wavelength of the perturbation must be relatively large such that the magnetic pressure gradient is strong enough to overcome the restoring tension force and drive the tearing mode unstable, leading to the formation of a series of X and 0-points. The tearing mode configuration is shown in Figure 1.2. A boundary layer develops at the centre of the current sheet. The solution to the resistive

tearing mode is found by carrying out a boundary layer analysis to determine the inner and outer solutions and the dispersion relation (e.g. Schindler 2007). In the case of a more general $\mathbf{k}$ vector the tearing mode occurs at singular layers where $\mathbf{k} \cdot \mathbf{B} = 0$. These are known as resonant layers.

The growth rate of the tearing mode is given approximately by (Priest 1984),

$$\gamma = \left(\tau_d^3 \tau_A^2 (kl)^2\right)^{-1/5}, \tag{1.48}$$

where k is the wavenumber, l is the thickness of the current sheet, τ_d is the diffusion time and τ_A is the characteristic Alfvén travel time to cross the sheet moving at the Alfvén speed, for wavelengths in the approximate range $(\tau_A/\tau_D)^{1/4} < kl < 1$. The mode with the longest wavelength has the fastest growth, namely $\gamma = (\tau_A \tau_D)^{-1/2}$, a value that is the geometric mean of the diffusion and Alfvén travel times (Priest 1984). For typical values for an active region in the solar corona (see Table 1.1) the diffusion time is of the order of 10^{15} seconds and the Alfvén travel time of the order seconds which is not fast enough to explain the impulsive phase of a flare which represents a release of magnetic energy over a time scale of 100-1000s. This suggests that the length scales must be extremely small (100-1000m) if the tearing mode is to be used to describe the impulsive phase of a flare.

In all the MHD models described above magnetic reconnection seems to require the development of very small length scales to give fast reconnection rates. On these length scales the plasma in many parts of the magnetosphere and also in the corona of the Sun can be described as collisionless. This corresponds to the resistive term in Ohm's law, Eq. (1.43) being neglected. Writing the generalised Ohm's law in the form,

$$\mathbf{E} + \mathbf{u_e} \times \mathbf{B} = \frac{1}{n_e q_e} \nabla \cdot \mathbf{P_e} + \frac{m_e}{q_e} \left(\frac{\partial \mathbf{u_e}}{\partial t} + \mathbf{u_e} \cdot \nabla \mathbf{u_e} \right), \tag{1.49}$$

then the terms that can now give rise to the large reconnection electric field and break the frozen in condition are the pressure term and the electron inertia term. In the majority of studies of collisionless reconnection, it is found that the dominant contribution to the reconnection electric field is due to gradients of the off-diagonal components of the electron pressure tensor (e.g. Hesse et al. 1999, 2001a; Pritchett 2001; Hesse et al. 2004; Kuznetsova et al. 2001). Therefore modelling reconnection in the corona using an isotropic, scalar pressure is questionable, at least if you want to get the electron physics of the diffusion region correct.

The majority of collisionless reconnection studies start from the Harris sheet (Harris 1962) and reconnection proceeds via the collisionless tearing mode. This is similar in many ways to the resistive tearing mode where a boundary layer develops at the centre of the current sheet and the instability leads to reconnection with a series of X and O-points being formed. A linear stability analysis for the collisionless tearing mode has been carried out for the Harris sheet by solving the

linear Vlasov equation. The classical paper on the collisionless tearing mode is by Laval et al. (1966). Biskamp (2000) gives a qualitative derivation of the growth rate. The growth rate is approximately,

$$\gamma \approx \frac{v_{th,e}}{L}\left(\frac{r_{Le}}{L}\right)^{3/2}\left(1+\frac{T_e}{T_i}\right)\left(1-k^2L^2\right), \tag{1.50}$$

where r_{Le} is the electron Larmor radius in the asymptotic magnetic field, k is the wavenumber of the perturbation, $v_{th,e}$ is the electron thermal speed, T_e and T_i are the electron and ion temperatures and L is the width of the box. It is clear that for $kL = 1$ the growth rate is zero. The growth rate is in fact proportional to $m_e^{1/4}$.

The Geospace Environmental Modelling (GEM) Magnetic Reconnection Challenge (Birn and Hesse 2001) was an investigation of collisionless reconnection using a variety of different numerical codes from a non-linear MHD code all the way through to a full electromagnetic particle-in-cell (PIC) code. The initial condition was chosen to be a Harris sheet with no guide field, i.e. the challenge seeked to understand and compare the results from different codes of modelling reconnection in a collisionless high-β plasma. In particular they compared the reconnection rates and found that the evolutions were almost identical as long as the Hall term was included. The pure resistive MHD code in comparison did not match the reconnection rate very well and was significantly slower. Therefore, on the large scale the reconnection rate is independent of the method by which the frozen in constraint is broken as long as the Hall term is included. On the other hand, for a detailed understanding of the electron physics in the diffusion region a full particle picture is necessary, which includes the full electron pressure tensor.

1.4 Aims

The magnetic field in the corona of the Sun satisfies to a good approximation the force-free condition $\mathbf{j} \times \mathbf{B} = \mathbf{0}$. On the small length scales that magnetic reconnection can occur the plasma can be described as collisionless. The majority of collisionless reconnection studies start from the Harris sheet (e.g. Pritchett 2001; Hesse et al. 2001a; Shay et al. 2001; Scholer et al. 2003). The Harris sheet is most appropriate for studying high-β plasmas due to the fact that the plasma-β at the centre of the sheet is infinite. A constant guide field can be added to the Harris sheet to model lower-β plasmas (e.g. Ricci et al. 2004a; Pritchett and Coroniti 2004; Hesse et al. 2004) but importantly the guide field does not change the characteristic properties of the equilibrium. The constant guide field does introduce a field aligned current but the field aligned current density is completely independent of the strength of the guide field that is added. The constant guide field is also a potential magnetic field and therefore does not add any free-energy to the magnetic field. In a force-free field where the current density is coupled to the shear and twist of the field, if you

increase the current density you increase the shear of the field and also the free-energy. Therefore, to study collisionless reconnection in the solar corona it would seem more appropriate to use force-free magnetic field configurations as initial conditions.

As already mentioned plasma equilibria are suitable starting points for investigating non-ideal plasma processes. For collisionless plasmas, the most relevant equilibria are self-consistent solutions of the Vlasov-Maxwell (VM) equations Krall and Trivelpiece (1973); Schindler (2007). Due to the generic structure of current sheets they can be modelled by 1D equilibria as a first approximation. Up until this point the only 1D force-free Vlasov-Maxwell (VM) equilibrium that is known is that of a periodic linear force-free magnetic field (Sestero 1967; Bobrova and Syrovatskiĭ 1979; Correa-Restrepo and Pfirsch 1993; Bobrova et al. 2001). This solution is not ideal as in general the magnetic field in the corona is a non-linear force-free field. Also the periodic nature of the solution does not represent a very realistic magnetic field configuration. One of the major aims of this work was therefore to extend the theory of 1D Vlasov-Maxwell equilibria to go beyond the Harris sheet to include a range of sheared magnetic field configurations. In particular finding a distribution function that corresponds to the force-free Harris sheet was of great interest. In addition to finding a distribution function for the force-free Harris sheet, it was also important to find distribution functions that depending on the choice of parameters give a range of equilibria that can describe the transition between an anti-parallel magnetic field configuration with a strong plasma pressure gradient through to a force-free field where the magnetic pressure due to the shear component of the magnetic field maintains the force balance and the plasma pressure is constant.

The aim was then to use these Vlasov-Maxwell equilibria as initial conditions in simulations of magnetic reconnection using a fully electromagnetic particle in cell code. The main focus of these investigations was to compare simulations starting from anti-parallel magnetic field configurations with varying strengths of guide magnetic field to simulation runs starting from self-consistent force-free Vlasov-Maxwell equilibria. The results were to be compared to simulations starting from the Harris sheet with varying strengths of guide field. In particular the structure of the diffusion region was investigated with emphasis on understanding the dominant term in the collisionless Ohm's law which gives rise to the reconnection electric field and to confirm that this is equivalent to reconnection simulations starting from the Harris sheet. It will be shown that the dominant contribution to the reconnection electric field in the vicinity of the X-point is due to gradients of off-diagonal components of the electron pressure tensor. An investigation of the structure of these off-diagonal pressure tensor components as the strength of the guide field increases and for the force-free cases is given.

Therefore this thesis is laid out with a discussion of simple 1D MHD equilibria and multi-fluid equilibria in Chap. 2 . Chapter 3 gives a detailed discussion of 1D Vlasov-Maxwell equilibria, with particular emphasis on the general properties of 1D force-free VM equilibria. Chapter 4 describes in detail the methods of particle in cell simulation for studying collisionless plasma

dynamics and Chap. 5 presents particle in cell simulation results starting from a wide range of initial conditions with the focus on investigating the structure of the diffusion region. The conclusions and future work are presented in Chap. 6.

Chapter 2

MHD and Multi-Fluid Equilibrium Theory

2.1 Magnetohydrostatics

Magnetohydrostatics is the theory of the static equilibria of the MHD equations. It considers the states for which $\partial/\partial t = 0$ and the bulk velocity $\mathbf{u} = \mathbf{0}$. Examination of the MHD equations given in Chap. 1 shows that under these assumptions these equations reduce to the equations of magnetohydrostatics. Immediately you can see that the continuity equation is automatically satisfied. Ignoring gravity, the momentum equation reduces to,

$$\nabla P - \mathbf{j} \times \mathbf{B} = \mathbf{0}. \tag{2.1}$$

Ampère's law and the solenoidal condition remain unchanged,

$$\mu_0 \mathbf{j} = \nabla \times \mathbf{B}, \tag{2.2}$$

$$\nabla \cdot \mathbf{B} = 0. \tag{2.3}$$

In addition the electric field can be written as the gradient of a scalar function ϕ,

$$\nabla \times \mathbf{E} = \mathbf{0} \Rightarrow \mathbf{E} = -\nabla\phi. \tag{2.4}$$

In summary, the three magnetohydrostatic equations are

$$\nabla P - \mathbf{j} \times \mathbf{B} = \mathbf{0}, \tag{2.5}$$

$$\mu_0 \mathbf{j} = \nabla \times \mathbf{B}, \tag{2.6}$$

$$\nabla \cdot \mathbf{B} = 0. \tag{2.7}$$

These equations must be solved in addition to an equation of state that must be specified.

So why study magnetohydrostatics? A good answer to this question is given in Neukirch (1998). In these notes the author states that the MHD equations can be thought of as 'a set of equations describing extremely complicated dynamical systems. In the study of dynamical systems it is always useful to start with a study of the simplest solutions and their bifurcation properties. These are usually the stationary states, in the MHD case the static equilibria.'

Therefore, if you are interested in understanding the complicated dynamical processes that can occur through investigating the MHD equations it is important to understand the properties of the equilibria that satisfy the MHS equations. For many numerical simulations that examine the evolution of the plasma an understanding of equilibria is vital. It is these equilibria that will often act as the initial state in any simulation run. The physical properties of the equilibria are important as they represent different initial plasma states and can lead to different dynamical behaviour. Therefore, by understanding the different equilibria, it may be possible to consider those which have properties closer to the particular space plasma you wish to model. For example, the solar corona is often described as a low-β plasma, where the fields can be described as approximately force-free.

A force-free field magnetic field satisfies the condition that,

$$\mathbf{j} \times \mathbf{B} = \mathbf{0}, \tag{2.8}$$

which means that the other forces in the momentum equation, Eq. (2.5) are negligible or balance each other. In the simplest case this condition can be met by setting $\mathbf{j} = \mathbf{0}$. A solution of this form is known as a potential field. It follows that to satisfy (2.8) generally, the condition

$$\mu_0 \mathbf{j} = \alpha \mathbf{B} \tag{2.9}$$

must be satisfied where α is in general a function that varies in space. This states that for force-free equilibria the current density is completely aligned with the magnetic field. It is easily shown that α must be constant along magnetic field lines. Taking the divergence of $\mathbf{j}$,

$$\nabla \cdot (\mu_0 \mathbf{j}) = \nabla \cdot (\nabla \times \mathbf{B}) = \nabla \cdot (\alpha \mathbf{B}) = \alpha \nabla \cdot \mathbf{B} + \mathbf{B} \cdot \nabla \alpha = \mathbf{B} \cdot \nabla \alpha = 0, \tag{2.10}$$

which implies that α must be constant on field lines. If α is a constant everywhere then you have the special case of a linear force-free field. In Sec. 2.1.1 important examples of these types of equilibria are shown.

2.1.1 1D Equilibria

In this section a number of important examples of 1D equilibria are discussed. The reason that it is important to discuss 1D MHD equilibria is that in Chap. 3 one of the major aims is to find analogous equilibra in Vlasov-Maxwell theory to those already known in MHD, in particular to find a distribution function that has the force-free Harris sheet as a solution. Therefore it is important to understand the properties of these equilibria in the framework of MHD. Consider a model where the magnetic field and all other quantities are dependent only on the z coordinate. The magnetic field has components B_x and B_y. It is assumed that they can be derived from a vector potential $\mathbf{A}$ such that $\nabla \cdot \mathbf{B} = 0$ is automatically satisfied. Considering the momentum equation, Eq. (2.5), then the force balance condition that must be met is,

$$\frac{d}{dz}\left(\frac{B^2}{2\mu_0} + P\right) = 0, \tag{2.11}$$

$$\Rightarrow \frac{B^2}{2\mu_0} + P = P_T = a\,constant. \tag{2.12}$$

This states that the plasma pressure must always balance the magnetic pressure to give the total pressure P_T in the system. The field lines will always be straight for these 1D models so there is no magnetic tension force. So within the framework of this model a valid equilibrium is any magnetic field and plasma pressure combination that satisfies the condition of force balance in Eq. (2.12).

The Harris Sheet

The Harris Sheet (Harris 1962) is perhaps the most well known 1D current sheet equilibrium. It has a one to one correspondence in MHD and Vlasov Theory. It consists of a simple antiparallel magnetic field configuration where,

$$B_x = B_0 \tanh\left(\frac{z}{L}\right) \tag{2.13}$$

$$P = \frac{P_0}{\cosh^2\left(\frac{z}{L}\right)}, \tag{2.14}$$

$$j_y = \frac{B_0}{\mu_0 L}\frac{1}{\cosh^2\left(\frac{z}{L}\right)}, \tag{2.15}$$

$$\frac{B_0^2}{2\mu_0} = P_T = P_0. \tag{2.16}$$

The profiles of the magnetic field, current density and pressure are shown in Figure 2.1(a) and a 3D plot of magnetic field lines is shown in Figure 2.1(b). In Figure 2.1(a) it should be noted that for the Harris sheet the pressure and current density have identical profiles and are therefore indis-

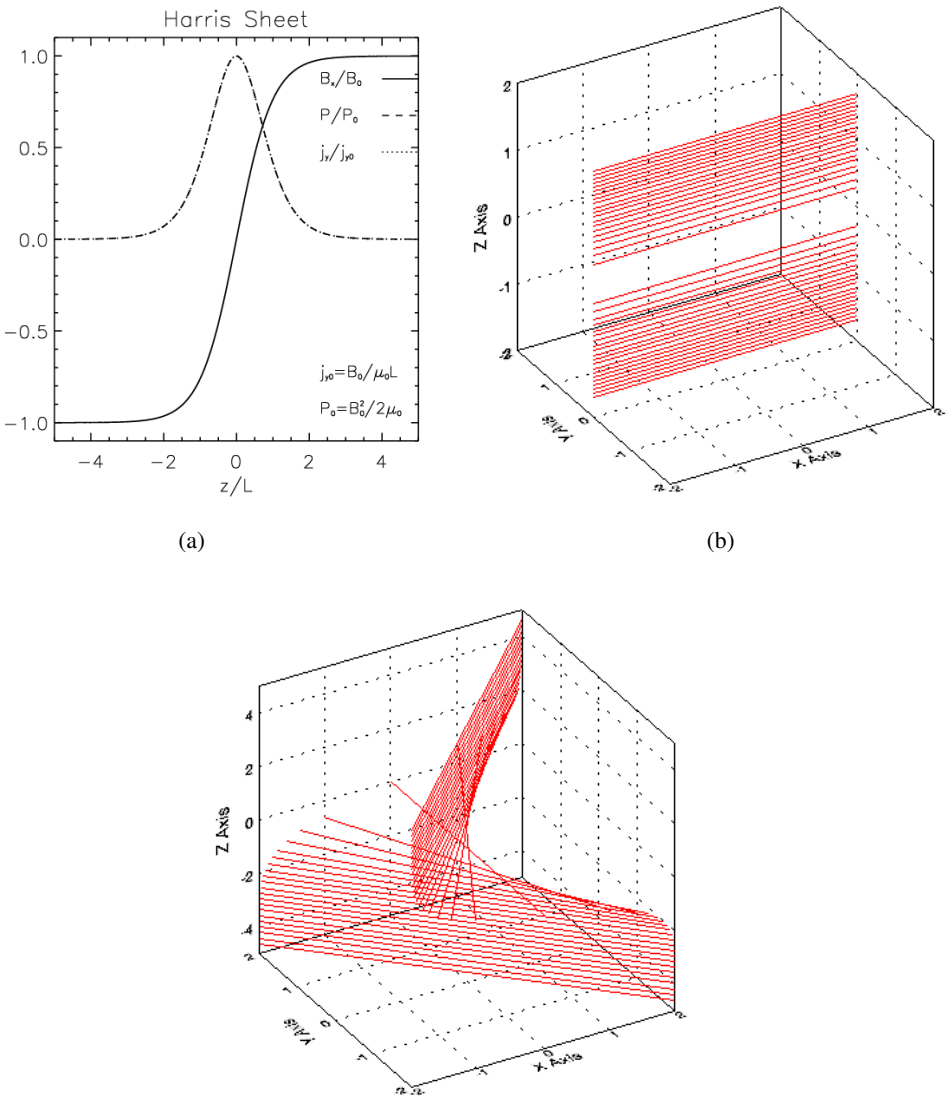

(a) (b)

(c)

Figure 2.1: A 1D plot of the profiles of the magnetic field, current density and pressure for the Harris Sheet (2.1(a)) combined with a 3D plot of magnetic field lines along z passing through $x = 0$, $y = 0$ for the Harris sheet with no guide field (2.1(b)) and for the case with $B_y = B_0$ (2.1(c)).

tinguishable. There is no y component of the magnetic field and the current density is completely perpendicular to the magnetic field. For this equilibrium it is the plasma pressure gradient that maintains the force balance, with the maximum plasma pressure at the centre of the sheet.

The Harris Sheet with Constant Guide Field

A constant guide magnetic field in the y direction can be added to the Harris sheet without altering the structure of the equilibrium. This guide field introduces a field aligned current but it is important to remember that the current density is completely independent of the strength of the guide magnetic field added. So adding a guide field to introduce a field aligned current is not the same as a force-free equilibrium where increasing the shear of the magnetic field increases the current density in the system. The constant guide field also adds no free energy to the system. Figure 2.1(c) shows a 3D plot of magnetic field lines for a constant guide field of $B_y = B_0$. It can be clearly seen how the constant guide field adds shear and twist to the system.

Linear Force-Free Field

A simple linear force-free field is given by,

$$B_x = B_0 \sin(\alpha z), \tag{2.17}$$

$$B_y = B_0 \cos(\alpha z), \tag{2.18}$$

$$B^2 = constant \tag{2.19}$$

$$j_x = \frac{\alpha B_0}{\mu_0} \sin(\alpha z), \tag{2.20}$$

$$j_y = \frac{\alpha B_0}{\mu_0} \cos(\alpha z), \tag{2.21}$$

$$P = P_T - \frac{B_0^2}{2\mu_0} = constant. \tag{2.22}$$

The profiles of the magnetic field components and current density components are shown in Figure 2.2(a) and a 3D plot of magnetic field lines is shown in Figure 2.2(b) where $\alpha = 1.0$. The magnetic fields are periodic and the pressure is constant. The current density is completely aligned with the magnetic field.

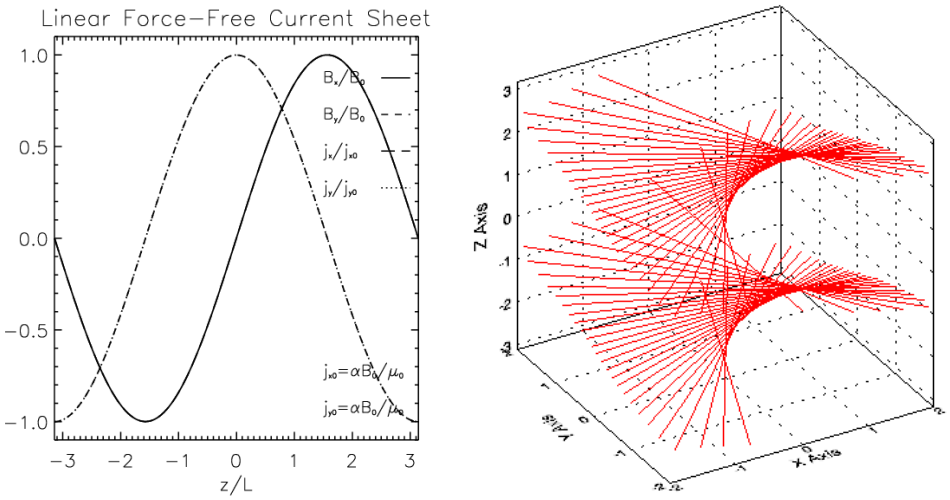

(a) (b)

Figure 2.2: 1D plots of the profiles of the magnetic field components and current density components for a linear force-free current sheet (2.2(a)) combined with a 3D plot of magnetic field lines along z passing through $x = 0$, $y = 0$ (2.2(b)).

The Force-Free Harris Sheet

In contrast to the Harris sheet there is the force-free Harris sheet. This is a 1D non-linear force-free equilibrium where,

$$B_x = B_0 \tanh\left(\frac{z}{L}\right), \tag{2.23}$$

$$B_y = \frac{B_0}{\cosh\left(\frac{z}{L}\right)}, \tag{2.24}$$

$$B^2 = constant \tag{2.25}$$

$$j_x = \frac{B_0}{\mu_0 L}\frac{\tanh\left(\frac{z}{L}\right)}{\cosh\left(\frac{z}{L}\right)}, \tag{2.26}$$

$$j_y = \frac{B_0}{\mu_0 L}\frac{1}{\cosh^2\left(\frac{z}{L}\right)}, \tag{2.27}$$

$$P = P_T - \frac{B_0^2}{2\mu_0} = constant. \tag{2.28}$$

The profiles of the magnetic field components and current density components with a 3D plot of magnetic field lines are shown in Figure 2.3. There is in this case a spatially varying symmetric y component of the magnetic field which is non-zero at the centre of the current sheet. The magnetic pressure is constant. It is the y component of the magnetic field, rather than the plasma pressure, that maintains the force balance. The current density is completely aligned with the magnetic field and the size of the current density is now directly related to the shearing of the magnetic field.

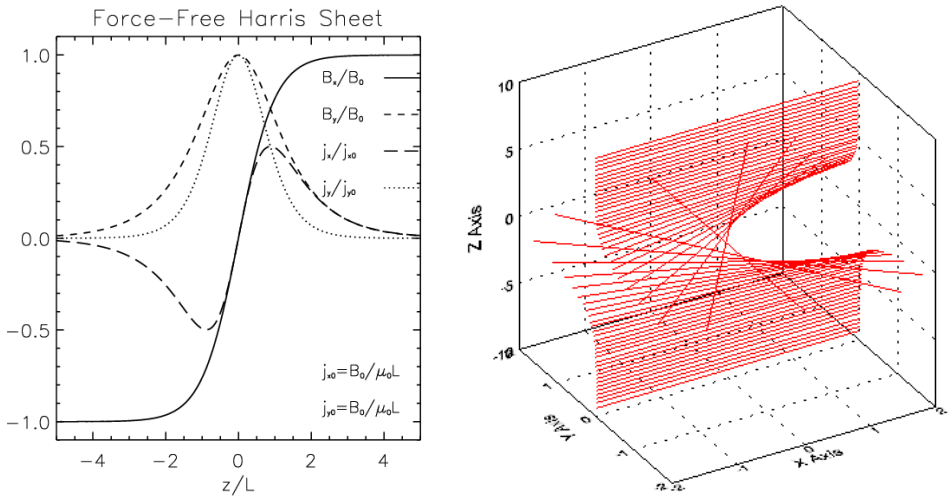

(a) (b)

Figure 2.3: 1D plots of the profiles of the magnetic field components and current density components for the force-free Harris Sheet (2.3(a)) combined with a 3D plot of magnetic field lines along z passing through $x = 0$, $y = 0$ (2.3(b)).

Increasing the shear of the field also increases the free energy in the system.

The Combined Harris Sheet

It is also possible to consider the equilbria in between these two extremes where the force balance is maintained by a balance between the y component of the magnetic field and the plasma pressure where,

$$B_x = B_{x0} \tanh\left(\frac{z}{L}\right), \tag{2.29}$$

$$B_y = \frac{\sqrt{B_{x0}^2 - 2\mu_0 P_0}}{\cosh\left(\frac{z}{L}\right)} = \frac{B_{y0}}{\cosh\left(\frac{z}{L}\right)}, \tag{2.30}$$

$$P = \frac{P_0}{\cosh^2\left(\frac{z}{L}\right)} = \frac{\left(B_{x0}^2 - B_{y0}^2\right)}{2\mu_0} \frac{1}{\cosh^2\left(\frac{z}{L}\right)}, \tag{2.31}$$

$$j_x = \frac{B_{y0}}{\mu_0 L} \frac{\tanh\left(\frac{z}{L}\right)}{\cosh\left(\frac{z}{L}\right)}, \tag{2.32}$$

$$j_y = \frac{B_{x0}}{\mu_0 L} \frac{1}{\cosh^2\left(\frac{z}{L}\right)} \tag{2.33}$$

$$2\mu_0 P_T = B_{x0}^2, \tag{2.34}$$

$$\frac{B_{x0}^2}{2\mu_0} \geq P_0. \tag{2.35}$$

These types of equilibria will have current densities which are neither completely perpendicular, nor completely aligned with the magnetic field. They will exhibit some of the properties of both the Harris sheet and the force-free Harris sheet, depending on for example the strength of the imposed shear field. A simple example is shown in Figure 2.4 which shows the profiles of the magnetic field components, current density components and the pressure in Figure 2.4(a) and a 3D plot of magnetic field in Figure 2.4(b). In this example the ratio of the the maximum value of B_y to the maximum value of B_x has been set to $B_{y0}/B_{x0} = 1/\sqrt{5}$ and the maximum value of the plasma pressure corresponds to $4/5$ of the total pressure in the system ($P_0 = 4/5P_T$).

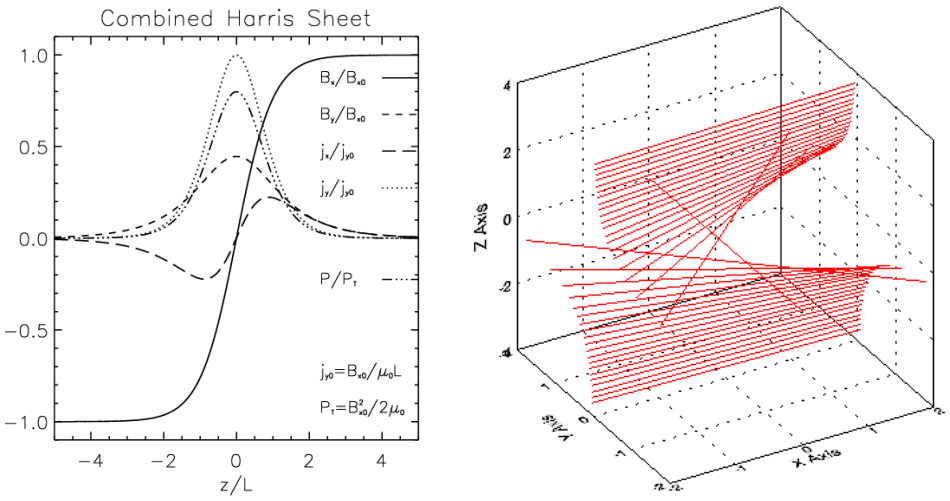

(a) (b)

Figure 2.4: 1D plots of the profiles of the magnetic field components, current density components and pressure for the combined Harris Sheet (2.4(a)) combined with a 3D plot of magnetic field lines along z passing through $x = 0$, $y = 0$ (2.4(b)).

2.2 Multi-Fluid Theory

In the Sec. 2.1.1 important 1D MHD equilibria were described. These examples gave insight in to some of the basic properties of different types of equilibria. It is highlighted, for example that a force-free equilibrium must have a field aligned current and that the field will be highly sheared and twisted, with the force balance being maintained by the magnetic pressure due to the shear field and not the plasma pressure gradient. The opposite of this is for example the Harris sheet (Harris 1962), where the force balance is maintained by the plasma pressure gradient and the current density is completely perpendicular to the magnetic field. The main aim of this work was to find kinetic equilibria analogous to the MHD equilibria shown so that the reconnection process

starting from a pure pressure gradient balanced equilibrium, for example the Harris sheet (Harris 1962), could be compared to simulations starting from a completely force-free equilibrium, for example the force-free Harris sheet. The motivation to study multi-fluid theory is that it treats each particle species as a separate fluid. This means that although it is still not as complex as the full kinetic theory it does already allow us to gain insight into the bulk properties of each particle species. This information is useful in identifying key properties that will be needed when trying to find Vlasov-Maxwell equilibria.

2.2.1 Multi-Fluid Equilibrium Equations

Consider the static states of the collisionless multi-fluid equations ($\partial/\partial t = 0$). The primary equations that must be solved are,

$$\nabla \cdot (n_s \mathbf{u_s}) = 0, \tag{2.36}$$

$$m_s n_s \left[(\mathbf{u_s} \cdot \nabla)\, \mathbf{u_s}\right] = n_s q_s \left[\mathbf{E} + \mathbf{u_s} \times \mathbf{B}\right] - \nabla P_s, \tag{2.37}$$

$$\mu_0 \mathbf{j} = \nabla \times \mathbf{B}, \tag{2.38}$$

$$\nabla \cdot \mathbf{B} = 0, \tag{2.39}$$

where the assumption of isotropic pressure has been made. These equations are the continuity equation, the momentum equation, Ampère's law and the solenoidal condition. The electric field can also be written as the gradient of a scalar function ϕ where,

$$\mathbf{E} = -\nabla\phi. \tag{2.40}$$

2.2.2 1D Equilibria

Assuming that all quantities depend only on the z coordinate and that the magnetic field can be derived from a vector potential $\mathbf{A}$. The components of the magnetic field can then be written as

$$B_x = -\frac{dA_y}{dz}, \tag{2.41}$$

$$B_y = \frac{dA_x}{dz}. \tag{2.42}$$

It is also assumed that the bulk velocities for each particle species only have components in the x and y directions,

$$\mathbf{u}_s = u_{xs}\mathbf{e_x} + u_{ys}\mathbf{e_y}. \tag{2.43}$$

By making this assumption the continuity equation, Eq. (2.36) is automatically satisfied as $u_{zs} = 0$, i.e.

$$\frac{d}{dz}(n_s u_{zs}) = 0. \tag{2.44}$$

Also the LHS of the momentum equation, Eq. (2.37) reduces to zero. Hence the primary equation that must be solved is the momentum balance for each species,

$$n_s q_s \left[\mathbf{E} + \mathbf{u_s} \times \mathbf{B}\right] - \nabla P_s = \mathbf{0}. \tag{2.45}$$

The electric field only has a z component,

$$\mathbf{E} = -\frac{d\phi}{dz}\mathbf{e_z}. \tag{2.46}$$

The magnetic field is determined by Ampère's law,

$$\nabla \times \mathbf{B} = \mu_0 \mathbf{j} \tag{2.47}$$

$$= \mu_0 \sum_s n_s q_s \mathbf{u_s}. \tag{2.48}$$

It must be assumed that n_s and P_s are related by an appropriate equation of state which can be used later to determine the separate species quantities. To determine the equilibria, a sum of the momentum equation over all species is carried out. Assuming quasineutrality,

$$\sum_s n_s q_s = 0, \tag{2.49}$$

the electric field can be eliminated. Summing the momentum equation over all species results in,

$$\mathbf{E}\left(\sum_s n_s q_s\right) + \left(\sum_s n_s q_s \mathbf{u_s}\right) \times \mathbf{B} - \sum_s \nabla P_s = \mathbf{0}, \tag{2.50}$$

and using quasineutrality the electric field is eliminated and the equation that is left to be solved is,

$$\mathbf{j} \times \mathbf{B} = \nabla P = \frac{dP}{dz}\mathbf{e_z}, \tag{2.51}$$

where the total plasma pressure is defined as

$$P = \sum_s P_s. \tag{2.52}$$

There is no field line curvature so this is just the condition that the sum of the magnetic pressure and plasma pressure across the sheet must be equal to a constant,

$$\frac{B^2}{2\mu_0} + P = P_T = a\ constant. \tag{2.53}$$

The above equations show that the equilibrium solutions are exactly the same as those in MHD. This includes the Harris sheet (Harris 1962) and the force-free Harris sheet. For a detailed description of these equilibria refer back to Sec. 2.1.1.

Two-Fluid Case

The advantage of multi-fluid theory is that information about the separate species quantities can be gained. In this section, the bulk properties for each particle species for the 1D equilibria are discussed where a two-fluid picture is assumed for simplicity. An equation of state for each fluid is given by,

$$P_s = k_B T_s n_s, \tag{2.54}$$

where T_s is the temperature of each particle species s and is assumed to be constant. Assuming quasineutrality and a two component plasma where, $q_i = -q_e = e$,

$$P = k_B n \sum_s T_s. \tag{2.55}$$

This implies the total pressure and the number density have the same profile,

$$P\ \alpha\ n. \tag{2.56}$$

Also, due to quasineutrality,

$$P_s = k_B T_s n, \tag{2.57}$$

which implies that each species has the same pressure profile as the total pressure,

$$P_s\ \alpha\ P. \tag{2.58}$$

The bulk velocities can also be calculated in this case. The equation for the current density gives one equation,

$$\mathbf{j} = n \sum_s q_s \mathbf{u_s}. \tag{2.59}$$

Without loss of generality (in line with MHD), the overall bulk velocity of the fluid is set to zero. This gives the added condition,

$$\sum_s m_s \mathbf{u_s} = \mathbf{0}. \tag{2.60}$$

For just two species this is sufficient to calculate $\mathbf{u_s}$ as there are 4 equations and 4 unknowns. Performing this calculation, the Harris sheet drift velocities are constant for each species and are only in the y direction where,

$$u_{xi} = u_{xe} = 0, \tag{2.61}$$

$$u_{yi} = -\frac{m_e u_{ye}}{m_i} = \frac{B_0}{e n_0 \mu_0 L}\frac{m_e}{m_e + m_i} = a\ constant. \tag{2.62}$$

In the case of the force-free Harris sheet there is a spatially varying drift velocity for each species in the x and y directions,

$$u_{xi} = -\frac{m_e u_{xe}}{m_i} = \frac{1}{e\mu_0 n_0 L}\frac{m_e}{(m_e + m_i)}\frac{B_x}{\cosh(\frac{z}{L})}, \tag{2.63}$$

$$u_{yi} = -\frac{m_e u_{ye}}{m_i} = \frac{1}{e\mu_0 n_0 L}\frac{m_e}{(m_e + m_i)}\frac{B_y}{\cosh(\frac{z}{L})}. \tag{2.64}$$

Finally the electric field can be calculated. Multiplying the equation of motion by m_s and summing over all species, the electric field is written as,

$$\mathbf{E} = \frac{\sum_s \frac{m_s}{q_s}\nabla P_s}{n\sum_s m_s}. \tag{2.65}$$

It is concluded that $\mathbf{E} = \mathbf{0}$ in the force-free case as the pressure for each species, P_s, must be equal to a constant. As a final remark, the equation of motion only determines the component of $\mathbf{u_s}$ perpendicular to $\mathbf{B}$. The parallel component will remain free apart from the constraint provided by the parallel component of $\mathbf{j}$. The important properties to note are that, in the case of the Harris sheet, it is the spatially varying number density that maintains the force balance. The particle density for each species is a maximum at the centre of the current sheet and drops away to zero as you move away from the centre. There is a constant average drift velocity in the y direction for each species which gives rise to the perpendicular current density j_y. In the force-free case the force balance is maintained by a spatially varying drift velocity for each species in both the x and y directions. The particles drift faster at the centre of the sheet than far away from the centre. It is these differences that are important when considering an investigation to find analogous equilibria in Vlasov theory.

2.3 Summary

In this chapter an overview of important MHD equilibria has been presented. One of the aims of this work is to investigate 1D Vlasov-Maxwell which are analogous to 1D MHD equilibria, to determine general conditions for force-free VM equilibria and in particular to find distribution functions that have the force-free Harris sheet as a solution of the steady state Vlasov-Maxwell equations. Therefore in this chapter the general properties of 1D MHD equilibria and some important cases have been discussed, as preparation for the discussion of 1D VM equilibria in Chapter 3.

Two examples of force-free fields are shown. A periodic linear force-free field and the non-linear force-free Harris sheet. In both cases in comparison to the Harris sheet the force-free solutions have highly sheared magnetic fields. In the force-free cases the force balance is always maintained by the shear magnetic field and the pressure is constant. In the opposite Harris sheet case the current density is completely perpendicular to the magnetic field and there is no shearing of the field. The force balance is maintained by the plasma pressure gradient across the sheet. A combined Harris sheet case is also shown where the force balance is maintained by a balance between the shear field and the plasma pressure gradient. In this case the magnetic fields are sheared but the shear is not as great as in the force-free case. The combined Harris sheet case shows that as you make the transition from the anti-parallel Harris sheet through to the force-free Harris sheet the magnetic fields become more sheared and there is a trade off between the plasma pressure and the shear field in the force-balance equation.

Multi-fluid equilibria have also been considered. Multi-fluid theory treats each particle species as a separate fluid and therefore gives an insight in to the bulk particle properties. Firstly it was shown that, assuming a quasineutral plasma and an isotropic pressure that the overall equilibria are identical to the MHD cases. The Harris sheet, combined Harris sheet and the force-free Harris sheet are all solutions of the multi-fluid equations.

In particular the two fluid case was considered where $q_i = -q_e = e$ and assuming an ideal equation of state and constant temperatures it was shown that the pressure profile for each species will be proportional to the quasineutral number density. Making the assumption that the overall fluid is at rest which is equivalent to the MHD case where there is no bulk velocity the average drift velocities for each particle species for the Harris sheet and force-free Harris sheet were found. In the Harris sheet case there is a constant drift in the y direction consistent with the current density being completely perpendicular to the magnetic field. In the force-free Harris sheet case there is an average drift of each particle species in the x and y directions which is spatially varying and aligned with the magnetic field, which is consistent with the definition of a force-free field. Knowledge of the average drift velocites for each particle species are important as it shows that in the Harris sheet case with a constant average drift of each particle species in the y direction

there must be a large number density at the centre of the current sheet which drops off to zero far away from the current sheet that maintains the force balance across the sheet. In the opposite case of the force-free Harris sheet case the particles drift in a direction aligned with the magnetic field and they drift faster at the centre of the current sheet and slower far away. It is the spatially varying drift velocity that maintains the force balance. Therefore a distribution function which can describe a force-free solution must give rise to a constant number density and spatially varying average drift velocities for each particle species. It will now be shown how this can be achieved in Vlasov-Maxwell equilibrium theory.

Chapter 3

Vlasov Equilibrium Theory

Parts of the work in this chapter can be found in Harrison and Neukirch (2009b) and Harrison and Neukirch (2009a).

3.1 Introduction

Plasma equilibria are suitable starting points for investigations of, for example, plasma instabilities and plasma waves. In Chap. 2, 1D fluid equilibria have been mentioned including single fluid MHD and also collisionless multi-fluid theory with the assumption of isotropic pressure. For collisionless plasmas though, the most relevant equilibria are self-consistent solutions of the stationary Vlasov-Maxwell (VM) equations, (see e.g. Krall and Trivelpiece 1973; Schindler 2007).

This chapter focuses exclusively on non-relativistic one-dimensional quasi-neutral VM equilibria with translational symmetry, with the distribution functions depending only on the Hamiltonian and the two canonical momenta corresponding to the invariant directions (here chosen to be the x- and y-directions). A large amount of work on translationally invariant 1D VM equilibria of this kind has been done before (e.g. Tonks 1959; Grad 1961; Harris 1962; Bertotti 1963; Hurley 1963; Nicholson 1963; Sestero 1964, 1966; Sestero and Zannetti 1967; Lam 1967; Parker 1967; Lerche 1967; Davies 1968, 1969; Alpers 1969; Su and Sonnerup 1971; Kan 1972; Channell 1976; Lemaire and Burlaga 1976; Roth 1976; Mynick et al. 1979; Lee and Kan 1979b,a; Greene 1993; Roth et al. 1996; Attico and Pegoraro 1999; Mottez 2003, 2004; Fu and Hau 2005; Yoon et al. 2006), especially on one-dimensional current sheets and plasma boundary layers, which are of fundamental importance for the structure and stability of plasmas as many plasma activity processes, especially magnetic reconnection, (see e.g Biskamp 2000; Priest and Forbes 2000) happen there preferentially.

The aim of this work is not only to add to the solutions of 1D VM that already exist, but to use some generic properties of the 1D VM equilibrium problem to investigate the conditions for the existence of force-free 1D VM equilibria (see e.g. Tassi et al. 2008) and to find a VM equivalent of the force-free Harris sheet. An obvious property of 1D VM equilibria is that the structure needs to be in force balance. In the quasi-neutral case this means that the sum of the magnetic pressure and one of the diagonal components of the pressure tensor has to be constant. The relevant component of the pressure tensor is the one for the single spatial coordinate upon which the equilibria depend. The z coordinate is chosen, so the component of the pressure tensor in the force balance equation will be P_{zz}. In a number of papers it has also been noticed that the translationally invariant 1D VM problem is equivalent to the motion of a pseudo-particle in a conservative pseudo-potential and/or that the force balance for the 1D VM structure is equivalent to pseudo-energy conservation (see e.g. Grad 1961; Sestero 1966; Lam 1967; Parker 1967; Lerche 1967; Alpers 1969; Su and Sonnerup 1971; Kan 1972; Channell 1976; Mynick et al. 1979; Lee and Kan 1979b,a; Greene 1993; Attico and Pegoraro 1999); the pseudo-particle analogy has also recently been used for MHD equilibria in Tassi et al. (2008).

Directly connected to the pseudo-particle analogy and the related pseudo-energy conservation law (equivalent to force balance of the 1D VM equilbrium) is the special role played by P_{zz}. As was first noticed by Grad (Grad 1961) for the case of vanishing electric potential and only one non-vanishing magnetic field and vector potential component, but otherwise arbitrary distribution functions, the derivative of P_{zz} with respect to the non-vanishing component of the vector potential equals (modulo constants) the current density. This was generalized by Bertotti (Bertotti 1963) who included a non-vanishing electric potential and showed that the partial derivative of P_{zz} with respect to the electric potential is proportional to the charge density (see also Schindler et al. 1973; Schindler 2007, for the same conclusion for 2D VM equilibria). Lerche (Lerche 1967) then generalized this to equilibria with two magnetic field, vector potential and current density components, but for a restricted class of distribution functions. Channell (Channell 1976) investigated the case of vanishing electric potential and a special class of distribution functions for which he showed that the two components of the current density are, again modulo constant factors, given by the partial derivatives of the particle density with respect to the components of the vector potential. If investigated carefully one can see that the full expressions including the constant factors are again the partial derivatives of P_{zz} with respect to the components of the vector potential. Using the force balance condition, Mynick et al. (Mynick et al. 1979) then showed that, independently of the distribution function, the partial derivatives of P_{zz} with respect to the electric potential and the two components of the vector potential are always proportional to the charge density and the components of the current density, respectively. They also showed that this property is maintained under the assumption of quasi-neutrality. The authors then use this property to construct 1D VM equilibria with certain defined properties. The special role of P_{zz} in the context of 1D VM equilibria has also been emphasized by Attico and Pegoraro (Attico and Pegoraro 1999), again for the

case of vanishing electric potential. Similarly to Channell (Channell 1976), they used this property to construct a number of special distribution functions for 1D VM equilibria. More recently, Mottez (Mottez 2004) gave a detailed discussion of the role of the full pressure tensor (not just of one component) for distribution functions of the same type as discussed by Channell (Channell 1976), but including the case of non-vanishing electric potential.

The properties of P_{zz} make it a very useful quantity to start any investigation of 1D VM equilibria, since all other quantities such as particle density, charge density and current density can be derived by differentiation. P_{zz} is also equivalent to the pseudo-potential of the analogous pseudo-particle problem and can thus be used to study the properties of 1D VM equilibria qualitatively without the need to solve the equilibrium differential equations. In particular, the pseudo-particle analogy can be used to formulate conditions on P_{zz} that it has to satisfy to allow the existence of 1D force-free VM equilibria (Tassi et al. 2008). So far only linear force-free 1D VM equilibria are known (Sestero 1967; Bobrova and Syrovatskiĭ 1979; Correa-Restrepo and Pfirsch 1993; Bobrova et al. 2001) and the pseudo-particle analogy can also give some insight into the types of distribution functions permitting a linear force-free solution.

Therefore this chapter is laid out such that in Sec. 3.2 the basic general theory of quasi-neutral 1D VM equilibria with three constants of motion is presented, rederiving the basic equations given first by Mynick et al. (Mynick et al. 1979) directly from the definitions of the basic quantities. In Sections 3.3 - 3.5 several examples of 1D Vlasov-Maxwell equilibria are given which emphasise the usefulness of the properties of P_{zz}. In Sec. 3.6 general properties of 1D force-free VM equilibria are discussed based on the one-to-one correspondence of the mathematical problem with the motion of a pseudo-particle in a conservative 2D pseudo-potential. Finally Sec. 3.7 and 3.8 show how the P_{zz} component of the pressure tensor can be used to determine a distribution function for the force-free Harris sheet and how this can be extended to a complete family of equilibria that describe the transition between the Harris sheet and the force-free Harris sheet. The conclusions are presented in Sec. 3.9.

3.2 General Theory

It is assumed that all quantities depend only on z and that the magnetic field has components B_x and B_y. The magnetic field components are written in terms of a vector potential $\mathbf{A} = (A_x, A_y, A_z)$ where,

$$B_x = -\frac{dA_y}{dz}, \tag{3.1}$$

$$B_y = \frac{dA_x}{dz}, \tag{3.2}$$

and the electric field is the gradient of an electric potential ϕ such that,

$$\mathbf{E} = -\nabla\phi = -\frac{d\phi}{dz}\mathbf{e_z}. \tag{3.3}$$

In this case $\mathbf{B}$ and $\mathbf{E}$ automatically satisfy the homogeneous steady state Maxwell equations $\nabla \cdot \mathbf{B} = 0$ and $\nabla \times \mathbf{E} = \mathbf{0}$.

Due to the symmetries of the system (time independence and spatial independence of x and y) the three obvious constants of motion for each particle species are the Hamiltonian or particle energy for each species s,

$$H_s = \frac{1}{2}m_s(v_x^2 + v_y^2 + v_z^2) + q_s\phi, \tag{3.4}$$

the canonical momentum in the x direction, p_{xs},

$$p_{xs} = m_s v_x + q_s A_x, \tag{3.5}$$

and the canonical momentum in the y direction, p_{ys},

$$p_{ys} = m_s v_y + q_s A_y, \tag{3.6}$$

where m_s and q_s are the mass and charge of each species. All positive functions f_s satisfying the appropriate conditions for existence of the velocity moments and depending only on the constants of motion,

$$f_s = f_s\left(H_s, p_{xs}, p_{ys}\right), \tag{3.7}$$

solve the steady-state Vlasov equation,

$$\mathbf{v} \cdot \frac{\partial f_s}{\partial \mathbf{r}} + \frac{q_s}{m_s}(\mathbf{E} + \mathbf{v} \times \mathbf{B}) \cdot \frac{\partial f_s}{\partial \mathbf{v}} = 0. \tag{3.8}$$

To calculate the 1D Vlasov-Maxwell equilibria the remaining inhomogeneous steady-state Maxwell equations, $\nabla \cdot \mathbf{E} = \sigma/\epsilon_0$ and $\nabla \times \mathbf{B} = \mu_0\mathbf{j}$ must be solved. These equations reduce to,

$$-\frac{d^2\phi}{dz^2} = \frac{1}{\epsilon_0}\sigma\left(A_x, A_y, \phi\right), \tag{3.9}$$

$$-\frac{d^2A_x}{dz^2} = \mu_0 j_x\left(A_x, A_y, \phi\right), \tag{3.10}$$

$$-\frac{d^2A_y}{dz^2} = \mu_0 j_y\left(A_x, A_y, \phi\right), \tag{3.11}$$

where the source terms are the electric charge density and the current densities in the x and z directions, which are defined as velocity moments of the equilibrium distribution functions, f_s, in

the following way,

$$\sigma\left(A_x, A_y, \phi\right) = \sum_s q_s \int_{-\infty}^{\infty} f_s \left(\frac{m_s v^2}{2} + q_s\phi, m_s v_x + q_s A_x, m_s v_y + q_s A_y\right) d^3v, \tag{3.12}$$

$$j_x(A_x, A_y, \phi) = \sum_s q_s \int_{-\infty}^{\infty} v_x f_s \left(\frac{m_s v^2}{2} + q_s\phi, m_s v_x + q_s A_x, m_s v_y + q_s A_y\right) d^3v, \tag{3.13}$$

$$j_y(A_x, A_y, \phi) = \sum_s q_s \int_{-\infty}^{\infty} v_y f_s \left(\frac{m_s v^2}{2} + q_s\phi, m_s v_x + q_s A_x, m_s v_y + q_s A_y\right) d^3v. \tag{3.14}$$

Here, the dependence of the charge and current densities on the electric and vector potentials has been made visible explicitly. Independent of the choice of distribution function f_s, it can be shown (see appendix A) that the charge and current density components always satisfy the equations,

$$\frac{\partial\sigma}{\partial A_x} + \frac{\partial j_x}{\partial\phi} = 0, \tag{3.15}$$

$$\frac{\partial\sigma}{\partial A_y} + \frac{\partial j_y}{\partial\phi} = 0, \tag{3.16}$$

$$\frac{\partial j_x}{\partial A_y} - \frac{\partial j_y}{\partial A_x} = 0. \tag{3.17}$$

These equations are completely analogous to the relation derived by Schindler and co-workers (Schindler et al. 1973; Schindler 2007) for the case of distribution functions depending only on the Hamiltonian and a single canonical momentum. Equations (3.15) - (3.17) imply the existence of a potential P (Schindler 2007), where P is given by,

$$P(A_x, A_y, \phi) = \sum_s \int_{-\infty}^{\infty} m_s v_z^2 f_s d^3v, \tag{3.18}$$

which is identified as the P_{zz} component of the pressure tensor. The Eqs. (3.15) - (3.17) are necessary conditions for the force balance of the Vlasov-Maxwell equilibria, which has been emphasized before by many authors for special cases (see e.g. Grad 1961; Hurley 1963; Lam 1967; Parker 1967; Lerche 1967; Alpers 1969; Su and Sonnerup 1971; Kan 1972; Channell 1976; Lemaire and Burlaga 1976; Roth 1976; Lee and Kan 1979b,a; Greene 1993; Roth et al. 1996; Attico and Pegoraro 1999); the sum of the plasma pressure and magnetic pressure must be equal to a constant. The charge density, σ, and the current densities, j_x and j_y, are given by partial derivatives of the pressure tensor with respect to the electric potential, ϕ and the components of the vector potential, A_x and A_y, in the following way (see Appendix A for details):

$$\sigma = -\frac{\partial P}{\partial\phi}, \tag{3.19}$$

$$j_x = \frac{\partial P}{\partial A_x}, \tag{3.20}$$

$$j_y = \frac{\partial P}{\partial A_y}. \tag{3.21}$$

They highlight the important relations between the current density components and the P_{zz} component of the pressure tensor. Throughout this work a quasineutral plasma consisting of two species (electrons and ions) of opposite charge ($|q_s| = e$) will always be assumed. Quasineutrality can be assumed as long as all length scales are much larger than the Debye length. Quasineutrality does not generally imply that the electric field vanishes (Schindler 2007; Schindler and Birn 2002; Neukirch 1993).

Quasineutrality corresponds to (3.9) being replaced by

$$\sigma\left(A_x, A_y, \phi\right) = -\frac{\partial P}{\partial \phi} = 0. \tag{3.22}$$

This in general can then be inverted to give the quasineutral electric potential ϕ_{qn} where,

$$\phi_{qn} = \phi_{qn}\left(A_x, A_y\right). \tag{3.23}$$

The potential P is then replaced by its quasineutral version P_{qn}, where P_{qn} is a function only of A_x and A_y,

$$P_{qn}(A_x, A_y) = P(A_x, A_y, \phi_{qn}(A_x, A_y)). \tag{3.24}$$

It should be noted that due to Eq. (3.22),

$$\left(\frac{\partial P_{qn}}{\partial A_x}\right)_{A_y} = \left(\frac{\partial P}{\partial A_x}\right)_{A_y,\phi} + \left(\frac{\partial \phi_{qn}}{\partial A_x}\right)_{A_y}\left(\frac{\partial P}{\partial \phi}\right)_{A_x,A_y} = \left(\frac{\partial P}{\partial A_x}\right)_{A_y,\phi}, \tag{3.25}$$

where it is understood that on the right hand side P is evaluated using the quasineutral electric potential and the subscripts indicate explicitly which quantities are being kept constant during the differentiation. An analogous equation holds for the derivative of P_{qn} with respect to A_y. Thus in Eqs. (3.20) and (3.21) the derivatives of P can be replaced by derivatives of P_{qn} in the quasineutral case. Using Eqs. (3.20) and (3.21) Ampère's law can be written as,

$$-\frac{d^2 A_x}{dz^2} = \mu_0 \frac{\partial P_{qn}}{\partial A_x}, \tag{3.26}$$

$$-\frac{d^2 A_y}{dz^2} = \mu_0 \frac{\partial P_{qn}}{\partial A_y}. \tag{3.27}$$

The resulting Vlasov-Maxwell equilibria can now be found by solving these two coupled second order differential equations.

It has been noticed before for particular distribution functions that the charge and current densities can be written as partial derivatives of a single function of the electric and the vector potential (Kan 1972; Lee and Kan 1979b,a) as shown in Eqs. (3.19)-(3.21).

Grad (Grad 1961) seems to have been the first to notice the special role played by P_{zz} for the 1D VM equilibrium problem, but he only investigated the special case of vanishing electric potential and only one non-vanishing component of the magnetic field and vector potential. In that case there is no need to invoke the quasi-neutrality condition and only one of the two Eqs. (3.20) and (3.21) is non-trivial.

For the $\phi = 0$ case and a set of special assumptions for the distribution functions, Lerche (Lerche 1967) was able to relate the derivatives of P_{zz} with respect to A_x and A_y to the respective current densities. For $\phi = 0$ and a similar assumption for the distribution functions, other authors (Parker 1967; Su and Sonnerup 1971) also noticed that the current density is related to derivatives of a single function with respect to A_x and A_y, but did not relate that function to P_{zz}.

Channell (Channell 1976) showed that for $\phi = 0$ and distribution functions of the type

$$f_s = f_{0s} \exp(-\beta_s H_s) g_s(p_{xs}, p_{ys}),$$

the current density components are given by the equations,

$$\begin{aligned} j_x &= \left(\frac{1}{\beta_e} + \frac{1}{\beta_i}\right) \frac{\partial N}{\partial A_x}, \\ j_y &= \left(\frac{1}{\beta_e} + \frac{1}{\beta_i}\right) \frac{\partial N}{\partial A_y}. \end{aligned}$$

Here the plasma has been assumed to consist of two particle species (electron and ions), $\beta_s = 1/(k_B T_s)$ and $N(A_x, A_y)$ is the particle density of one of the species. Another assumption made by Channell (Channell 1976) is that $N_e(A_x, A_y)$ is the same function of A_x and A_y as $N_i(A_x, A_y)$, which has implications for the distribution functions as well. It is easy to see that under these assumptions,

$$P_{zz} = \left(\frac{1}{\beta_e} + \frac{1}{\beta_i}\right) N(A_x, A_y),$$

which is, of course, consistent with the Eqs. (3.20) and (3.21).

Using force balance as an argument to show the validity of Eqs. (3.19) - (3.21), Mynick et al. (Mynick et al. 1979) then ultimately derived the general theory presented above. Their approach is of course completely equivalent to the one shown here, but here these equations are shown starting from the velocity moments and Eqs. (3.15) - (3.16).

Attico and Pegoraro (Attico and Pegoraro 1999) also noticed the connection between the current density and the partial derivatives of P_{zz}, again for the case $\phi = 0$ and for basically the same class of distribution functions used by Channell (Channell 1976). In their case the distribution functions are constructed by linear superpositions of distribution functions of the Harris sheet (Harris 1962) type

$$f_s = f_{0s} \exp(-\beta_s H_s) \int \Phi(u_{xs}, u_{ys}) \exp[\beta_s (u_{xs} p_{xs} + u_{ys} p_{ys})] du_{xs} du_{ys}.$$

The authors point out that for their case Eq. (3.17) is a necessary condition for the existence of a single function from which the current density can be derived by differentiation, and show that it is satisfied for their class of distribution functions and that this function is P_{zz} (modulo constant factors).

Equations (3.26) and (3.27) are just the Hamiltonian equations for a pseudo particle with coordinates (A_x, A_y) moving in a conservative pseudo 2D potential $\mu_0 P_{qn}(A_x, A_y)$. The differential equations (3.26) and (3.27) can be derived from the Hamiltonian,

$$H_A = \frac{1}{2} \left(\frac{dA_x}{dz} \right)^2 + \frac{1}{2} \left(\frac{dA_y}{dz} \right)^2 + \mu_0 P_{qn} \left(A_x, A_y \right). \tag{3.28}$$

The Hamiltonian represents the total energy of the pseudo particle and is equivalent to the Vlasov-Maxwell equilibrium condition that the total pressure P_T is constant. The magnetic pressure is equivalent to the kinetic energy and the plasma pressure to the potential energy. Knowledge of P_{qn} as function of A_x and A_y allows us to predict the nature of the solution using pseudo-energy conservation without solving Eqs. (3.26) and (3.27) explicitly. The gradient of the potential corresponds to the gradient of the magnetic fields, so that where the potential surface has steep gradients, there will be steep gradients in the magnetic field components and therefore large current densities. Again, one or several of these properties have been noticed by a large number of authors for special cases (see e.g. Grad 1961; Bertotti 1963; Nicholson 1963; Sestero 1966; Lam 1967; Parker 1967; Lerche 1967; Alpers 1969; Su and Sonnerup 1971; Kan 1972; Channell 1976; Lemaire and Burlaga 1976; Roth 1976; Mynick et al. 1979; Lee and Kan 1979b,a; Greene 1993; Attico and Pegoraro 1999; Mottez 2003).

3.3 Examples of 1D-VM Equilibria

In this section the general theory that has been discussed in Sec. 3.2 will be applied to discuss examples of 1D Vlasov-Maxwell equilibria. The distribution functions are exponential functions whose arguments are at most quadratic in the velocity components. This class of distribution function contains many well known special cases.

The most general function which can be constructed out of the constants of motion and which is quadratic in the velocities is a function of a multiple of

$$\bar{H}_s = H_s - \frac{a_s}{m_s} p_{xs}^2 - \frac{b_s}{m_s} p_{ys}^2 - \frac{c_s}{m_s} p_{xs} p_{ys} - u_{xs} p_{xs} - u_{ys} p_{ys}, \tag{3.29}$$

where a_s, b_s, c_s, u_{xs} and u_{ys} are constants. The coefficients a_s, b_s and c_s have no dimension, whereas u_{xs} and u_{ys} have the dimension of velocity. The constant c_s is set to zero for reasons of simplicity. Each term quadratic in the canonical momenta gives rise to a similar term in the vector potentials after the distribution function is integrated over velocity space. Thus the $p_{xs}p_{ys}$ term corresponds to an $A_x A_y$ term in the particle density, current density and pressure. Such a mixed quadratic term can, however, always be eliminated by an appropriate choice of coordinate system. This would not necessarily imply $c_s = 0$ at distribution function level, but the mixed term is not of critical importance for the discussion and thus is omitted here. It is remarked that the velocity space integral (3.18) defining P only exists if $a_s > 1/2$ and $b_s > 1/2$. The coefficients a_s and b_s can be related to the temperature anisotropy of the distribution function (see e.g. Bobrova et al. 2001).

A distribution function of the form,

$$f_s = \frac{n_{0s}}{v_{th,s}^3} \exp(-\beta_s \bar{H}_s), \tag{3.30}$$

is assumed where n_{0s} is a constant normalizing particle density, $\beta_s = 1/k_B T_s$ is the inverse temperature and $v_{th,s} = (2\pi/m_s\beta_s)^{1/2}$ is the thermal velocity. Clearly, these distribution functions are part of the class of distribution functions discussed by Channell (Channell 1976) and by Attico and Pegoraro (Attico and Pegoraro 1999).

For the distribution function (3.30) the zz-component of the pressure tensor is given by,

$$P = \sum_s \frac{1}{\beta_s} \exp(-\beta_s q_s \phi) N_s(A_x, A_y), \tag{3.31}$$

where,

$$N_s(A_x, A_y) = \bar{n}_{0s} \exp(r_{1s} A_x^2 + r_{2s} A_y^2 + r_{3s} A_x + r_{4s} A_y). \tag{3.32}$$

Equation (3.32) uses the definitions,

$$\bar{n}_{0s} = \sqrt{1/[(1-2a_s)(1-2b_s)]} \exp\{\beta_s m_s [u_{xs}^2/(1-2a_s) + u_{ys}^2/(1-2b_s)]/2\} n_{0s} \tag{3.33}$$

$$r_{1s} = \beta_s a_s q_s^2/[m_s(1-2a_s)], \tag{3.34}$$

$$r_{2s} = \beta_s b_s q_s^2/[m_s(1-2b_s)], \tag{3.35}$$

$$r_{3s} = \beta_s u_{xs} q_s/(1-2a_s), \tag{3.36}$$

$$r_{4s} = \beta_s u_{ys} q_s/(1-2b_s). \tag{3.37}$$

The charge density is calculated using Eq. (3.19):

$$\sigma = \sum_s q_s \exp(-\beta_s q_s \phi) N_s(A_x, A_y), \tag{3.38}$$

and the quasi-neutrality condition $\sigma = 0$ then gives,

$$\phi_{qn} = \frac{1}{e(\beta_e+\beta_i)} \ln\left(\frac{N_i}{N_e}\right). \tag{3.39}$$

One can see immediately that the quasi-neutral electric field will only vanish for a choice of parameters such that $N_e(A_x, A_y) \propto N_i(A_x, A_y)$.

The quasi-neutral P_{zz} is given by,

$$\begin{aligned} P_{qn} &= \frac{\beta_e+\beta_i}{\beta_e\beta_i} N_e^{\beta_i/(\beta_e+\beta_i)} N_i^{\beta_e/(\beta_e+\beta_i)} \\ &= P_0 \exp(r_{1,qn}A_x^2 + r_{2,qn}A_y^2 + r_{3,qn}A_x + r_{4,qn}A_y), \end{aligned} \tag{3.40}$$

with

$$P_0 = \frac{\beta_e+\beta_i}{\beta_e\beta_i} \bar{n}_{0e}^{\beta_i/(\beta_e+\beta_i)} \bar{n}_{0i}^{\beta_e/(\beta_e+\beta_i)}, \tag{3.41}$$

$$r_{1,qn} = \frac{\beta_e\beta_i}{\beta_e+\beta_i} e^2 \left[\frac{a_e}{m_e(1-2a_e)} + \frac{a_i}{m_i(1-2a_i)}\right], \tag{3.42}$$

$$r_{2,qn} = \frac{\beta_e\beta_i}{\beta_e+\beta_i} e^2 \left[\frac{b_e}{m_e(1-2b_e)} + \frac{b_i}{m_i(1-2b_i)}\right], \tag{3.43}$$

$$r_{3,qn} = \frac{\beta_e\beta_i}{\beta_e+\beta_i} e \left[\frac{u_{xi}}{1-2a_i} - \frac{u_{xe}}{1-2a_e}\right], \tag{3.44}$$

$$r_{4,qn} = \frac{\beta_e\beta_i}{\beta_e+\beta_i} e \left[\frac{u_{yi}}{1-2b_i} - \frac{u_{ye}}{1-2b_e}\right]. \tag{3.45}$$

The x- and y-components of the current density can be calculated from Eqs. (3.20) and (3.21), resulting in

$$j_x = P_0(2r_{1,qn}A_x + r_{3,qn}) \exp(r_{1,qn}A_x^2 + r_{2,qn}A_y^2 + r_{3,qn}A_x + r_{4,qn}A_y), \tag{3.46}$$

$$j_y = P_0(2r_{2,qn}A_y + r_{4,qn}) \exp(r_{1,qn}A_x^2 + r_{2,qn}A_y^2 + r_{3,qn}A_x + r_{4,qn}A_y). \tag{3.47}$$

At this point it is convenient to normalize all quantities. Normalizing the magnetic field to a typical value B_0 and the coordinate z to a typical length scale L. The components of the vector potential are then normalized by $B_0 L$ and the normalized coefficients are defined by $\bar{r}_{1,qn} = B_0^2 L^2 r_{1,qn}$,

$\bar{r}_{2,qn} = B_0^2 L^2 r_{2,qn}$, $\bar{r}_{3,qn} = B_0 L r_{3,qn}$ and $\bar{r}_{4,qn} = B_0 L r_{4,qn}$. The pressure P_{qn} is normalized by B_0^2/μ_0 and, finally, the current density components are normalized by $\mu_0 L/B_0$. From now on it is assumed that all quantities have been normalized in the way just described and the notation for normalization is suppressed in what follows, with the exception of one example where the dimensional form is used to show the explicit parameter dependence.

The vector potential components A_x and A_y are determined by the solutions of the two coupled nonlinear ODEs (3.26) and (3.27), which for the most general case, in which none of the coefficients $r_{i,qn}$ vanishes, would have to be solved by numerical methods. However, using the equivalence of the problem to the in plane motion of a pseudo-particle in a potential $P_{qn}(A_x, A_y)$, one can usually see what types of solutions can be expected. In the following discussion solutions which have been obtained using a standard fourth-order Runge-Kutta method are also shown (Press et al. 1992).

3.3.1 The case $r_{1,qn}$ and $r_{2,qn}$ non-zero

Without loss of generality, in this case a different gauge can be chosen by letting $(A'_x, A'_y) = (A_x - A_{x0}, A_y - A_{y0})$, where $(A_{x0}, A_{y0}) = (-r_{3,qn}/2r_{1,qn}, -r_{4,qn}/2r_{2,qn})$. This removes the linear terms in the exponential function in P_{qn} and changes the current densities accordingly in the following way

$$P_{qn} = \bar{P}_0 \exp(r_{1,qn} {A'_x}^2 + r_{2,qn} {A'_y}^2), \tag{3.48}$$

$$j_x = 2\bar{P}_0 r_{1,qn} A'_x \exp(r_{1,qn} {A'_x}^2 + r_{2,qn} {A'_y}^2), \tag{3.49}$$

$$j_y = 2\bar{P}_0 r_{2,qn} A'_y \exp(r_{1,qn} {A'_x}^2 + r_{2,qn} {A'_y}^2), \tag{3.50}$$

where

$$\bar{P}_0 = P_0 \exp[-r_{3,qn}^2/(4r_{1,qn}) - r_{4,qn}^2/(4r_{2,qn})]. \tag{3.51}$$

This simply amounts to a shift of the origin of the coordinate system in the equivalent pseudo-particle problem.

3.3.2 The case $r_{1,qn}$ and $r_{2,qn}$ negative

In the case of $a_s < 0$, $b_s < 0$, both $r_{1,qn}$ and $r_{2,qn}$ are negative and the pseudo-potential $P_{qn}(A_x, A_y)$ is a 2D Gaussian with elliptic contours with semi-axis $r_{1,qn}^{-1/2}$ and $r_{2,qn}^{-1/2}$ having its maximum value $\bar{P}_0$ at the origin. The motion of a pseudo-particle can be thought of as a scattering problem with the details depending on the initial conditions (see Fig. 3.1).

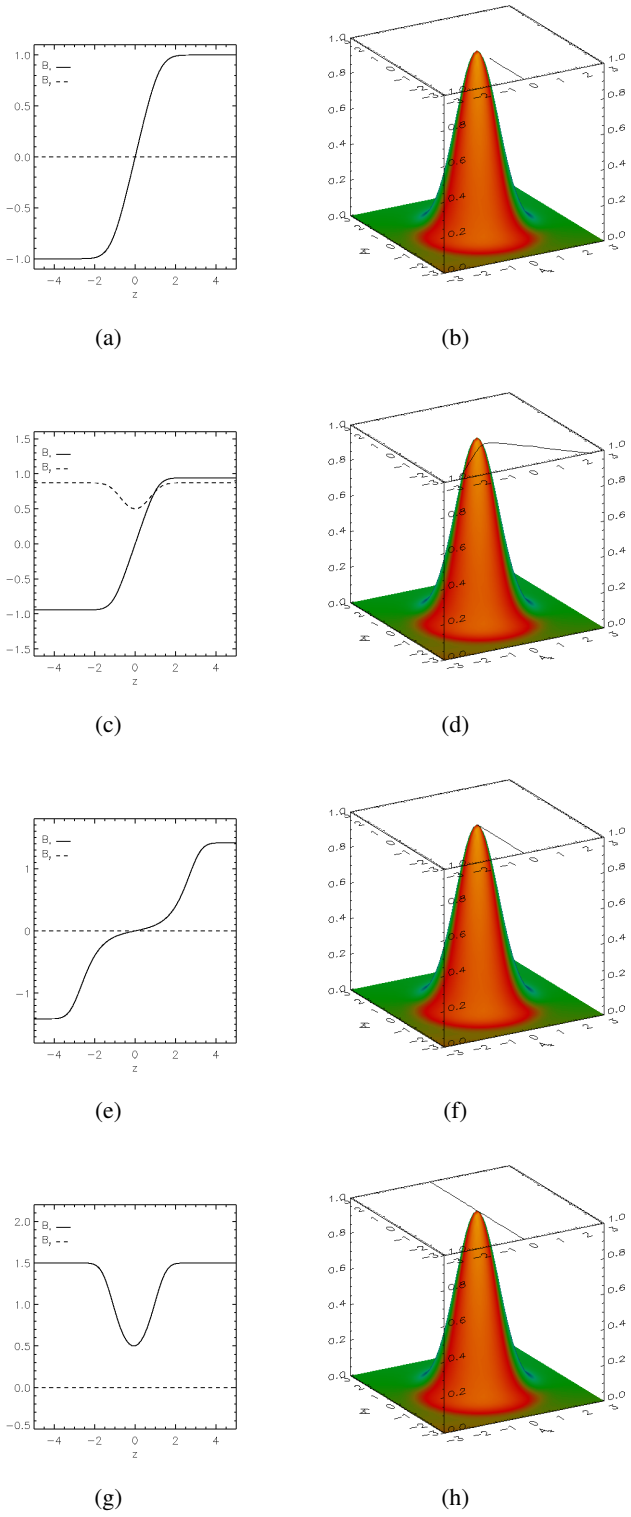

Figure 3.1: Plots for the case with $r_{1,qn} = -1$, $r_{2,qn} = -1$ and $\bar{P}_0 = 1$. In each example the figure on the right shows a surface plot of the potential P_{qn} with the pseudo-particle trajectory in the A_x-A_y-plane plotted above it, that corresponds to the magnetic field profiles shown on the left for different initial conditions.

If the initial kinetic energy of the particle (equivalent to the initial magnetic pressure in the VM equilibrium) is smaller than the maximum value of the potential the particle will usually move over the flanks of the potential hill, changing direction in the process. The change in direction will depend on the initial coordinates and also on the initial direction of approach as P_{qn} is usually not a central potential. For example, if the particle approaches the origin exactly along one of the coordinate axes, it will eventually stop, turn around and go back along the same trajectory, eventually returning to its initial coordinates with a velocity which has the same magnitude, but opposite direction to the initial velocity. The equivalent VM equilibrium would be a neutral sheet with a constant, but oppositely directed magnetic field at large distances on both sides of the sheet and a vanishing magnetic field in the centre of the sheet (corresponding, of course, to the turning point where the particle velocity vanishes). Both the vector potential and the magnetic field will only have one non-vanishing component in this special case. An example of this type is shown in the top two plots of Fig. 3.1. Figure 3.1(b) shows the potential surface with the particle trajectory in the A_x-A_y-plane overlaid. Solutions of this type have been discussed by Lam (Lam 1967), but starting from a pressure function depending only on one vector potential component.

Figure 3.1(c) and 3.1(d) are for the case where the initial kinetic energy of the particle is less than the maximum value of the potential but the vector potential and magnetic field now both have two non-vanishing components. In this case the particle is scattered by the potential but importantly is still reflected and therefore the x component of the field is still oppositely directed either side of $z = 0$.

If the particle happens to have an initial kinetic energy which is exactly equal to the maximum value of the potential and approaches the origin along one of the coordinate axes, it will asymptotically approach the origin itself and thus the maximum of the potential. This solution has also been previously discussed by Lam (Lam 1967) and also corresponds to Case A discussed in the paper by Channell (Channell 1976), albeit in both cases using a pseudo-potential depending only on one component of the vector potential. The solution, however, will be the same. Figures 3.1(e) and 3.1(f) show an example where the particle's initial kinetic energy is almost equal to the maximum value of the potential. The particle approaches along the A_y axis and therefore there is only one non-vanishing component of the vector potential and magnetic field. The particle trajectory, shown overlaid on the pressure potential in Figure 3.1(f) gets very close to the peak of the potential surface. The significant slowing of the particle as it gets close to the peak of the potential is evident in the flattening of the profile of the x component of the magnetic field around $z = 0$.

For any other approach trajectory the particle will not return to its initial A_y coordinate and the velocity will not vanish at any point along the trajectory. These particle trajectories correspond to 1D current sheets with a sheared magnetic field, for which the magnetic field strength on both sides of the sheet is the same, but the field direction is not anti-parallel as in the case of the neutral sheet and these solutions will have two non-vanishing components of the vector potential and the

magnetic field.

If the initial kinetic energy is larger than the maximum of the pseudo-potential similar conclusions apply, but now if the particle approaches the origin along one the coordinate axes, it will only slow down, move over the maximum and accelerate back to its initial velocity. This corresponds to 1D VM equilibria for which the field does not change direction, but merely shows a decrease in field strength in the centre of the sheet. In this case, the current density has a spatial structure which is quite different from the neutral sheet case, because it has two layers of currents flowing in opposite directions with vanishing current density at the centre of the sheet (Nicholson 1963; Lam 1967). Figures 3.1(g) and 3.1(h) shows an example of this type of solution. Figure 3.1(g) shows the profile of the x component of the field. The decrease in the magnetic field strength corresponding to the slowing of the particle is evident. Figure 3.1(h) showing the particle trajectory illustrates that the particle is not reflected but simply keeps moving in the same direction, despite being slowed as it moves close to the maximum of the potential.

3.3.3 The case $r_{1,qn}$ and $r_{2,qn}$ positive

If a_s and b_s are positive, $r_{1,qn}$ and $r_{2,qn}$ are also positive. In this case P_{qn} has a minimum at the origin and tends to infinity for $|A_x|$, $|A_y| \to \infty$. The corresponding potential will therefore confine the particle to a finite domain about the origin, with the size of the domain depending on the total energy. The nature of the particle motion in each direction will be quasi-periodic, but with different and usually incommensurate periods in the A_x and A_y directions. The trajectories will therefore generally not be closed trajectories. An example of such a solution is shown in Fig. 3.2 with initial conditions $A_x = 0, A_y = 0.45, B_x = 0, B_y = 0.45$ at $z = 0$ and the parameter values have been chosen such that $r_{1,qn} = 1$, $r_{2,qn} = 2$ and $\bar{P}_0 = 1$. Figure 3.2(a) shows the profiles of the magnetic field components. It can be clearly seen that the magnetic fields, rather than having a localised current sheet like structure, now exhibit oscillatory motion. Figure 3.2(b) shows a plot of the pressure function with the particle trajectory overlaid. The particle moves in an oscillatory way but the orbit is not closed. It can be shown that $\mathbf{j} \cdot \mathbf{B} \neq 0$ which confirms that there are field aligned components of the current density. One can show that the drift velocity for each particle species is spatially varying, which was found from the study of collisionless two fluid theory in Sec. 2.2 of Chap. 2 to be an important property of force-free equilibria. The orbits of the pseudo particle in this potential will in general be quasi-periodic with a corresponding behaviour of the magnetic field components. There are also oscillatory current density components.

An interesting special case, is when $r_{1,qn} = r_{2,qn} = r_{qn}$. In this case the pseudo-potential is a central potential and among other orbits, also allows for circular orbits, because the (pseudo-) angular momentum is conserved. Circular orbits correspond to $A_x^2 + A_y^2 =$ constant, which makes Eqs. (3.49) and (3.50) linear and allows analytical solutions. This case has been discussed by

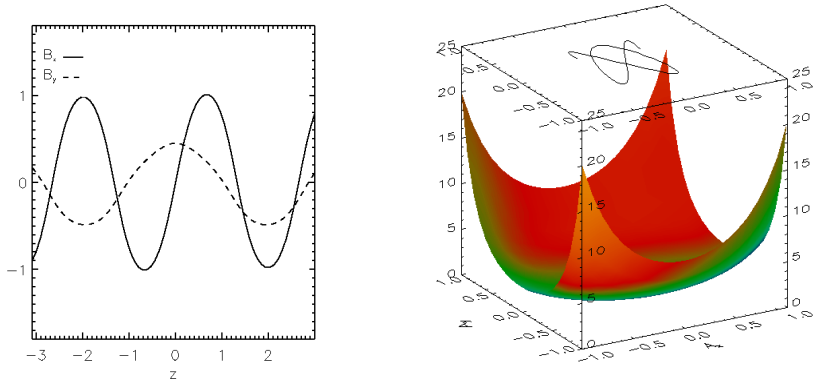

(a) (b)

Figure 3.2: Plots for the case with $r_{1,qn} = 1$, $r_{2,qn} = 2$ and $\bar{P}_0 = 1$. The figure on the right shows a surface plot of the potential P_{qn} with the pseudo-particle trajectory in the A_x-A_y-plane plotted above it, that corresponds to the magnetic field profiles shown on the left.

Sestero (1967), Correa-Restrepo and Pfirsch (1993), Bobrova and Syrovatskiĭ (1979), Bobrova et al. (2001) and Harrison and Neukirch (2009b) and leads to linear force-free solutions of the form

$$\mathbf{B} = B_0(\sin \alpha z \mathbf{e}_x + \cos \alpha z \mathbf{e}_y), \tag{3.52}$$

where the boundary conditions are chosen to be $B_x = 0$, $B_y = B_0$ for $z = 0$. It is interesting to discuss this case in more detail where the analysis by Bobrova et al. (2001) is followed, in which a slightly different notation is used which shows explicitly how a_s and b_s can be related to the temperature anisotropy. Dropping the previous normalisation, the distribution function in dimensional form is,

$$f_s = c_s \exp\left[-\frac{1}{T_{s\perp}} H_s + \frac{\Delta T_s}{2 m_s T_{s\perp} T_{s\parallel}} \left(p_{xs}^2 + p_{ys}^2\right)\right], \tag{3.53}$$

where c_s is a normalising constant,

$$c_s = \frac{n_{0s} m_s^{3/2}}{(2\pi)^{3/2} T_{s\perp}^{1/2} T_{s\parallel}}, \tag{3.54}$$

$T_{s\perp}$ is the temperature in the z direction, $T_{s\parallel}$ is the temperature in the x and y directions for each particle species and

$$\Delta T_s = T_{s\parallel} - T_{s\perp} \geq 0. \tag{3.55}$$

In terms of this notation the drift velocities for each particle species are

$$\mathbf{V_d^s}(z) = \frac{q_s}{m_s}\frac{\Delta T_s}{T_{s\perp}}\mathbf{A}. \tag{3.56}$$

Examination of the distribution function leads to the conclusion that for an equilibrium solution to exist at least one of the plasma species must have a temperature anisotropy. This means that at least one particle species must satisfy the condition that $\Delta T_s = T_{s\|} - T_{s\perp} \neq 0$.

For the distribution function (3.53) the zz-component of the pressure tensor is given by,

$$P = \sum_s T_{s\perp} \exp\left(-\frac{q_s\phi}{T_{s\perp}}\right) N_s(A_x, A_y), \tag{3.57}$$

where

$$N_s(A_x, A_y) = n_{0s} \exp\left(r_s A^2\right), \tag{3.58}$$

and the definitions of r_s is

$$r_s = \frac{1}{2}\frac{q_s^2}{m_s}\frac{\Delta T_s}{T_{s\perp}^2}A^2. \tag{3.59}$$

The charge density is calculated using Eq. (3.19):

$$\sigma = \sum_s q_s \exp\left(-\frac{q_s\phi}{T_{s\perp}}\right) N_s(A_x, A_y), \tag{3.60}$$

and the quasi-neutrality condition $\sigma = 0$ then gives

$$\phi_{qn} = \frac{T_{e\perp}T_{i\perp}}{e(T_{e\perp}+T_{i\perp})} \ln\left(\frac{N_i}{N_e}\right). \tag{3.61}$$

One can see immediately that the quasi-neutral electric field will only vanish for a choice of parameters such that $N_e(A_x, A_y) \propto N_i(A_x, A_y)$.

The quasi-neutral P_{zz} is given by

$$\begin{aligned} P_{qn} &= (T_{e\perp}+T_{i\perp})\, N_e^{T_{e\perp}/(T_{e\perp}+T_{i\perp})} N_i^{T_{i\perp}/(T_{e\perp}+T_{i\perp})} \\ &= P_0 \exp\left(r_{qn}A^2\right), \end{aligned} \tag{3.62}$$

with

$$P_0 = (T_{e\perp}+T_{i\perp})\, n_0, \tag{3.63}$$

$$n_0 = n_{0e}^{T_{e\perp}/(T_{e\perp}+T_{i\perp})} n_{0i}^{T_{i\perp}/(T_{e\perp}+T_{i\perp})}, \tag{3.64}$$

$$r_{qn} = \frac{1}{2}\frac{1}{(T_{e\perp}+T_{i\perp})}\left(\frac{e^2}{m_e}\frac{\Delta T_e}{T_{e\perp}}+\frac{e^2}{m_i}\frac{\Delta T_i}{T_{i\perp}}\right). \tag{3.65}$$

The x- and y-components of the current density can be calculated from Eqs. (3.20) and (3.21), resulting in,

$$j_x = 2r_{qn}P_0A_x\exp\left(r_{qn}A^2\right), \tag{3.66}$$
$$j_y = 2r_{qn}P_0A_y\exp\left(r_{qn}A^2\right). \tag{3.67}$$

Setting $A_x^2+A_y^2=$ constant reduces the quasineutral electric potential $\phi_{qn}=$ a constant which for simplicity can be set to zero. The Eqs. (3.26) and (3.27) are now linear and have the explicit form

$$-\frac{d^2A_x}{dz^2} = \frac{n_0e^2}{\epsilon_0m_ec^2}\left(\frac{\Delta T_e}{T_{e\perp}}+\frac{m_e}{m_i}\frac{\Delta T_i}{T_{i\perp}}\right)A_x, \tag{3.68}$$
$$-\frac{d^2A_y}{dz^2} = \frac{n_0e^2}{\epsilon_0m_ec^2}\left(\frac{\Delta T_e}{T_{e\perp}}+\frac{m_e}{m_i}\frac{\Delta T_i}{T_{i\perp}}\right)A_y, \tag{3.69}$$

where the constant factor $\exp\left(r_{qn}A^2\right)$ has been absorbed into n_0. Normalising against A_{x0} and a length L where L is equal to the electron skin depth,

$$L^2=\left(\frac{c}{\omega_{pe}}\right)^2=\frac{\epsilon_0m_ec^2}{n_0e^2}, \tag{3.70}$$

then Eqs. (3.68) and (3.69) become,

$$-\frac{d^2A_x}{dz^2} = \alpha^2A_x, \tag{3.71}$$
$$-\frac{d^2A_y}{dz^2} = \alpha^2A_y, \tag{3.72}$$

where

$$\alpha=\left(\frac{\Delta T_e}{T_{e\perp}}+\frac{m_e}{m_i}\frac{\Delta T_i}{T_{i\perp}}\right)^{\frac{1}{2}}. \tag{3.73}$$

The solution to these differential equations is

$$\mathbf{A}(z) = \left(\frac{B_0}{\alpha}\sin(\alpha z),\frac{B_0}{\alpha}\cos(\alpha z),0\right), \tag{3.74}$$
$$\mathbf{B}(z) = (B_0\sin(\alpha z),B_0\cos(\alpha z),0), \tag{3.75}$$

where the boundary conditions are chosen to be $B_x=0$, $B_y=B_0$ for $z=0$. It is easy to see that the solution satisfies the force-free condition $B_x^2+B_y^2=$ a constant and that

$$\mathbf{j}=\alpha\mathbf{B}. \tag{3.76}$$

It should be noted that this linear force-free solution is a special solution of this distribution function for a particular initial condition and that other initial conditions will produce non-force-free magnetic fields.

The linear force-free solution is shown in Figure 3.3. The magnetic field is normalised to 1 and $\alpha = 1$. Figure 3.3(a) shows the periodic structure of the magnetic field components and Figure 3.3(b) shows the potential with the particle orbit overlaid. The particle's orbit in this case corresponds to circular motion. In addition to this Figure 3.3(c) shows a 3D plot of magnetic field lines along z passing through $x = 0$, $y = 0$. It easy to see the shearing and twisting of the field lines that is a characteristic feature of a force-free magnetic field. The possibility of other force-free VM equilibria are discussed in more detail in Sec. 3.6.

3.3.4 The case $r_{1,qn}$ positive and $r_{2,qn}$ negative

There are two possibilities for mixed sign cases of $r_{1,qn}$ and $r_{2,qn}$, but as none of the coordinates x or y is preferred these cases are equivalent. Therefore only one of them is discussed. In the mixed sign case there is a saddle point of the pressure/pseudo-potential at the origin.

The structure of the solutions will depend again on the initial conditions and on whether the pseudo-particle has enough energy to overcome the saddle or will be reflected. Note that the condition for the particle crossing the saddle is not simply given by the total pressure (pseudo-energy) being bigger than the value of the pressure (potential) at the saddle, because the trajectory may not come close to the saddle at all and a higher energy will usually be required for solutions to cross the saddle structure. Therefore, the condition that the total initial pressure is larger than the pressure at the saddle point is a necessary, but not sufficient condition for a crossing solution.

Generally, the solutions for A_y will have a non-oscillatory nature and will be of neutral sheet type if the particle is reflected and of single direction field type if the particle crosses the saddle. For the A_x component some form of both oscillatory and non-oscillatory behaviour are possible depending on initial conditions. A few examples are shown in Figure 3.4. Figures 3.4(a) and 3.4(b) are for a particle with an initial kinetic energy less than the maximum value of the potential at the saddle point. There is only one non-vanishing component of the magnetic field and vector potential. Figure 3.4(b) shows the pressure function with the particle trajectory overlaid. The particle approaches along the A_y axis and is reflected resulting in the anti-parallel x component of the magnetic field where the profile of the magnetic field is shown in figure 3.4(a). Figures 3.4(c) and 3.4(d) are for the case where the vector potential and magnetic field both have two non-vanishing components. In this example the initial kinetic energy of the particle is greater than the maximum value of the potential at the saddle point but because the particle approaches the saddle structure along a different direction than the A_y axis, in this case it would require a much larger

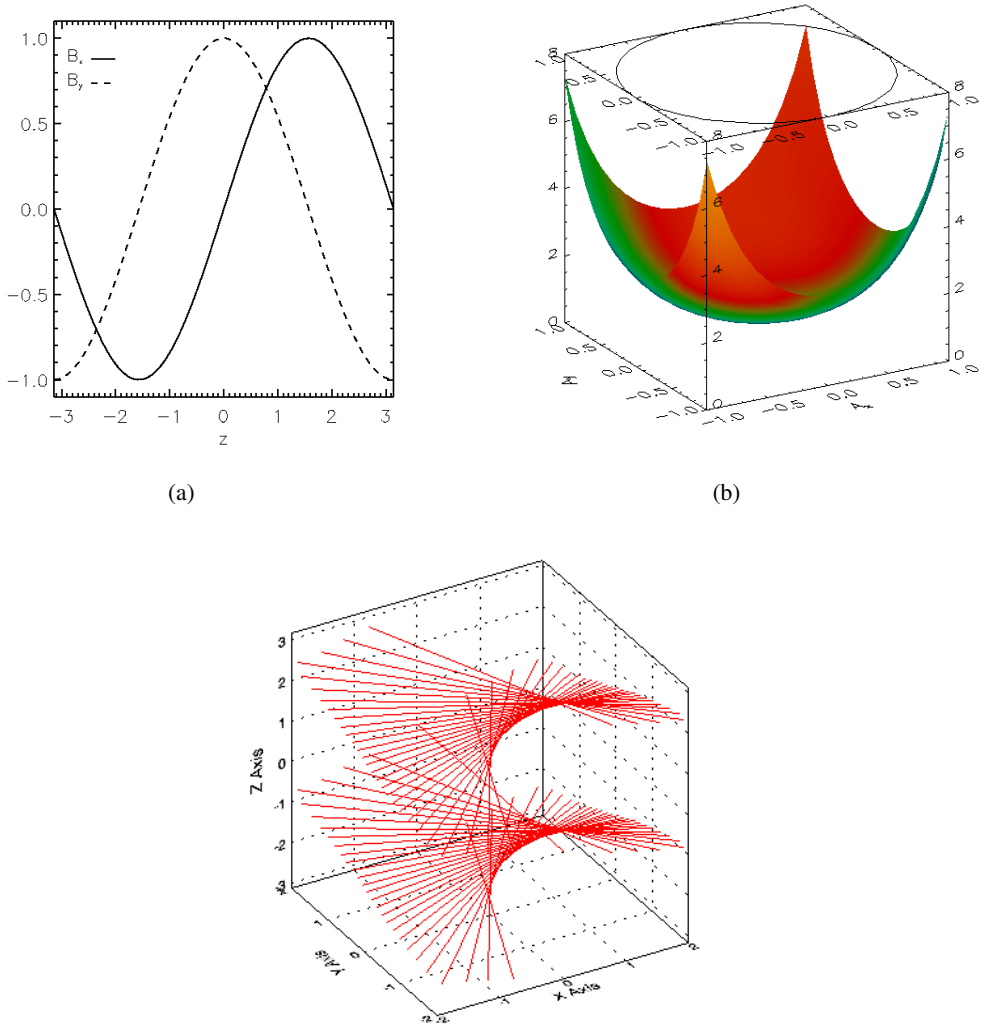

(a) (b)

(c)

Figure 3.3: An example of the special case when $r_{1,qn} = r_{2,qn} = r$ and $A_x^2 + A_y^2 = 1$. The magnetic field is normalised to 1 and $\alpha = 1$. Figure 3.3(b) shows a surface plot of the potential P_{qn} with the circular pseudo-particle trajectory in the A_x-A_y-plane plotted above it, that corresponds to the linear force-free magnetic field profiles shown in Figure 3.3(a).

initial energy to cross the saddle structure. Figure 3.4(d) shows the particle trajectory overlaid on the potential illustrating that the particle is reflected. The profiles of the magnetic field components are shown in Figure 3.4(c). Both B_x and B_y have an anti-parallel structure. Finally Figures 3.4(e) and 3.4(f) are for the case where a particle has a kinetic energy greater than the maximum value of the potential at the saddle point and approaches the saddle point along the A_y axis. In this case, as shown by the particle trajectory in Figure 3.4(f) the particle crosses the saddle and is not reflected. The magnetic field profile in Figure 3.4(e) shows that the magnetic field decreases as the particle moves over the potential, i.e. the particle is slowed down as it crosses the saddle.

3.3.5 The case $r_{1,qn} \neq 0$ and $r_{2,qn} = 0$

This case is again equivalent (modulo a 90° rotation of the coordinate system) to the case $r_{1,qn} = 0$ and $r_{2,qn} \neq 0$. Again A_x can be gauged in the same way as discussed in Sec. 3.3.2 and thus without loss of generality it can be assumed that $r_{3,qn} = 0$ and $r_{4,qn} \neq 0$. The sign of r_{4qn} is also largely irrelevant as it only determines whether the pseudo-particle/VM solution approaches from $+\infty$ or $-\infty$. Thus, without loss of generality it can be assumed that $r_{4,qn} > 0$.

The case $r_{1,qn}$ negative

This case has been studied extensively by Kan (Kan 1972). The solutions resemble the solutions found by Nicholson (Nicholson 1963) and Lam (Lam 1967) for A_x (see Sec. 3.3.2) and the Harris sheet (Harris 1962) (see Sec. 3.3.6) for A_y. An example is shown in Figure 3.5. Figures 3.5(a) and 3.5(b) shows an example where a particle approaches along the A_y axis. Figure 3.5(b) shows the particle trajectory overlaid on the potential. The particle slows, eventually stops, turns around and goes back along the same trajectory, eventually returning to its A_y coordinate with a velocity which has the same magnitude, but opposite direction to the initial velocity. Figure 3.5(a) shows the corresponding profile of the x component of the magnetic field. It is a neutral sheet with oppositely directed magnetic field components either side of the neutral line. At large distances the magnetic field approaches a constant value on each side of the sheet, although it is oppositely directed. Figures 3.5(c) and 3.5(d) are an example where A_x and B_y are now non-zero. The potential has the effect of scattering the particle. Figure 3.5(d) shows the particle trajectory. The particle is still reflected by the potential and therefore the profile of B_x shown in Figure 3.5(c) is still oppositely directed across $z = 0$.

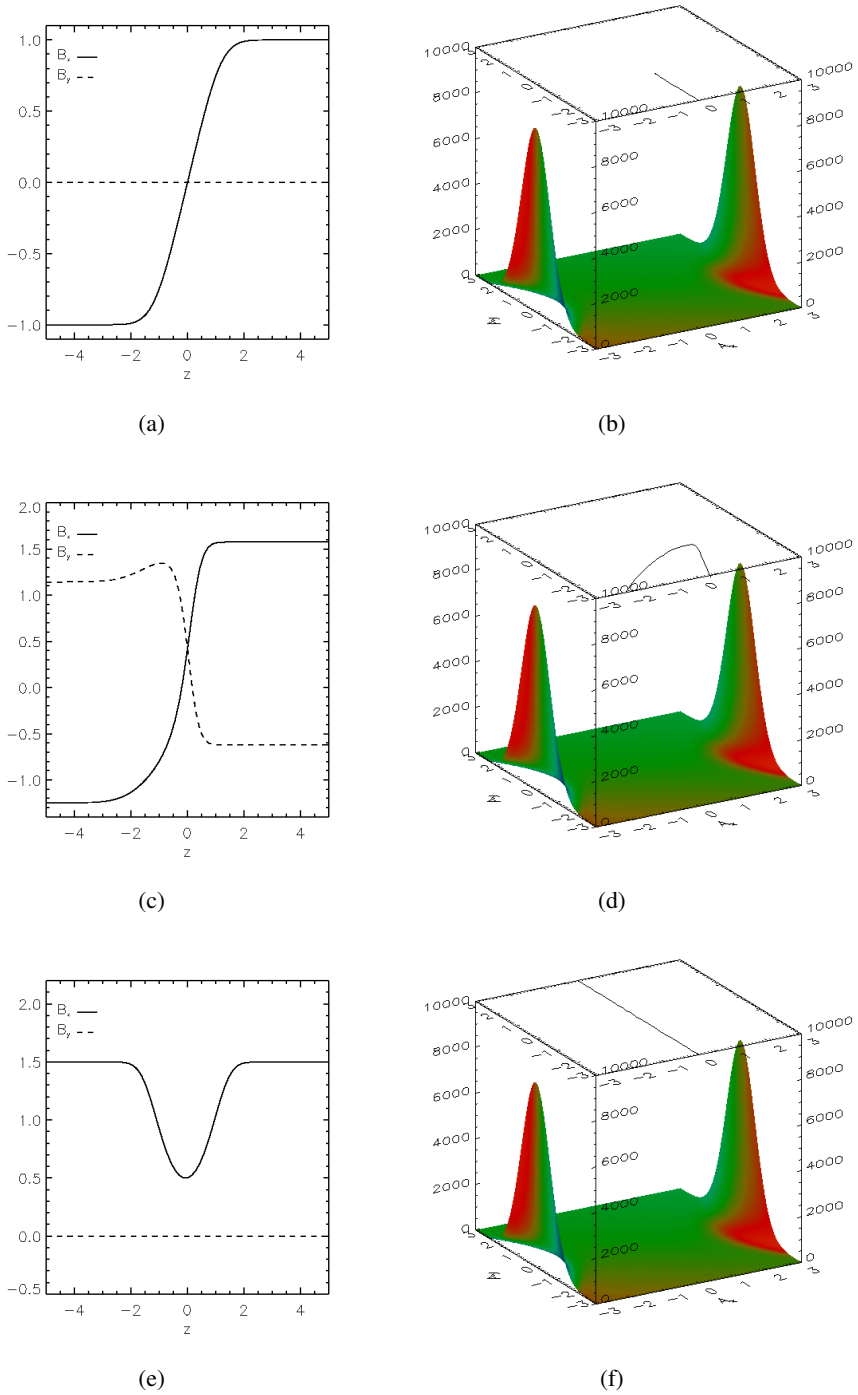

Figure 3.4: Plots for the case with $r_{1,qn} = 1$, $r_{2,qn} = -1$ and $\bar{P}_0 = 1$. In each example the figure on the right shows a surface plot of the potential P_{qn} with the pseudo-particle trajectory in the A_x-A_y-plane plotted above it, that corresponds to the magnetic field profiles shown on the left for different initial conditions.

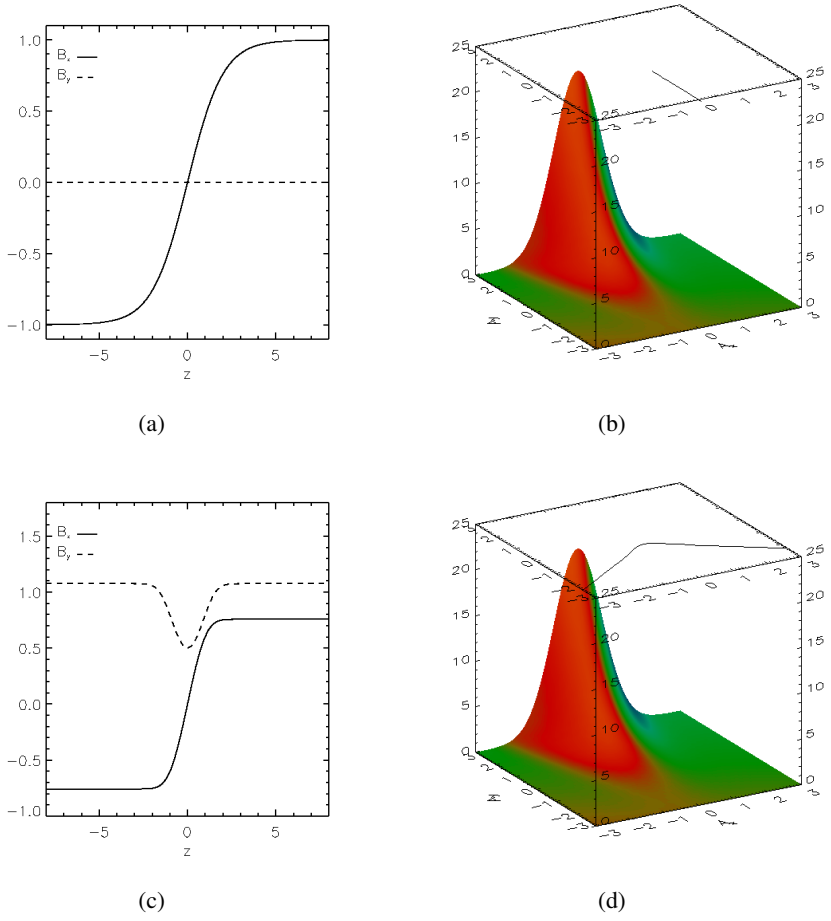

Figure 3.5: Plots for the case with $r_{1,qn} = -1$, $r_{2,qn} = 0$, $r_{3,qn} = 0$, $r_{4,qn} = 1$ and $P_0 = 1$. In each example the figure on the right shows a surface plot of the potential P_{qn} with the pseudo-particle trajectory in the A_x-A_y-plane plotted above it, that corresponds to the magnetic field profiles shown on the left for different initial conditions.

The case $r_{1,qn}$ positive

In this case the solutions will have a neutral sheet structure for A_y, whereas the structure of A_x can be either oscillatory or non-oscillatory, depending on initial conditions. Solution examples are shown in Figure 3.6. Figures 3.6(a) and Figure 3.6(b) are for a case where a particle moves along the A_y axis. The particle trajectory is shown in Figure 3.6(b) overlaid on the potential. The particle slows, eventually stops, turns around and goes back along the same trajectory, eventually returning to its initial A_y coordinate with a velocity which has the same magnitude, but opposite direction to the initial velocity. The resulting anti-parallel profile of the x component of the magnetic field is shown in Figure 3.6(a). Figures 3.6(c) and 3.6(d) are for a case where the magnetic field and vector potential have two non-vanishing components. In this case the particle trajectory, shown in Figure 3.6(d) is modified as the particle has an additional velocity component. The structure of the potential in the A_y direction means that the particle at some point will be reflected. The magnetic field profile is shown in Figure 3.6(c). Finally Figures 3.6(e) and 3.6(f) are for a case where the initial velocity in the A_x direction is larger than in the second example. In this case the particle is once again reflected but the profile of the y component of the field shown in Figure 3.6(e) has a stronger oscillatory nature close to $z = 0$.

3.3.6 The case $r_{1,qn} = r_{2,qn} = 0$

If $r_{1,qn} = r_{2,qn} = 0$ the argument of the exponential pressure function contains only terms linear in A_x and A_y. In this case the Eqs. (3.26) and (3.27) can be solved analytically. The quasinuetral potential P_{qn} in this case is,

$$P_{qn} = P_0 \exp\left(r_{3,qn} A_x + r_{4,qn} A_y\right). \tag{3.77}$$

The x and y components of the current density can be calculated from the Eqs. (3.20) and (3.21), resulting in,

$$j_x = r_{3,qn} P_0 \exp\left(r_{3,qn} A_x + r_{4,qn} A_y\right), \tag{3.78}$$

$$j_y = r_{4,qn} P_0 \exp\left(r_{3,qn} A_x + r_{4,qn} A_y\right). \tag{3.79}$$

In terms of our normalisation the two coupled ODEs to be solved are,

$$-\frac{\mathrm{d}^2 A_x}{\mathrm{d}z^2} = P_0 r_{3,qn} \exp\left(r_{3,qn} A_x + r_{4,qn} A_y\right), \tag{3.80}$$

$$-\frac{\mathrm{d}^2 A_y}{\mathrm{d}z^2} = P_0 r_{4,qn} \exp\left(r_{3,qn} A_x + r_{4,qn} A_y\right). \tag{3.81}$$

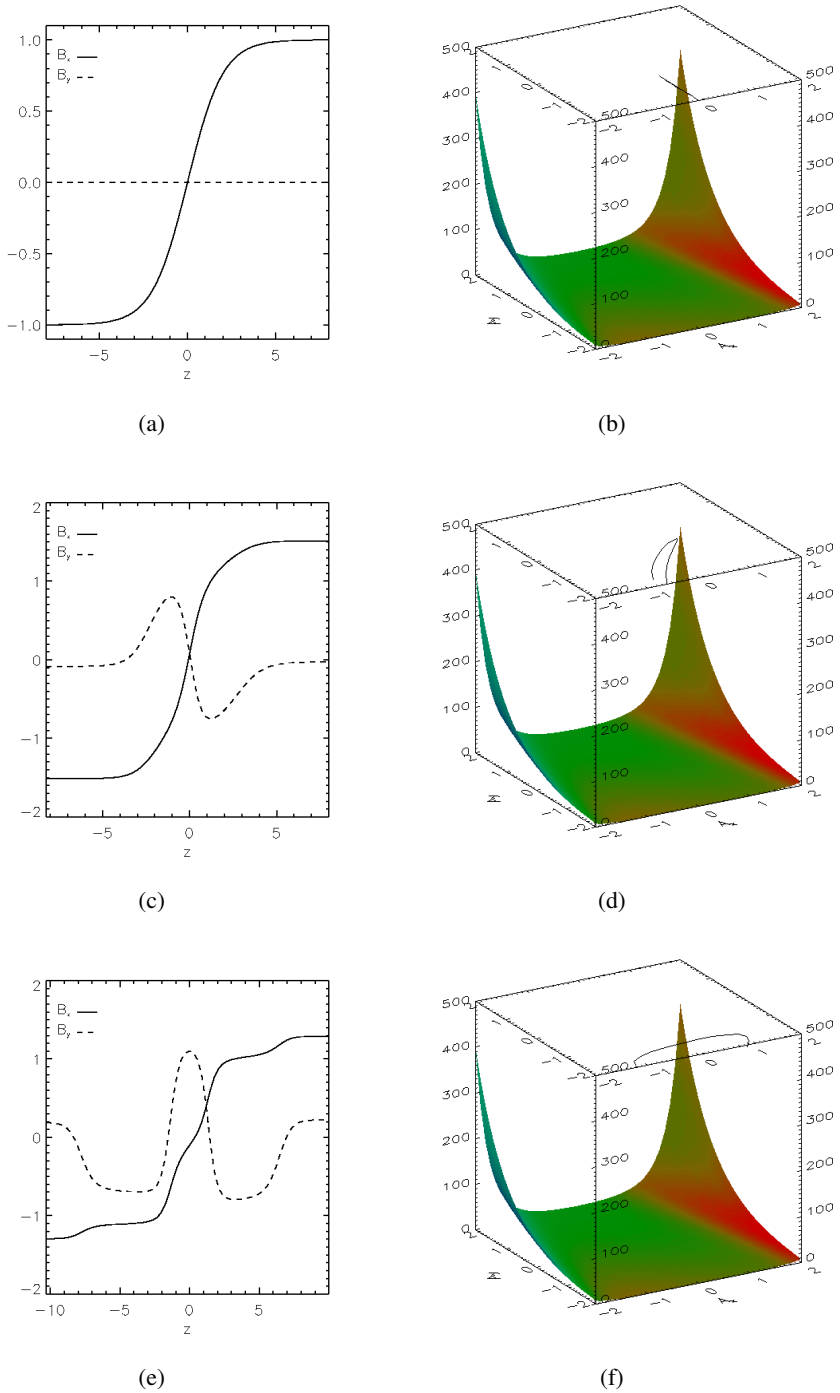

Figure 3.6: Plots for the case with $r_{1,qn} = 1$, $r_{2,qn} = 0$, $r_{3,qn} = 0$, $r_{4,qn} = 1$ and $P_0 = 1$. In each example the figure on the right shows a surface plot of the potential P_{qn} with the pseudo-particle trajectory in the A_x-A_y-plane plotted above it, that corresponds to the magnetic field profiles shown on the left for different initial conditions.

To get solutions, multiply Eq. (3.80) by $r_{3,qn}$ and Eq. (3.81) by $r_{4,qn}$ and add them together:

$$-\frac{\mathrm{d}^2}{\mathrm{d}z^2}(r_{3,qn}A_x + r_{4,qn}A_y) = P_0(r_{3,qn}^2 + r_{4,qn}^2)\exp\left(r_{3,qn}A_x + r_{4,qn}A_y\right). \tag{3.82}$$

Multiplying Eq. (3.80) by $r_{4,qn}$ and Eq. (3.81) by $r_{3,qn}$ and subtracting them results in,

$$-\frac{\mathrm{d}^2}{\mathrm{d}z^2}(r_{4,qn}A_x - r_{3,qn}A_y) = 0. \tag{3.83}$$

Excluding any asymmetries and gauging both A_x and A_y to zero at $z = 0$, then

$$r_{3,qn}A_y = r_{4,qn}A_x. \tag{3.84}$$

Solving (3.82) gives,

$$r_{3,qn}A_x + r_{4,qn}A_y = -2\ln\cosh\left(\sqrt{\frac{K}{2}}z\right), \tag{3.85}$$

where

$$K = P_0(r_{3,qn}^2 + r_{4,qn}^2). \tag{3.86}$$

Finally,

$$A_x = -\frac{2r_{3,qn}}{r_{3,qn}^2 + r_{4,qn}^2}\ln\cosh\left(\sqrt{\frac{K}{2}}z\right), \tag{3.87}$$

$$A_y = -\frac{2r_{4,qn}}{r_{3,qn}^2 + r_{4,qn}^2}\ln\cosh\left(\sqrt{\frac{K}{2}}z\right), \tag{3.88}$$

and the magnetic field components are

$$B_x = \frac{2r_{4,qn}}{r_{3,qn}^2 + r_{4,qn}^2}\sqrt{\frac{K}{2}}\tanh\left(\sqrt{\frac{K}{2}}z\right), \tag{3.89}$$

$$B_y = -\frac{2r_{3,qn}}{r_{3,qn}^2 + r_{4,qn}^2}\sqrt{\frac{K}{2}}\tanh\left(\sqrt{\frac{K}{2}}z\right). \tag{3.90}$$

It is in fact easy to convince oneself that without loss of generality that this solution is in fact completely equivalent to the Harris sheet, but in a rotated coordinate system. Consider the following matrix transformations of the vector potential $\mathbf{A}$, the magnetic field $\mathbf{B}$ and the current densities j_x and j_y. Consider a general matrix rotation in the x-y-plane of the coordinate system defined by the vector $\mathbf{M}$, to a new coordinate system defined by the vector $\mathbf{M}'$, with the rotation matrix

defined as $\mathbf{R}$, then the coordinate rotation is given by

$$\mathbf{M} = \mathbf{R}\mathbf{M}'. \tag{3.91}$$

Inverting this,

$$\mathbf{M}' = \mathbf{R}^{\mathbf{T}}\mathbf{M}, \tag{3.92}$$

where

$$R = \begin{pmatrix} \cos(\theta) & \sin(\theta) \\ -\sin(\theta) & \cos(\theta) \end{pmatrix}, \tag{3.93}$$

$$R^T = \begin{pmatrix} \cos(\theta) & -\sin(\theta) \\ \sin(\theta) & \cos(\theta) \end{pmatrix}. \tag{3.94}$$

Consider a rotation of the Cartesian coordinate system where

$$\cos(\theta) = 1/r_{3,qn} \quad \sin(\theta) = 1/r_{4,qn} \ , \tag{3.95}$$

then in this new coordinate system the vector potentials are now,

$$A'_x = 0, \tag{3.96}$$

$$A'_y = -\frac{2}{r_{3,qn}r_{4,qn}} \ln\cosh\left(\sqrt{\frac{K}{2}}z\right), \tag{3.97}$$

and the magnetic field is

$$B'_x = \frac{2}{r_{3,qn}r_{4,qn}}\sqrt{\frac{K}{2}}\tanh\left(\sqrt{\frac{K}{2}}z\right), \tag{3.98}$$

$$B'_y = 0, \tag{3.99}$$

and the current densities are,

$$j'_x = 0, \tag{3.100}$$

$$j'_y = \frac{2}{r_{3,qn}r_{4,qn}}\frac{K}{2}\frac{1}{\cosh^2\left(\sqrt{\frac{K}{2}}z\right)}. \tag{3.101}$$

This is clearly a Harris sheet (Harris 1962) in a rotated coordinate system. Therefore one can either set $r_{3,qn} = 0$ or $r_{4,qn} = 0$ because it is always possible to rotate the coordinate system so that one of the two terms vanishes. As an example $r_{3,qn} = 0$ is chosen. The sign of the remaining

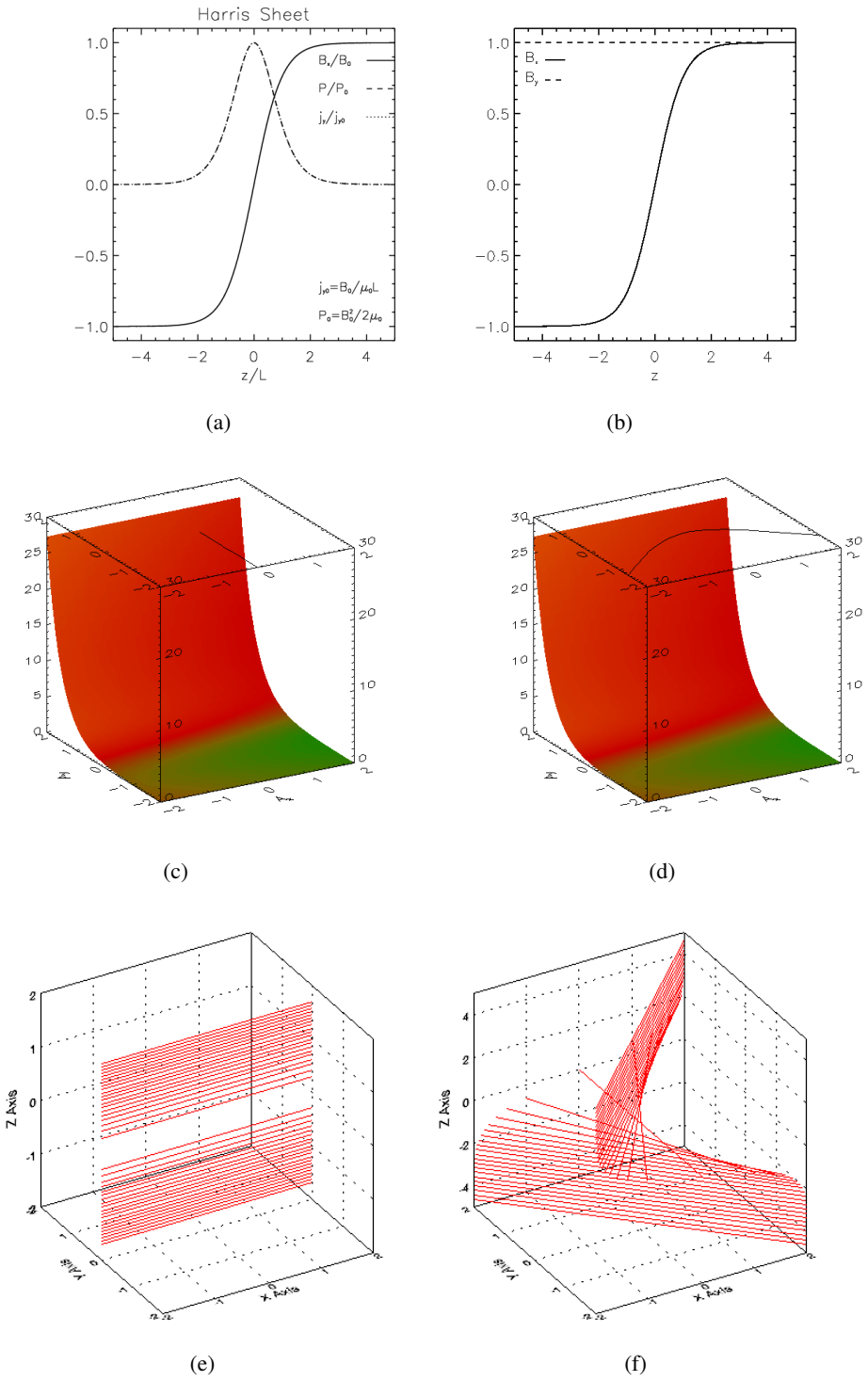

Figure 3.7: Plots for the case with $r_{1,qn} = r_{2,qn} = r_{3,qn} = 0$, $r_{4,qn} = 2$ and $P_0 = 0.5$. The analytical solution to this case is well known and is given by the Harris sheet (Harris 1962).

coefficient does not matter either for the same reason mentioned in Sec. 3.3.5. Here $r_{4,qn} > 0$. In this case the analytical solution is well-known and is given by the Harris sheet (Harris 1962), shown in Figure 3.7. Figures 3.7(a), 3.7(c) and 3.7(e) show the Harris sheet with zero constant guide field added. Figure 3.7(a) shows the profile of the magnetic field, current density and plasma pressure where it should be noted that the profiles of the plasma pressure and current density are identical and hence indistinguishable in the plot. The gradient of the plasma pressure maintains the force balance with the magnetic pressure due to the x component of the field, with the maximum plasma pressure at the centre of the sheet. Figure 3.7(c) shows the particle trajectory overlaid on the potential. The particle approaches along the A_y axis, it slows, eventually stops, turns around and goes back along the same trajectory, eventually returning to its initial A_y coordinate with a velocity which has the same magnitude, but opposite direction to the initial velocity. When the particle encounters the steep gradient it leads to strong gradients in the magnetic field and hence a strong current density. Also Figure 3.7(e) shows a 3D plot of magnetic field lines along z passing through $x = 0$, $y = 0$ for the Harris sheet. The magnetic field lines are not sheared in the case of zero guide field.

Because the pressure (pseudo-potential) in this case does not depend on A_x, an A_x depending linearly on z can be added to the solution. This gives rise to a constant y-component of the magnetic field which corresponds to a constant y-velocity of the pseudo-particle. It is remarked that this is possible for every case in which the pressure (pseudo-potential) depends only upon one component of the vector potential (coordinate) (Kan 1972). Figure 3.7(b) and 3.7(d) are for the Harris sheet with a constant guide field of $B_{y0} = 1.0$. The profile of the magnetic field, current density and plasma pressure remains unchanged. The particle trajectory is shown in Figure 3.7(d). Figure 3.7(f) shows a 3D plot of magnetic field lines along z passing through $x = 0$, $y = 0$ for a constant guide field of $B_y = B_0$. It can be clearly seen how the constant guide field adds shear and twist to the system.

3.4 An Extension to the Linear Force-Free Distribution Function

The distribution function (3.53) given in Sec. 3.3.3 can be extended to construct a series of Vlasov-Maxwell equilibria that make the transition from an anti-parallel neutral sheet through to the linear force-free equilibria described in Sec. 3.3.3. The case of an anti-parallel neutral sheet of this type has previously been discussed by Lam (Lam 1967) and Attico and Pegoraro (Attico and Pegoraro 1999). The distribution function in dimensional form is, using the notation of Bobrova et al. (2001),

$$f_s = c_s \exp\left[-\frac{1}{T_{s\perp}}H_s + \frac{\Delta T_s}{2m_s T_{s\perp} T_{s\parallel}} b_s p_{xs}^2 + \frac{\Delta T_s}{2m_s T_{s\perp} T_{s\parallel}} p_{ys}^2\right], \tag{3.102}$$

where

$$\Delta T_s = T_{s\parallel} - T_{s\perp} \geq 0. \tag{3.103}$$

The constant c_s is a normalising constant and is defined as,

$$c_s = \frac{n_{0s} m_s^{3/2} \left((1-b_s)T_{s\parallel} + b_s T_{s\perp}\right)^{1/2}}{(2\pi)^{3/2} T_{s\perp} T_{s\parallel}}. \tag{3.104}$$

The distribution function is identical to the previous distribution function (3.53) with the addition of a dimensionless parameter b_s. The value of this dimensionless parameter is varied to construct a family of Vlasov-Maxwell equilibria that describe the transition between an anti-parallel periodic neutral sheet through to the linear force-free field.

For the distribution function (3.102) the zz-component of the pressure tensor is given by

$$P = \sum_s \frac{1}{\beta_s} \exp(-\beta_s q_s \phi) N_s(A_x, A_y), \tag{3.105}$$

where

$$N_s(A_x, A_y) = n_{0s} \exp(r_{1s} A_x^2 + r_{2s} A_y^2). \tag{3.106}$$

Equation (3.106) uses the definitions,

$$r_{1s} = \frac{1}{2}\frac{q_s^2}{m_s}\frac{\Delta T_s}{T_{s\perp}}\frac{b_s}{\left(T_{s\parallel}(1-b_s) + b_s T_{s\perp}\right)}, \tag{3.107}$$

$$r_{2s} = \frac{1}{2}\frac{q_s^2}{m_s}\frac{\Delta T_s}{T_{s\perp}^2}. \tag{3.108}$$

The charge density is calculated using Eq. (3.19):

$$\sigma = \sum_s q_s \exp\left(-\frac{q_s \phi}{T_{s\perp}}\right) N_s(A_x, A_y), \tag{3.109}$$

and the quasi-neutrality condition $\sigma = 0$ then gives,

$$\phi_{qn} = \frac{T_{e\perp} T_{i\perp}}{e(T_{e\perp} + T_{i\perp})} \ln\left(\frac{N_i}{N_e}\right). \tag{3.110}$$

One can see immediately that the quasi-neutral electric field will only vanish for a choice of parameters such that $N_e(A_x, A_y) \propto N_i(A_x, A_y)$.

The quasi-neutral P_{zz} is given by

$$\begin{aligned} P_{qn} &= (T_{e\perp} + T_{i\perp})\, N_e^{T_{e\perp}/(T_{e\perp}+T_{i\perp})} N_i^{T_{i\perp}/(T_{e\perp}+T_{i\perp})} \\ &= P_0 \exp\left(r_{1,qn} A_x^2 + r_{2,qn} A_y^2\right), \end{aligned} \tag{3.111}$$

with

$$P_0 = (T_{e\perp} + T_{i\perp})\, n_0, \tag{3.112}$$

$$n_0 = n_{0e}^{T_{e\perp}/(T_{e\perp}+T_{i\perp})} n_{0i}^{T_{i\perp}/(T_{e\perp}+T_{i\perp})}, \tag{3.113}$$

$$r_{1,qn} = \frac{1}{2(T_{e\perp}+T_{i\perp})}\left(\frac{e^2}{m_e}\frac{b_e \Delta T_e}{(1-b_e)T_{e\|} + b_e T_{e\perp}} + \frac{e^2}{m_i}\frac{b_i \Delta T_i}{(1-b_i)T_{i\|} + b_i T_{i\perp}}\right), \tag{3.114}$$

$$r_{2,qn} = \frac{1}{2(T_{e\perp}+T_{i\perp})}\left(\frac{e^2}{m_e}\frac{\Delta T_e}{T_{e\perp}} + \frac{e^2}{m_i}\frac{\Delta T_i}{T_{i\perp}}\right). \tag{3.115}$$

The x- and y-components of the current density can be calculated from Eqs. (3.20) and (3.21), resulting in

$$j_x = 2 r_{1,qn} P_0 A_x \exp\left(r_{1,qn} A_x^2 + r_{2,qn} A_y^2\right), \tag{3.116}$$

$$j_y = 2 r_{2,qn} P_0 A_y \exp\left(r_{1,qn} A_x^2 + r_{2,qn} A_y^2\right). \tag{3.117}$$

In all the example solutions the boundary conditions are $B_x = 0$, $B_y = B_{y,max}$, $A_x = 0$ and $A_y = A_{y,max}$ at $z = 0$, where $B_{y,max}$ and $A_{y,max}$ are the maximum of the y components of the magnetic field and vector potential and they must all have the same period. For convenience the definition of the maximum value of the pressure P_{max} is introduced where,

$$P_{max} = P_0 \exp(r_{2,qn} A_{y,max}^2). \tag{3.118}$$

The quasineutral pressure is now,

$$P_{qn} = P_{max} \exp\left(r_{1,qn} A_x^2 + r_{2,qn}(A_y^2 - A_{y,max}^2)\right), \tag{3.119}$$

where by introducing the definition of P_{max} it is clear that the maximum value of the plasma pressure will always be at $z = 0$ and at periodic distances along z. The two coupled ODE's (3.26) and (3.27) that must be solved are,

$$-\frac{d^2 A_x}{dz^2} = \mu_0 2 r_{1,qn} P_{max} A_x \exp\left(r_{1,qn} A_x^2 + r_{2,qn}(A_y^2 - A_{y,max}^2)\right), \tag{3.120}$$

$$-\frac{d^2 A_y}{dz^2} = \mu_0 2 r_{2,qn} P_{max} A_y \exp\left(r_{1,qn} A_x^2 + r_{2,qn}(A_y^2 - A_{y,max}^2)\right). \tag{3.121}$$

The magnetic field is normalised to a typical value B_{x0} and the coordinate z to a typical length scale L. The components of the vector potential are then normalized by $B_{x0}L$ and the normalized coefficients are defined by $\bar{r}_{1,qn} = B_{x0}^2 L^2 r_{1,qn}$ and $\bar{r}_{2,qn} = B_{x0}^2 L^2 r_{2,qn}$. The pressure P is

normalized by B_{x0}^2/μ_0. In this case L is the electron skin depth,

$$L^2 = \frac{m_e}{\mu_0 e^2 n_{max}} = \left(\frac{c}{\omega_{pe}}\right)^2, \tag{3.122}$$

and the differential equations that must be solved to determine A_x and A_y are

$$-\frac{d^2A_x}{dz^2} = 2\bar{r}_{1,qn}\bar{P}_{max}A_x \exp\left(\bar{r}_{1,qn}A_x^2 + \bar{r}_{2,qn}(A_y^2 - A_{y,max}^2)\right), \tag{3.123}$$

$$-\frac{d^2A_y}{dz^2} = 2\bar{r}_{2,qn}\bar{P}_{max}A_y \exp\left(\bar{r}_{1,qn}A_x^2 + \bar{r}_{2,qn}(A_y^2 - A_{y,max}^2)\right), \tag{3.124}$$

and the quasineutral pressure is

$$\bar{P}_{qn} = \bar{P}_{max} \exp\left(\bar{r}_{1,qn}A_x^2 + \bar{r}_{2,qn}(A_y^2 - A_{y,max}^2)\right), \tag{3.125}$$

with

$$\bar{P}_{max} = \mu_0 P_{max}/B_{x0}^2, \tag{3.126}$$

$$\bar{r}_{1,qn} = \frac{1}{2}\frac{B_{x0}^2}{\mu_0 P_{max}}\left(\frac{b_e\Delta T_e}{(1-b_e)T_{e\|} + b_e T_{e\perp}} + \frac{m_e}{m_i}\frac{b_i\Delta T_i}{(1-b_i)T_{i\|} + b_i T_{i\perp}}\right), \tag{3.127}$$

$$\bar{r}_{2,qn} = \frac{1}{2}\frac{B_{x0}^2}{\mu_0 P_{max}}\left(\frac{\Delta T_e}{T_{e\perp}} + \frac{m_e}{m_i}\frac{\Delta T_i}{T_{i\perp}}\right). \tag{3.128}$$

To illustrate the transition between an anti-parallel configuration and the linear force-free configuration, several equilibrium examples are shown below for increasing strength of the shear field B_y. In each case the solution has been found by a shooting method where a fourth order Runge-Kutta method is used to integrate the differential equations. The shooting method is used to determine the value of b_s for which B_x, B_y, A_x and A_y satisfy the initial conditions that $B_x = 0$, $B_y = B_{y,max}$, $A_x = 0$ and $A_y = A_{y,max}$ at $z = 0$ and that they all have the same period. In these example cases B_x is always normalised against $B_{x,max}$ and the strength of the shear field B_y is measured relative to that. For these examples $T_{e\perp} = T_{i\perp} = 0.5$ and $T_{e\|} = T_{i\|} = 0.625$ and note also that $b_e = b_i = b$. The mass ratio has been set equal to one $(m_i/m_e = 1)$. Figure 3.8 shows plots of the profiles of the magnetic field components as you go along z. In the examples considered the maximum value of the shear field $B_{y,max}$ takes the values $B_{y,max} = 0.0, 0.1, 0.3, 0.5, 0.9, 1.0$. In each of these different cases the value of the parameter b is given. Figure 3.9 shows the plasma pressure gradient as one makes the transition from an anti-parallel field through to a force-free field. It is clear to see that as the strength of the shear field increases the force balance across the sheet is dominated by the shear field rather than the plasma pressure gradient, with the extreme case being the linear force-free case where the plasma pressure is constant. Figure 3.10 shows 3D plots of magnetic field lines passing through $x = 0$,

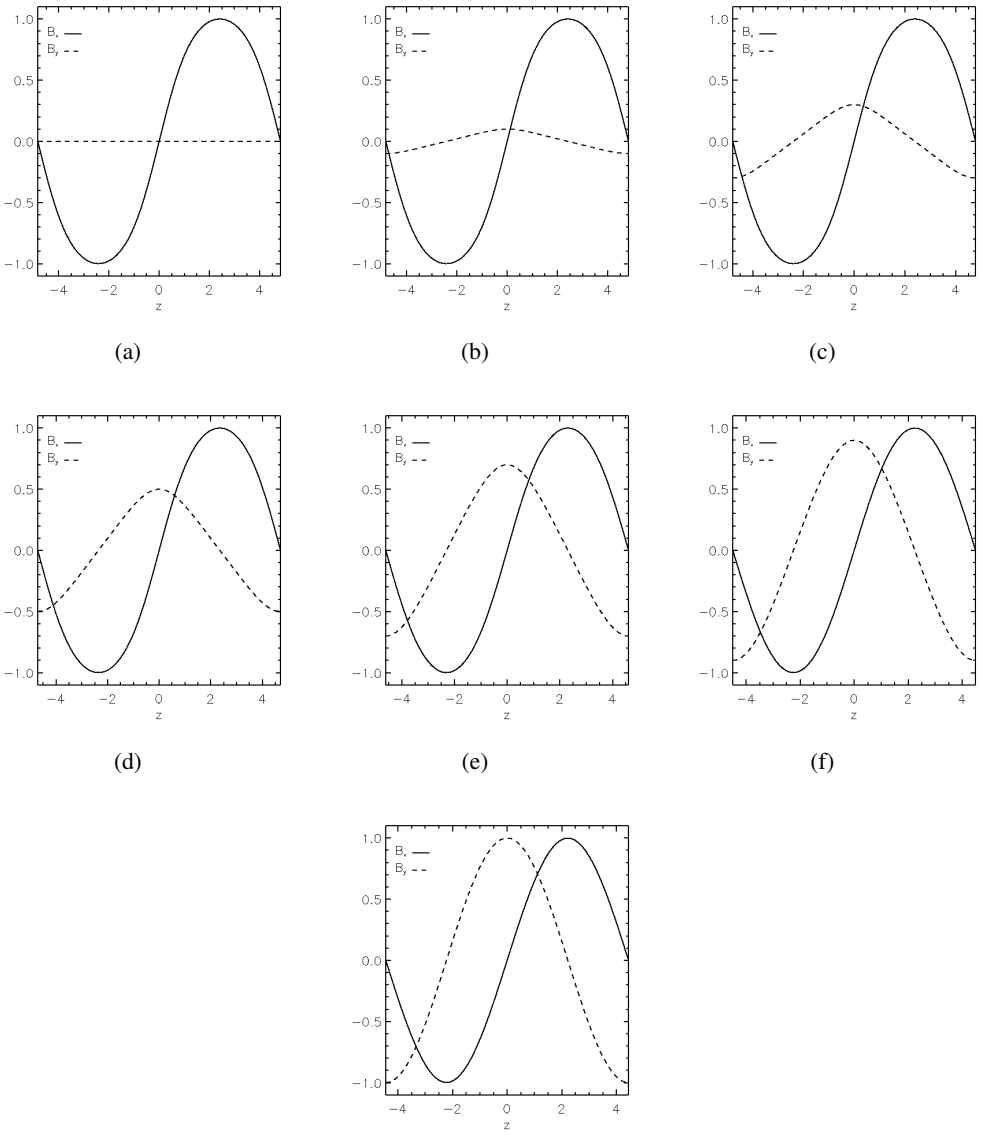

Figure 3.8: Plots of the profiles of the magnetic field components B_x and B_y as one makes the transition from an anti-parallel configuration through to a linear force-free configuration ($b_e = b_i = b$ in each case). (a) $B_{y,max} = 0.0$ ($b = 0.0$), (b) $B_{y,max} = 0.1$ ($b = 1.30$), (c) $B_{y,max} = 0.3$ ($b = 1.26$), (d) $B_{y,max} = 0.5$ ($b = 1.20$), (e) $B_{y,max} = 0.7$ ($b = 1.12$), (f) $B_{y,max} = 0.9$ ($b = 1.04$), (g) $B_{y,max} = 1.0$ ($b = 1.0$).

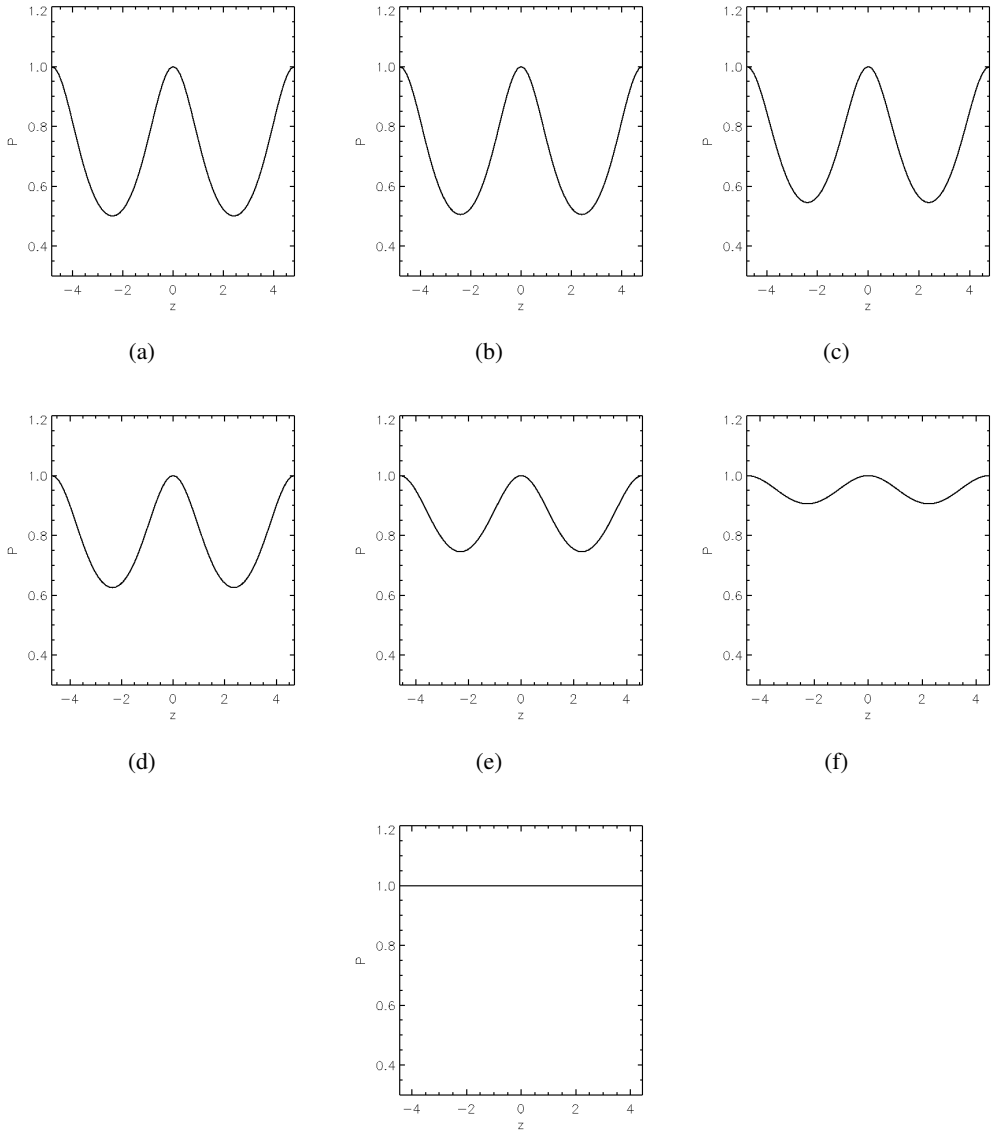

Figure 3.9: Plots of the profiles of the plasma pressure component P as one makes the transition from an anti-parallel configuration through to a linear force-free configuration ($b_e = b_i = b$ in each case). (a) $B_{y,max} = 0.0$ ($b = 0.0$), (b) $B_{y,max} = 0.1$ ($b = 1.30$), (c) $B_{y,max} = 0.3$ ($b = 1.26$), (d) $B_{y,max} = 0.5$ ($b = 1.20$), (e) $B_{y,max} = 0.7$ ($b = 1.12$), (f) $B_{y,max} = 0.9$ ($b = 1.04$), (g) $B_{y,max} = 1.0$ ($b = 1.0$).

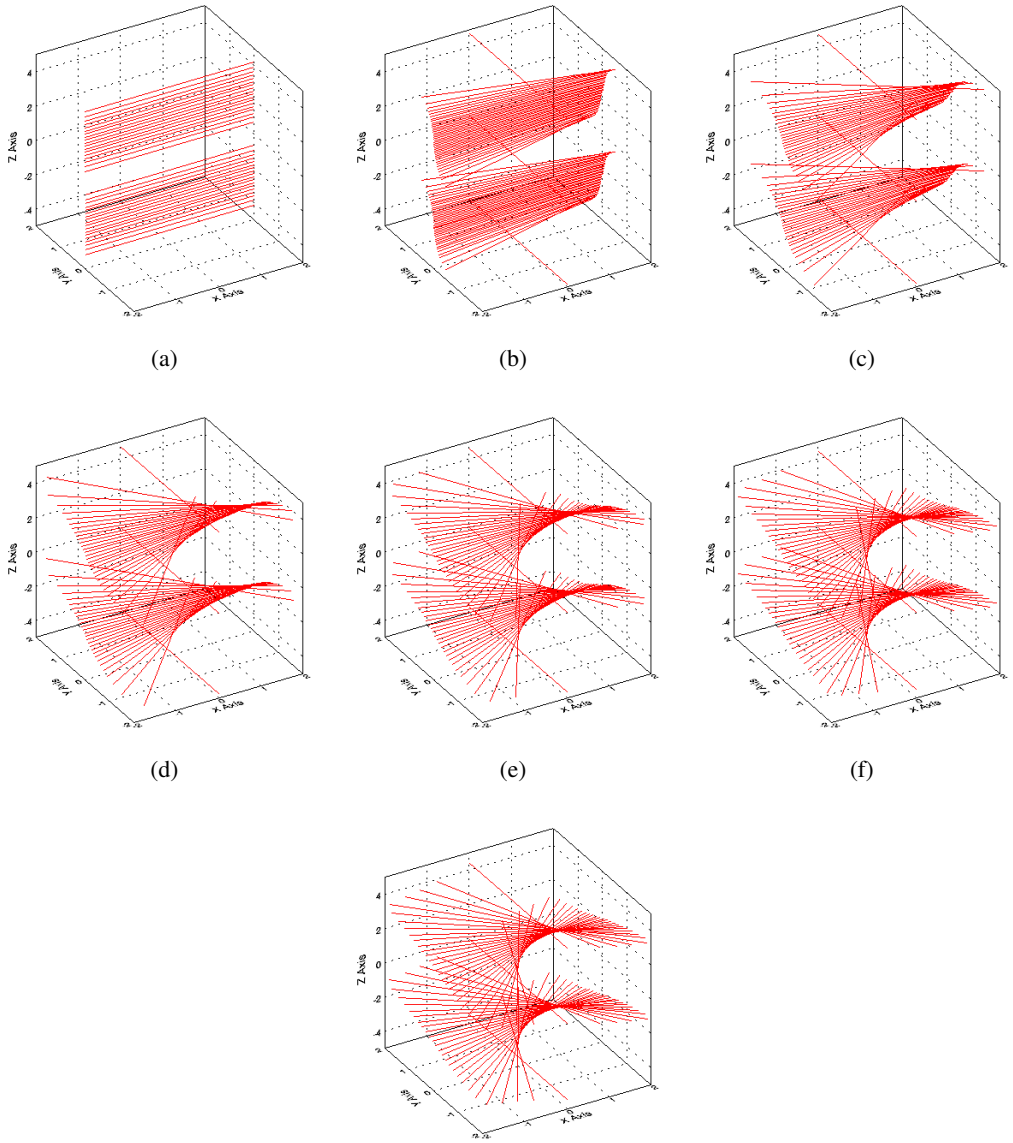

(a) (b) (c)

(d) (e) (f)

(g)

Figure 3.10: 3D plots of magnetic field lines for different values of z passing through $x = 0$, $y = 0$ as one makes the transition from an anti-parallel configuration through to a linear force-free configuration ($b_e = b_i = b$ in each case). (a) $B_{y,max} = 0.0$ ($b = 0.0$), (b) $B_{y,max} = 0.1$ ($b = 1.30$), (c) $B_{y,max} = 0.3$ ($b = 1.26$), (d) $B_{y,max} = 0.5$ ($b = 1.20$), (e) $B_{y,max} = 0.7$ ($b = 1.12$), (f) $B_{y,max} = 0.9$ ($b = 1.04$), (g) $B_{y,max} = 1.0$ ($b = 1.0$).

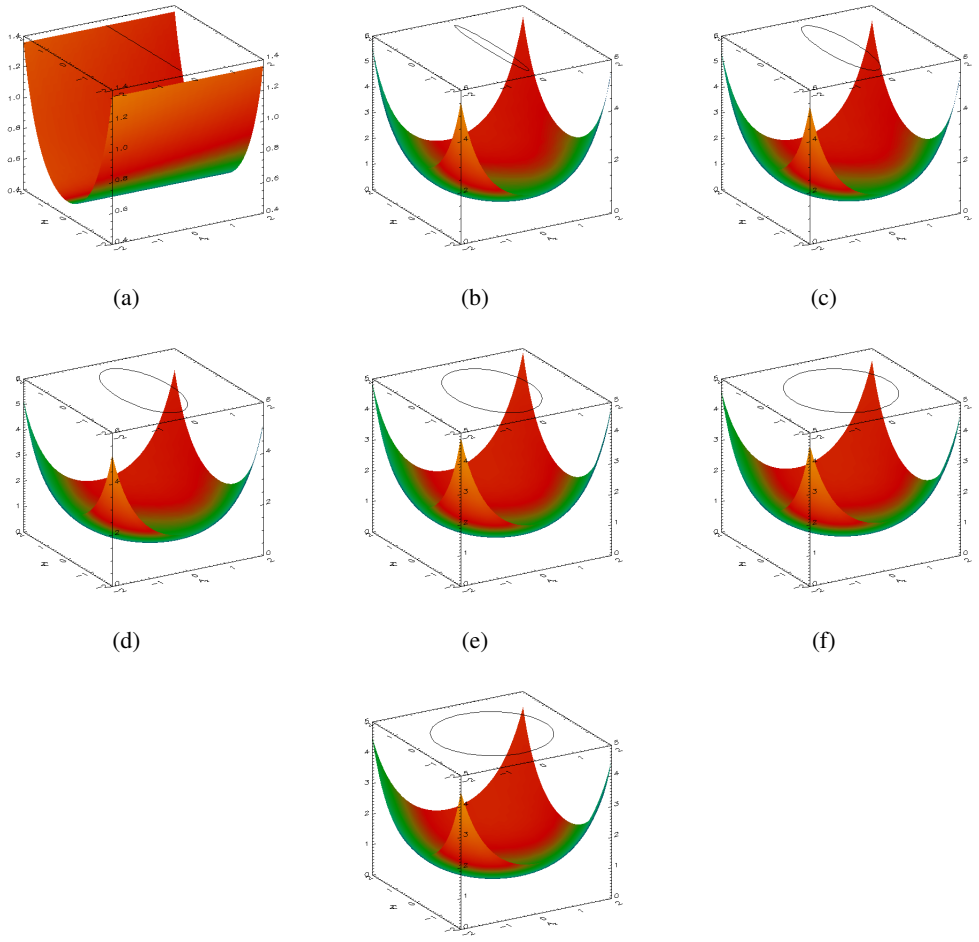

Figure 3.11: Plots of the potential surface $\bar{P}_{qn}$ as one makes the transition from an anti-parallel configuration through to a linear force-free configuration ($b_e = b_i = b$ in each case). (a) $B_{y,max} = 0.0$ ($b = 0.0$), (b) $B_{y,max} = 0.1$ ($b = 1.30$), (c) $B_{y,max} = 0.3$ ($b = 1.26$), (d) $B_{y,max} = 0.5$ ($b = 1.20$), (e) $B_{y,max} = 0.7$ ($b = 1.12$), (f) $B_{y,max} = 0.9$ ($b = 1.04$), (g) $B_{y,max} = 1.0$ ($b = 1.0$).

$y = 0$ at different z values. As the strength of the shear field increases the twist of the magnetic field increases. Finally the potential surface $\bar{P}_{qn}$ is plotted in each case in Figure 3.11 with the trajectory of the pseudo particle in the A_x-A_y-plane overlaid . In the anti-parallel case the motion of the particle corresponds simply to oscillation back and forth along the A_y direction. The particle trajectories are oscillatory with closed orbits for the cases with a non-zero y component of the magnetic field, with the trajectory approaching a circle for the linear force-free case.

3.5 A Sum of Two Harris Sheet Distribution Functions

A slightly different example is the case of a linear combination of two Harris sheet type distribution functions i.e. a sum of two drifting Maxwellians. This distribution function was considered to investigate what effect adding two distribution functions would have where the first distribution function depends only on the x component of the canonical momenta p_{xs} and the second distribution function only on the y component of the canonical momenta p_{ys}. One of the major aims of this thesis was to determine a distribution function that gives the force-free Harris sheet. Therefore, the distribution function that depends only on p_{ys} was chosen to have the standard Harris sheet form. This, as will be shown will retain the Harris sheet structure with the x component of the magnetic field still having a hyperbolic tangent profile. Therefore this left the distribution function that depends only on p_{xs} free to be chosen. As a first attempt this distribution function was chosen to be of the same form as the Harris sheet but depending on p_{xs} instead of p_{ys}. The distribution function is,

$$f_s = \frac{n_{0s}}{v_{th,s}^3} \exp(-\beta_s H_s) \left[a_s \exp(\beta_s u_{xs} p_{xs}) + b_s \exp(\beta_s u_{ys} p_{ys}) \right], \tag{3.129}$$

where n_{0s} is a constant normalizing particle density, $\beta_s = 1/k_B T_s$ is the inverse temperature and $v_{th,s} = (2\pi/m_s\beta_s)^{1/2}$ is the thermal velocity and a_s and b_s are dimensionless constants. This distribution function is still of the general form as discussed by Channell (Channell 1976) and by Attico and Pegoraro (Attico and Pegoraro 1999).

The zz-component of the pressure tensor is given by,

$$P = \sum_s \frac{1}{\beta_s} \exp(-\beta_s q_s \phi) N_s(A_x, A_y), \tag{3.130}$$

where

$$N_s(A_x, A_y) = n_{0s} \left[a_s \exp(\beta_s q_s u_{xs} A_x) + b_s \exp(\beta_s q_s u_{ys} A_y) \right]. \tag{3.131}$$

The charge density is calculated using Eq. (3.19):

$$\sigma = \sum_s q_s \exp(-\beta_s q_s \phi) N_s(A_x, A_y), \tag{3.132}$$

and the quasi-neutrality condition $\sigma = 0$ then gives,

$$\phi_{qn} = \frac{1}{e(\beta_e + \beta_i)} \ln\left(\frac{N_i}{N_e}\right). \tag{3.133}$$

One can see immediately that the quasi-neutral electric field will only vanish for a choice of parameters such that $N_e(A_x, A_y) \propto N_i(A_x, A_y)$. The quasineutral P_{zz} is given by

$$P_{qn} = \frac{\beta_e + \beta_i}{\beta_e \beta_i} N_e^{\beta_i/(\beta_e+\beta_i)} N_i^{\beta_e/(\beta_e+\beta_i)}. \tag{3.134}$$

The x- and y-components of the current density can be calculated from Eqs. (3.20) and (3.21) resulting in

$$\begin{aligned} j_x &= e n_{qn} \left[a_i u_{xi} \frac{\exp(e\beta_i u_{xi} A_x)}{a_i \exp(\beta_i e u_{xi} A_x) + b_i \exp(\beta_i e u_{yi} A_y)} \right. \\ &\quad \left. - a_e u_{xe} \frac{\exp(-e\beta_e u_{xe} A_x)}{a_e \exp(-\beta_e e u_{xe} A_x) + be \exp(-\beta_e e u_{ye} A_y)} \right] \\ &= e n_{qn} \left(\langle v_x \rangle_i - \langle v_x \rangle_e \right), \end{aligned} \tag{3.135}$$

$$\begin{aligned} j_y &= e n_{qn} \left[b_i u_{yi} \frac{\exp(e\beta_i u_{yi} A_y)}{a_i \exp(\beta_i e u_{xi} A_x) + b_i \exp(\beta_i e u_{yi} A_y)} \right. \\ &\quad \left. - b_e u_{ye} \frac{\exp(-e\beta_e u_{ye} A_y)}{a_e \exp(-\beta_e e u_{xe} A_x) + b_e \exp(-\beta_e e u_{ye} A_y)} \right] \\ &= e n_{qn} \left(\langle v_y \rangle_i - \langle v_y \rangle_e \right), \end{aligned} \tag{3.136}$$

where $\langle v \rangle_s$ are the average drift velocities of the ions and electrons respectively. For this distribution function the drift velocities are spatially varying due to the dependence upon A_x and A_y. Making the choice of the parameters for which the quasineutral potential ϕ_{qn} can be set to zero corresponds to setting $a_e = a_i$, $b_i = b_e$, $n_{0e} = n_{0i} = n_0$ and

$$\beta_e u_{xe} + \beta_i u_{xi} = 0, \tag{3.137}$$

$$\beta_e u_{ye} + \beta_i u_{yi} = 0. \tag{3.138}$$

The quasineutral pressure can now be written as

$$P_{qn} = P_0 \left[a \exp\left(\frac{A_x}{A_{x0}}\right) + b \exp\left(\frac{A_y}{A_{y0}}\right) \right], \tag{3.139}$$

with

$$P_0 = \frac{\beta_e + \beta_i}{\beta_e \beta_i} n_0 \tag{3.140}$$

$$\frac{1}{A_{x0}} = e\beta_i u_{xi} = -e\beta_e u_{xe}, \tag{3.141}$$

$$\frac{1}{A_{y0}} = e\beta_i u_{yi} = -e\beta_e u_{ye}. \tag{3.142}$$

The equilibria can be found from solving the two coupled nonlinear ODEs (3.26) and (3.27), which in this example are explicitly,

$$-\frac{d^2 A_x}{dz^2} = \frac{\mu_0 P_0}{A_{x0}} a \exp\left(\frac{A_x}{A_{x0}}\right), \tag{3.143}$$

$$-\frac{d^2 A_y}{dz^2} = \frac{\mu_0 P_0}{A_{y0}} b \exp\left(\frac{A_y}{A_{y0}}\right). \tag{3.144}$$

Normalizing lengths to a length L and A_x and A_y to A_{x0} then

$$-\frac{d^2 A_x}{dz^2} = \left[1 + \frac{\beta_e}{\beta_i}\right] a\lambda_{ex} \exp(A_x), \tag{3.145}$$

$$-\frac{d^2 A_y}{dz^2} = \left[1 + \frac{\beta_e}{\beta_i}\right] br\lambda_{ex} \exp(rA_y), \tag{3.146}$$

where

$$\lambda_{ex} = \frac{\mu_0 n_0 L^2}{\beta_e A_{x0}^2}, \tag{3.147}$$

$$r = \frac{A_{x0}}{A_{y0}}. \tag{3.148}$$

These two differential equations can be solved analytically to give

$$A_x = -2 \ln\left(\sqrt{\frac{\kappa_1}{K_1}} \cosh\left(\sqrt{\frac{K_1}{2}}(z - \alpha_1)\right)\right), \tag{3.149}$$

$$A_y = -\frac{2}{r} \ln\left(\sqrt{\frac{\kappa_2}{K_2}} \cosh\left(r\sqrt{\frac{K_2}{2}}(z - \alpha_2)\right)\right), \tag{3.150}$$

where

$$\kappa_1 = \left[1 + \frac{\beta_e}{\beta_i}\right] a\lambda_{ex}, \tag{3.151}$$

$$\kappa_2 = \left[1 + \frac{\beta_e}{\beta_i}\right] b\lambda_{ex}, \tag{3.152}$$

and $K_1, K_2, \alpha_1, \alpha_2$ are integration constants to be determined from the boundary conditions. A

particular solution is found by setting

$$K_1 = \kappa_1, \tag{3.153}$$

$$K_2 = \kappa_2, \tag{3.154}$$

and gauging $A_x = 0$ and $A_y = 0$ at $z = 0$. This gives,

$$A_x = -2\ln\left(\cosh\left(\sqrt{\frac{K_1}{2}}z\right)\right), \tag{3.155}$$

$$A_y = -\frac{2}{r}\ln\left(\cosh\left(r\sqrt{\frac{K_2}{2}}z\right)\right), \tag{3.156}$$

$$B_x = 2\sqrt{\frac{K_2}{2}}\tanh\left(r\sqrt{\frac{K_2}{2}}z\right), \tag{3.157}$$

$$B_y = -2\sqrt{\frac{K_1}{2}}\tanh\left(\sqrt{\frac{K_1}{2}}z\right). \tag{3.158}$$

A particular solution is shown in Figure 3.12, where $A_x = 0, A_y = 0$ at $z = 0$. The parameter values have been chosen such that $a = 1/16$, $b = 1/4$, $\beta_e = \beta_i$, $\lambda_{ex} = 1$ and $r = 1$. Figure 3.12(a) is a 1D plot of the profiles of the magnetic field components. Both components of the magnetic field have a neutral sheet structure with oppositely directed magnetic field lines either side of the neutral line. In this case the y component of the current density is larger than the x component of the current density. An important feature of this equilibrium is that the parameters a and b can be varied to tune the relative sizes of the current densities in the x and y directions. The drift velocities are spatially varying for each particle species and depending on how you choose the parameters the shearing of the field can be increased or decreased. Figure 3.12(b) shows a plot of the potential surface with the particle trajectory in the A_x-A_y-plane overlaid. The particle approaches from negative infinity with constant velocity in both the A_x and A_y directions. The particle slows down when it encounters the steep gradient in the potential surface and at some point stops and turns around, moving off in the opposite direction and eventually having velocity components of equal magnitude but opposite direction to the initial velocity components. This particle trajectory is consistent with the magnetic field plots. The gradient of the potential surface corresponds to the gradient of the magnetic field components. Figure 3.12(c) shows a plot of magnetic field lines at different z values passing through $x = 0$, $y = 0$. There is a slight shearing of the field lines. The shear of the field lines in the current region is due to the fact that B_x and B_y are not equal to each other for all values of z. Therefore the larger the change in one of the magnetic field components relative to the other as you go along z the larger the twisting and shearing of the field in the current region.

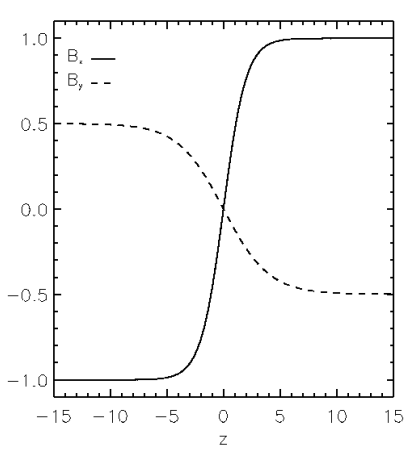

(a)

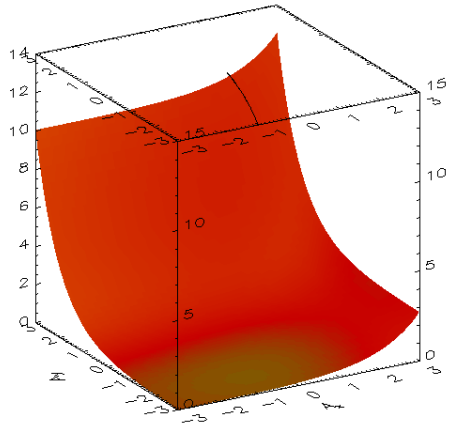

(b)

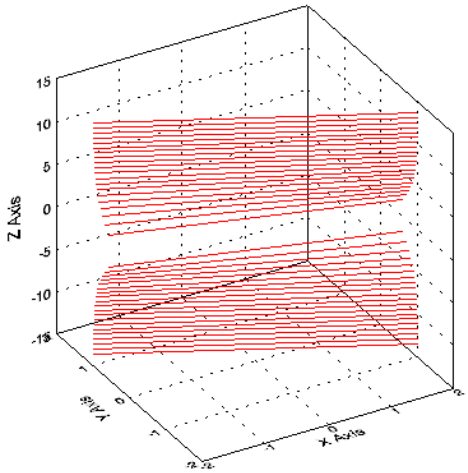

(c)

Figure 3.12: Plots of the solution for example 3 where 3.12(a) shows the 1D profiles of the magnetic field components, 3.12(b) shows the pressure function and 3.12(c) shows a plot of magnetic field lines at different z values passing through $x = 0$, $y = 0$.

This distribution function was investigated to see if it could give insight into the problem of finding a distribution function that gave the force-free Harris sheet. As has been shown the resulting equilibrium is not the force-free Harris sheet. It does show though that by choosing the distribution function that depends only on p_{ys} to have the form of the standard Harris sheet distribution function that the x component of the field and the y component of the current density correspond to the Harris sheet equilibrium. By choosing the distribution function that depends only on p_{xs} to also have the same form as the Harris sheet distribution function the y component of the magnetic field and the x component of the current density also have Harris sheet profiles. Therefore, even though this distribution function was not successful in giving the force-free Harris sheet, it suggests that to determine a distribution function for the force-free Harris sheet the correct form of the distribution function that depends only on p_{xs} must be found. As will be shown in Sec. 3.7 a Fourier transform method can be used to determine the correct form of the distribution function p_{xs} which results in a distribution function that gives the force-free Harris sheet.

3.6 Conditions for Force-Free 1D VM Equilibria

The pseudo-particle analogy can be used to specify the necessary conditions that all force-free solutions of the 1D VM equations have to satisfy. So far only linear force-free 1D VM solutions are known (Sestero 1967; Channell 1976; Bobrova and Syrovatskiĭ 1979; Correa-Restrepo and Pfirsch 1993; Bobrova et al. 2001) and the analogy could help to answer the question (see e.g. Tassi et al. 2008) whether other, in particular non-linear, force-free solutions exist and how to find them.

The force-free condition

$$\mathbf{j} \times \mathbf{B} = \mathbf{0}, \tag{3.159}$$

implies that the current density $\mathbf{j} = \nabla \times \mathbf{B}/\mu_0$ is parallel to $\mathbf{B}$. In the 1D situation discussed here Eq. (3.159) can be written as

$$\frac{d}{dz}\left(\frac{B^2}{2\mu_0}\right) = 0. \tag{3.160}$$

Because the total pressure is always constant for 1D VM equilibria, this implies that for a force-free solution P_{zz} must also be constant.

At first sight, this may seem to be at variance with Eqs. (3.20) and (3.21) which clearly imply that the current density is only non-zero if the partial derivatives of P_{zz} with respect to A_x and A_y are

non-zero. A closer look, however, reveals that the condition $P_{zz} =$ constant only implies

$$\frac{dP_{zz}}{dz} = \frac{dA_x}{dz}\frac{\partial P_{zz}}{\partial A_x} + \frac{dA_y}{dz}\frac{\partial P_{zz}}{\partial A_y} = 0, \tag{3.161}$$

for the force-free solution only. Equation (3.161), which is, of course, equivalent to Eq. (3.159), can be satisfied for one solution even if the partial derivatives of P_{zz} are non-zero. When translated into the pseudo-particle picture, it is seen that to obtain a pseudo-particle trajectory corresponding to a force-free magnetic field, a pseudo-potential (P_{zz}) which has at least one equipotential line (contour) that is also a particle trajectory is needed. This is a necessary condition for the existence of a 1D force-free VM equilibrium.

Of course, finding such a potential (pressure) is not yet the complete solution of the problem, but only a first step. For a complete solution it is necessary to find the distribution functions giving rise to the pressure function (pseudo-potential). In simple cases this may be achievable by using the transform methods presented by Channell (Channell 1976) and Attico and Pegoraro (Attico and Pegoraro 1999). In more general cases, numerical methods as described by Mynick et al. (Mynick et al. 1979) could be used.

There is, however, a well-known family of pseudo-potentials that satisfies the condition of allowing trajectories which are identical to contours of the pseudo-potential. These are attractive central potentials. These have to be restricted to nonsingular pseudo-potentials because the equivalent pressure must be positive and nonsingular. This rules out, for example, all potentials which are negative powers of the radial coordinate. For central pseudo-potentials, there is not only pseudo-energy conservation, but also pseudo-angular momentum conservation. The pseudo-angular momentum is given by

$$L_{pseudo} = A_x\frac{dA_y}{dz} - A_y\frac{dA_x}{dz} = -(A_xB_x + A_yB_y),$$

and is equal to the negative of the magnetic helicity density.

An example of a distribution function resulting in a central attractive potential has already been given by Sestero (1967); Bobrova and Syrovatskiĭ (1979); Correa-Restrepo and Pfirsch (1993); Bobrova et al. (2001) and has been discussed in Sec. 3.3.3 and has the form

$$f_s = \frac{n_{0s}}{v_{th,s}^3}\exp(-\beta_s\bar{H}_s), \tag{3.162}$$

with

$$\bar{H}_s = H_s - \frac{a_s}{m_s}(p_{xs}^2 + p_{ys}^2), \tag{3.163}$$

where a_s is a dimensionless constant, which can be related to the temperature anisotropy of the

distribution function (see e.g. Bobrova et al. 2001, and Sec. 3.3.3). It is remarked again that the velocity space integral (3.18) defining P only exists if $a_s > 1/2$. Here n_{0s} is a constant normalizing particle density, $\beta_s = 1/k_B T_s$ is the inverse temperature and $v_{th,s} = (2\pi/m_s\beta_s)^{1/2}$ is the thermal velocity. The distribution function allows linear force-free solutions of the form,

$$B_x = \alpha A_x = k\alpha \sin \alpha z, \tag{3.164}$$
$$B_y = \alpha A_y = k\alpha \cos \alpha z, \tag{3.165}$$

so $B_x^2 + B_y^2 = k^2\alpha^2 =$ constant as is required, and that

$$\mu_0 \mathbf{j} = \alpha \mathbf{B}, \tag{3.166}$$

where the particle trajectories are circles in the A_x-A_y-plane which are also contours of the pseudo potential.

Another distribution function giving rise to the same magnetic field solution has been presented by Channell (Channell 1976) (see his case C). In this case a complete solution is available, which has not been discussed in the context of force-free fields, but it is obvious that for the correct choice of initial conditions and parameters the same linear force-free field as given above results. In this case P_{zz} (pseudo-potential) has the form of a 2D harmonic oscillator potential

$$P_{zz}(A_x, A_y) = P_{00} + \frac{1}{2} P_{01}(A_x^2 + A_y^2), \tag{3.167}$$

with P_{00} and P_{01} both positive parameters. In this case Ampére's law is always linear and has the form

$$-\frac{d^2 A_x}{dz^2} = P_{01} A_x, \tag{3.168}$$
$$-\frac{d^2 A_y}{dz^2} = P_{01} A_y. \tag{3.169}$$

The general solution as given by Channell is

$$A_x = A_{x0} \sin(\sqrt{P_{01}} z + \delta_x), \tag{3.170}$$
$$A_y = A_{y0} \sin(\sqrt{P_{01}} z + \delta_y). \tag{3.171}$$

One can see that by choosing $A_{x0} = A_{y0} = k$, $\delta_x = 0$ and $\delta_y = \pi/2$ the solution from above is recovered with $\alpha = \sqrt{P_{01}}$. The corresponding distribution functions are of the form (Channell 1976)

$$f_s(H_s, p_{xs}, p_{ys}) = \exp(-\beta_s H_s)[f_{0s} + f_{1s}(p_{xs}^2 + p_{ys}^2)]. \tag{3.172}$$

The same type of P_{zz} and corresponding distribution function has also been found by Attico and

Pegoraro, (Attico and Pegoraro 1999) but without giving explicit solutions for the magnetic field.

It is actually straightforward to see that all distribution functions of the type

$$f_s = f_s(H_s, p_s^2), \tag{3.173}$$

with $p_s^2 = p_{xs}^2 + p_{ys}^2$ lead to a P_{zz} corresponding to a central pseudo-potential. Defining $p_{xs} = p\cos\theta$, $p_{ys} = p\sin\theta$, $v_x = v\cos\theta$, $v_y = v\sin\theta$, $A_x = A\cos\theta$, $A_y = A\sin\theta$, so that $v^2 = v_x^2 + v_y^2$ and $A^2 = A_x^2 + A_y^2$. It is obvious that

$$p_s^2 = m_s^2 v^2 + 2m_s q_s A v + q_s^2 A^2,$$

which does not depend on the angle θ. Since H_s does not depend upon the vector potential, the integrals defining $P(A_x, A_y)$ (see Eq. (3.18)) define a function depending only upon the magnitude of the vector potential, A, but not upon its direction. The corresponding pseudo-potential will therefore be a central potential and if it is attractive it will admit circular orbits, i.e. linear force-free solutions of the same type as discussed before, so obviously there are many distribution functions leading to the same magnetic field solution.

Another property which is common to all force-free 1D VM solutions is the following. Assume that a $P_{zz}(A_x, A_y)$ admitting a force-free solution $A_{x,ff}(z)$ and $A_{y,ff}(z)$ is known, and that the constant value of P_{zz} for the force free solution is P_{ff}. Then any (positive) function $F(x)$ can be used to construct a new $\bar{P}_{zz}(A_x, A_y)$ admitting exactly the same force-free solution, by letting

$$\bar{P}_{zz}(A_x, A_y) = \frac{1}{F'(P_{ff})} F(P_{zz}(A_x, A_y)), \tag{3.174}$$

where $F'(x)$ is the derivative of F with respect to its argument. Using this definition, Ampére's law for the new $\bar{P}_{zz}$ has the form

$$-\frac{d^2 A_x}{dz^2} = \frac{1}{F'(P_{ff})} F'(P_{zz}(A_x, A_y)) \frac{\partial P_{zz}}{\partial A_x}, \tag{3.175}$$

$$-\frac{d^2 A_y}{dz^2} = \frac{1}{F'(P_{ff})} F'(P_{zz}(A_x, A_y)) \frac{\partial P_{zz}}{\partial A_y}. \tag{3.176}$$

For the force-free solution $P_{zz} = P_{ff}$ and thus Eqs. (3.175) and (3.176) reduce to the equations generated by P_{zz}, but only for $(A_x, A_y) = (A_{x,ff}, A_{y,ff})$.

3.7 The Force-Free Harris Sheet

A discussion of a large part of the work of this section can be found in Harrison and Neukirch (2009a).

3.7.1 The Pressure Function

The force-free Harris sheet is an example of a 1D non-linear force-free field. One of the main aims of this work was to determine a distribution function that gives this magnetic field configuration. To determine the distribution function the first step is to find the corresponding quasineutral pressure function P_{qn} which generates the force-free Harris sheet configuration. The magnetic field components for the force-free Harris sheet are

$$B_x = B_0 \tanh\left(\frac{z}{L}\right) = -\frac{dA_y}{dz}, \tag{3.177}$$

$$B_y = \frac{B_0}{\cosh\left(\frac{z}{L}\right)} = \frac{dA_x}{dz}, \tag{3.178}$$

and they satisfy the force-free condition that,

$$B_x^2 + B_y^2 = B_0^2, \tag{3.179}$$

where B_0 is a constant. The components of the vector potentials are

$$A_x = 2B_0 L \tan^{-1}\left(e^{\frac{z}{L}}\right), \tag{3.180}$$

$$A_y = -B_0 L \ln\left(\cosh\left(\frac{z}{L}\right)\right). \tag{3.181}$$

The current densities for the force-free Harris sheet are,

$$j_x = \frac{B_0}{\mu_0 L}\frac{\tanh\left(\frac{z}{L}\right)}{\cosh\left(\frac{z}{L}\right)}, \tag{3.182}$$

$$j_y = \frac{B_0}{\mu_0 L}\frac{1}{\cosh^2\left(\frac{z}{L}\right)}, \tag{3.183}$$

and they satisfy the force-free condition that

$$\mu_0 \mathbf{j} = \alpha \mathbf{B}, \tag{3.184}$$

where

$$\alpha = \frac{1}{L}\frac{1}{\cosh\left(\frac{z}{L}\right)}. \tag{3.185}$$

An important assumption to be able to make analytical progress is that the pressure potential (3.24) is assumed to be of the form

$$P_{qn}(A_x, A_y) = P_1(A_x) + P_2(A_y). \tag{3.186}$$

Equations (3.26) and (3.27) then give the differential equations that must be satisfied,

$$-\frac{d^2 A_x}{dz^2} = \mu_0 \frac{\partial P_1}{\partial A_x}, \tag{3.187}$$

$$-\frac{d^2 A_y}{dz^2} = \mu_0 \frac{\partial P_2}{\partial A_y}. \tag{3.188}$$

These, combined with the force-free condition give three conditions that represent the force balance across the sheet,

$$\left(\frac{dA_x}{dz}\right)^2 + 2\mu_0 P_1(A_x) = 2\mu_0 P_{01}, \tag{3.189}$$

$$\left(\frac{dA_y}{dz}\right)^2 + 2\mu_0 P_2(A_y) = 2\mu_0 P_{02}, \tag{3.190}$$

$$\left(\frac{dA_x}{dz}\right)^2 + \left(\frac{dA_y}{dz}\right)^2 = B_0^2, \tag{3.191}$$

where P_{01}, P_{02} and B_0 are constants. Of course, one must also have that

$$P_1(A_x) + P_2(A_y) = \textit{a constant}. \tag{3.192}$$

Solving (3.189) for $P_1(A_x)$ and solving (3.190) for $P_2(A_y)$ the pressure function for the force-free Harris sheet can be written as

$$P_{qn}(A_x, A_y) = P_1(A_x) + P_2(A_y) \tag{3.193}$$

$$= \frac{B_0^2}{2\mu_0}\left[\frac{1}{2}\cos\left(\frac{2A_x}{B_0 L}\right) + \exp\left(\frac{2A_y}{B_0 L}\right)\right] + P_{03}, \tag{3.194}$$

where $P_2(A_y)$ is the standard Harris sheet pressure function whilst the new contribution $P_1(A_x)$ has a cosine dependence on A_x and P_{03} is a constant. The problem of determining the distribution function though still remains.

3.7.2 Force-Free Harris Sheet Distribution Function

The pressure function for the force-free Harris sheet is made up of a sum of two different pressure contributions $P_1(A_x)$ and $P_2(A_y)$. It is possible to use these to find a distribution function that gives the force-free Harris sheet via the Fourier transform method that is presented by Channell

(1976). As P_{qn} is a sum of a function that only depends on A_x and a function that depends only on A_y the distribution function f_s is assumed to be of the form

$$f_s = \exp(-\beta_s H_s)[g_{1s}(p_{xs}) + g_{2s}(p_{ys})]. \tag{3.195}$$

It is immediately obvious that $g_{2s}(p_{ys})$ must be equivalent to the standard Harris sheet distribution function as this will give rise to the $P_2(A_y)$ part of the pressure function which as already discussed corresponds to the Harris sheet. Therefore, using the microscopic notation previously used in Sec. 3.3, $g_{2s}(p_{ys})$ will have the general form,

$$g_{2s}(p_{ys}) = \frac{n_{0s}}{v_{th,s}^3} \exp\left(\beta_s u_{ys} p_{ys}\right), \tag{3.196}$$

where n_{0s} is a constant normalizing particle density, u_{ys} is a constant with dimensions of velocity, $\beta_s = 1/k_B T_s$ is the inverse temperature and $v_{th,s} = (2\pi/m_s\beta_s)^{1/2}$ is the thermal velocity. So it is left to determine the form of $g_{1s}(p_{xs})$. In general for a distribution function of the form

$$f_s = \exp(-\beta_s H_s) g_s(p_{xs}, p_{ys}), \tag{3.197}$$

it is possible to write down an integral equation for $g_s(p_{xs}, p_{ys})$ in terms of the quasineutral pressure function $P_{qn}(A_x, A_y)$ as long as one assumes there is a choice of parameters for which the quasineutral electric potential ϕ_{qn} can be set to zero (Channell 1976):

$$\frac{1}{m_s^2}\left(\frac{2\pi}{m_s\beta_s}\right)^{1/2} \int_{-\infty}^{\infty} \exp\left[-\frac{\beta_s}{2m_s}\left[(p_{xs} - q_s A_x)^2 + (p_{ys} - q_s A_y)^2\right]\right] g_s\left(p_{xs}, p_{ys}\right) dp_{xs} dp_{ys} = \frac{\beta_e\beta_i P_{qn}(A_x, A_y)}{(\beta_e + \beta_i)}. \tag{3.198}$$

Equation (3.198) simplifies for $g_{1s}(p_{xs})$ and the integral equation to be solved is,

$$\frac{2\pi}{\beta_s m_s^2} \int_{-\infty}^{\infty} \exp\left(-\frac{\beta_s}{2m_s}(p_{xs} - q_s A_x)^2\right) g_{1s}(p_{xs}) dp_{xs} = n_{0s} \cos\left(q_s\beta_s u_{xs} A_x\right), \tag{3.199}$$

where on the right hand side P_{qn} has been written in the general microscopic form introduced in Sec. 3.3 with u_{xs} a constant that has dimensions of velocity. The specific choice of the microscopic parameters which results in the force-free Harris sheet will be shown in Sec. 3.7.3. This integral equation is solved for $g_{1s}(p_{xs})$. Taking the Fourier transform of both sides of the integral equation in terms of A_x and denoting transformed variables by a tilde then this results in

$$\left(\frac{2\pi}{\beta_s m_s}\right)^{3/2} \tilde{g}_{1s}(k) \exp\left(-\frac{2m_s\pi^2}{\beta_s}k^2\right) = \frac{n_{0s}}{2}\left[\delta\left(k - \frac{q_s\beta_s u_{xs}}{2\pi}\right) + \delta\left(k + \frac{q_s\beta_s u_{xs}}{2\pi}\right)\right]. \tag{3.200}$$

Rearranging, $\tilde{g}_{1s}(k)$ is given by,

$$\tilde{g}_{1s}(k) = \frac{n_{0s}}{2}\left(\frac{\beta_s m_s}{2\pi}\right)^{3/2} \exp\left(\frac{2m_s\pi^2}{\beta_s}k^2\right)\left[\delta\left(k - \frac{q_s\beta_s u_{xs}}{2\pi}\right) + \delta\left(k + \frac{q_s\beta_s u_{xs}}{2\pi}\right)\right]. \tag{3.201}$$

Inverting this gives $g_{1s}(p_{xs})$,

$$g_{1s}(p_{xs}) = \frac{a_s n_{0s}}{v_{th,s}^3}\cos\left(\beta_s u_{xs} p_{xs}\right), \tag{3.202}$$

where a_s is a dimensionless constant. The method of solving the integral equation via a Fourier transform method has led to a distribution function that for the correct choice of parameters has the force-free Harris sheet as a solution. The complete distribution function is of the general form,

$$f_s = \frac{n_{0s}}{v_{th,s}^3}\exp(-\beta_s H_s)\left[a_s\cos\left(\beta_s u_{xs}p_{xs}\right) + \exp\left(\beta_s u_{ys}p_{ys}\right) + b_s\right], \tag{3.203}$$

where $n_{0s}b_s$ is a constant background density which is necessary to ensure that the distribtution function always remains positive.

3.7.3 Testing the Force-Free Harris Sheet Distribution Function

To check that the distribution function for the force-free Harris sheet is indeed given by (3.203) the distribution function is now used as the starting point and the moment integrals are calculated. The differential equations resulting from Eqs. (3.26) and (3.27) are then solved under certain conditions to show that the distribution function does indeed give the non-linear force-free Harris sheet magnetic field configuration. In fact it is only necessary to calculate the velocity moment that corresponds to the P_{zz} component of the pressure tensor from the general theory described in Sec. 3.2 from which the charge density and current density can then be calculated via differentiation.

For the distribution function (3.203) the zz-component of the pressure tensor is given by

$$P = \sum_s \frac{1}{\beta_s}\exp(-\beta_s q_s\phi)N_s(A_x, A_y), \tag{3.204}$$

where

$$N_s(A_x, A_y) = n_{0s}\exp\left(\frac{\beta_s m_s}{2}u_{ys}^2\right)\left[a_s\exp\left(-\frac{\beta_s m_s}{2}(u_{xs}^2 + u_{ys}^2)\right)\cos(\beta_s q_s u_{xs}A_x)\right.$$

$$+\exp(\beta_s q_s u_{ys} A_y) + b_s \exp\left(-\frac{\beta_s m_s}{2} u_{ys}^2\right)\Bigg]. \tag{3.205}$$

The charge density is calculated using Eq. (3.19):

$$\sigma = \sum_s q_s \exp(-\beta_s q_s \phi) N_s(A_x, A_y), \tag{3.206}$$

and the quasi-neutrality condition $\sigma = 0$ then gives,

$$\phi_{qn} = \frac{1}{e(\beta_e + \beta_i)} \ln\left(\frac{N_i}{N_e}\right). \tag{3.207}$$

One can see immediately that the quasi-neutral electric field will only vanish for a choice of parameters such that $N_e(A_x, A_y) \propto N_i(A_x, A_y)$.

The quasi-neutral P_{zz} is given by

$$P_{qn} = \frac{\beta_e + \beta_i}{\beta_e \beta_i} N_e^{\beta_i/(\beta_e+\beta_i)} N_i^{\beta_e/(\beta_e+\beta_i)}. \tag{3.208}$$

The condition of vanishing electric potential implies that $N_i(A_x, A_y) = N_e(A_x, A_y)$, which is true if,

$$n_{0e} \exp\left(\frac{\beta_e m_e}{2} u_{ye}^2\right) = n_{0i} \exp\left(\frac{\beta_i m_i}{2} u_{yi}^2\right) = n_0, \tag{3.209}$$

$$a_e \exp\left(-\frac{\beta_e m_e}{2}(u_{xe}^2 + u_{ye}^2)\right) = a_i \exp\left(-\frac{\beta_i m_i}{2}(u_{xi}^2 + u_{yi}^2)\right) = a, \tag{3.210}$$

$$b_e \exp\left(-\frac{\beta_e m_e}{2} u_{ye}^2\right) = b_i \exp\left(-\frac{\beta_i m_i}{2} u_{yi}^2\right) = b, \tag{3.211}$$

$$-\beta_e u_{xe} = \beta_i u_{xi}, \tag{3.212}$$

$$-\beta_e u_{ye} = \beta_i u_{yi}. \tag{3.213}$$

Supposing that β_e and β_i are given, there are ten parameters needing to satisfy only five equations which is always possible. Therefore, this provides the justifcation for applying Channell's method (Channell 1976) to determine the distribution function. On the basis of these conditions, the quasineutral potential P_{qn} becomes

$$P_{qn} = \frac{\beta_e + \beta_i}{\beta_e \beta_i} n_0 \left[a \cos\left(e\beta_e u_{xe} A_x\right) + \exp\left(-e\beta_e u_{ye} A_y\right) + b\right]. \tag{3.214}$$

Comparing the coefficients of the quasineutral pressure (3.214) to the force-free pressure function (3.194) then this shows that the connection between the microscopic notation and the original

macroscopic notation used in (3.194) is given by

$$\frac{B_0^2}{2\mu_0} = \left(\frac{1}{\beta_e}+\frac{1}{\beta_i}\right) n_0, \tag{3.215}$$

$$L = \left(\frac{2\beta_i}{\mu_0 e^2 n_0 u_{ye}^2 \beta_e(\beta_e+\beta_i)}\right)^{1/2}, \tag{3.216}$$

$$a = \frac{1}{2}, \tag{3.217}$$

$$b = 2\mu_0 P_{03}/B_0^2. \tag{3.218}$$

The quasineutral pressure (3.214) is now identical to the force-free pressure function (3.194),

$$P_{qn} = \frac{B_0^2}{2\mu_0}\left[\frac{1}{2}\cos\left(\frac{2A_x}{B_0 L}\right)+\exp\left(\frac{2A_y}{B_0 L}\right)\right]+P_{03}. \tag{3.219}$$

The x- and y-components of the current density can be calculated from Eqs. (3.20) and (3.21), resulting in

$$j_x = -\frac{B_0}{2\mu_0 L}\sin\left(\frac{2A_x}{B_0 L}\right), \tag{3.220}$$

$$j_y = \frac{B_0}{\mu_0 L}\exp\left(\frac{2A_y}{B_0 L}\right). \tag{3.221}$$

The differential equations resulting from Eqs. (3.26) and (3.27) are,

$$-\frac{d^2 A_x}{dz^2} = -\frac{B_0}{2L}\sin\left(\frac{2A_x}{B_0 L}\right), \tag{3.222}$$

$$-\frac{d^2 A_y}{dz^2} = \frac{B_0}{L}\exp\left(\frac{2A_y}{B_0 L}\right). \tag{3.223}$$

You can immediately integrate both of these differential equations once to give,

$$\left(\frac{dA_x}{dz}\right)^2+\frac{B_0^2}{2}\cos\left(\frac{2A_x}{B_0 L}\right) = \kappa_1, \tag{3.224}$$

$$\left(\frac{dA_y}{dz}\right)^2+B_0^2\exp\left(\frac{2A_y}{B_0 L}\right) = \kappa_2. \tag{3.225}$$

Setting $\kappa_1 = B_0^2/2$ and $\kappa_2 = B_0^2$ and also choosing $A_x = B_0 L\pi/2$ and $A_y = 0$ at $z = 0$ leads to the force-free Harris sheet solution where,

$$A_x = 2B_0 L\tan^{-1}\left(e^{z/L}\right), \tag{3.226}$$

$$A_y = -B_0 L\ln\left(\cosh\left(\frac{z}{L}\right)\right), \tag{3.227}$$

which give the magnetic field components

$$B_x = B_0 \tanh\left(\frac{z}{L}\right), \tag{3.228}$$

$$B_y = \frac{B_0}{\cosh\left(\frac{z}{L}\right)}. \tag{3.229}$$

Figure 3.13 shows plots of profiles of the magnetic field components in Figure 3.13(a). A plot of magnetic field lines along z passing through $x = 0$, $y = 0$ is shown in Figure 3.13(b) where the shear of the magnetic fields lines in the current sheet region is clearly visible. The potential surface is shown in Figure 3.13(c) with the particle trajectory overlaid in the A_x-A_y-plane. The particle trajectory is a contour of the potential surface which is a characteristic property of a force-free Vlasov-Maxwell equilibria.

3.8 The Combined Harris Sheet

It can be shown that the distribution function (3.203), for different choices of the parameters, describes a complete family of equilibria that make the transition between the Harris sheet and the force-free Harris sheet. The magnetic field components and the plasma pressure for the combined Harris sheet are,

$$B_x = B_{x0} \tanh\left(\frac{z}{L}\right) = -\frac{dA_y}{dz}, \tag{3.230}$$

$$B_y = \frac{B_{y0}}{\cosh\left(\frac{z}{L}\right)} = \frac{dA_x}{dz}, \tag{3.231}$$

$$P = \frac{P_0}{\cosh^2\left(\frac{z}{L}\right)} + P_{00} \tag{3.232}$$

where

$$B_{y0} = \sqrt{B_{x0}^2 - 2\mu_0 P_0}, \tag{3.233}$$

and they satisfy the force balance condition that

$$\frac{B_x^2 + B_y^2}{2\mu_0} + P = \frac{B_{x0}^2}{2\mu_0} + P_{00}, \tag{3.234}$$

where B_{x0}, B_{y0}, P_0 and P_{00} are constants. The components of the vector potentials can be written as,

$$A_x = 2B_{y0}L \tan^{-1}\left(e^{\frac{z}{L}}\right), \tag{3.235}$$

$$A_y = -B_{x0}L \ln\left(\cosh\left(\frac{z}{L}\right)\right). \tag{3.236}$$

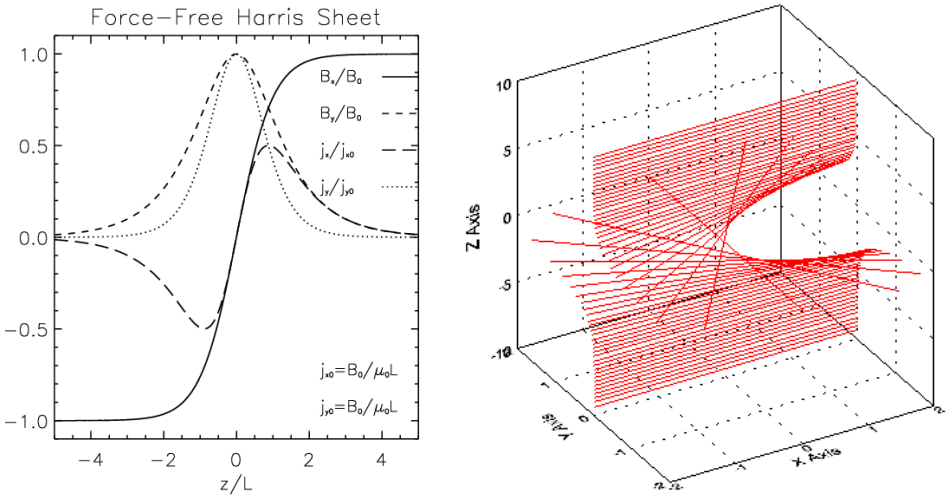

(a) (b)

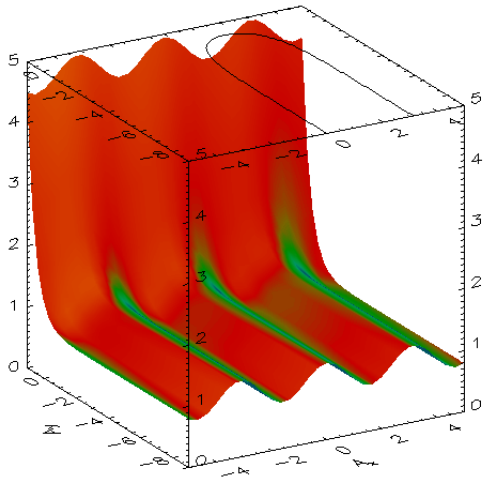

(c)

Figure 3.13: Plots showing the force-free Harris sheet solution where 3.13(a) shows the 1D profiles of the magnetic field components, 3.13(b) shows a plot of magnetic field lines at different z values passing through $x = 0$, $y = 0$ and 3.13(c) shows the pressure function.

The quasineutral pressure function (3.24) is assumed to be of the form

$$P_{qn}(A_x, A_y) = P_1(A_x) + P_2(A_y), \tag{3.237}$$

in the same way as before. Equations (3.26) and (3.27) then give the differential equations that must be satisfied,

$$-\frac{d^2 A_x}{dz^2} = \mu_0 \frac{\partial P_1}{\partial A_x}, \tag{3.238}$$

$$-\frac{d^2 A_y}{dz^2} = \mu_0 \frac{\partial P_2}{\partial A_y}. \tag{3.239}$$

These give three conditions that represent the force balance across the sheet,

$$\left(\frac{dA_x}{dz}\right)^2 + 2\mu_0 P_1(A_x) = 2\mu_0 P_{01}, \tag{3.240}$$

$$\left(\frac{dA_y}{dz}\right)^2 + 2\mu_0 P_2(A_y) = 2\mu_0 P_{02}, \tag{3.241}$$

$$\left(\frac{dA_x}{dz}\right)^2 + \left(\frac{dA_y}{dz}\right)^2 + 2\mu_0 P_1(A_x) + 2\mu_0 P_2(A_y) = 2\mu_0 P_{01} + 2\mu_0 P_{02}, \tag{3.242}$$

where P_{01}, P_{02} are constants. Solving (3.240) for $P_1(A_x)$ and solving (3.241) for $P_2(A_y)$ the quasineutral pressure function for the combined Harris sheet is,

$$P_{qn}(A_x, A_y) = P_1(A_x) + P_2(A_y) \tag{3.243}$$

$$= \frac{1}{2}\frac{B_{y0}^2}{2\mu_0} \cos\left(\frac{2A_x}{B_{y0}L}\right) + \frac{B_{x0}^2}{2\mu_0} \exp\left(\frac{2A_y}{B_{x0}L}\right) + P_{03}, \tag{3.244}$$

where $P_2(A_y)$ is the standard Harris sheet pressure function whilst the new contribution $P_1(A_x)$ has a similar cosine dependence on A_x as the force-free Harris sheet. In the case that $P_0 = 0$, this would then give the force-free Harris sheet quasineutral potential. In the case of $P_0 = B_{x0}^2/2\mu_0$ this would correspond to the Harris sheet quasineutral potential.

Comparing the coefficients of the quasineutral pressure (3.214) to the combined Harris sheet pressure function (3.244) then this shows that the connection between the microscopic notation and the macroscopic notation used in (3.244) is

$$\frac{B_0^2}{2\mu_0} = \left(\frac{1}{\beta_e} + \frac{1}{\beta_i}\right) n_0, \tag{3.245}$$

$$L = \left(\frac{2\beta_i}{\mu_0 e^2 n_0 u_{ye}^2 \beta_e(\beta_e + \beta_i)}\right)^{1/2}, \tag{3.246}$$

$$B_{y0} = \left(\frac{2\mu_0(\beta_e+\beta_i)n_0u_{ye}^2}{\beta_e\beta_i u_{xe}^2}\right)^{1/2}, \tag{3.247}$$

$$a = \frac{1}{2}\frac{B_{y0}^2}{B_{x0}^2}, \tag{3.248}$$

$$b = 2\mu_0 P_{03}/B_0^2. \tag{3.249}$$

The quasineutral pressure (3.214) is now identical to the combined pressure function (3.244). The differential equations that result from Eqs. (3.26) and (3.27) that must be solved are,

$$-\frac{d^2A_x}{dz^2} = -\frac{B_{y0}}{2L}\sin\left(\frac{2A_x}{B_{y0}L}\right), \tag{3.250}$$

$$-\frac{d^2A_y}{dz^2} = \frac{B_{x0}}{L}\exp\left(\frac{2A_y}{B_{x0}L}\right). \tag{3.251}$$

You can immediately integrate both of these differential equations once to give

$$\left(\frac{dA_x}{dz}\right)^2 + \frac{B_{y0}^2}{2}\cos\left(\frac{2A_x}{B_{y0}L}\right) = \kappa_1, \tag{3.252}$$

$$\left(\frac{dA_y}{dz}\right)^2 + B_{x0}^2\exp\left(\frac{2A_y}{B_{x0}L}\right) = \kappa_2. \tag{3.253}$$

Setting $\kappa_1 = B_{y0}^2/2$ and $\kappa_2 = B_{x0}^2$ and also choosing $A_x = (B_{y0}L\pi)/2$ and $A_y = 0$ at $z = 0$ leads to the combined Harris sheet solution where,

$$A_x = 2B_{y0}L\tan^{-1}\left(e^{z/L}\right), \tag{3.254}$$

$$A_y = -B_{x0}L\ln\left(\cosh\left(\frac{z}{L}\right)\right), \tag{3.255}$$

which give the magnetic field components

$$B_x = B_{x0}\tanh\left(\frac{z}{L}\right), \tag{3.256}$$

$$B_y = \frac{B_{y0}}{\cosh\left(\frac{z}{L}\right)}. \tag{3.257}$$

In the limiting case of $P_0 \to B_{x0}^2/2\mu_0$ then the contribution in the pressure function due to $P_1(A_x)$ is zero and the solution is the Harris sheet. In the limit of $P_0 \to 0$ then this results in the force-free Harris sheet solution. Figure 3.14 show plots of the profiles of B_x, B_y, j_x, j_y and P as you make the transition from the Harris sheet ($2\mu_0P_0/B_{x0}^2 = 1$) through to the force-free Harris sheet ($2\mu_0P_0/B_{x0}^2 = 0$). It can be seen that the plasma pressure decreases as the shear field component B_y increases. This demonstrates the trade off between the plasma pressure and the magnetic pressure due to the shear field component B_y in the force balance equation. In

the Harris sheet case the current is completely perpendicular to the magnetic fields whereas in the force-free case it is completely aligned with the magnetic field direction. In the Harris sheet case the profile of the plasma pressure and the current density are identical and hence they are indistinguishable in Figure 3.14(a). Figure 3.15 are plots of magnetic field lines along z passing through $x = 0$, $y = 0$ for each of the cases shown in Figure 3.14 and these show that as expected, as the strength of the shear field is increased the twisting of the magnetic field in the localised current region is increased. Finally Figure 3.16 shows the potential surface P_{qn} for each of the cases shown in Figure 3.14 with the particle trajectories overlaid. Clearly as $2\mu_0 P_0/B_{x0}^2 \rightarrow 1$ the cosine contribution in the pressure function tends to zero and the particle trajectory approaches that of the Harris sheet that has already been discussed. This is seen by the fact that the cosine profile in A_x flattens as you tend closer to the Harris sheet solution.

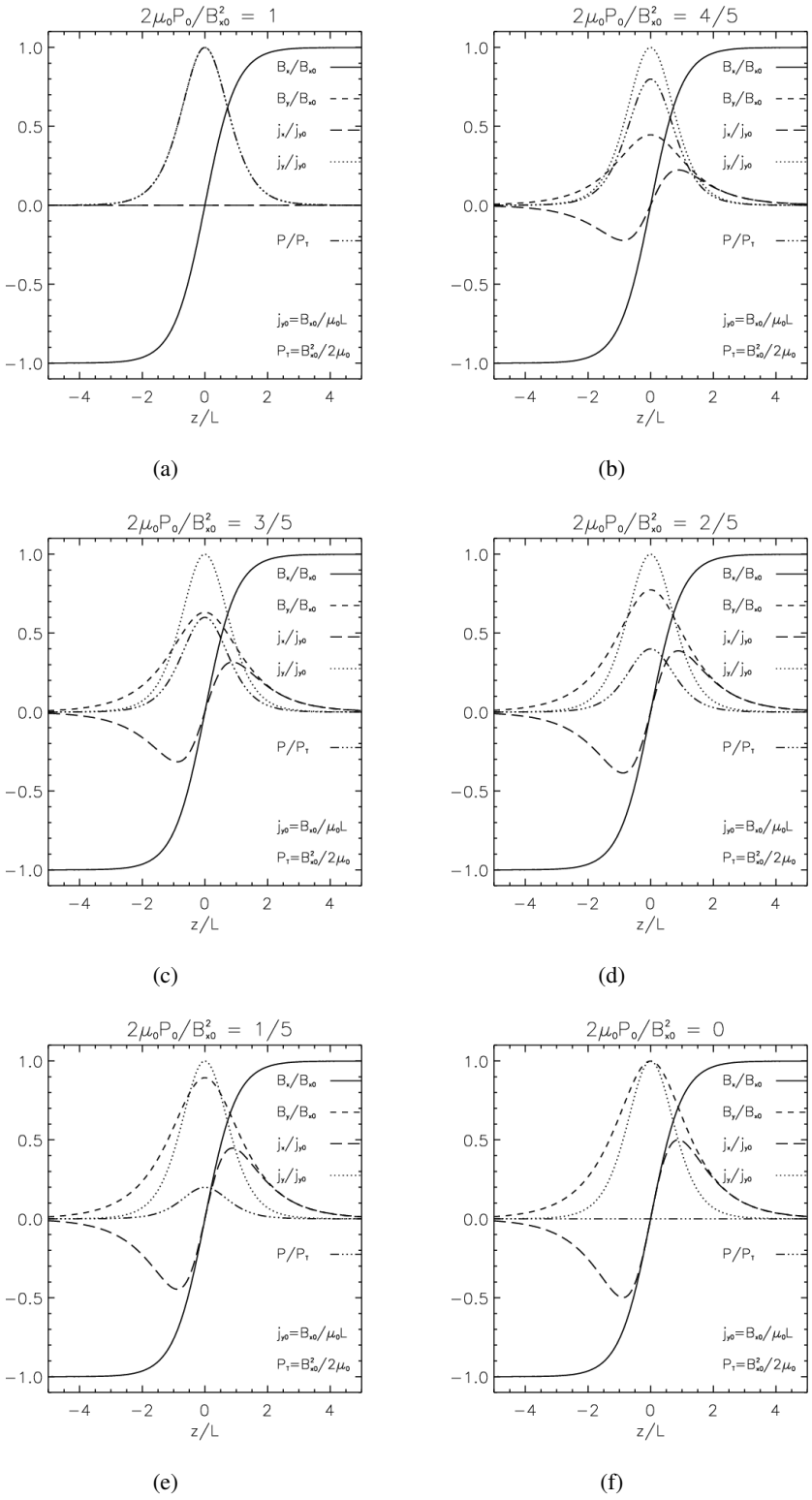

Figure 3.14: Plots of the profiles of B_x, B_y, j_x, j_y and P as one makes the transition from the Harris sheet ($2\mu_0 P_0/B_{x0}^2 = 1$) through to the force-free Harris sheet ($2\mu_0 P_0/B_{x0}^2 = 0$).

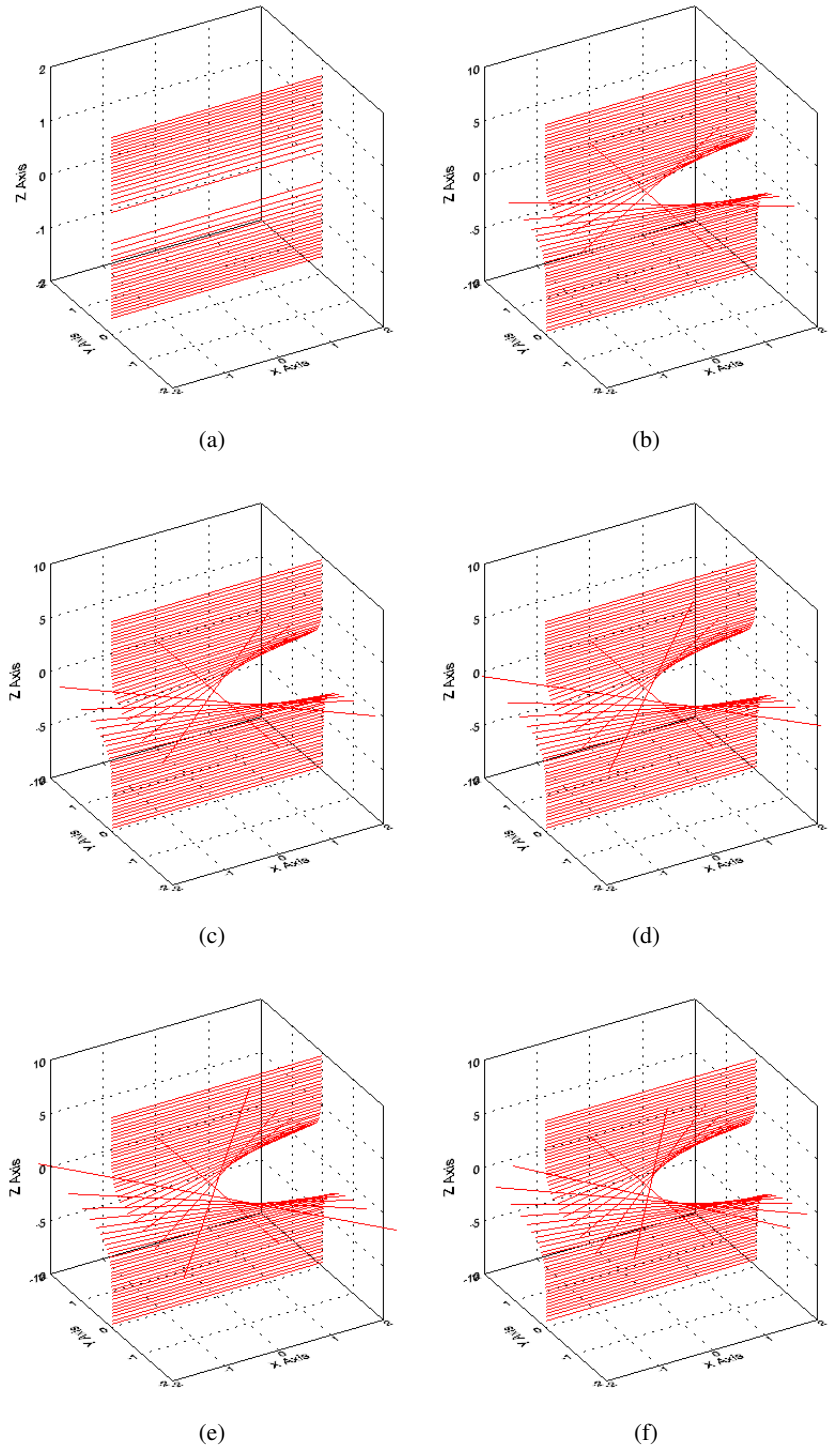

(a) (b) (c) (d) (e) (f)

Figure 3.15: 3D plots of the magnetic field lines for different values of z passing through $x = 0$, $y = 0$ as one makes the transition from the Harris sheet ($2\mu_0 P_0/B_{x0}^2 = 1$) through to the force-free Harris sheet ($2\mu_0 P_0/B_{x0}^2 = 0$). (a) $2\mu_0 P_0/B_{x0}^2 = 1$, (b) $2\mu_0 P_0/B_{x0}^2 = 4/5$, (c) $2\mu_0 P_0/B_{x0}^2 = 3/5$, (d) $2\mu_0 P_0/B_{x0}^2 = 2/5$, (e) $2\mu_0 P_0/B_{x0}^2 = 1/5$, (f) $2\mu_0 P_0/B_{x0}^2 = 0$.

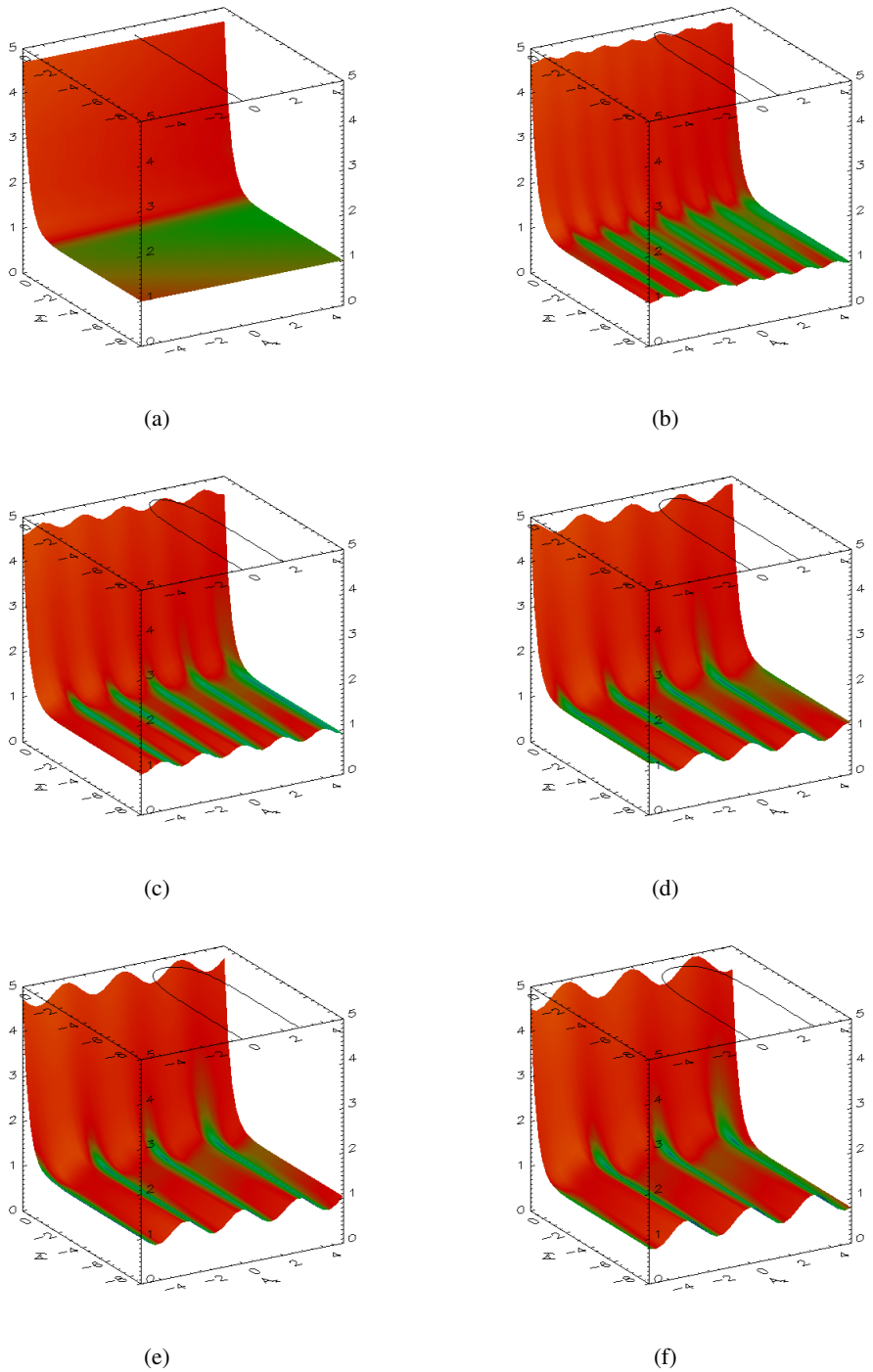

(a) (b) (c) (d) (e) (f)

Figure 3.16: Plots of the potential surface P_{qn} as one makes the transition from the Harris sheet ($2\mu_0 P_0/B_{x0}^2 = 1$) through to the force-free Harris sheet ($2\mu_0 P_0/B_{x0}^2 = 0$). (a) $2\mu_0 P_0/B_{x0}^2 = 1$, (b) $2\mu_0 P_0/B_{x0}^2 = 4/5$, (c) $2\mu_0 P_0/B_{x0}^2 = 3/5$, (d) $2\mu_0 P_0/B_{x0}^2 = 2/5$, (e) $2\mu_0 P_0/B_{x0}^2 = 1/5$, (f) $2\mu_0 P_0/B_{x0}^2 = 0$.

3.9 Summary

In this chapter a general theory of 1D Vlasov-Maxwell equilibria has been given where the distribution functions are always chosen to depend on the three constants of motion which correspond to the particle energy (the Hamiltonian) and the two canonical momenta. It has been shown that the charge density and current densities can all be determined from a general potential P where P is in fact the P_{zz} component of the pressure tensor. In general the potential P will be a function of the electric potential ϕ and the magnetic vector potential components A_x and A_y. If one assumes a quasineutral plasma it is in general possible to invert the quasineutral number density so that P becomes a function of only A_x and A_y. This quasineutral pressure is then denoted by P_{qn}. The properties of P_{qn} make it a very useful quantity to start any investigation of 1D VM equilibria with, since all other quantities such as particle density, charge density and current density can be derived by differentiation.

Ampère's law, in terms of the potential P_{qn} reduces to Hamilton's equations for a particle with coordinates (A_x, A_y) moving in a conservative 2D potential $\mu_0 P_{qn}$. The potential P_{qn} is especially useful in cases where an analytical solution to the magnetic field configuration cannot be easily found as gradients of the potential surface correspond to gradients of the magnetic field components so that large gradients of the potential surface indicates large current densities in the solution. Therefore without actually solving Ampère's law the potential surface can give insight into the expected solution. The pseudo-particle analogy can be used to formulate conditions on P_{qn} that it has to satisfy to allow the existence of 1D force-free VM equilibria (Harrison and Neukirch 2009b). For a force-free VM equilibrium there must be at least one particle trajectory which is a contour of P_{qn}. A particular family of potentials that satisfy this are non-singular attractive central potentials. Finally, knowledge of the pressure function for a specific field configuration results in an integral equation for $g_s(p_{xs}, p_{ys})$ which in some cases can be solved to find the distribution function.

Examples of 1D Vlasov-Maxwell equilibria starting from distribution functions that are exponential functions whose arguments are at most quadratic in velocity was given in Sec. 3.3. Several examples were investigated which illustrated for different P_{qn} the usefulness of the pseudo particle picture in determining the expected solution.

One example of a linear force-free magnetic field was shown, where in that case the particle trajectories were circles in the A_x-A_y-plane. In Sec. 3.4 the distribution function given by (Bobrova et al. 2001) was extended to incude an additional dimensionless parameter b_s in front of the x component of the canonical momenta. This distribution function allowed a family of periodic solutions to be constructed which show a transition from an anti-parallel ($b_s = 0$) magnetic field configuration through to a linear force-free field configuration ($b_s = 1$). As the transition is made the dominant contribution to the force balance comes from the gradient of the shear field rather

than the plasma pressure gradient, whereas in the force-free case the plasma pressure across the sheet is constant. The shearing and twisting of the field increases as the y component of the field increases relative to B_x. In terms of the particle trajectories the solutions are in general oscillatory, with trajectories approaching a circle for the force-free solution.

Another example considered a sum of two Harris sheet type distribution functions, where the first depended on the p_{xs} component of the canonical momenta and the second on the p_{ys} component of the canonical momenta. It was shown that by not only making the assumption of quasineutrality but by also choosing the set of parameters for which the quasineutral electric potential ϕ_{qn} is zero that an analytical solution for the magnetic field can be found. The magnetic field components both have hyperbolic tangent profiles and hence a localised current region but the average drift velocities were spatially varying. The magnetic field is sheared in the localised current region. The inclusion of two free parameters in the distribution function allows the amount of shear in the magnetic field to be adjusted.

This distribution function also added insight into the problem of finding a distribution function that gives the force-free Harris sheet. As has been shown the resulting equilibrium is not the force-free Harris sheet. It showed that by choosing the distribution function that depends only on p_{ys} to have the form of the standard Harris sheet distribution function that the x component of the field and the y component of the current density correspond to the Harris sheet equilibrium. By choosing the distribution function that depends only on p_{xs} to also have the same form as the Harris sheet distribution function, the y component of the magnetic field and the x component of the current density also had Harris sheet profiles. Therefore, even though this distribution function was not successful in giving the force-free Harris sheet, it suggested that to determine a distribution function for the force-free Harris sheet the correct form of the distribution function that depends only on p_{xs} must be found. This was applied in Sec. 3.7, where by assuming the quasineutral pressure function to be made up of two independent functions, one that depended only on A_x which corresponds to p_{xs} in the distribution function and one that depended only on A_y which corresponds to p_{ys} in the distribution function that a Fourier transform method could be applied to determine the correct form of the distribution function for the force-free Harris sheet.

Finally, and most importantly a distribution function which has the force-free Harris sheet as a solution has been shown (Harrison and Neukirch 2009a). This is the first ever self-consistent non-linear force-free 1D Vlasov Maxwell solution known. The distribution function was found by first finding the quasi-neutral pressure function that corresponds to the force-free Harris sheet magnetic field configuration. This pressure function was then used to write down an integral equation for the $g_s(p_{xs}, p_{ys})$ function which was solved via a Fourier transform method, where it was assumed that there must be a choice of parameters for which the quasineutral electric potential ϕ_{qn} can be set to zero. The resulting $g_s(p_{xs}, p_{ys})$ function was found to be a sum of two contributions. The first contibution has a cosine dependence on p_{xs} and the second contribution an exponential

dependence on p_{ys} which is equivalent to the Harris sheet case. To check the validity of the distribution function it was used as the starting point from which the moment equations were calculated. It was shown that there is a choice of parameters which set the quasineutral electric potential ϕ_{qn} to zero. The differential equations resulting from Ampère's law were then solved to give the force-free Harris sheet magnetic field solution. This distribution function was also extended to show that for the correct choice of parameters a family of equilibria can be constructed that describe the transition from the Harris sheet through to the force-free Harris sheet.

This new family of VM equilibria will generate new possibilities for studies of linear and nonlinear instabilities of force-free current sheets. The stability of the VM equilibria presented here have yet to be investigated. It must be pointed out that the p_{xs}-dependent part of the distribution function (3.203) may have multiple peaks in the v_x-direction and this may give rise to instabilities. It is also remarked that although the $B_x(z)$ and $j_y(z)$-profiles are identical to the Harris sheet, $j_x(z)$ is anti-symmetric with respect to $z = 0$. This is closely linked to the fact that in the Harris sheet solution the spatial structure of the current density is determined by the density structure with the average velocity of each particle species being constant, whereas in the force-free solution presented here the particle density is constant and the spatial structure of the current density is determined by the spatial structure of the average velocity. Further investigations will be needed to clarify exactly what the implications are for the stability of the new solution, but on the basis of the physical differences just mentioned one would expect the stability properties of the force-free solution to differ considerably from those of the Harris sheet. Apart from studying the stability properties of the solution class presented here, it will be also be very interesting to investigate whether the general method employed here can be used to find other non-linear force-free solutions.

Chapter 4

Particle in Cell Methods for Simulating Collisionless Plasma Dynamics

4.1 Introduction

Particle in cell methods are now an extremely popular method of studying plasma physics. In particular they are used widely as tools for studying the physical processes of collisionless plasmas. One very important area of application is the study of collisionless reconnection (e.g. Hesse et al. 1999, 2001a; Pritchett 2001; Scholer et al. 2003; Pritchett and Coroniti 2004). Particle in cell codes are widely used in the study of collisionless reconnection as they include the kinetic physics that underly the dissipation and transport mechanisms which are key to understanding the physics of the reconnection region.

Particle in cell codes employ the technique of representing many millions of real physical particles in terms of finite sized superparticles. These superparticles can be thought of as 'finite sized clouds of electrons or ions, the position of the superparticles being the centre of mass of the clouds and their velocities being the mean velocities of the clouds' (Hockney and Eastwood 1988). Importantly though the charge to mass ratio in Maxwell's equations remains unchanged. This representation, assuming that there are enough superparticles in a Debye sphere gives an accurate interpretation of a collisonless plasma. The equations of motion for these superparticles are then solved together with Maxwell's equations to advance the positions and velocities of the superparticles in time and to evolve the electric and magnetic fields.

A brief description of the general method of a particle in cell code is given by Birdsall and Langdon (1985). The initial stage of the particle in cell code is to initialise the particle positions and particle velocities. This is usually based on an equilibrium distribution function. The electric and magnetic

fields that correspond to this initial distribution must also be specified. At each time step the program solves for the electric and magnetic fields from the particle positions and velocities and moves the particles forward in time.

The particle quantities such as position and velocity can take a continuous range of values in the phase space $\mathbf{x}, \mathbf{v}$. The particles are labelled with an index. The labelling of the particles is chosen such that you can correctly identify the 'electrons' and 'ions'. The electric and magnetic fields are located at discretely spaced grid points. To solve for the new particle positions and velocities which are calculated from the electric and magnetic fields, the electric and magnetic fields must be interpolated to the particle positions. The method used here is a first order weighting which interpolates the electric and magnetic fields to the particle position from the 4 nearest grid points. Higher order weighting methods can be used but this will be at the cost of computational time. There are many ways in which the equation of motion can be integrated. In general second order leapfrog schemes are often used as they are accurate and fairly fast in terms of computational time. A second order implicit leapfrog scheme will be described in detail in what follows.

Once the new positions of the particles and velocities are known the number densities and average drift velocites or charge densities and current densities are calculated on the grid. This is done by taking the position and velocity of each particle and interpolating the weighted values of these quantities to the four nearest grid points and then summing up over all particles. Once the new densities are known then the new electric and magnetic fields can be solved for. An implicit solver is described in detail in this chapter. An important point to note is that in general it is necessary to employ a method of ensuring that the electric field satisfies Poisson's equation. This cycle then continues until the final timestep is reached.

In this chapter a detailed description of the particle in cell code `Im2dp4hf` is given. The main program and each of the separate subroutines that make up the full algorithm is discussed. `Im2dp4hf` is a 2 1/2 dimensional fully electromagnetic particle in cell code developed by Michael Hesse (e.g. Hesse et al. 1999). The code utilizes the Buneman layout (Villasenor and Buneman 1992) and integrates the electromagnetic fields implicitly. Density and fluxes are accumulated on the grid, on the basis of a rectangular particle shape function. Charge conservation is guaranteed by the iterative application of a Langdon-Marder type (Langdon 1992; Marder 1987) correction to the electric field.

4.2 Basic Equations

The principle equations that must be solved for the particles are the equations of motion. The equations of motion for particles with a charge q_s and mass m_s are

$$\frac{d\mathbf{v}}{dt} = \frac{q_s}{m_s}(\mathbf{E} + \mathbf{v} \times \mathbf{B}), \tag{4.1}$$

$$\frac{d\mathbf{r}}{dt} = \mathbf{v}. \tag{4.2}$$

Maxwell's equations for the electric field $\mathbf{E} = (E_x, E_y, E_z)$ and the magnetic field $\mathbf{B} = (B_x, B_y, B_z)$ are

$$\nabla \times \mathbf{B} = \mu_0 \mathbf{j} + \frac{1}{c^2}\frac{\partial \mathbf{E}}{\partial t}, \tag{4.3}$$

$$\nabla \times \mathbf{E} = -\frac{\partial \mathbf{B}}{\partial t}. \tag{4.4}$$

The electromagnetic fields are used to push the particles on the grid. The new positions and velocities are used to calculate the new densities and fluxes, and in turn the new fields are calculated. The $\mathbf{E}$, $\mathbf{B}$ and $\mathbf{j}$ are defined at spatial grid points, while particles can take any positions on the grid.

4.3 Grid Assignment

In the code there are full integer grid points defined at $-L_x + (i-2)\Delta x$ $(i = 1, 2, 3.., nx)$, $-L_z + (j-2)\Delta z$ $(j = 1, 2, 3, .., nz)$ and half grid points defined at $-L_x + (i - 3/2)\Delta x$, $-L_z + (j - 3/2)\Delta z$ where L_x and L_z are the halfwidths of the box in the x and z directions and $\Delta x = 2L_x/(nx-2)$, $\Delta z = 2L_z/(nz-2)$. An illustration of the grid is shown in Figure 4.1. This grid layout is chosen such that the code is second order in space.

4.3.1 Debye Length

A condition of the code is that the grid spacing Δx should not be much larger than the Debye length λ_D given by

$$\lambda_D = \frac{v_{th,e}}{w_{pe}}. \tag{4.5}$$

In fact the grid spacing should satisfy the condition that

$$\lambda_D \leq \Delta x \leq 3\lambda_D. \tag{4.6}$$

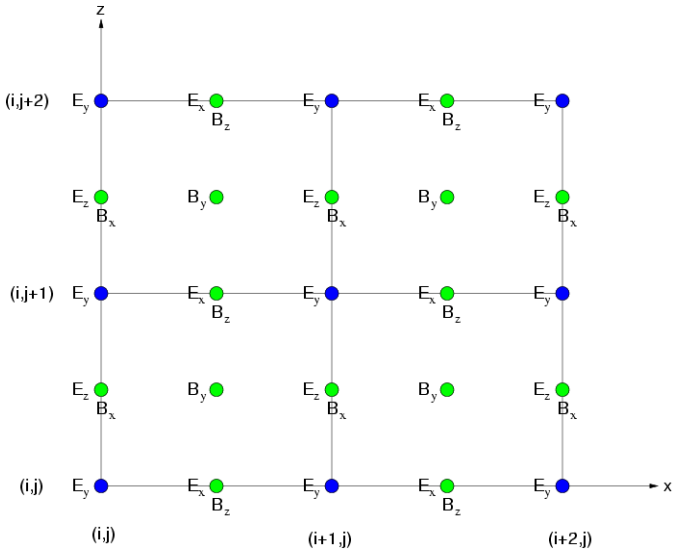

Figure 4.1: The grid assignment

4.4 Timestep chart

The general cycle of the code is shown in Figure 4.2. The particle positions and velocities are given some suitable initial condition at $t = 0$. The positions and velocities are used to calculate the charge and current densities. Once these have been calculated the electric and magnetic fields are calculated on the grid. These fields are interpolated to the particle positions to apply the correct force to each individual particle. This cycle then continues for many time steps.

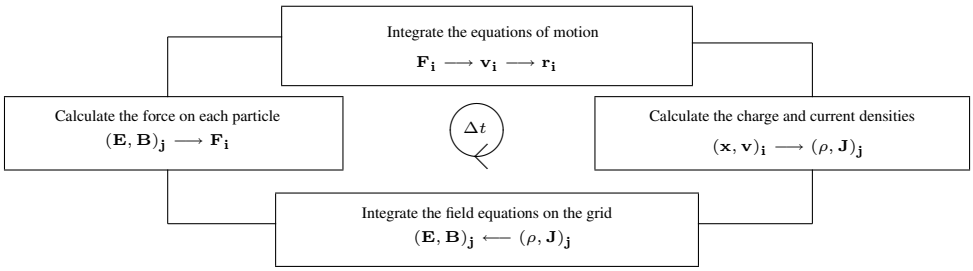

Figure 4.2: Time chart showing the general cycle of a PIC code

4.4.1 Courant condition

The electromagnetic fields are integrated implicitly, thereby eliminating the Courant constraint on the time step generated by light waves,

$$\Delta x > c\Delta t. \tag{4.7}$$

4.5 Normalisations

The code is normalised in the following way. Most importantly time is normalised against the inverse electron plasma frequency. This then has consequences for the other normalisations. The normalisation factors are as follows:

- Time is normalised against the inverse electron plasma frequency.

$$t = \omega_{pe}^{-1} \tag{4.8}$$

- Length is normalised against the electron skin depth.

$$L = \frac{c}{\omega_{pe}} \tag{4.9}$$

- Number density is normalised against n_0 which is a free parameter.

$$n = n_0 \tag{4.10}$$

- Mass is normalised in units of the electron mass.

$$m = m_e \tag{4.11}$$

- Velocity is normalised against the speed of light.

$$v = c \tag{4.12}$$

- The magnetic field is normalised in terms of B_0 and the ratio of the electron plasma frequency to the electron cyclotron frequency as a consequence of choosing time to be normalised against ω_{pe}^{-1}.

$$B = \frac{m_e}{q_e t} = \frac{m_e \omega_{pe}}{q_e} = \frac{m_e}{q_e}\frac{\omega_{pe}}{\Omega_e}\Omega_e = \frac{\omega_{pe}}{\Omega_e}B_0 \tag{4.13}$$

- The electric field is normalised in terms of B_0 and the ratio of the electron plasma frequency to the electron cyclotron frequency.

$$E = cB = \frac{\omega_{pe}}{\Omega_e} B_0 c \tag{4.14}$$

- The temperature is normalised by the fact that velocity is normalised in units of c,

$$T = \frac{m_e c^2}{k_B}. \tag{4.15}$$

- The pressure normalisation factor is given by

$$p = m_e n_0 c^2 = n_0 k_B T. \tag{4.16}$$

4.6 The Main Program

The main level program calls several subroutines which solve for the new electromagnetic fields and the new particle positions and velocities. There is a call to an initialisation subroutine that initialises the spatial grids, the fields and the particle positions and velocities for each species.

The main loop consists of a call to a particle pusher subroutine which pushes the particles and calculates the new density and current density moments. Calls to separate subroutines calculates the new electromagnetic fields. Finally there is a call to a subroutine that ensures charge conservation is satisfied.

4.7 Initialisation

This subroutine sets up the initial condition of the simulation run. The spatial grids, fields, particle positions and particle velocities are initialised. The first step of the initialisation consists of setting up the spatial grid. The spatial grid runs from $-(L_x + \Delta x), -(L_z + \Delta z)$ to L_x, L_z where L_x and L_z are the halfwidths in the x and z directions. The fields are then initialised on the grid points according to the grid layout in Figure 4.1.

The first half of the initialisation sets up the foreground species. These are the two species that carry the current. Once the number density n_s for each species is set, then a subroutine is called which returns the total number of real particles for each species. This is used to calculate the density factors which makes sure the number of superparticles per cell matches up to the real number density. In this code the density factors for each species are always equal. The number of

superparticles per cell in the code is calculated by considering the following. Denoting the total number of real particles for each species by N_s then N_s can be written as

$$N_s = \int dxdz\, n(x,z). \tag{4.17}$$

Denoting the total number of real particles in a cell by N_c then this can be written as

$$N_c = dxdz\, n(x,z), \tag{4.18}$$

and denoting the number of superparticles by N_p then the number of superparticles per cell is

$$\begin{aligned} no.\ of\ superparticles\ per\ cell &= \frac{no.\ of\ real\ particles\ per\ cell}{total\ no.\ of\ particles} \\ &\times \ (number\ of\ superparticles) \\ &= \frac{N_c}{N_s} \times N_p. \end{aligned} \tag{4.19}$$

In the code, the density factor for each particle species is defined as

$$density\ factor = \frac{N_s}{N_p dxdz}. \tag{4.20}$$

The number of superparticles per cell for each species is then calculated in the code by dividing n for each grid cell by the density factor.

The thermal velocities $v_{th,e}$ and $v_{th,i}$ for each particle species in units of c are set using the temperature ratio T_e/T_i. An important point to remember is the choice of $T_e + T_i$ is chosen so that the initial equilibrium satisfies force balance. As an example, in the Harris sheet case this means the plasma pressure at the centre of the sheet must balance the magnetic pressure of the asymptotic magnetic field, far away from the centre of the current sheet. This gives the requirement that,

$$\left(\frac{B^2}{2}\right)_{z\to\infty} = p(z=0) = n(z=0) \times (T_e + T_i), \tag{4.21}$$

which consequently means that if you want the magnetic field and density to be normalised to unity you must set $T_e + T_i = 0.5$. This addition of the temperatures can be changed for different initial conditions but it must be chosen such that the initial equilibrium satisfies the force balance condition.

In the case of a drifting Maxwellian distribution function, initialising the velocity distribution is relatively straight forward. A uniform random number generator is used to set up a Guassian distribution which is scaled by the thermal velocity and shifted by a Gallilean transformation which adds the correct drift velocities for each species $v_{dx,e}, v_{dx,i}, v_{dy,e}, v_{dy,i}, v_{dz,e}$ and $v_{dz,i}$. In the majority of examples considered in Chap. 5 these velocity distributions will be of the form of

a drifting Maxwellian.

In Chap. 5 an example is also given where in one velocity direction the distribution function is not in the form of a drifting Maxwellian. In this case a slightly different approach has to be used to initialise the distribution function. Assuming that the velocity distribution that is to be initialised is given by the 1D distribution $f(v)$ then define

$$r(v) = \int_{-v}^{v} dv^{'} f(v^{'}), \tag{4.22}$$

where $r(v)$ is the probability of finding a particle in the velocity interval $[-v, v]$ and it satisfies the condition that

$$\lim_{v \to \infty} r(v) = 1. \tag{4.23}$$

To produce the desired velocity distribution it is necessary to use the inverse map $v(r)$ which can be used to map a random number between $[0, 1]$ to v. In practice this is done by defining an n element array, say $v[i]$, where each element is set to,

$$v[i] = -v_{max} + 2 * (i-1)/(n-1) * v_{max}, \tag{4.24}$$

where v_{max} is the maximum velocity that you want to consider. You then define another n element array $r[i]$ and fill it by numerical integration where,

$$r[i] = \int_{-vmax}^{v[i]} dv^{'} f(v^{'}), \tag{4.25}$$

ensuring normalisation by setting

$$r[i] \leftarrow r[i]/r[n] \quad \forall i. \tag{4.26}$$

The particle velocities are then set as follows. For each particle you create a random number $s \in [0, 1]$, evenly distributed. You then search for the largest index j for which $r[j] \leq s$ and then assign the velocity $v[j]$ to that particle. This procedure will give a pretty good representation of $f(v)$. There are improvements that could be made, particularly for example by varying the spacing in velocity space, i.e. $v[i]$ not evenly spaced. In practice an evenly spaced array works well enough provided you take n large enough.

This initialisation process is then repeated for the background populations. A background population is introduced to ensure that the number density does not reduce to very small values in any grid cell. These are given a uniform density and a Maxwellian velocity distribution. They carry no current. To initialise the density and current density moments on the grid the particle move subroutine is called with the timestep Δt set to zero.

4.8 Particle Pushing Subroutine

This is the subroutine that calculates the new position and velocities of the particles and then uses these to calculate the new density and current density moments on the grid.

The first step of this subroutine sets all the moment arrays to zero. To solve for the new particle positions and velocities the electric and magnetic fields must be known at the particle positions. To simplify this calculation all the field components are interpolated to the full integer grid points. As an example of this consider the following example lines from the code which says

```
do iz=1,nz
  do ix=2,nx
    exh(ix,iz)=0.5*(ex(ix,iz)+ex(ix-1,iz))
  enddo
enddo
```

The x component of the electric field is defined on the grid at half integer grid points in x and full integer grid points in z directions. The lines of code above show that this component of the electric field is interpolated so it is known at the full integer grid point for both x and z where `exh` is the interpolated value of the x component of the electric field. The same procedure is followed for the other electric and magnetic field components. An illustration of this process for the x component of the electric field is shown in Figure 4.3.

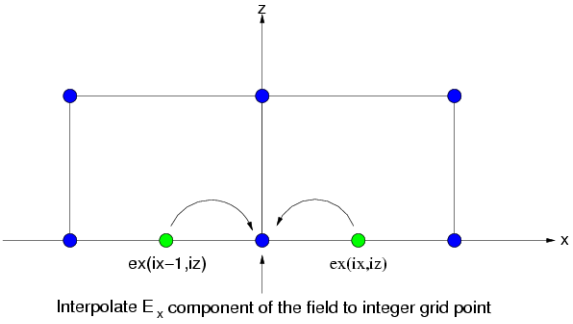

Figure 4.3: An illustration to show how the field components on half integer grid points are interpolated to the full integer grid points for the particle move subroutine. This x component of the electric field is used as an example which is located on half integer grid points in the x direction.

The next step is to get the fields at the particle locations. For each individual particle its position is found. To calculate the interpolation factors the next lowest index of the nearest grid point is calculated and hence the distance in the x and z directions between the particle and the position of the four nearest grid points. These lengths are used to calculate the area weightings which are used to interpolate the fields on the grid points to the particle position. Figure 4.4 shows graphically how this is done and which interpolation factor multiplies which grid point's field value. The black

circle represents the particle. It can be seen clearly that it is the opposite area to the grid point which multiplies the field value at that grid point. This is emphasised where the coloured areas correspond to the colours of the grid points for which that area weighting is used. Once the fields

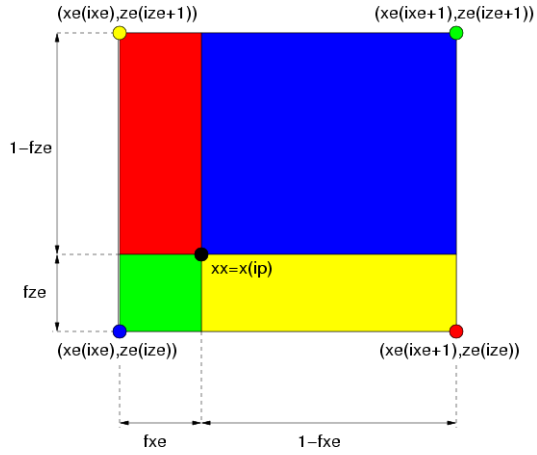

Figure 4.4: An illustration to show the interpolation of the fields to the particle positions for the particle move subroutine.

have been interpolated to the particle positions then the velocities are advanced by integrating the equation of motion,

$$\frac{d\mathbf{v}}{dt} = \frac{q_s}{m_s}(\mathbf{E} + \mathbf{v} \times \mathbf{B}). \tag{4.27}$$

The difference equation that must be solved is

$$\frac{\mathbf{v}^{t+\Delta t} - \mathbf{v}^t}{\Delta t} = \frac{q_s}{m_s}(\mathbf{E} + \mathbf{v}^{t+\frac{\Delta t}{2}} \times \mathbf{B}), \tag{4.28}$$

which can be written in the form,

$$\mathbf{v}^{t+\Delta t} = \mathbf{v}^t + \frac{\beta}{\alpha}(\mathbf{E} + (\alpha\mathbf{v}^{t+\Delta t} + (1-\alpha)\mathbf{v}^t) \times \mathbf{B}), \tag{4.29}$$

where α is an implicit factor and $\mathbf{v}^{t+\frac{\Delta t}{2}}$ has been rewritten as

$$\mathbf{v}^{t+\frac{\Delta t}{2}} = \alpha\mathbf{v}^{t+\Delta t} + (1-\alpha)\mathbf{v}^t, \tag{4.30}$$

where

$$\frac{\beta}{\alpha} = \frac{q_s}{m_s}\Delta t. \tag{4.31}$$

This can then be rewritten as

$$\mathbf{v}^{t+\Delta t} - \beta \mathbf{v}^{t+\Delta t} \times \mathbf{B} = \mathbf{v}^t + \frac{\beta}{\alpha}(\mathbf{E} + (1-\alpha)\mathbf{v}^t \times \mathbf{B}) = \mathbf{T}, \tag{4.32}$$

which can be rearranged to give

$$\mathbf{v}^{t+\Delta t} \times \mathbf{B} = \frac{1}{\beta}(\mathbf{v}^{t+\Delta t} - \mathbf{T}). \tag{4.33}$$

Taking the cross product of this equation with $\mathbf{B}$ this becomes

$$\mathbf{v}^{t+\Delta t} \times \mathbf{B} + \beta \mathbf{v}_\perp^{t+\Delta t} B^2 = \mathbf{T} \times \mathbf{B}. \tag{4.34}$$

This in turn implies that

$$\mathbf{v}^{t+\Delta t} + \beta^2 \mathbf{v}_\perp^{t+\Delta t} B^2 = \beta \mathbf{T} \times \mathbf{B} + \mathbf{T}. \tag{4.35}$$

Splitting up $\mathbf{v}^{t+\Delta t}$ into parallel and perpendicular components this can be written as

$$\mathbf{v}_\parallel^{t+\Delta t} + \mathbf{v}_\perp^{t+\Delta t}(1 + \beta^2 B^2) = \beta \mathbf{T} \times \mathbf{B} + \mathbf{T}. \tag{4.36}$$

Now taking the cross product of this again with $\mathbf{B}$ this equation becomes

$$\mathbf{v}_\perp^{t+\Delta t} \times \mathbf{B} = \frac{1}{(1 + \beta^2 B^2)}(\beta(\mathbf{T} \times \mathbf{B}) \times \mathbf{B} + \mathbf{T} \times \mathbf{B}). \tag{4.37}$$

Finally, substituting into Eq. (4.33) and expanding the triple vector product the expression for $\mathbf{v}^{t+\Delta t}$ is

$$\mathbf{v}^{t+\Delta t} = \mathbf{T} + \frac{\beta}{(1 + \beta^2 B^2)}(-\beta(\mathbf{T}B^2 - \mathbf{B}(\mathbf{T} \cdot \mathbf{B})) + \mathbf{T} \times \mathbf{B}). \tag{4.38}$$

The new velocities are used to advance the particle positions. The difference equations for this step are given by

$$x^{t+\Delta t} = x^t + v_x^{t+\Delta t} \Delta t \tag{4.39}$$

$$z^{t+\Delta t} = z^t + v_z^{t+\Delta t} \Delta t. \tag{4.40}$$

The only thing left to do is to make sure the boundary conditions are satisfied. In the examples considered in the next chapter two different sets of boundary conditions are used. In the Harris sheet cases the boundary conditions in the x direction are periodic and in the z direction the particles are specularly reflected at the boundaries. Illustrations of these two boundary conditions are shown in Figure 4.5. In examples using periodic equilibria as initial conditions the boundary conditions are doubly periodic so that the z boundary is periodic as well.

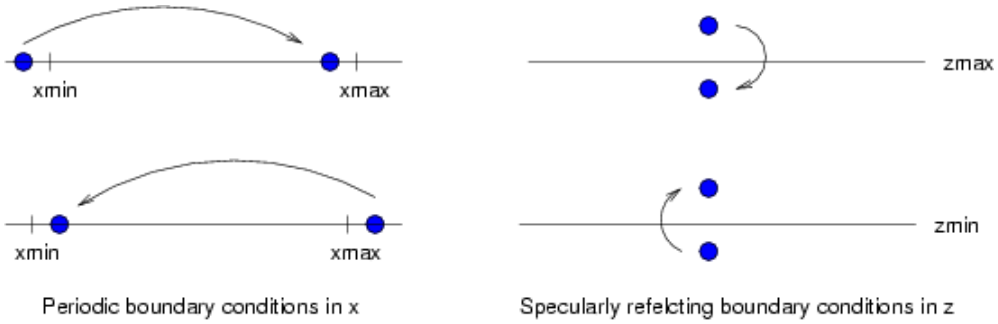

Figure 4.5: An illustration to show the boundary conditions for the particle positions

The second part of the particle move subroutine is to use the new positions and velocities of the particles to calculate the 1st and 2nd order moments for each particle species at the grid points. This is done in a similar way to the particle move calulation except that now the new particle positions and velocities are used to calculate and interpolate the new number densities and average drift velocities to the grid points. The weightings for each grid point are exactly the same as shown in Figure 4.4. The actual quantities calculated by the code are essentially the following first and second order moments for each species.

$$n_s = \int_{-\infty}^{\infty} f_s d^3v, \tag{4.41}$$

$$n_s \langle \mathbf{v} \rangle_s = \int_{-\infty}^{\infty} \mathbf{v} f_s d^3v. \tag{4.42}$$

To calculate the new densities and average drift velocities on the grid points you sum over each particle species finding the position and velocity of each particle and then using the area weightings shown in Figure 4.4 to allocate the number density and average drift velocity contribution at each grid point.

In all cases the boundary conditions in the x direction are periodic. It is important to note though that the way the densities are gathered on the grid the outer cells only receive half the total density. So assuming symmetry the amount the outer cells receive is just doubled. The boundary conditions on the z boundary for the Harris sheet cases is that the densities at `iz=2` and `iz=nz` are set to the densities at `iz=3` and `iz=nz-1` . On the z boundary the velocities are set to zero. In the case of a periodic initial condition the boundary conditions on the z boundary are periodic.

4.9 Advancing the Magnetic Field

To start off, the old magnetic field components are stored. The current density components on the grid are also found. The right hand side of the equation for the implicit solve is calculated first in

one subroutine, which in turn calls a separate subroutine which solves for the new magnetic field components.

To see how this process is done consider the following calculation. The differential equation to be solved is

$$\frac{\partial \mathbf{B}}{\partial t} = -\nabla \times \mathbf{E}, \tag{4.43}$$

which together with the differential equation

$$\frac{1}{c^2}\frac{\partial \mathbf{E}}{\partial t} = \nabla \times \mathbf{B} - \mu_0 \mathbf{j}, \tag{4.44}$$

can be solved implicitly to find the new magnetic field components. The corresponding difference equations are

$$\mathbf{B}^{t+\Delta t} - \mathbf{B}^t = -\Delta t \, \nabla \times \mathbf{E}^{t+\frac{\Delta t}{2}}, \tag{4.45}$$

which can be written using the implicit factor α as

$$\mathbf{B}^{t+\Delta t} - \mathbf{B}^t = -\Delta t \, \nabla \times [\alpha \mathbf{E}^{t+\Delta t} + (1-\alpha)\mathbf{E}^t]. \tag{4.46}$$

The second difference equation is

$$\mathbf{E}^{t+\Delta t} - \mathbf{E}^t = -\Delta t \, c^2 [\mu_0 \mathbf{j} - \nabla \times \mathbf{B}^{t+\frac{\Delta t}{2}}], \tag{4.47}$$

which again can be written using the implicit factor α as

$$\mathbf{E}^{t+\Delta t} - \mathbf{E}^t = -\Delta t \, c^2 [\mu_0 \mathbf{j} - \nabla \times (\alpha \mathbf{B}^{t+\Delta t} + (1-\alpha)\mathbf{B}^t)]. \tag{4.48}$$

Now substituting for $\mathbf{E}^{t+\Delta t}$ from Eq. (4.48) into Eq. (4.46),

$$\begin{aligned} \mathbf{B}^{t+\Delta t} - \mathbf{B}^t \;=\; & -\Delta t \, \alpha \, \nabla \times \left[\mathbf{E}^t - \Delta t \, c^2 [\mu_0 \mathbf{j} - \nabla \times (\alpha \mathbf{B}^{t+\Delta t} + (1-\alpha)\mathbf{B}^t)]\right] \\ & -\Delta t (1-\alpha) \, \nabla \times \mathbf{E}^t, \end{aligned} \tag{4.49}$$

which reduces to

$$\begin{aligned} \mathbf{B}^{t+\Delta t} - \mathbf{B}^t \;=\; & -\Delta t \, \nabla \times \mathbf{E}^t + \Delta t^2 \, \alpha c^2 \mu_0 \, \nabla \times \mathbf{j} \\ & -\Delta t^2 \, c^2 \alpha^2 (\nabla \times \nabla \times \mathbf{B}^{t+\Delta t}) - \Delta t^2 \, c^2 \alpha (1-\alpha)(\nabla \times \nabla \times \mathbf{B}^t). \end{aligned} \tag{4.50}$$

Expanding the vector triple products and remembering that $\nabla \cdot \mathbf{B} = 0$ and separating new and old

variables, the difference equation is

$$\begin{aligned}\mathbf{B}^{t+\Delta t} - \Delta t^2\, c^2\alpha^2\, \nabla^2\mathbf{B}^{t+\Delta t} &= \mathbf{B}^t - \Delta t\, \nabla\times\mathbf{E}^t + \Delta t^2\, \alpha c^2\mu_0\, \nabla\times\mathbf{j} \\ &\quad +\Delta t^2\, c^2\alpha(1-\alpha)\, \nabla^{\mathbf{2}}\mathbf{B}^t. \end{aligned} \tag{4.51}$$

Denoting the RHS of this equation as $\mathbf{S}$ the final difference equation is

$$\mathbf{B}^{t+\Delta t} - \Delta t^2\, c^2\alpha^2\, \nabla^{\mathbf{2}}\mathbf{B}^{t+\Delta t} = \mathbf{S}. \tag{4.52}$$

Now the last part of the calculation shown here is to illustrate how Eq. 4.52 is solved to determine the magnetic field components at the new time step. The calculation shown below is just for the x component of the magnetic field as an illustration. So expanding Eq. (4.52) in terms of its spatial derivatives,

$$\begin{aligned}&-\Delta t^2\, \alpha^2 c^2\left[\frac{B_x^{t+\Delta t}(ix+1,iz) - 2B_x^{t+\Delta t}(ix,iz) + B_x^{t+\Delta t}(ix-1,iz)}{\Delta x^2}\right. \\ &\left.+\frac{B_x^{t+\Delta t}(ix,iz+1) - 2B_x^{t+\Delta t}(ix,iz) + B_x^{t+\Delta t}(ix,iz-1)}{\Delta z^2}\right] + B_x^{t+\Delta t}(ix,iz) = S_x. \end{aligned} \tag{4.53}$$

Rearranging this to solve for $B_x^{t+\Delta t}$ then gives,

$$\begin{aligned}B_x^{t+\Delta t}(ix,iz) &= \frac{1}{1+\frac{2\Delta t^2\,\alpha^2c^2}{\Delta x^2}+\frac{2\Delta t^2\,\alpha^2c^2}{\Delta z^2}}\left[S_x\right. \\ &\quad +\frac{\Delta t^2\,\alpha^2c^2}{\Delta x^2}\left(B_x^{t+\Delta t}(ix+1,iz)+B_x^{t+\Delta t}(ix-1,iz)\right) \\ &\quad \left.+\frac{\Delta t^2\,\alpha^2c^2}{\Delta z^2}\left(B_x^{t+\Delta t}(ix,iz+1)+B_x^{t+\Delta t}(ix,iz-1)\right)\right]. \end{aligned} \tag{4.54}$$

A similar calculation can be shown for B_y and B_z. Therefore to advance the magnetic field the first subroutine calculates S_x, S_y and S_z. A separate subroutine is then called which uses a relaxation method to converge towards the new magnetic field component values by solving Eq. (4.52).

The boundary conditions for the magnetic field components in the x direction are periodic. In the Harris sheet cases the magnetic field components B_x and B_z at the z boundaries are set using the condition that $\mu_0\mathbf{j} = \nabla\times\mathbf{B}$. The y component of the magnetic field must be set explicitly. In the case of a periodic initial condition the z boundaries also satisfy periodic boundary conditions.

4.10 Advancing the Electric Field

The next step is to solve for the new electric field components. To do this the difference equation

$$\mathbf{E}^{t+\Delta t} - \mathbf{E}^{t} = -\Delta t c^2 \left(\mu_0 \mathbf{j} - \nabla \times \mathbf{B}^{t+\frac{\Delta t}{2}}\right), \tag{4.55}$$

is solved. This is rewritten using the implicit factor α in terms of the magnetic field at the old and new timestep.

$$\mathbf{E}^{t+\Delta t} - \mathbf{E}^{t} = -\Delta t c^2 \left[\mu_0 \mathbf{j} - \nabla \times \left(\alpha \mathbf{B}^{t+\Delta t} + (1-\alpha)\mathbf{B}^{t}\right)\right]. \tag{4.56}$$

The first stage of the routine is to loop over all the particles to calculate the total current densities. It is important to remember that the current densities must be defined on the grid at the points at which each component of the electric field is located on the grid. The particle move routine calculates the average drift velocities for each particle species at the integer grid points. Therefore as well as summing over each particle species to calculate the total current densities, it is also necessary, for particular components of the electric field, to interpolate the average drift velocities for each species to half integer grid points in the x or z directions so they are located at the same position on the grid as that component of the electric field. An example of this is the x component of the electric field. The x component of the electric field is located on the grid at half integer grid points in the x direction and full integer grid points in the z direction. Hence the average drift velocity component in the x direction $v_{dx,s}$ must be interpolated so that it now has the correct value at the half integer grid point in the x direction, whilst also looping over all particle species to calculate the total current density there. This can be seen in the example lines of code below and is also shown in Figure 4.6.

```
do k=1,nss
  do iz=2,nz
    do ix=2,nx-1
      jx(ix,iz)=jx(ix,iz)
                +0.5*q(k)*dfac(k)*(vxs(ix,iz,k)+vxs(ix+1,iz,k))
    enddo
  enddo
enddo
```

Once the total current densities j_x, j_y and j_z are calculated then it is straight forward to solve for the new electric field components by solving Eq. (4.56), where the values of the magnetic field components at the new time step are known because they were already calculated by the subroutine that advances the magnetic field and the magnetic field components at the previous timestep are also saved before the new magnetic field components are calculated.

Now the final matter to deal with is to correct the electric field components properly at the bound-

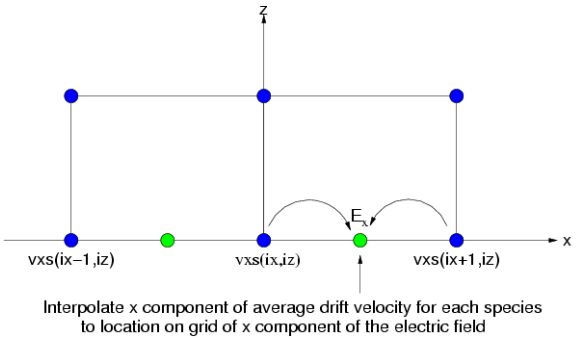

Figure 4.6: An illustration to show how the average drift velocities located at full integer grid points are interpolated to half integer grid points in the x and z directions so that the total current densities are calculated at the position of each component of the electric field on the grid. The x component of the electric field is used as an example which is located on half integer grid points in the x direction.

aries. The boundary conditions in the x direction are always periodic. In the Harris sheet simulation runs the electric field components at the z boundaries are set to zero. In the case of a periodic initial condition periodic boundary conditions are used in the z direction.

4.11 Ensuring Charge Conservation

In all PIC codes it is necessary to correct for the electric field to ensure that Poisson's equation is satisfied. In `Im2dp4hf` charge conservation is guaranteed by the iterative application of a Langdon-Marder type (Langdon 1992; Marder 1987) correction to the electric field. The method is described below. Consider the Ampère-Maxwell equation,

$$\frac{\partial \mathbf{E}}{\partial t} = c^2 \nabla \times \mathbf{B} - \frac{\mathbf{j}}{\epsilon_0} + \nabla F, \tag{4.57}$$

where F is a correction term to ensure charge conservation and is defined as

$$F = k(\nabla \cdot \mathbf{E} - \rho), \tag{4.58}$$

where k is in general allowed to vary in space. Leap-frog time differencing of Eq. (4.57) and Eq. (4.58) gives,

$$\mathbf{E}^{t+\Delta t} = \mathbf{E}^t + c^2 \Delta t \nabla \times \mathbf{B}^{t+\frac{\Delta t}{2}} - \frac{\Delta t}{\epsilon_0} \mathbf{j}^{t+\frac{\Delta t}{2}} + \Delta t \nabla F^t, \tag{4.59}$$

$$F^t = k(\nabla \cdot \mathbf{E}^t - \rho^t). \tag{4.60}$$

Defining ${}^{(0)}\mathbf{E}^{t+\Delta t}$ as the electric field calculated in the code at time $t+\Delta t$ and ${}^{(0)}F^{t+\Delta t}$ as the correction term to the electric field at $t+\Delta t$ then define,

$$
\begin{aligned}
{}^{(0)}\mathbf{E}^{t+\Delta t} &= \mathbf{E}^{t} + c^2\Delta t\nabla\times\mathbf{B}^{t+\frac{\Delta t}{2}} - \frac{\Delta t}{\epsilon_0}\mathbf{j}^{t+\frac{\Delta t}{2}}, && (4.61)\\
{}^{(0)}F^{t+\Delta t} &= k(\nabla\cdot\mathbf{E}^{t+\Delta t} - \rho^{t+\Delta t}), && (4.62)
\end{aligned}
$$

and then the correction to the electric field is

$$
\begin{aligned}
\mathbf{E}^{t+\Delta t} &= {}^{(0)}\mathbf{E}^{t+\Delta t} + \Delta t\nabla {}^{(0)}F^{t+\Delta t} && (4.63)\\
&= {}^{(0)}\mathbf{E}^{t+\Delta t} + \Delta t\nabla\left(k(\nabla\cdot^{(0)}\mathbf{E}^{t+\Delta t} - \rho^{t+\Delta t})\right). && (4.64)
\end{aligned}
$$

Defining the correction to the electric field as $\mathbf{E}_c = -\nabla\phi$ then

$$
\begin{aligned}
\mathbf{E}^{t+\Delta t} &= {}^{(0)}\mathbf{E}^{t+\Delta t} - \nabla\phi, && (4.65)\\
\nabla^2\phi &= \nabla\cdot^{(0)}\mathbf{E}^{t+\Delta t} - \rho^{t+\Delta t}. && (4.66)
\end{aligned}
$$

Solving for ϕ via an accelerated point Jacobi method,

$$
\begin{aligned}
&2\left(\frac{\phi_{i,j}^{(m+1)} - (1-\omega)\phi_{i,j}^{(m)}}{\omega}\right)\left(\frac{1}{\Delta x^2}+\frac{1}{\Delta z^2}\right) =\\
&\quad\frac{1}{\Delta x^2}\left(\phi_{i+1,j}^{(m)}+\phi_{i-1,j}^{(m)}\right)+\frac{1}{\Delta z^2}\left(\phi_{i,j+1}^{(m)}+\phi_{i,j-1}^{(m)}\right)-\left(\nabla\cdot^{(0)}\mathbf{E}^{t+\Delta t}-\rho^{t+\Delta t}\right) \qquad (4.67)
\end{aligned}
$$

and assuming that $\phi^{(0)}=0$ then,

$$
\phi_{i,j}^{(1)} = -\frac{\omega}{2}\frac{1}{\left(\frac{1}{\Delta x^2}+\frac{1}{\Delta z^2}\right)}\left(\nabla\cdot^{(0)}\mathbf{E}^{t+\Delta t}-\rho^{t+\Delta t}\right). \qquad (4.68)
$$

Substituting into Eq. (4.65)

$$
\mathbf{E}^{t+\Delta t} =^{(0)} \mathbf{E}^{t+\Delta t} + \nabla\left(\frac{\omega}{2}\frac{1}{\left(\frac{1}{\Delta x^2}+\frac{1}{\Delta z^2}\right)}\left(\nabla\cdot^{(0)}\mathbf{E}^{t+\Delta t}-\rho^{t+\Delta t}\right)\right), \qquad (4.69)
$$

which by comparing to Eq. (4.64) implies that a single pass of the point Jacobi scheme is equivalent to the improved Marder scheme (Langdon 1992) with

$$
k = \frac{\omega}{2\Delta t}\frac{1}{\left(\frac{1}{\Delta x^2}+\frac{1}{\Delta z^2}\right)}, \qquad (4.70)
$$

and therefore,

$$
\begin{aligned}
{}^{(0)}F^{t+\Delta t} &= \frac{\omega}{2\Delta t}\frac{1}{\left(\frac{1}{\Delta x^2}+\frac{1}{\Delta z^2}\right)}\left(\nabla\cdot^{(0)}\mathbf{E}^{t+\Delta t}-\rho^{t+\Delta t}\right), && (4.71)\\
\mathbf{E}^{t+\Delta t} &= {}^{(0)}\mathbf{E}^{t+\Delta t} + \Delta t\nabla {}^{(0)}F^{t+\Delta t}. && (4.72)
\end{aligned}
$$

This method is used iteratively in `Im2dp4hf` to correct for the electric field. An iterative loop is set up where

$$F^{(n)} = \frac{\omega}{2\Delta t}\frac{1}{\left(\frac{1}{\Delta x^2}+\frac{1}{\Delta z^2}\right)}\left(\nabla\cdot\mathbf{E}^{(n)}-\rho\right), \tag{4.73}$$

$$\mathbf{E}^{(n+1)} = \mathbf{E}^{(n)}+\Delta t\nabla F^{(n)}, \tag{4.74}$$

and n is the iteration number. This iteration loop is then performed many times. In the code $\omega = 1/2$.

4.12 Summary

In this chapter a detailed description of the particle in cell code `Im2dp4hf` developed by Michael Hesse (e.g. Hesse et al. 1999) has been given. Each of the main subroutines have been described. The first step initialises the particle positions and velocities according to a specific distribution and sets up the electric and magnetic fields that are consistent with this. It also establishes the densities and current densities on the grid. The main loop consists of calling several subroutines. The particle move subroutine pushes the particles by integrating the equation of motion via an implicit method. The new particle positions and velocities are used to calculate the new densities and current densities on the grid. Then subrotuines are called that advance the magnetic field components forward in time, also by an implicit method. The electric fields are then advanced and finally a subroutine is called that ensures charge conservation. In the Harris sheet cases the boundary conditions are periodic in x. Particles are specularly reflected at the z boundaries. The magnetic field components at the z boundaries are set using $\mu_0\mathbf{j} = \nabla\times\mathbf{B}$ and the electric field components are set to zero. In the case of a periodic initial condition the boundary conditions are periodic in both x and z.

Chapter 5

PIC Simulations of Collisionless Reconnection

5.1 Introduction

Magnetic reconnection is considered to be one of the most important plasma processes that facilitates the release of large amounts of stored magnetic energy which is converted into heat and kinetic energy of fast particles. It is thought to have fundamental importance in flares, coronal mass ejections and also coronal heating (e.g. Priest 1984). It is also plays a major role in the transfer of energy from the solar wind into the magnetosphere (e.g. Schindler 2007).

In many of the regimes of interest in astrophysical plasmas the plasma can be considered as collisionless. Therefore the aim of understanding the physics underlying reconnection in a collisionless plasma has become an important area of research. In particular there have been many studies to try and understand the dissipation mechanism which gives rise to the reconnection electric field E_y and allows the frozen in constraint to be broken (e.g. Shay et al. 1998; Birn et al. 2001; Hesse et al. 1999, 2001a,b, 2004, 2005; Kuznetsova et al. 1998, 2000, 2001; Nishimura et al. 2003; Ricci et al. 2004a; Pritchett 2001; Pritchett and Coroniti 2004; Pritchett 2005; Bowers and Li 2007). The frozen in constraint is given by the ideal Ohm's law,

$$\mathbf{E} + \mathbf{u} \times \mathbf{B} = \mathbf{0}. \tag{5.1}$$

The frozen in constraint is broken when the right hand side of Eq. (5.1) becomes non zero. Taking the first order moment of the electron Vlasov equation the collisionless Ohm's law is,

$$\mathbf{E} + \mathbf{u_e} \times \mathbf{B} = \frac{1}{n_e q_e} \nabla \cdot \mathbf{P_e} + \frac{m_e}{q_e} \left(\frac{\partial \mathbf{u_e}}{\partial t} + \mathbf{u_e} \cdot \nabla \mathbf{u_e} \right). \tag{5.2}$$

Ohm's law refers to the electrons as in general it is the electrons that are the dominant current carriers. The terms that can give rise to the E_y electric field that break the frozen in constraint can therefore only be gradients of the off-diagonal components of the electron pressure tensor or the electron bulk inertia.

The process by which the frozen in constraint is broken has been studied extensively in 2D starting from a Harris sheet (Harris 1962) both without a guide field (e.g. Hesse et al. 1999, 2001a; Kuznetsova et al. 1998, 2000, 2001; Pritchett 2001) and with a guide field (e.g. Hesse et al. 2004; Ricci et al. 2004a; Pritchett 2005). These have shown that the dominant contribution to the reconnection electric field in the vicinity of the X-point is due to gradients of the off-diagonal components of the electron pressure tensor when the full electron pressure tensor is included on the right hand side of Ohm's law.

In the case of zero guide field it has been shown that the scale lengths of the electron dissipation region are determined by the trapping lengths of an electron in a field reversal (Hesse et al. 1999; Kuznetsova et al. 2000, 2001) where the trapping lengths λ_x and λ_z are given as approximately,

$$\lambda_x = \left[\frac{2m_eT_e}{e^2\left(\frac{\partial B_z}{\partial x}\right)^2}\right]^{1/4}, \tag{5.3}$$

$$\lambda_z = \left[\frac{2m_eT_e}{e^2\left(\frac{\partial B_x}{\partial z}\right)^2}\right]^{1/4}. \tag{5.4}$$

These lengths are simply the distances away from the X-point which are equivalent to the electron gyroradius in the field reversal. Hesse et al. (1999) compared two simulations starting from identical Harris sheet magnetic field configurations varying only the mass ratio in each case from $m_i/m_e = 9$ to $m_i/m_e = 100$. They showed that the profile of B_z is almost identical in both runs indicating that the length scales of the electron dissipation region are proportional to the fourth root of the electron mass.

Kuznetsova et al. (1998, 2000, 2001) have carried out several studies using hybrid simulations in 2D which included electron non-gyrotropic effects in the hybrid simulation model and they have also compared these results to full electromagnetic particle in cell results (Kuznetsova et al. 2001). They found that the hybrid simulation reproduced the full particle code results very well and that the dominant contribution to the reconnection electric field is due to gradients of off-diagonal terms of the electron pressure tensor or what can also be described as kinetic quasi-viscous effects. It is found that the bulk electron inertia contributes very little to the reconnection electric field. In these studies estimates of the reconnection electric field due to the non-gyrotropic kinetic effects were calculated and it was suggested that these could be incorporated into large scale MHD models. Analytical estimates of the time evolution of the reconnected flux for the MHD model with the non-gyrotropic correction agreed very well with the results from the hybrid

and full particle simulations.

A detailed study of 2D reconnection was carried out in the Geospace Environmental Modelling (GEM) Magnetic Reconnection Challenge (Birn et al. 2001). This study used a simple Harris sheet configuration without a guide field with a specified set of initial conditions including a finite amplitude magnetic island perturbation to trigger the dynamics. The question of reconnection onset was not addressed. The aim of the challenge was to understand the important physics of collisionless reconnection and to determine the minimum requirements to facilitate fast reconnection. A variety of different numerical codes were used including MHD codes (Birn and Hesse 2001; Otto 2001), Hall MHD codes (Ma and Bhattacharjee 2001; Birn and Hesse 2001), hybrid codes (Kuznetsova et al. 2001; Shay et al. 2001) and full particle codes (Hesse et al. 2001a; Pritchett 2001; Shay et al. 2001). It was concluded that the minimum requirement for fast reconnection is inclusion of the Hall term in the generalised Ohm's law. The reconnection rate was essentially independent of the method by which the frozen in constraint was broken, whether it was resistivity, electron inertia, or non-gyrotropic pressure effects. A plot showing the evolution of the reconnected magnetic flux for the GEM challenge for a full particle, hybrid, Hall MHD and MHD code is shown in Figure 5.1. The slope of the reconnected flux is equivalent to the reconnection rate.

Figure 5.1: Time evolution of the reconnected magnetic flux for the GEM reconnection challenge for a full particle, hybrid, Hall MHD and MHD code (Birn et al. 2001).

The Hall term introduces a scale separation between the electrons and ions. The electrons are decoupled from the magnetic field on the scale length of the electron skin depth c/ω_{pe} and the ions decouple from the electrons and the magnetic field on the scale length of the ion skin depth c/ω_{pi} (Shay et al. 1998). A characteristic feature of the scale separation between the electrons

and the ions is the development of a quadrupolar out of the plane magnetic field (e.g. Hesse et al. 2001a; Kuznetsova et al. 2001; Ma and Bhattacharjee 2001; Shay et al. 2001; Pritchett 2001; Ricci et al. 2004a). This is due to the fact that in the Hall zone, the region in which the ions are decoupled from the magnetic field and electrons are frozen into the magnetic field, the electron flow speeds are found to be significantly larger than the ion flow speeds (Hesse et al. 2001a). The difference between these flow speeds results in an in plane current. The gradients of the quadrupolar magnetic field supports this current. The importance of the Hall term is that it introduces the dynamics of whistler waves into the system (Shay et al. 2001; Ma and Bhattacharjee 2001). The quadratic dispersion relation of the whistler waves ($\omega \sim k^2$) results in a phase speed that is inversely proprotional to the width of the electron dissipation region. Thus the electron flux out of the electron dissipation region is independent of the sheet width. As a consequence of this the inflow velocity is independent of the width of the electron dissipation region and it is the ions that control the reconnection rate (Shay et al. 2001).

Hesse et al. (1999) have shown that the reconnection electric field in the vicinity of the X-point is independent of the mass ratio. This is shown in Figure 5.2 from Hesse et al. (1999). The evolution of the reconnected flux in each case for varying values of the mass ratio is virtually identical indicating that the reconnection electric field is approximately the same in all runs. In particular they compared two simulation runs, one with a mass ratio of $m_i/m_e = 9$ and the other with mass ratio $m_i/m_e = 100$ and they showed that although the pressure anisotropy was larger in the case of the lower mass ratio by a factor of about 3, the gradient of the off-diagonal components of the pressure tensors gave rise to the same reconnection electric field indicating that the electron physics adjusts itself to the large scale requirements of the system. A similar result was found by Pritchett (Pritchett 2001). To verify this result Hesse et al. (1999) made an order of magnitude estimate of the reconnection electric field E_y based on the contribution from gradients of off-diagonal components of the electron pressure tensor and found it to be given approximately by,

$$E_{y,rec} \approx \frac{1}{e}\frac{\partial v_{xe}}{\partial x}\sqrt{2m_e T_e}, \tag{5.5}$$

where v_{xe} is the electron flow velocity, T_e the electron temperature and m_e the electron mass. They therefore concluded that for the reconnection electric field to be independent of the mass ratio the electron flow velocity must scale as the inverse square root of the electron mass which was confirmed by their simulation results.

The reconnection rate has also been shown to depend on the initial sheet width (Hesse et al. 2001a). They compared simulation runs for total sheet thinkness 0.25, 0.5 and $2c/\omega_{pi}$. They found that the evolution was much faster for the thinner current sheets, shown in Figure 5.3. In one diagnostic they plotted the maximum value of the reconnection electric field against the inverse sheet thickness and found an exact linear relationship. This is shown in Figure 5.3(a). They also

Figure 5.2: Time evolution of the reconnected magnetic flux for runs with increasing mass ratio. Their evolutions are identical indicating that the reconnection rate is independent of the mass ratio (Hesse et al. 1999).

plotted the time taken to reach certain values of total reconnected magnetic flux against sheet thickness. This, in contrast to the first diagnostic suggested some non-linear behaviour, where for larger sheet thickness the evolution times increased more strongly. This is shown in Figure 5.3(b).

The dominant current carriers for the y component of the current density around the X-point was found to be the electrons (e.g. Pritchett 2001; Hesse et al. 2001a). It is stated by Pritchett (2001) for a simulation starting from the GEM challenge configuration that the electron current is 2.5 times larger than the ion current. This is due to the increased electron drift in the y direction due to the enhanced E_y electric field component. This increased electron drift is found to peak at the X-line and remains strong out to $\mid x \mid \approx 3 - 4c/\omega_{pi}$ which is in contrast to the ion drift which is nearly constant over this region and much smaller than the electron drift (Hesse et al. 2001a; Pritchett 2001). It is found that the magnetic island size in the z direction is of the order of the ion inertial length c/ω_{pi} but in fact the region of enhanced electron current around the X-point is limited to a much smaller region of half thickness of the order $1 - 2c/\omega_{pe}$ in which electrons are expelled at super Alfvénic speeds (Hesse et al. 1999, 2001a; Pritchett 2001; Kuznetsova et al. 2001). Outside of this electron diffusion region the ions are the dominant current carriers.

The results of the GEM challenge and several other 2D reconnection studies have led to the model description (Hesse et al. 2001a) that the 'large scale MHD-like behaviour transitions into a region known as the Hall zone where the ions are demagnetised, whereas the electrons are still frozen into the magnetic field. This region is associated with the formation of a quadrupolar structure

(a)

(b)

Figure 5.3: Two figures that show the evolution dependence on the half width of the current sheet from Hesse et al. (2001a). In Figure 5.3(a) the maximum reconnection electric field is plotted against the inverse sheet thickness which is in units of the ion inertial length. In Figure 5.3(b) the elapsed simulation times, in units of the inverse ion cyclotron period, until a certain level of magnetic flux normal to the current sheet is reached is plotted. This shows some deviation from the predicted linear dependence on current sheet width (Hesse et al. 2001a).

of the normal magnetic field B_y, with gradients supporting the current flow in the plane of the X-type magnetic field structure. The scale size of the Hall zone is a few to 10 ion inertial lengths. Embedded in this region lies the electron dissipation region, where electrons become demagnetised from the magnetic field, thus enabling the reconnection process. The edges of this region are marked by peaks in nongyrotropic electron pressure. Scale sizes here are defined by the electron bounce motion in the reversals of both B_x and B_z, which typically correspond to just over an electron inertial length in the z direction and a few electron inertial lengths in the x direction. In the magnetotail these lengths correspond to lengths of tens to hundreds of kilometres.' In the solar corona, using typical values for an active region (see Table 1.1) the electron inertial length is approximately of the order of a tenth of a metre and the ion inertial length of the order of ten metres. This model description is shown in Figure 5.4.

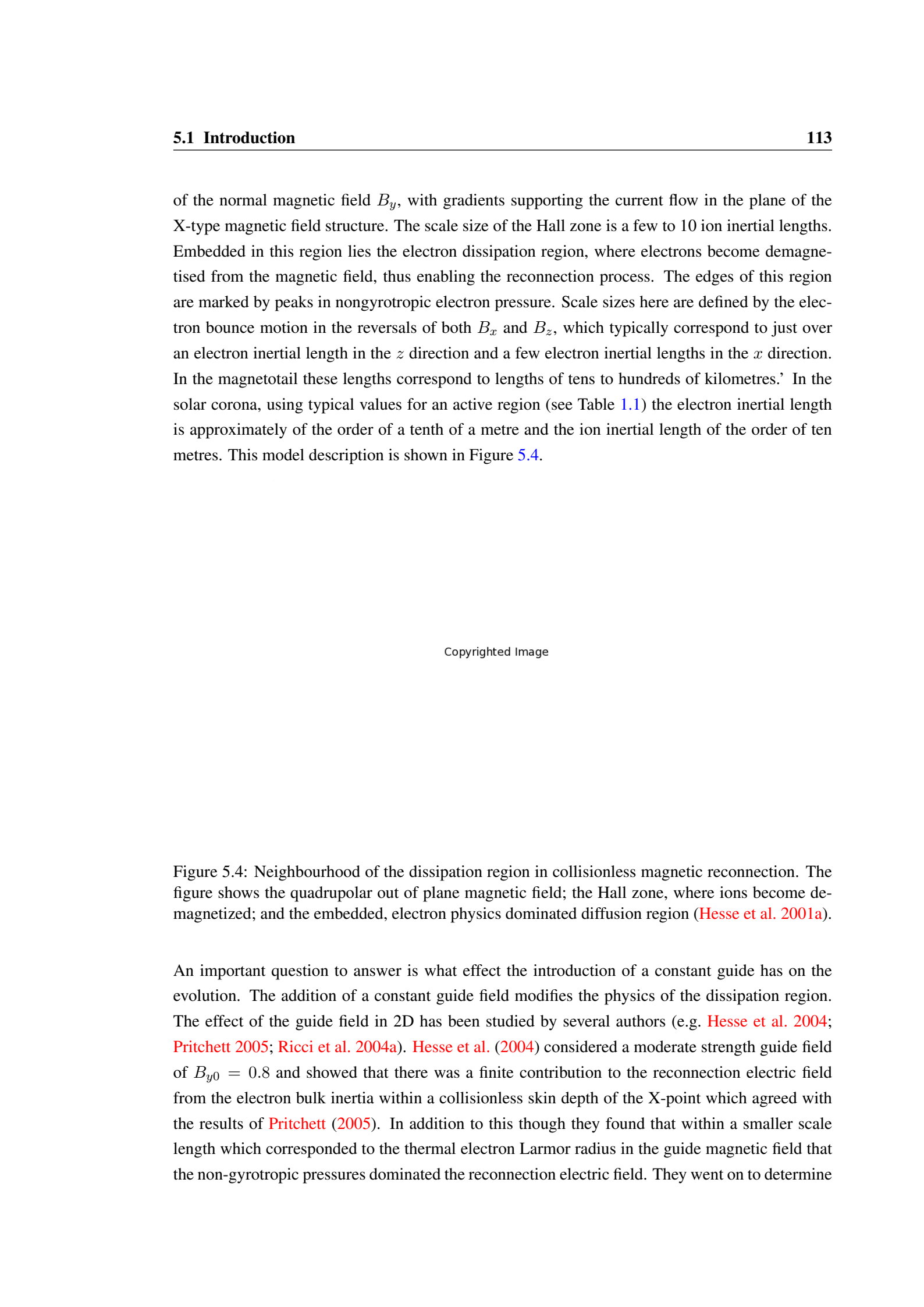

Figure 5.4: Neighbourhood of the dissipation region in collisionless magnetic reconnection. The figure shows the quadrupolar out of plane magnetic field; the Hall zone, where ions become demagnetized; and the embedded, electron physics dominated diffusion region (Hesse et al. 2001a).

An important question to answer is what effect the introduction of a constant guide has on the evolution. The addition of a constant guide field modifies the physics of the dissipation region. The effect of the guide field in 2D has been studied by several authors (e.g. Hesse et al. 2004; Pritchett 2005; Ricci et al. 2004a). Hesse et al. (2004) considered a moderate strength guide field of $B_{y0} = 0.8$ and showed that there was a finite contribution to the reconnection electric field from the electron bulk inertia within a collisionless skin depth of the X-point which agreed with the results of Pritchett (2005). In addition to this though they found that within a smaller scale length which corresponded to the thermal electron Larmor radius in the guide magnetic field that the non-gyrotropic pressures dominated the reconnection electric field. They went on to determine

approximations for the off-diagonal components of the electron pressure tensor $P_{xy,e}$ and $P_{yz,e}$ and found that for the $P_{yz,e}$ component of the electron pressure tensor that gradients of the heat flux tensor were important. Ricci et al. (2004a) have shown that even in the case of a guide field of $B_{y0} = 5.0$ the dominant non-ideal term in the dissipation region is due to the electron pressure terms.

The introduction of a guide field has the effect of reducing the reconnection rate. This effect has been shown in both 2D (e.g. Pritchett 2001; Ricci et al. 2004a), and 3D (e.g. Pritchett and Coroniti 2004) for simulations starting from a Harris sheet configuration. The reconnection rate is slowed significantly if $B_{y0} \gg B_0$ where B_0 is the asymptotic value of the x component of the magnetic field. Examples of the time history of the reconnected flux for different strengths of guide field where the initial configuration is identical to that of the GEM challenge (Birn et al. 2001) is given in the paper by Pritchett (2001) and is shown in Figure(5.5). The gradients of the reconnected flux correspond to the reconnection rate. It is therefore clear to see that the effect of the guide field is to reduce the reconnection rate.

Figure 5.5: The time history of the reconnected flux $\Delta\psi$ for three different values of the uniform initial B_{0y} (Pritchett 2001).

In the zero guide field case the ions and electrons flow towards the X-point along the z direction due to an $\mathbf{E} \times \mathbf{B}$ drift. They are accelerated in the y direction via the reconnection electric field and flow outwards along the x diection with the electrons reaching super Alfvénic velocities (e.g. Hesse et al. 1999, 2001a; Ricci et al. 2004a). The addition of the guide field destroys the symmetry of this flow pattern. The electrons and ions can now drift in directions that were not possible in the zero guide field case. The electrons have strong flows along the separatrices, with the flow being inwards in the first and third quadrants and outwards in the second and fourth quadrants

(Pritchett 2005; Ricci et al. 2004a). The ions are diverted in an antisymmetric way with respect to the $x = 0$ line when they approach the X-point with their outflow motion primarily along x (Ricci et al. 2004a). The guide field also reduces the size of the outflow region.

The quadrupolar out of the plane magnetic field is changed by the addition of a guide field. In the cases of guide fields of the order $B_{y0} \sim B_0$ the out of the plane component of the magnetic field still has a quadrupolelike structure imposed on top of the guide magnetic field which is strongly distorted from the zero guide field case (Hesse et al. 2004; Ricci et al. 2004a). In the case of guide fields where $B_{y0} \gg B_0$ the quadrupolar structure of the out of the plane magnetic field is completely removed (Rogers et al. 2003; Ricci et al. 2004a). The decoupling of ions and electrons is still present which is evident in the fact that the maximum in plane electron flow is of the order of several times the Alfvén speed whilst the maximum in plane ion flow is significantly slower (Pritchett 2005).

In the zero guide field case it is the whistler dynamics that is important for fast reconnection. In the strong guide field (low plasma β) case it has been argued that the dynamics are dominated by kinetic Alfvén waves (KAW's) which has a dispersion similar to the dispersion of the whistler wave ($\omega \sim k^2$) and are characterised by a scale length of the gyroradius rather than the ion inertial length (Pritchett 2005; Ricci et al. 2004a). The characteristic signature of the KAW is a quadrupolar structure of the electron density near to the X-point which has been shown by Ricci et al. (2004a).

An important question to try and answer is whether the properties of 2D reconnection carry over to 3D reconnection. In the paper by Hesse et al. (2001b) they carried out two simulations. The first run started from a Harris sheet equilibrium with a perturbation to the magnetic field similar to that of the GEM challenge (Birn et al. 2001) and the second run started from a Harris sheet with no initial perturbation specified. They showed that reconnection starting from a case with an imposed perurbation remained essentially 2D throughout the reconnection process whilst the run with no perturbation initially formed patchy areas of reconnection but at later times these patches merged to form a much larger reconnection channel. They also confirmed for the unperturbed run that the reconnection electric field is again due to gradients of off-diagonal components of the electron pressure tensor. The quadrupolar structure of the out of the plane magnetic field component was also seen. In both simulation runs a lower hybrid drift instability also developed due to the density gradient at the edge of the current sheet layer.

A similar study was performed by Pritchett and Coroniti (2004) in 3D starting from the GEM challenge configuration with varying strengths of guide field. They found similar conclusions to the 2D case that the effect of the guide field is to reduce the reconnection rate. A significant reduction in the reconnection rate was observed for $B_{y0} \gg B_0$. The quadrupolar out of the plane magnetic field component of the zero guide field case was replaced by an out of the plane

magnetic field that was enhanced between the separatrices and reduced outside of the separatrices. The electron flows were strongest along the separatrices in the lower left and upper right quadrants which is consistent with the 2D case. In the cases with $B_{y0} \gg B_0$ the flows away from the X-line were reduced, and thus the Hall currents were reduced. This is consistent with a reduced reconnection rate for the strong guide field cases.

The dominant mechanism for breaking the frozen in constraint at the X-line was found to be due to the divergence of the electron pressure tensor which is consistent with the results of 2D guide field reconnection. Hesse et al. (2005) carried out a 3D simulation starting from an approximate force-free Harris sheet equilibrium with a guide field of $B_{y0} = 0.8$. An approximate force-free Harris sheet was used to avoid the unrealistic growth of the lower hybrid drift instability (LHDI) and drift kink instability (DKI) for the mass ratio considered. An initial perturbation similar to that of the GEM challenge was added. They showed that the dominant contribution to the reconnection electric field came from gradients of the $P_{yz,e}$ term of the electron pressure tensor with a characteristic scale length of the thermal electron Larmor radius, consistent with 2D studies (Hesse et al. 2004). In Sec. 3.7 of Chap. 3 the first self consistent non-linear Vlasov-Maxwell equilibrium for the force-free Harris sheet was shown. This equilbrium could be used as an initial configuration for studies of 3D reconnection where the uniform initial density should suppress the growth of the LHDI. This equilibrium would also be most appropriate for studying magnetic reconnection in the solar corona.

In the studies of the GEM challenge the magnetic field configuration is initialised with a large magnetic island amplitude. This is done so that the non-linear phase of magnetic reconnection can be studied i.e. it does not address the important question of reconnection onset. The onset of reconnection is thought to be due to the development of a collisionless tearing mode. The collisionless tearing mode has been shown to saturate when the island width approaches the electron skin depth (Biskamp 2000). This island width is too small to introduce the decoupling of the electrons and ions which is a characteristic feature of fast collisionless reconnection (e.g. Hesse et al. 2001a; Birn et al. 2001; Shay et al. 2001). Therefore without the inclusion of a significant initial perturbation it is questionable that the collisonless tearing mode ever reaches large enough amplitudes for fast reconnection to occur. This has led to a large number of authors to consider the effect of current aligned microinstabilities which may have the effect of coupling to the tearing mode and enhancing its growth rate (e.g. Büchner and Kuska 1999; Scholer et al. 2003; Lapenta 2003; Daughton et al. 2004; Karimabadi et al. 2004; Ricci et al. 2004b, 2005; Silin and Büchner 2003, 2005). These current aligned instabilities are particularly important for 3D in which the full range of wave numbers (k_x, k_y, k_z) are included.

It has been found that the lower hybrid drift instability (LHDI) may play a large role in the onset of fast collisionless reconnection (e.g. Lapenta 2003; Karimabadi et al. 2004; Ricci et al. 2004b, 2005; Scholer et al. 2003). The LHDI has been shown to heat the electrons preferentially in the

perpendicular direction ($T_{e\perp}/T_{i\parallel} > 1$) which is known to significantly increase the growth rate of the tearing mode (e.g. Ricci et al. 2004b, 2005; Karimabadi et al. 2004). Ricci et al. (2005) showed that the LHDI in thin current sheets of the order of the ion inertial length leads to a thinning of the current sheet and an increased current density perpendicular to the magnetic field which can enhance the growth of the tearing mode. In the case of larger current sheet widths the LHDI led to a bifurcation of the current sheet. Current sheet thinning due to the LHDI has also been reported by Scholer et al. (2003). The same authors have also shown the development of the drift kink instability (DKI) and a sausage mode for a 3D simulation with a mass ratio $m_i/m_e = 64$. At the onset of reconnection the DKI is dominant. In contrast they showed that for a higher mass ratio of $m_i/m_e = 150$ that reconnection starts before any kinking is observed and it is the thinning of the current sheet due to LHDI that causes the onset of reconnection. The reduced growth rate of the DKI at high mass ratio is in agreement with the linear analysis of the unstable modes of a Harris sheet given by Daughton (1999). The LHDI has also been shown to introduce velocity shear (Lapenta 2003; Ricci et al. 2005). The velocity shear can lead to the development of a Kelvin Helmholtz instability (KHI) which can cause compression and rarefaction of the magnetic fields which may lead to the onset of reconnection (Lapenta 2003).

Silin and Büchner (2005) carried out fully 3D simulations with a mass ratio of $m_i/m_e = 32$ using a Vlasov-code. They are argued that the lower hybrid waves that occur at the edge of the current layer due to pressure gradients in the plasma can interact with the ion flow via inverse Landau damping leading to the fast growth of an instability that would affect the entire current sheet. They define this as the drift resonant instability (DRI). This drift resonant instability will have a wavelength and frequency of the order of typical lower hybrid scales $\lambda \sim (d_i d_e)^{1/2}$ and $\omega \sim (\Omega_{0i}\Omega_{0e})^{1/2}$ where d_i and d_e are the ion and electron skin depths and Ω_{0i} and Ω_{0e} are the ion and electron cyclotron frequencies in the asymptotic magnetic field. The effect of adding a guide field on this instability is to slow its growth. The guide field causes the wave modes to now propagate obliquely to the current direction and as a consequence this reduces the number of ions that can amplify the lower hybrid drift waves due to inverse Landau damping.

One of the major aims of this work was to understand and investigate further the magnetic reconnection process for plasmas starting from different initial conditions. In particular to investigate the role of the guide field compared to using a force-free equilibrium as an initial condition. The magnetic fields for example in the corona of the Sun can be descibed as approximately force free ($\mathbf{j} \times \mathbf{B} = \mathbf{0}$), where the plasma β is low, and therefore it is of interest to investigate collisionless reconnection starting from a force-free initial state. As shown in Chap. 3 a linear force-free Vlasov-Maxwell equilibrium can be given by a special case of an anisotropic bi-Maxwellian distribution function (Sestero 1967; Bobrova and Syrovatskiĭ 1979; Correa-Restrepo and Pfirsch 1993; Bobrova et al. 2001) where at least one plasma species must have a temperature anisotropy. Several authors have used this equilibrium as an initial state to carry out 2.5D and 3D fully elec-

tromagnetic PIC simulations (Bobrova et al. 2001; Nishimura et al. 2003; Li et al. 2003; Sakai and Matsuo 2004; Bowers and Li 2007).

The linear force-free state is unstable to a tearing mode instability at resonant layers where $\mathbf{k} \cdot \mathbf{B} = 0$ (Bobrova et al. 2001; Nishimura et al. 2003; Li et al. 2003). Li et al. (2003) have shown that the linear growth rate for the tearing mode is,

$$\gamma = \frac{1}{\pi^{1/2}} \frac{1 - \cos(\sqrt{1-\kappa^2}\pi)}{\sin(\sqrt{1-\kappa^2}\pi)} \kappa \sqrt{1-\kappa^2} (d_e \alpha)^2 \alpha v_{te}, \tag{5.6}$$

where $\alpha = 2\pi/L_z$, L_z is the length of the simulation box in the z direction, $\kappa = k/\alpha$ is the wavenumber divided by the pitch of the magnetic field, $d_e = c/\omega_{pe}$ is the electron inertial length, $k = 2\pi n_x/L_x$ is the wave number in the x direction where L_x is the length of the simulation box in the x direction and v_{te} is the electron thermal speed. Therefore, for wavelengths shorter than the shear length $2\pi/\alpha$ or $L_x < L_z$ the factor $1 - \kappa^2$ is less than zero and there is no growth. The effect of this tearing mode has been shown to result in a global reorganisation of the initial magnetic field configuration.

Nishimura et al. (2003) carried out several runs using a 2.5D fully electromagnetic PIC code. They imposed a temperature anisotropy only in the electrons varying the box size, the pitch of the magnetic field α, the plasma β, the temperature anisotropy $T_{e\perp}/T_{e\parallel}$ and the ratio of the electron drift speed to electron thermal speed V_{de}/v_{te}. In addition to the tearing mode they found that in the initial phase of each simulation run a Buneman type electrostatic instability could be excited if the ratio of the electron drift velocity to the electron thermal velocity exceeded the threshold value of 1.44. This instability can lead to enhanced growth of the tearing mode at later times as it can lead to the formation of a new configuration with inhomogeneous electron density and temperature which is in direct contrast to the initial condition which is homogeneous in all scalar plasma parameters.

Li et al. (2003) also carried out 2.5D simulations where only a temperature anisotropy was imposed on the electrons and parameters were chosen such that the initial state was stable to the electrostatic Buneman type instability. The box size was chosen so that it was only unstable to the $n_x = 1$ mode of the tearing mode instability. They chose a mass ratio of $m_i/m_e = 100$. In agreement with the results from Nishimura et al. (2003) they found that following the linear growth of the tearing mode there was a period of magnetic reconnection followed by a saturation phase where the magnetic field organises itself into a new quasi steady state going from having only x and y components in the initial state to mainly having only y and z components in the final state. They defined the duration of reconnection to be the time it takes for the island width to grow and 'touch' the neighbouring reconnection layer so that the mutual interaction between them becomes dominant. Investigation into the dissipation mechanism around the X-point confirmed that the electric field was partially supported by gradients of the off-diagonal terms of the pressure

tensor which is in agreement with previous studies of collisionless reconnection (e.g. Hesse et al. 2001a, 2004, 2005; Pritchett 2001; Ricci et al. 2004a). They also found the scale separation of the dissipation region which is also reported in Birn et al. (2001) where the electron diffusion region was found to be of the order of 0.2 ion inertial lengths whereas the ion region had a width of about 0.8 ion inertial lengths.

Bowers and Li (2007) carried out a 3D PIC simulation starting from the linear force-free equilibrium which has been discussed by Sestero (1967); Bobrova and Syrovatskiĭ (1979); Correa-Restrepo and Pfirsch (1993); Bobrova et al. (2001) with a mass ratio of 100. The evolution was similar to the 2D case. The evolution consisted of a linear growth stage, followed by a shorter reconnection stage, with finally an extended saturation stage. During the growth of the tearing mode the current density becomes enhanced at the X-points. In the saturation stage the reconnection caused a complete reorganistion of the field from a (B_x, B_y) magnetic field configuration to a (B_y, B_z) magnetic field configuration. They showed that the electron pressure terms dominate the reconnection electric field which is in agreement with 2.5D studies starting from the same linear force-free initial condition (Li et al. 2003).

The aim of this work is to investigate the morphology of the off-diagonal components of the electron pressure tensor as one makes the transition from an anti-parallel magnetic field through to a strong guide field case. For comparison purposes in Sec 5.4 the evolution of the electron pressure tensor components are shown for the Harris sheet case with varying strengths of guide field. These will indicate the expected structures of the off-diagonal components of the electron pressure tensor during the reconnection process and will be important for comparison purposes. Detailed studies of the structure of the off diagonal components of the electron pressure tensor for the Harris sheet cases have already been carried out (Hesse et al. 1999, 2002, 2004). It is found that in the anti-parallel case the structure of the pressure tensor components in the vicinity of the X-point have a length scale determined by the electron bounce motion (Hesse et al. 1999) whilst in the strong guide field case this scale reduces down to the electron Larmor radius in the guide magnetic field (Hesse et al. 2004, 2005).

In Sec. 5.5 this transition is investigated using the equilibria resulting from the anisotropic bi-Maxwellian distribution function introduced in Sec. 3.4 of Chap. 3 as initial conditions in 2.5D PIC simulations of magnetic reconnection. These are investigated for equal mass ratio. In all these equilibria it is necessary to have a temperature anisotropy. An anti-parallel periodic equilibrium is investigated with various strengths of guide field added in each case, ranging from $B_{y0} = 0$ through to $B_{y0} = B_0$ where B_0 is the amplitude of the anti-parallel component of the magnetic field. These results are compared to the structure of the off-diagonal components of the electron pressure tensor for a simulation starting from a self-consistent linear force-free equilibrium. In Sec. 5.6 simulations starting from a double Harris sheet with a range of guide fields are also shown as another example of magnetic reconnection starting from a periodic equilibrium magnetic field.

These are also investigated for equal mass ratio. The anisotropic bi-Maxwellian simulations are extended to consider a mass ratio $m_i/m_e = 25$ in Sec. 5.7.

Finally in Sec. 5.8 two simulation runs are compared starting from the self-consistent force-free Harris sheet equilibrium given in Sec. 3.7 of Chap 3 for the mass ratios $m_i/m_e = 1$ and $m_i/m_e = 9$.

5.2 The Reconnection Electric Field

The reconnection electric field E_y in the vicinity of the X-point can be written approximately as

$$E_y \approx -\frac{m_e}{e}\left(u_{x,e}\frac{\partial u_{y,e}}{\partial x} + u_{z,e}\frac{\partial u_{y,e}}{\partial z}\right) - \frac{1}{n_e e}\left(\frac{\partial P_{xy,e}}{\partial x} + \frac{\partial P_{yz,e}}{\partial z}\right) - \left(u_{z,e}B_x - u_{x,e}B_z\right). \tag{5.7}$$

It is found that the dominant contribution to this electric field comes from gradients of the off-diagonal components of the electron pressure tensor $P_{xy,e}$ and $P_{yz,e}$. The focus of this study is therefore to investigate the morphology of these off-diagonal components of the pressure tensors as the transition is made from a weak guide field to a strong guide field and also to compare this to simulations starting from self consistent force-free equilibria.

5.3 The Simulation Code

In all the examples shown the 2.5D, fully electromagnetic particle-in-cell code developed by Michael Hesse (Hesse et al. 1999) has been used and is described in Chap. 4. The scheme is based on the Buneman layout of the currents and fields on a rectangular grid (e.g. Villasenor and Buneman 1992). Particles are integrated by a second order, implicit leapfrog scheme and densities and fluxes are accumulated on the grid using a rectangular particle shape function. The electromagnetic fields are integrated using an implicit method which avoids the Courant constraint on the propagation of light waves. Charge conservation is guaranteed by a Langdon-Marder type (Marder 1987; Langdon 1992) correction to the electric field.

5.4 Harris Sheet Simulations ($m_i/m_e = 1$)

The Harris sheet (Harris 1962) is well known and understood as the majority of studies of collisionless reconnection start from a Harris sheet, or a Harris sheet with a constant guide field (e.g.

Hesse et al. 2001a, 2004; Pritchett 2001; Pritchett and Coroniti 2004; Birn and Hesse 2001; Ricci et al. 2004a). The major aim of this work was to investigate the structure of the diffusion region for different initial conditions and to compare how the structure of the off-diagonal components of the electron pressure tensor changes as the guide field is varied. By showing the changing structures of the off diagonal components of the pressure tensors for the Harris sheet case as one moves from a weak guide field through to a strong guide field this allows a direct comparison to the results from the simulations runs starting from different initial conditions.

The reconnection rates of each simulation run were also investigated. It is a well known trend that for the Harris sheet case the effect of increasing the strength of the constant guide field slows the reconnection rate down. This behaviour for the Harris sheet is shown and is used to compare to simulation results starting from different initial conditions.

In the following simulation results, the ion to electron mass ratio is equal to one ($m_i/m_e = 1$). Lengths are normalized to the ion inertial length c/ω_{pi} and the number density is normalised to a value n_0. Times are normalised to the inverse of the ion cyclotron frequency $\Omega_i = eB_0/m_i$. The magnetic field is normalised to the value B_0, the amplitude of the initial magnetic field. The system dimensions are $L_x = 19.34\, c/\omega_{pi}$ and $L_z = 4.83\, c/\omega_{pi}$ where L_x and L_z are the half lengths of the box in the x and z directions, with a grid that is 140×70 in the x and z directions. A time step $\omega_{pe}\Delta t = 1$ is used. The ratio ω_{pe}/Ω_e is set to a numerical value of 5.

The initial configuration is a Harris sheet. The magnetic field is given by

$$B_x = \tanh\left(\frac{z}{L}\right), \tag{5.8}$$

where $L = 1.2$. The electron and ion densities are given by

$$n = \frac{1}{\cosh^2\left(\frac{z}{L}\right)}. \tag{5.9}$$

For each simulation run a perturbation of the form

$$B_{xp} = -a_0 x_m \frac{\pi}{2L_z} \exp\left(-\frac{x^2}{2x_m^2} + 0.5\right) \sin\left(\frac{\pi z}{2L_z}\right), \tag{5.10}$$

$$B_{zp} = a_0 \frac{x}{x_m} \exp\left(-\frac{x^2}{2x_m^2} + 0.5\right) \cos\left(\frac{\pi z}{2L_z}\right), \tag{5.11}$$

is also added where $a_0 = 0.1$ and $x_m = L_z/2$. This gives an X-point type reconnection site at the centre of the box. This is done so that the non-linear phase of magnetic reconnection can be studied. The question of reconnection onset is not addressed.

There are two particle populations. The foreground population consists of the first set of ions and electrons which establish the equilibrium pressures and currents. In the simulation runs tempera-

tures are set such that $T_i + T_e = 0.5$, with $T_e/T_i = 1$. The second population consists of the second set of ions and electrons and constitutes a constant background density $n_b = 0.2$. The background temperatures are identical to the foreground population $T_e + T_i = 0.5$, with $T_e/T_i = 1.0$. The simulation run used 2×10^7 ions and electrons each for the foreground and 3×10^7 ions and electrons for the background.

Periodic boundary conditions are employed at $x = -L_x$ and $x = L_x$. Particles are specularly reflected at $z = -L_z$ and $z = L_z$. The strength of the constant guide field $B_y = B_{y0}$ is varied from $B_{y0} = 0.0$ through to $B_{y0} = 1.0$ to show the effect of adding a constant guide field in the y direction.

Figure 5.6 shows the initial configuration for the Harris sheet at $t = 0$. A filled contour plot of the magnetic field component B_x is shown in Figure 5.6(a) with a line plot of the magnetic field profile plotted along z for $x = 0$ shown in Figure 5.6(b). Figure 5.6(c) is a filled contour plot of the y component of the current density with contours of the flux function overplotted showing the magnetic field lines. It is clear to see the hyperbolic tangent profile of B_x and also the current sheet structure of j_y with the X-point introduced by the perturbation to the equilibrium magnetic field. A range of constant guide fields B_{y0} are added to this initial configuration.

Figures 5.7 - 5.9 show the evolution of the magnetic field for three different runs with the y component of the current density colour coded. Figure 5.7 shows the evolution for the initial configuration with zero guide field. Figure 5.8 shows the evolution for the initial configuration with a guide field of value $B_{y0} = 0.5$ and Figure 5.9 shows the evolution for the initial configuration with a guide field of value $B_{y0} = 1.0$. Movies of the evolution for each case can be found on the CD which is attached to this thesis (see Appendix B). These figures show how magnetic reconnection proceeds and leads to large changes in the magnetic field structure. In the central X-point region the current density and particle density are strongly reduced. The reduction of the current density at the X-point as reconnection proceeds for all cases can be seen in Figures 5.7 - 5.9. In the zero guide field case, Figure 5.7 shows that the current density is enhanced and localised in small regions adjacent to the X-point along the $z = 0$ line. In the strong guide field case $B_{y0} = 1.0$ the current density is distributed around the O-points. Eventually in all cases reconnection slows due to the build up of magnetic flux in the magnetic islands which causes a magnetic pressure gradient which reduces the pulling of the magnetic field lines away for the reconnection site.

Figure 5.11 shows line plots along x for $z = 0$ of the electron number density n_e (blue lines) and the y component of the current density (red lines) for the cases with zero guide field, $B_{y0} = 0.5$ and $B_{y0} = 1.0$ at the time of maximum reconnection rate. These can be compared to the electron number density and y component of the current density at $t = 0$ for each run which are shown in Figure 5.10 plotted along x for $z = 0$. In all three cases Figures 5.11(a), 5.11(c) and 5.11(e) show a significant density depletion around the X-point. Figures 5.11(b), 5.11(d) and 5.11(f) show that

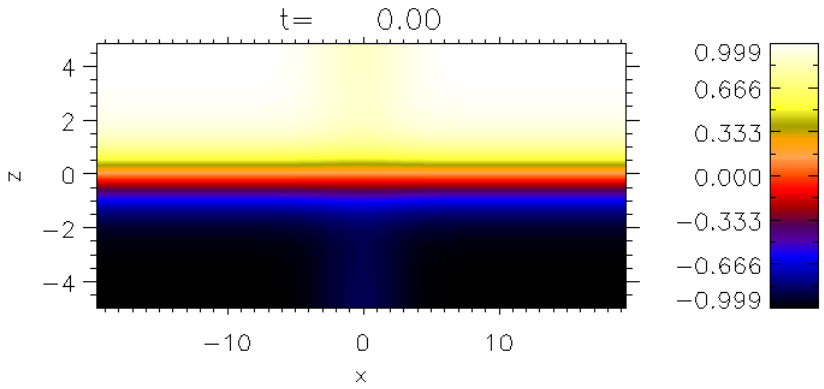

(a)

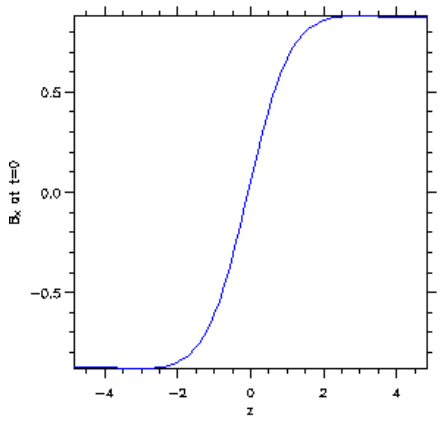

(b)

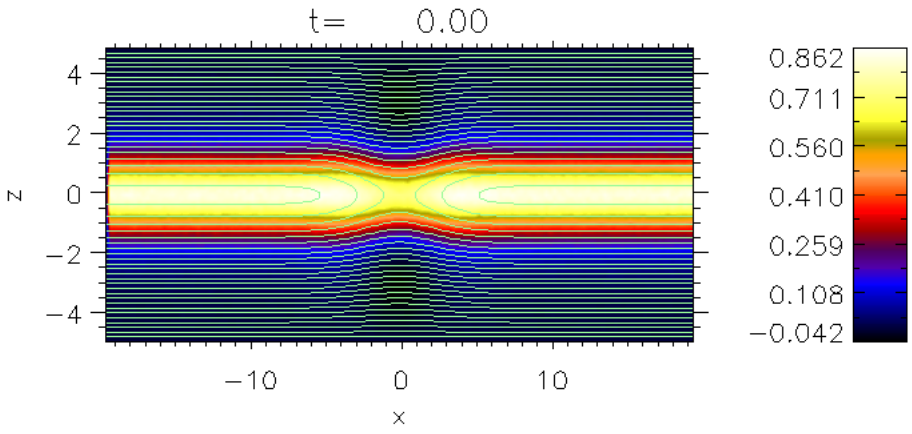

(c)

Figure 5.6: Plots showing the initial configuration for the Harris sheet. Figure 5.6(a) shows a colour contour plot of B_x and Figure 5.6(b) shows a line plot of the profile of B_x along z for $x = 0$. Figure 5.6(c) shows a filled contour plot of the y component of the current density with magnetic field lines corresponding to contours of the flux function overplotted.

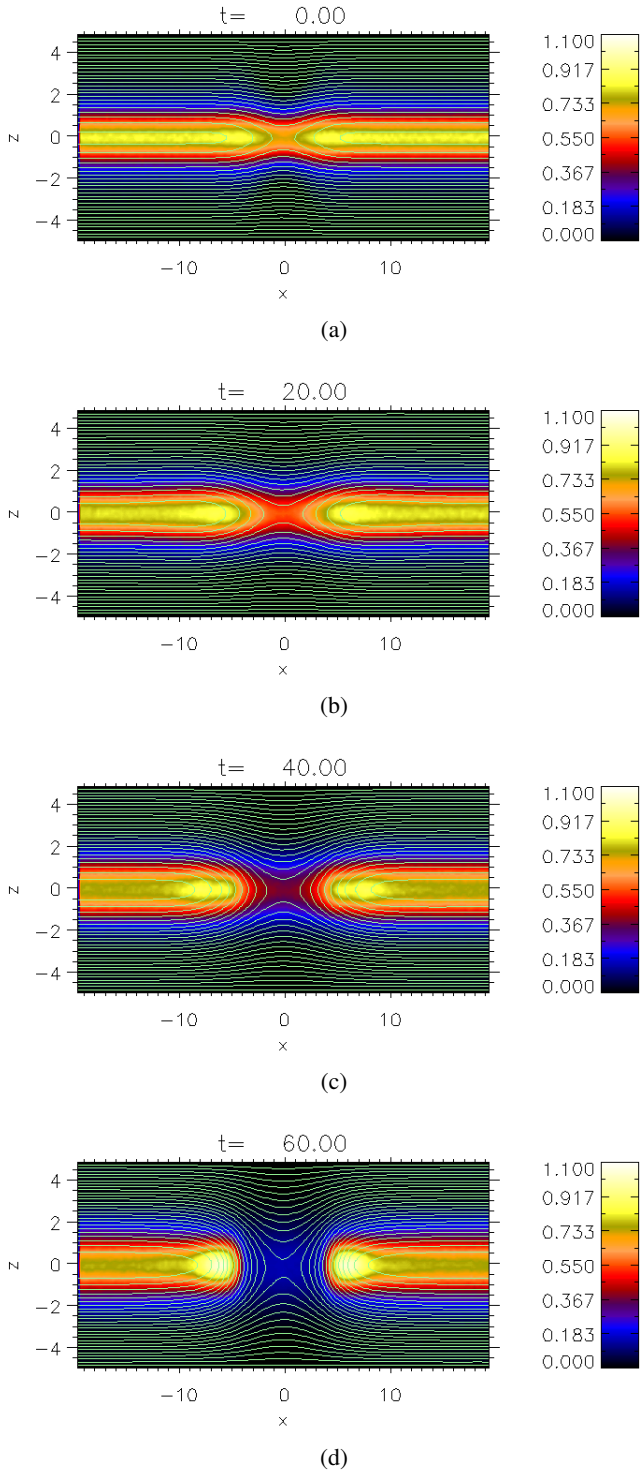

(a)

(b)

(c)

(d)

Figure 5.7: Plots of the y component of the current density with contours of the flux function overplotted for the Harris sheet run with zero guide field. The plots correspond to the different times (a) $t = 0$, (b) $t = 20$, (c) $t = 40$ and (d) $t = 60$.

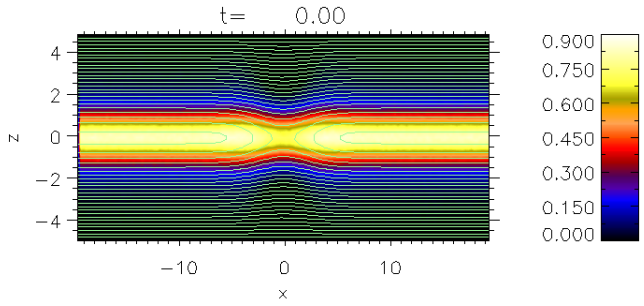

(a)

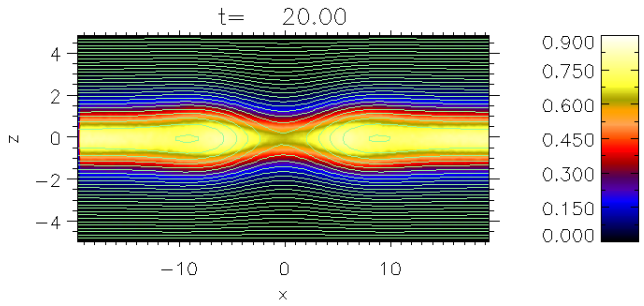

(b)

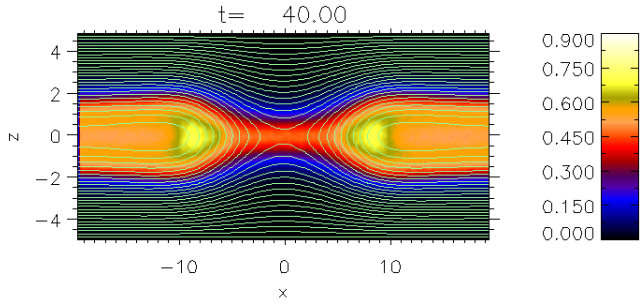

(c)

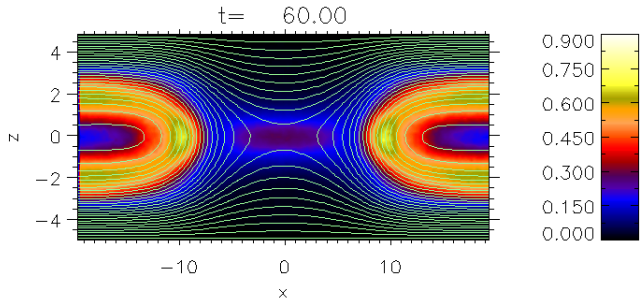

(d)

Figure 5.8: Plots of the y component of the current density with contours of the flux function overplotted for the Harris sheet run with a guide field of value $B_{y0} = 0.5$. The plots correspond to the different times (a) $t = 0$, (b) $t = 20$, (c) $t = 40$ and (d) $t = 60$.

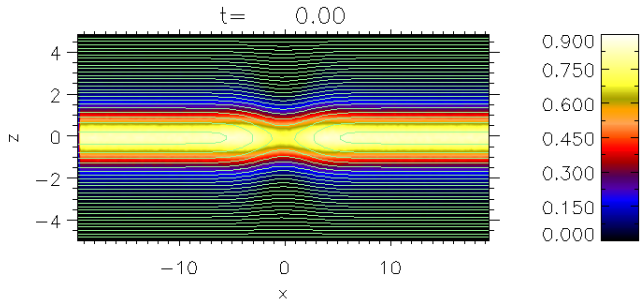

(a)

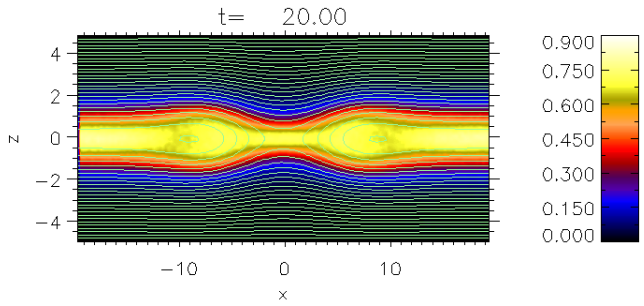

(b)

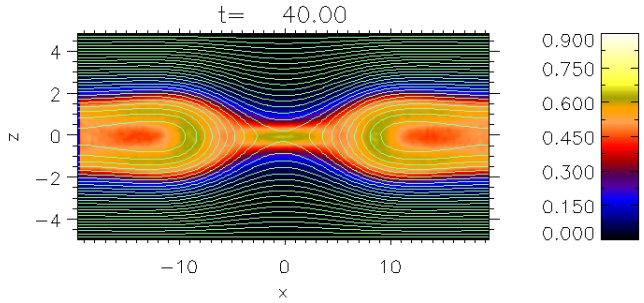

(c)

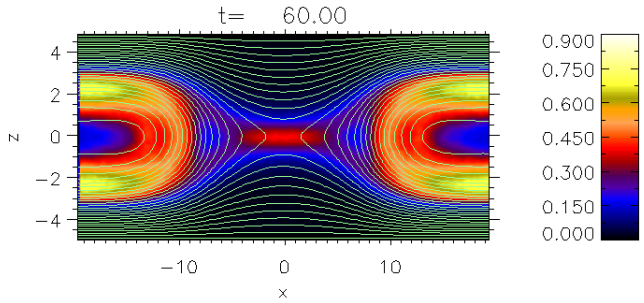

(d)

Figure 5.9: Plots of the y component of the current density with contours of the flux function overplotted for the Harris sheet run with a guide field of value $B_{y0} = 1.0$. The plots correspond to the different times (a) $t = 0$, (b) $t = 20$, (c) $t = 40$ and (d) $t = 60$.

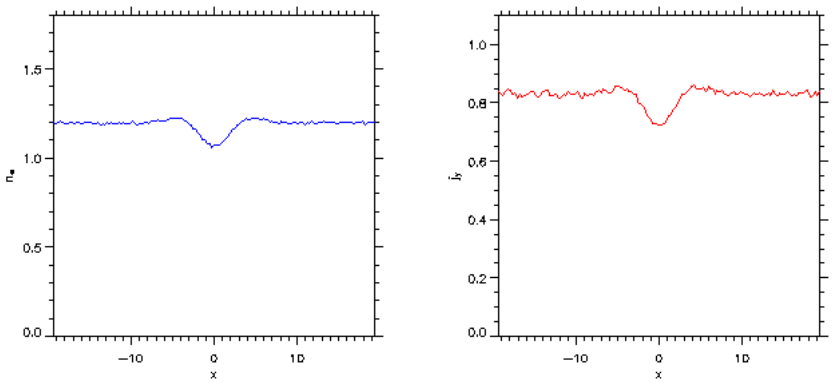

(a) (b)

Figure 5.10: Line plots of the electron number density n_e (blue line) and the y component of the current density (red line) plotted along x for $z = 0$ at $t = 0$.

in all cases the current density is significantly reduced at the X-point.

In the zero guide field case Figure 5.11(b) shows that in regions adjacent to the X-point the current is enhanced from its initial value at a distance $|x| \approx 7\, c/\omega_{pi}$ either side of the X-point. In the guide field case $B_{y0} = 0.5$, Figure 5.11(d) shows that the current density has peaks along the $z = 0$ line in the regions adjacent to the X-point and that the value of the current density at these peaks has a maximum value which is slightly reduced from the initial maximum value of the current density. The peaks of the current density along $z = 0$ are located adjacent to the X-point at $|x| \approx 9 - 10\, c/\omega_{pi}$ either side of the X-point. The current density at the X-point is also slightly larger than in the zero guide field case whilst still reduced from its initial value. Figure 5.11(f) shows that for the case with a guide field $B_{y0} = B_0$ the current density is significantly reduced from its initial value in the regions adjacent to the X-point along the $z = 0$ line. The peaks of the current density along $z = 0$ are though, still located adjacent to the X-point, at $|x| \approx 12\, c/\omega_{pi}$ either side of the X-point. The current density is larger at the X-point than in the zero guide field and $B_{y0} = 0.5$ cases, whilst also still reduced from its initial value. The value of the current density at the X-point in the zero guide field case has the value of ≈ 0.25 in comparison to the guide field $B_{y0} = 1.0$ case where the current density has a value of ≈ 0.5 at the X-point.

A comparison of the evolution of the runs is given in figure 5.12. This shows two plots, one for the reconnected flux for each case plotted using different colours to represent the strength of the guide field in each run where the reconnected flux is defined as

$$F(t) = \int_{B_z>0} dx\, B_z(z = 0), \tag{5.12}$$

and the other shows the reconnection rate where the reconnection rate is found by taking the

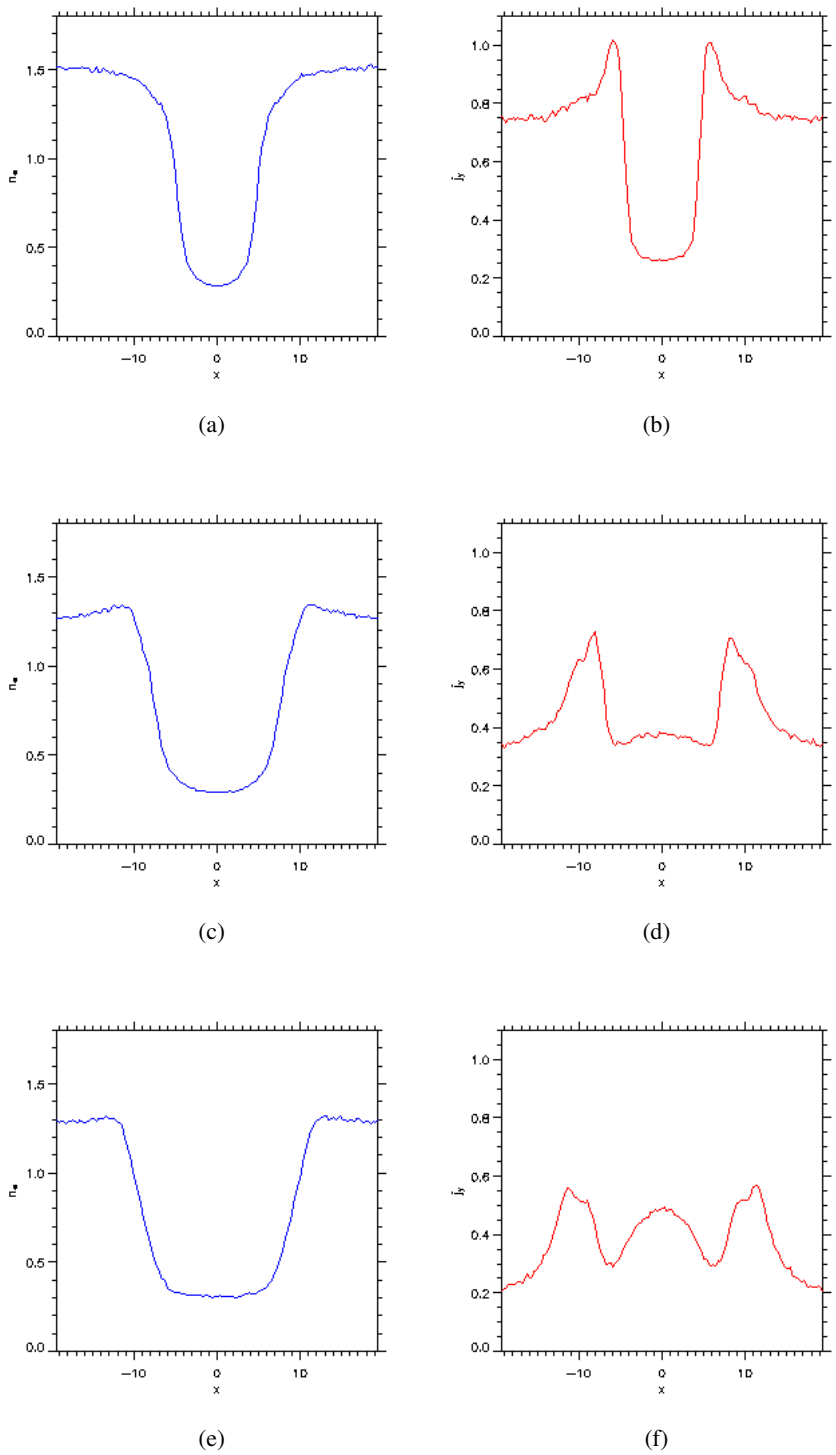

(a) (b)

(c) (d)

(e) (f)

Figure 5.11: Line plots of the electron number density n_e (blue lines) and the y component of the current density (red lines) plotted along x for $z = 0$ at the time of maximum reconnection rate for the Harris sheet runs with a guide field of value (a),(b) $B_{y0} = 0.0$ ($t = 50$) (c),(d) $B_{y0} = 0.5$ ($t = 50$), (e),(f) $B_{y0} = 1.0$ ($t = 52$).

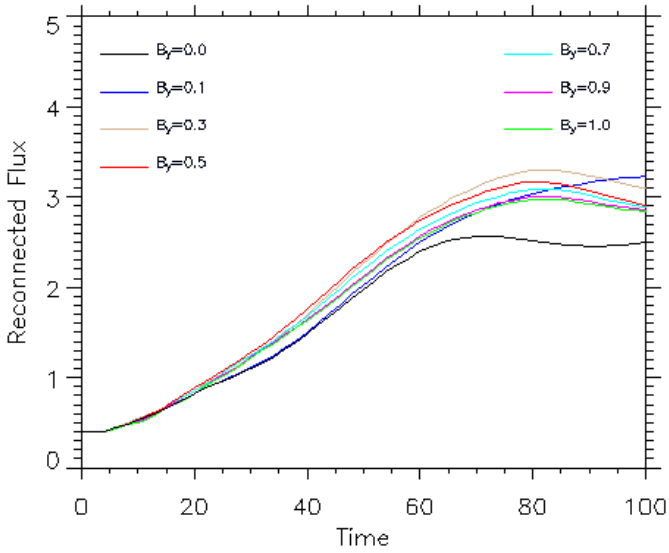

(a)

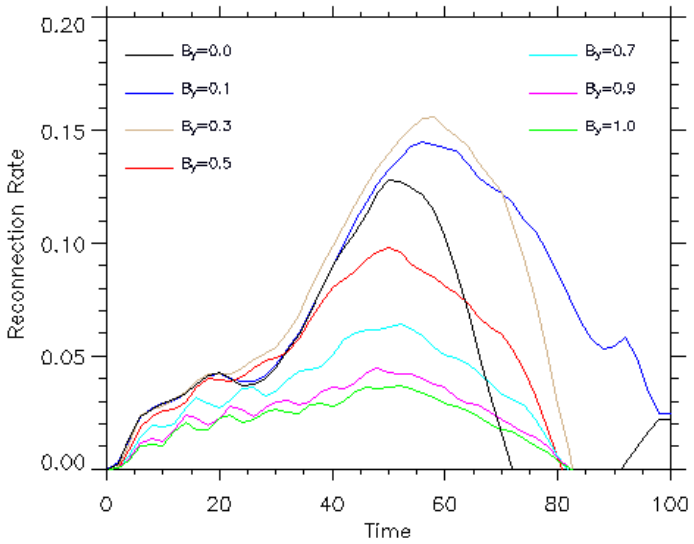

(b)

Figure 5.12: Figures showing the evolution of the simulations with varying strengths of guide field using the Harris sheet as an initial configuration. The reconnected flux is shown in Figure 5.12(a) and the corresponding reconnection rates in Figure 5.12(b). The colours represent the different strengths of the guide field in the initial configuration.

derivative of the reconnected flux and normalising it against the maximum Alfvén speed at each timestep.

Examining the evolution of the Harris sheet runs you can clearly see from the plots of the reconnection rate shown in Figure 5.12(b) that the reconnection rate reduces significantly when the guide field is of the order B_0. This is in agreement with previous studies that show that the reconnection rate is reduced once the guide field is large enough to significantly change the magnetic pressure in the system (e.g. Pritchett 2001; Ricci et al. 2004a).

5.4.1 The Structure of the Diffusion Region

In this section the morphology of the off-diagonal components of the pressure tensor components are shown for the Harris sheet cases. It is also shown how the different contributions in equation (5.7) make up the reconnection electric field in the vicinity of the X-point.

Figure 5.13 shows filled contour plots of the y component of the current density at the time of maximum reconnection rate for each simulation run. The time of maximum reconnection rate corresponds to the peaks of the graphs for each case shown in Figure 5.12(b). Figure 5.14 are filled contour plots of the y component of the electric field at the time of maximum reconnection rate. The electric field in each case has been averaged for $2\Omega_i^{-1}$ either side of the time of maximum reconnection rate. This shows how magnetic reconnection generates a strong y component of the electric field in the vicinity of the X-Point. The guide fields $B_{y0} = 0.0, 0.1, 0.3, 0.5, 0.7, 0.9, 1.0$ have been used. In all the figures x_0 refers to the approximate position along x of the position of the X-point. In all cases the position of the X-point along z is approximately at $z = 0$.

To demonstrate that the dominant contribution to the E_y electric field in the vicinity of the X-point is due to off-diagonal components of the electron pressure tensor Figure 5.15 and Figure 5.16 show line plots along x and z through the X-point of the contributions that make up the E_y electric field in Eq. (5.7) at the time of maximum reconnection rate. The quantities in each case have been averaged for $2\Omega_i^{-1}$ either side of the time of maximum reconnection rate. Examination of these figures clearly shows that the dominant contribution to the electric field in the vicinity of the X-point comes from the gradients of the off-diagonal components of the electron pressure tensor (green lines).

In each of the plots shown in Figure 5.15 and Figure 5.16 the gradients of the off-diagonal components of the electron pressure tensor (green lines) dominate the electric field out to the point at which the $\mathbf{u} \times \mathbf{B}$ term (purple lines) equals the contribution from the gradients of the electron pressure tensor terms. The plots shown in Figure 5.15 show that the contribution from the off diagonal pressure tensor components dominates to about $x \approx \pm 3\, c/\omega_{pi}$ either side of the X-point. For the plots shown in Figure 5.16 the contribution from the off diagonal pressure tensor components

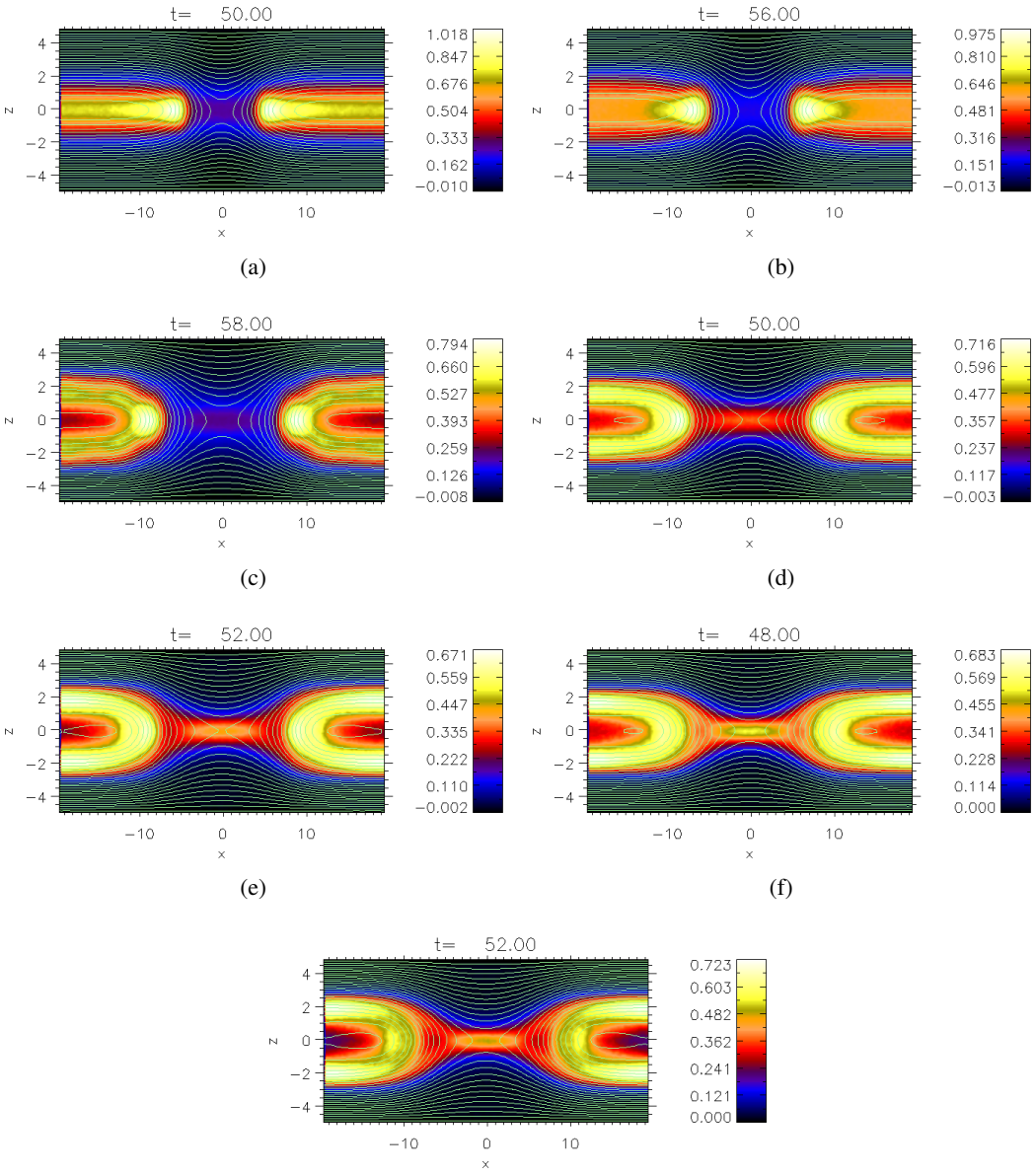

Figure 5.13: Plots of the y component of the current density with contours of the flux function overplotted for simulations with varying strengths of guide field at the time of maximum reconnection rate. (a) $B_{y0} = 0.0$ ($x_0 = -0.28$), (b) $B_{y0} = 0.1$ ($x_0 = -0.28$), (c) $B_{y0} = 0.3$ ($x_0 = 0.0$), (d) $B_{y0} = 0.5$ ($x_0 = 0.0$), (e) $B_{y0} = 0.7$ ($x_0 = -0.28$), (f) $B_{y0} = 0.9$ ($x_0 = 0.0$), (g) $B_{y0} = 1.0$ ($x_0 = -0.28$).

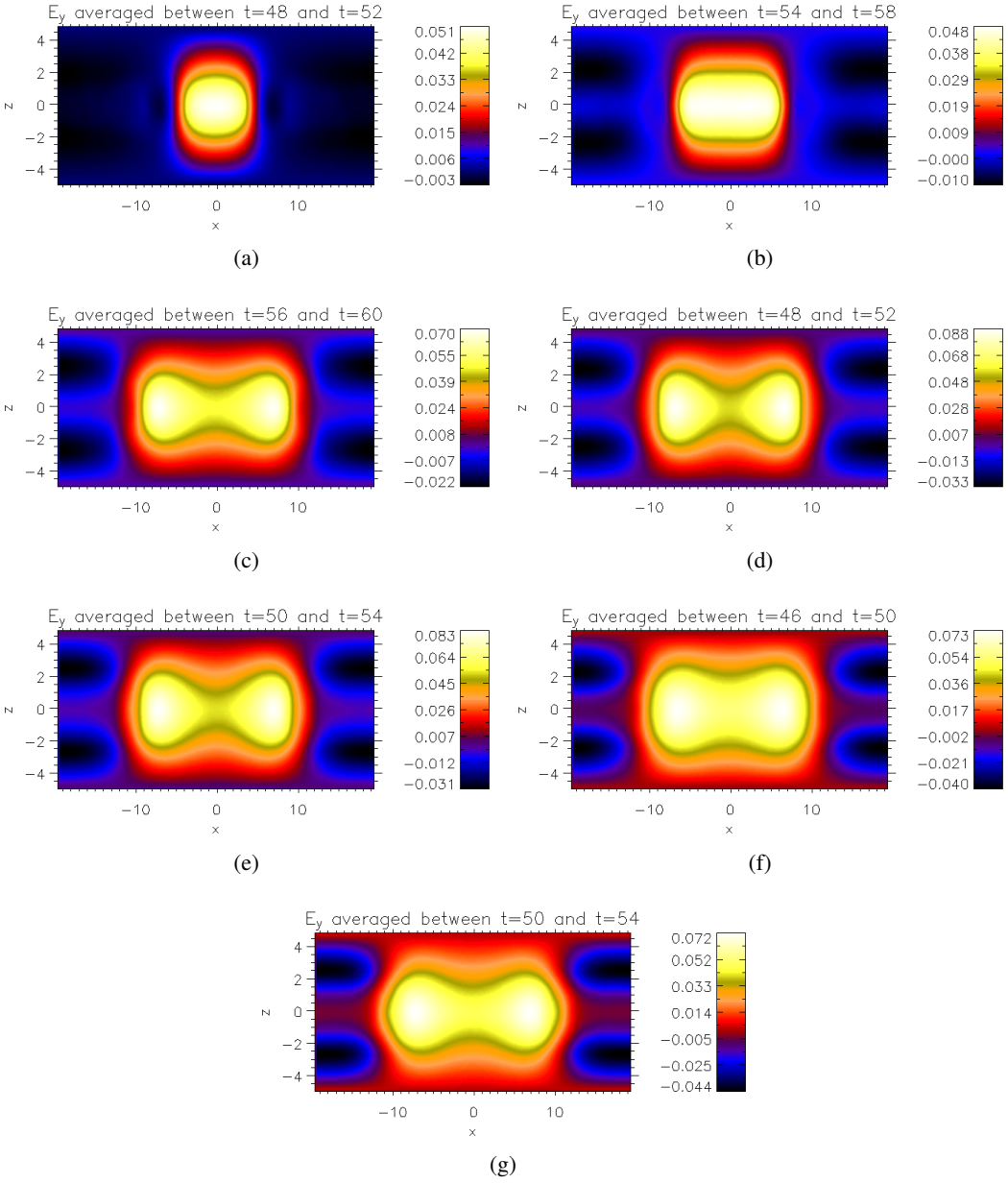

Figure 5.14: Plots of the E_y electric field for simulations with varying strengths of guide field at the time of maximum reconnection rate. (a) $B_{y0} = 0.0$ ($x_0 = -0.28$), (b) $B_{y0} = 0.1$ ($x_0 = -0.28$), (c) $B_{y0} = 0.3$ ($x_0 = 0.0$), (d) $B_{y0} = 0.5$ ($x_0 = 0.0$), (e) $B_{y0} = 0.7$ ($x_0 = -0.28$), (f) $B_{y0} = 0.9$ ($x_0 = 0.0$), (g) $B_{y0} = 1.0$ ($x_0 = -0.28$).

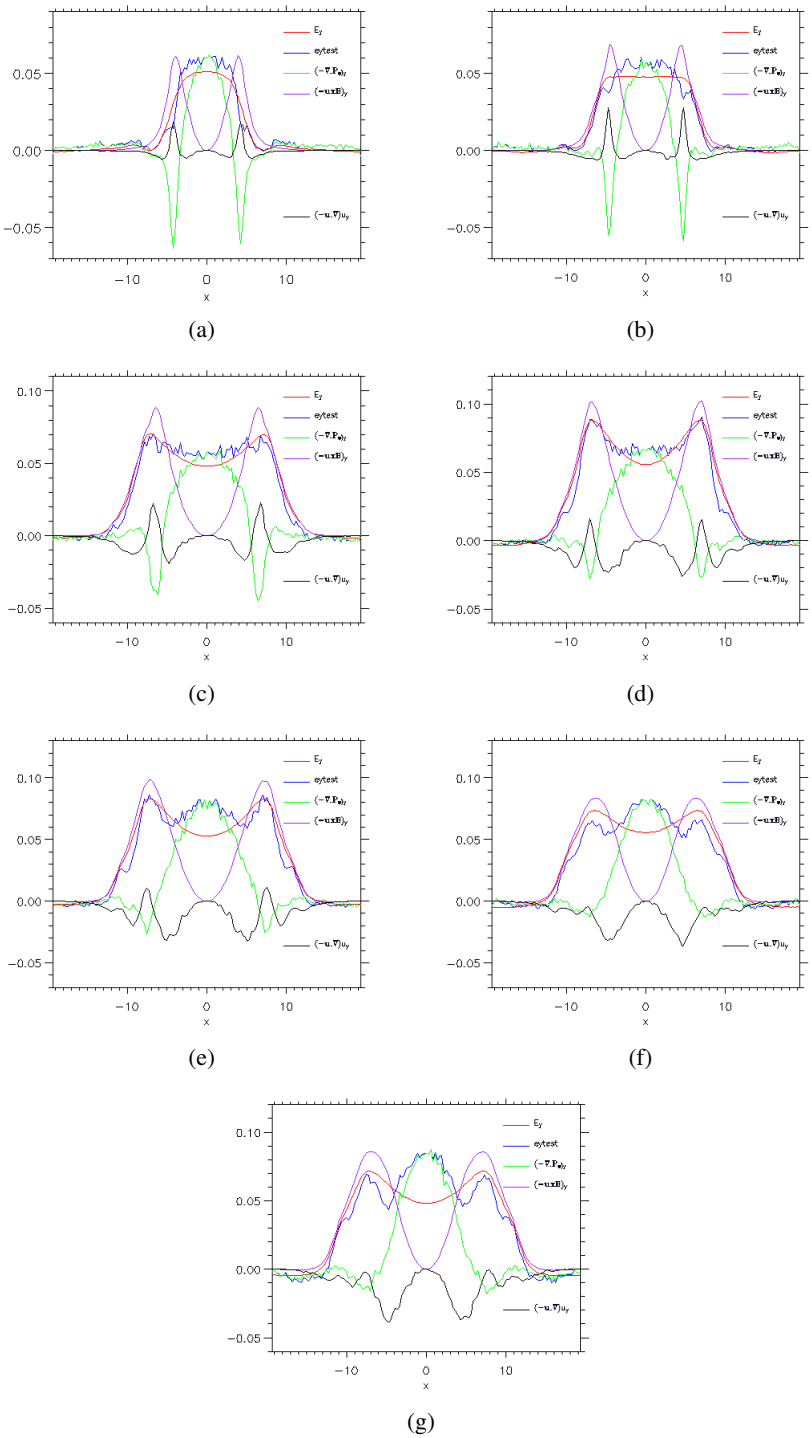

(a) (b) (c) (d) (e) (f) (g)

Figure 5.15: Plots along x for $z = 0$ of the contributions that make up the E_y electric field in Eq. (5.7) for simulations with varying strengths of guide field at the time of maximum reconnection rate. (a) $B_{y0} = 0.0$ ($x_0 = -0.28$), (b) $B_{y0} = 0.1$ ($x_0 = -0.28$), (c) $B_{y0} = 0.3$ ($x_0 = 0.0$), (d) $B_{y0} = 0.5$ ($x_0 = 0.0$), (e) $B_{y0} = 0.7$ ($x_0 = -0.28$), (f) $B_{y0} = 0.9$ ($x_0 = 0.0$), (g) $B_{y0} = 1.0$ ($x_0 = -0.28$).

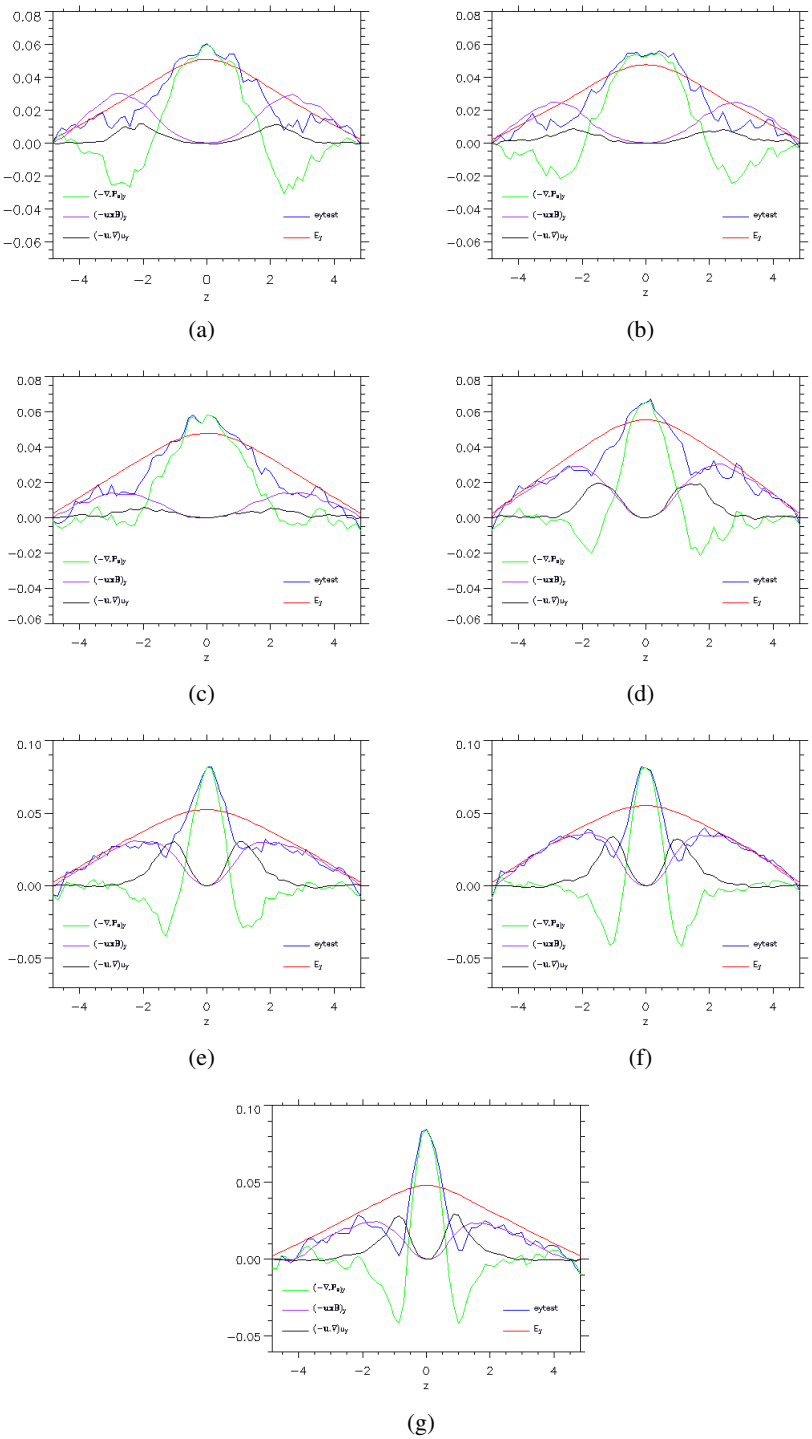

Figure 5.16: Plots along z for $x = x_0$ of the contributions that make up the E_y electric field in Eq. (5.7) for simulations with varying strengths of guide field at the time of maximum reconnection rate. (a) $B_{y0} = 0.0$ ($x_0 = -0.28$), (b) $B_{y0} = 0.1$ ($x_0 = -0.28$), (c) $B_{y0} = 0.3$ ($x_0 = 0.0$), (d) $B_{y0} = 0.5$ ($x_0 = 0.0$), (e) $B_{y0} = 0.7$ ($x_0 = -0.28$), (f) $B_{y0} = 0.9$ ($x_0 = 0.0$), (g) $B_{y0} = 1.0$ ($x_0 = -0.28$).

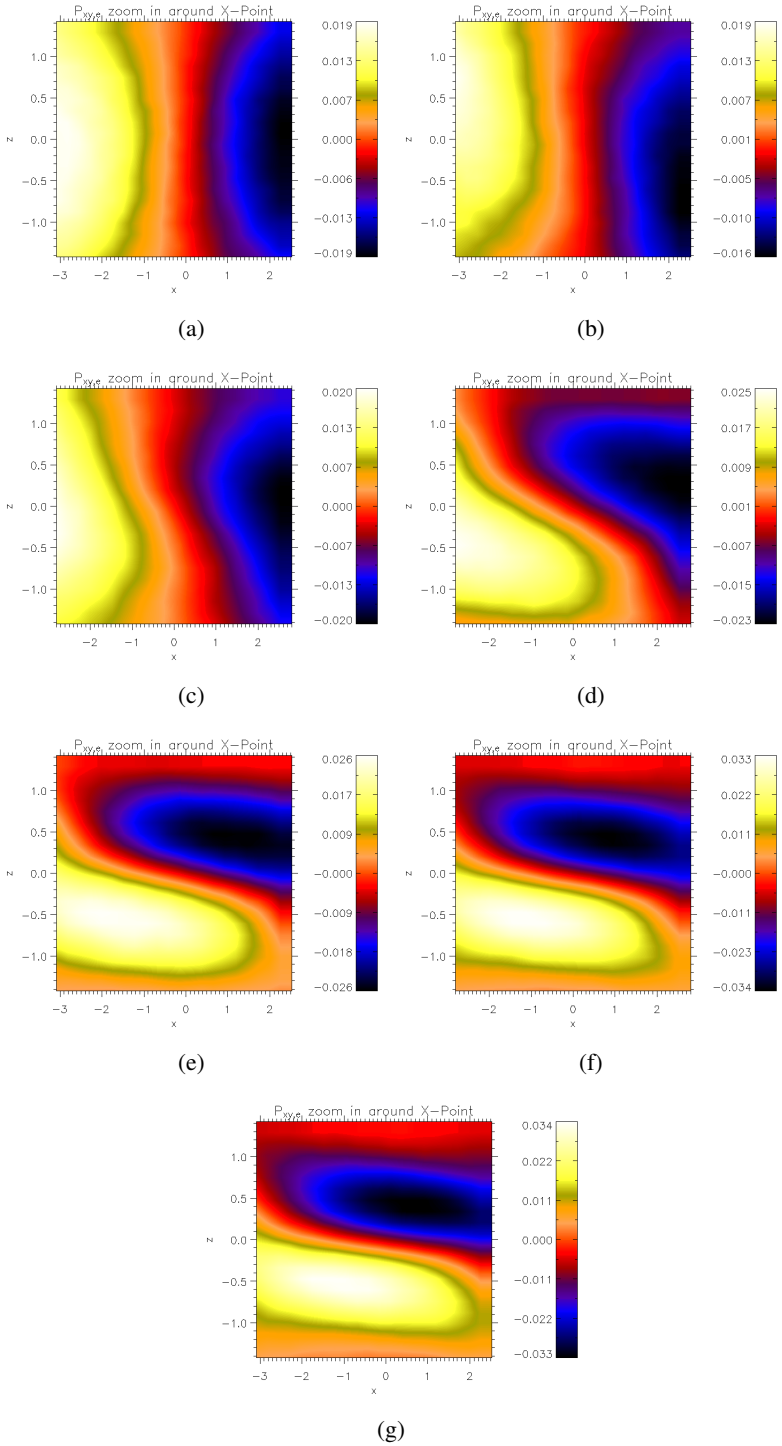

Figure 5.17: Plots of the $P_{xy,e}$ component of the electron pressure tensor for simulations with varying strengths of guide field at the time of maximum reconnection rate. (a) $B_{y0} = 0.0$ ($x_0 = -0.28$), (b) $B_{y0} = 0.1$ ($x_0 = -0.28$), (c) $B_{y0} = 0.3$ ($x_0 = 0.0$), (d) $B_{y0} = 0.5$ ($x_0 = 0.0$), (e) $B_{y0} = 0.7$ ($x_0 = -0.28$), (f) $B_{y0} = 0.9$ ($x_0 = 0.0$), (g) $B_{y0} = 1.0$ ($x_0 = -0.28$).

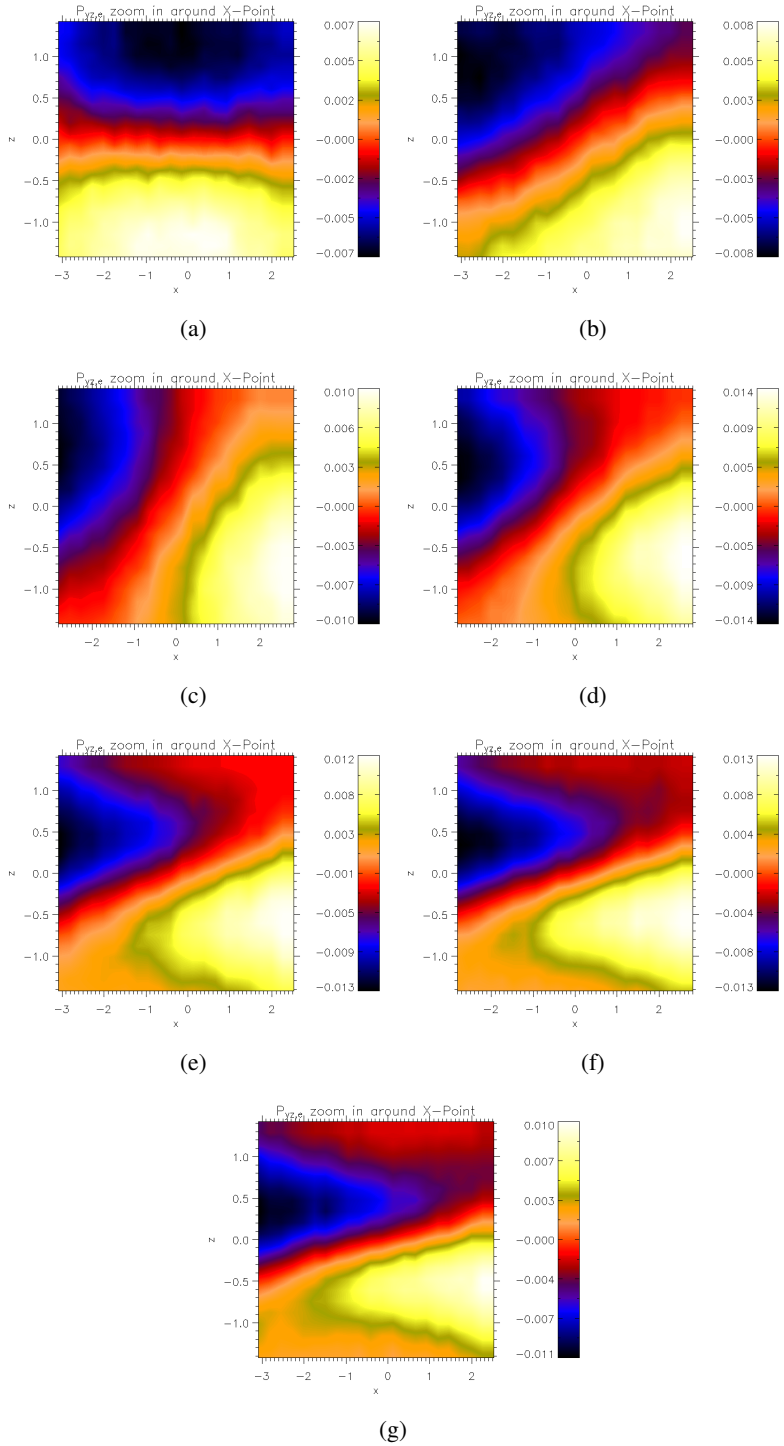

Figure 5.18: Plots of the $P_{yz,e}$ component of the electron pressure tensor for simulations with varying strengths of guide field at the time of maximum reconnection rate. (a) $B_{y0} = 0.0$ ($x_0 = -0.28$), (b) $B_{y0} = 0.1$ ($x_0 = -0.28$), (c) $B_{y0} = 0.3$ ($x_0 = 0.0$), (d) $B_{y0} = 0.5$ ($x_0 = 0.0$), (e) $B_{y0} = 0.7$ ($x_0 = -0.28$), (f) $B_{y0} = 0.9$ ($x_0 = 0.0$), (g) $B_{y0} = 1.0$ ($x_0 = -0.28$).

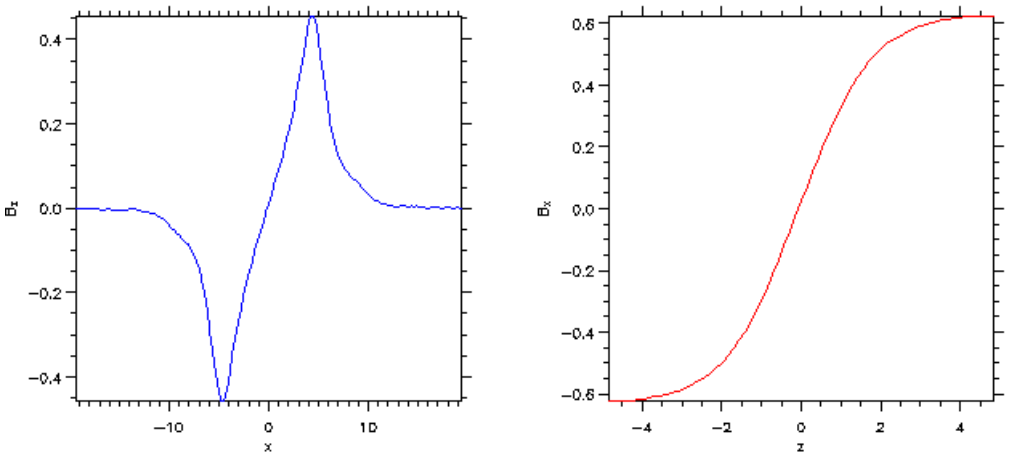

(a) (b)

Figure 5.19: Plots of the profile of B_z along x and of the profile of B_x along z going through the position of the X-point at the time of maximum reconnection rate for the zero guide field (anti-parallel) case.

dominates to about $z \approx \pm 1.8c/\omega_{pi}$ either side of the X-point for the weak guide field cases whilst for the strong guide field cases they dominate up to $z \approx \pm 0.5c/\omega_{pi}$ either side of the X-point.

Although the dominant term in the vicinity of the X-point is due to the gradients of the off-diagonal terms of the electron pressure tensor, there is a small contribution to the electric field from the electron inertia term at the edge of the diffusion regime. It can be seen in the plots along z of the contributions to the reconnection electric field shown in Figure 5.16 that as the guide field becomes larger the contribution from the electron inertia (black lines) at the edge of the diffusion region becomes larger. In the strong guide field cases this electron inertia term is in fact of equal magnitude to the $\mathbf{u} \times \mathbf{B}$ term. In a recent paper by Hesse et al. (2004) for a simulation starting from a Harris sheet with a guide field of $B_{y0} = 0.8$, it was shown that within a collisionless skin depth there was a finite contribution from the electron inertia at the edge of the localised current region. The main contribution to the E_y electric field close to the X-point was still due to the nongyrotropic pressures. The results shown here are consistent with this. The significant contribution from the electron inertia term is due the small scales associated with the electron Larmor radius in the strong guide field case.

To investigate further the structure of the off-diagonal electron pressure tensor components, Figures 5.17 and 5.18 show filled contour plots of the $P_{xy,e}$ and $P_{yz,e}$ components of the electron pressure tensor zoomed in around the position of the central X-point. In the anti-parallel case the $P_{xy,e}$ component is approximately symmetrical about the line $x = x_0$ which goes through the X-point with a gradient in x. The $P_{yz,e}$ component of the pressure tensor is approximately

symmetrical about the $z = 0$ line going through the X-point with a gradient in z. As the guide field is increased the structure of the $P_{xy,e}$ component starts to change. The symmetry along the line $x = x_0$ is broken and the structure is seen to rotate in an anti-clockwise direction until at the guide field $B_{y0} = 1.0$ case the $P_{xy,e}$ component is almost symmetrical along the line $z = 0$ with a gradient in z. The central region in all of the plots can also be seen to thin. The $P_{yz,e}$ component of the electron pressure tensor is seen to at first rotate in the anti-clockwise direction up to about a guide field of $B_{y0} = 0.5$ but then rotates clockwise until for a guide field of $B_{y0} = 1.0$ the symmetry along $z = 0$ has almost been restored. The thinning of the central region can again be observed as the guide field becomes stronger.

It is currently unclear why the structure of the $P_{xy,e}$ and $P_{yz,e}$ components of the electron pressure tensor have the behaviour shown in Figure 5.17 and Figure 5.18 for the intermediate cases between the zero guide field and strong guide field case. Analytical estimates of the $P_{xy,e}$ and $P_{yz,e}$ components of the electron pressure tensor in the vicinity of the X-point have been derived for the anti-parallel case (Hesse et al. 1999) and the strong guide field case (Hesse et al. 2004). A full analytical theory that can describe the changing structure of $P_{xy,e}$ and $P_{yz,e}$ shown in Figure 5.17 and Figure 5.18 as the transition between a zero guide field case to a strong guide field case is made is not currently available and is a problem for future work.

The thinning of the central region in Figure 5.17 and Figure 5.18 is due to the introduction of the guide field. In the case with zero guide field the characteristic length scale of $P_{xy,e}$ and $P_{yz,e}$ is given approximately by the electron bounce widths in a field reversal λ_x and λ_z (e.g. Hesse et al. 1999). In these simulations the electron bounce width in the x and z directions for the anti-parallel field configuration as given by Eqs. (5.3) and (5.4) at the time of maximum reconnection rate are of the order $\lambda_x \approx 2.5c/\omega_{pi}$ and $\lambda_z \approx 1.3c/\omega_{pi}$. Plots of the B_x and B_z profiles of the magnetic field along z and x respectively going through the X-point for the zero guide field case at the time of maximum reconnection rate are shown in Figure 5.19. These are used to calculate estimates of the bounce widths λ_x and λ_z. In the strong guide field case the characteristic length scale changes to that of the thermal electron Larmor radius $r_L = v_{th,e}/\Omega_e$ in the guide magnetic field (Hesse et al. 2004). The electron Larmor radius for the simulation with $B_{y0} = 1.0$ at the time of maximum reconnection rate is of the order $r_L \approx 0.5c/\omega_{pi}$. This characteristic change of length scale can be seen in Figure 5.17 and Figure 5.18.

5.5 Anisotropic Bi-Maxwellian Simulations ($m_i/m_e = 1$)

In this section simulation results that use the equilibria that were introduced in Sec. 3.3.3 and Sec. 3.4 in Chap. 3 as initial conditions are shown. The main focus of the study is to investigate the structure of the off-diagonal components of the electron pressure tensor for a periodic anti-

parallel equilibrium with varying strengths of guide field and compare this to a simulation run where a self consistent linear force-free equilibrium is used as the initial condition. This is the first time a systematic comparison of the reconnection process has been done comparing results from simulations starting from an anti-parallel configuration with a guide field to a simulation starting from a self-consistent linear force-free equilibrium. These results are compared to the Harris sheet cases.

The anti-parallel configuration and the force-free equilibrium can both be found from the anisotropic bi-Maxwellian distribution function (3.102) given in Chap. 3 which is an extension to the distribution function discussed by Bobrova et al. (2001). The anti-parallel configuration is given by setting $b_s = 0$ and the linear force-free equilibrium is found by setting $b_s = 1$. The distribution function for the anti-parallel case is explicitly given by

$$f_s = c_s \exp\left[-\frac{1}{T_{s\perp}} H_s + \frac{\Delta T_s}{2 m_s T_{s\perp} T_{s\parallel}} p_{ys}^2\right], \tag{5.13}$$

where

$$\Delta T_s = T_{s\parallel} - T_{s\perp} \geq 0. \tag{5.14}$$

The constant c_s is a normalising constant and is defined as,

$$c_s = \frac{n_{0s} m_s^{3/2}}{(2\pi)^{3/2} T_{s\perp} T_{s\parallel}^{1/2}}. \tag{5.15}$$

This can be written in terms of velocity as

$$\begin{aligned} f_s(z, \mathbf{v}) \quad = \quad & \frac{n_{0s} m_s^{3/2}}{(2\pi)^{3/2} T_{s\perp} T_{s\parallel}^{1/2}} \\ & \times \exp\left(- \frac{m_s}{2} \left[\frac{(v_y - V_{dy}^s(z))^2}{T_{s\parallel}} + \frac{v_z^2 + v_x^2}{T_{s\perp}} \right] \right. \\ & \left. - \left[\frac{q_s}{T_{s\perp}} \phi(z) - \frac{1}{2} \frac{q_s^2}{m_s} \frac{\Delta T_s}{T_{s\perp}^2} A_y^2 \right] \right), \end{aligned} \tag{5.16}$$

where

$$V_{dy}^s = \frac{q_s}{m_s} \frac{\Delta T_s}{T_{s\perp}} A_y, \tag{5.17}$$

are the average drift velocities in the y direction for each species.

The linear force-free equilibrium is given by the distribution function

$$f_s = c_s \exp\left[-\frac{1}{T_{s\perp}}H_s + \frac{\Delta T_s}{2m_s T_{s\perp} T_{s\parallel}}p_{xs}^2 + \frac{\Delta T_s}{2m_s T_{s\perp} T_{s\parallel}}p_{ys}^2\right], \tag{5.18}$$

where

$$\Delta T_s = T_{s\parallel} - T_{s\perp} \geq 0. \tag{5.19}$$

The constant c_s is a normalising constant and is defined as

$$c_s = \frac{n_{0s} m_s^{3/2}}{(2\pi)^{3/2} T_{s\perp}^{1/2} T_{s\parallel}}. \tag{5.20}$$

This can be written in terms of velocity as

$$\begin{aligned} f_s &= \frac{n_{0s} m_s^{3/2}}{(2\pi)^{3/2} T_{s\perp}^{1/2} T_{s\parallel}} \exp\left[-\frac{q_s}{T_s}\phi + \frac{1}{2}\frac{q_s^2}{m_s}\frac{\Delta T_s}{T_{s\perp}^2}A_x^2 + \frac{1}{2}\frac{q_s^2}{m_s}\frac{\Delta T_s}{T_{s\perp}^2}A_y^2\right] \\ &\times \exp\left[-\frac{m_s}{2}\frac{(v_x - V_{dx}^s)^2 + \left(v_y - V_{dy}^s\right)^2}{T_{s\parallel}}\right] \\ &\times \exp\left[-\frac{1}{T_{s\perp}}\frac{m_s}{2}v_z^2\right], \end{aligned} \tag{5.21}$$

where

$$V_{dx}^s = \frac{q_s}{m_s}\frac{\Delta T_s}{T_{s\perp}}A_x, \tag{5.22}$$

$$V_{dy}^s = \frac{q_s}{m_s}\frac{\Delta T_s}{T_{s\perp}}A_y, \tag{5.23}$$

are the average drift velocities in the x and y directions. In the anti-parallel case $T_{s\perp}$ is the temperature in the x and z directions and $T_{s\parallel}$ is the temperature in the y direction for each particle species. In the linear force-free case $T_{s\perp}$ is the temperature in the z direction and $T_{s\parallel}$ is the temperature in the x and y directions for each particle species.

The profiles of the magnetic field components for the two equilibria are shown in Figure 5.20. The anti-parallel solution is found by a fourth order Runga-Kutta method to solve the differential equations resulting from Ampère's law and was discussed in Sec. 3.4 of Chap. 3. The force-free solution can be found analytically and was discussed in Sec. 3.3.3 in Chap. 3. The magnetic field for the force-free case is

$$\mathbf{B} = B_0\left(\sin(\alpha z)\mathbf{e_x} + \cos(\alpha z)\mathbf{e_y}\right), \tag{5.24}$$

where α is given by

$$\alpha = \left(\frac{\Delta T_e}{T_{e\perp}} + \frac{m_e}{m_i} \frac{\Delta T_i}{T_{i\perp}} \right)^{\frac{1}{2}} . \tag{5.25}$$

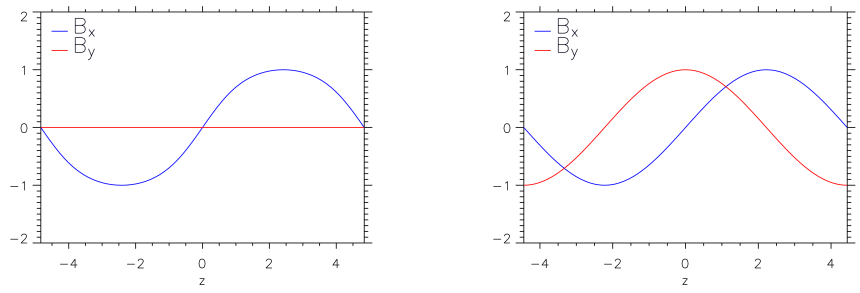

(a) (b)

Figure 5.20: Plots showing the two equilbrium which are used here as initial configurations in the simulation runs. Figure 5.20(a) shows the anti-parallel configuration and Figure 5.20(b) shows the linear force-free equilibrium.

In the anti-parallel case the quasi-neutral particle density is spatially varying and is strong in regions of strong current and is given by

$$n_{qn} = n_0 \exp \left[\frac{1}{2} \frac{e^2}{m_e} \frac{\Delta T_e}{T_{e\perp}^2} (A_y^2 - A_{y,max}^2) \right] . \tag{5.26}$$

In the force-free case the quasineutral number density is constant.

In all the simulations in this section the ion to electron mass ratio is equal to one $(m_i/m_e = 1)$. Lengths are normalized to the ion inertial length c/ω_{pi} and the number density is normalised to a value n_0. Times are normalised to the inverse of the ion cyclotron frequency $\Omega_i = eB_0/m_i$. The magnetic field is normalised to the value B_0, the amplitude of the initial magnetic field.

In the anti-parallel case the system dimensions are $L_x = 19.34\, c/\omega_{pi}$ and $L_z = 4.83\, c/\omega_{pi}$ where L_x and L_z are the half lengths of the box in the x and z directions, with a grid that is 140×70 in the x and z directions. The linear force-free case has system dimensions $L_x = 4\sqrt{2}\pi c/\omega_{pi} = 4\pi/\alpha$ and $L_z = \sqrt{2}\pi c/\omega_{pi} = \pi/\alpha$ where L_x and L_z are the half lengths of the box in the x and z directions with a grid that is 120×60 in the x and z directions. A time step $\omega_{pe}\Delta t = 1$ is used. The ratio ω_{pe}/Ω_e is set to a numerical value of 5 in both cases.

The initial configurations used consist of the anti-parallel case shown in Figure 5.21 where a range of different strengths of guide field were added and the linear force-free case that is shown

in Figure 5.22. For each simulation run a perturbation of the form,

$$B_{xp} = a_0 \frac{\pi}{L_z} \sin\left(\frac{\pi z}{L_z}\right), \tag{5.27}$$

$$B_{zp} = a_0 \frac{\pi}{L_x} \sin\left(\frac{\pi x}{L_x}\right), \tag{5.28}$$

is also added where L_x and L_z are the half lengths of the box in the x and z directions. This field perturbation gives X-points at $(0,0), (L_x, L_z), (L_x, -L_z), (-L_x, L_z)$ and $(-L_x, -L_z)$. O-Points are located at $(0, L_z), (0, -L_z), (-L_x, 0)$ and $(L_x, 0)$. In all cases periodic boundary conditions are employed at $x = -L_x$ and $x = L_x$ and $z = -L_z$ and $z = L_z$. The electron-ion temperature ratios are chosen as $T_{e\perp}/T_{i\perp} = T_{e\parallel}/T_{i\parallel} = 1.0$.

There are two particle populations in all simulation runs. The foreground population consists of the first set of ions and electrons which establish the equilibrium pressures and currents in all cases. In the anti-parallel runs there is both an electron and ion temperature anisotropy. The distribution of the ions and electrons is therefore specified by Eq. (5.13). The temperature anisotropy is set such that $T_{e\perp}/T_{e\parallel} = T_{i\perp}/T_{i\parallel} = 0.8$. The second population consists of the second set of ions and electrons and constitutes a constant background density $n_b = 0.2$. The background temperatures are identical to the foreground population $T_{e\perp} + T_{i\perp} = 1.0, T_{e\parallel} + T_{i\parallel} = 1.25$. The simluation run used 2×10^7 ions and electrons each for the foreground and 3×10^7 ions and electrons for the background.

In the force-free run there is both an electron and ion temperature anisotropy. The distribution of the ions and electrons is therefore specified by Eq. (5.18). This is one of the only studies in 2.5D starting from the linear force-free equilibrium discussed by (Bobrova and Syrovatskiĭ 1979; Bobrova et al. 2001) that has the initial current carried by both the electrons and the ions and is the only study to compare the reconnection process to an anti-parallel initial configuration. In the majority of previous studies that have been carried out the initial ion distribution function has been assumed to be isotropic (Bobrova et al. 2001; Nishimura et al. 2003; Li et al. 2003; Bowers and Li 2007). The temperature anisotropy is set such that $T_{e\perp}/T_{e\parallel} = T_{i\perp}/T_{i\parallel} = 0.8$. The second population consists of the second set of ions and electrons and once again this population constitutes a constant background density $n_b = 0.2$. The background temperatures are identical to the foreground population $T_{e\perp} + T_{i\perp} = 0.4, T_{e\parallel} + T_{i\parallel} = 0.5$ and $\alpha = 1/\sqrt{2}\,\omega_{pe}/c$. The simluation run used 2×10^7 ions and electrons each for the foreground and 3×10^7 ions and electrons for the background.

Results from simulation runs where the strength of the constant guide field $B_y = B_{y0}$ is varied from $B_{y0} = 0.0$ through to $B_{y0} = 1.0$ for the anti-parallel case are shown and compared to the linear force-free and to the Harris sheet cases.

Figure 5.21 and Figure 5.22 shows the initial configurations for the anti-parallel cases and the

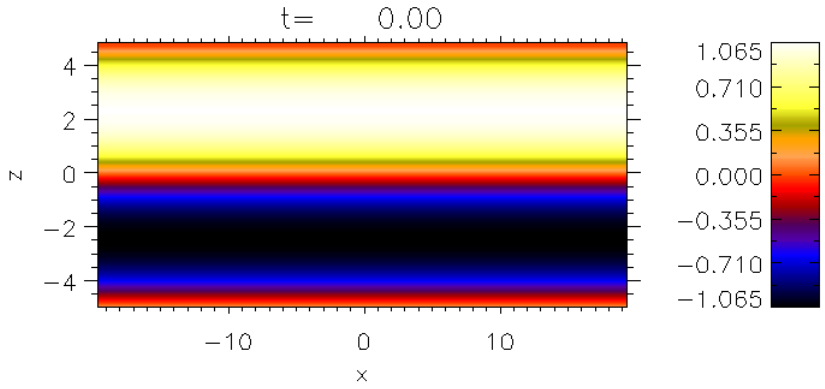

(a)

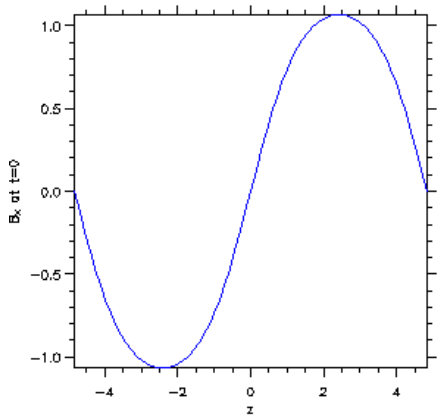

(b)

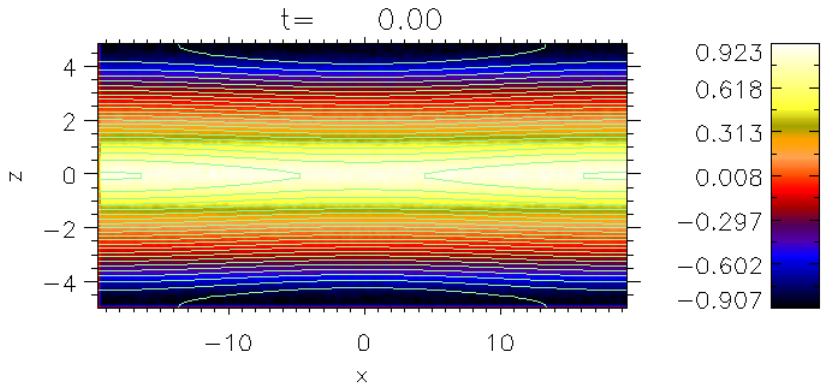

(c)

Figure 5.21: Plots showing the initial configuration for the anti-parallel case. Figure 5.21(a) shows a colour contour plot of B_x and figure 5.21(b) shows a line plot of the profile of B_x along z for $x = 0$. Figure 5.21(c) shows a filled contour plot of the y component of the current density with magnetic field lines corresponding to contours of the flux function overplotted.

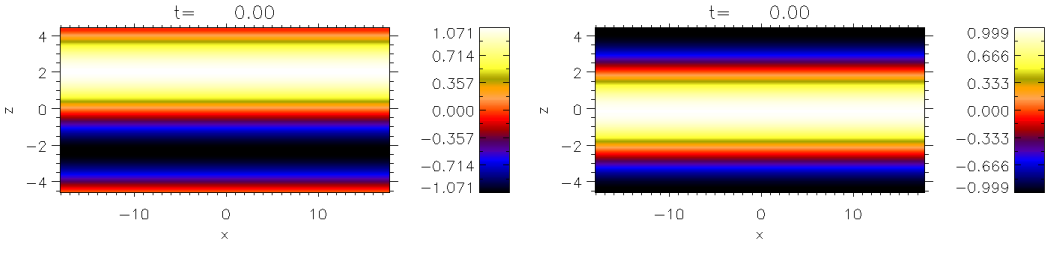

(a)

(b)

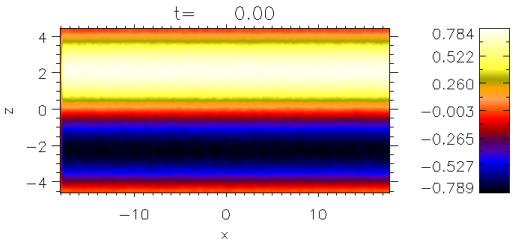

(c)

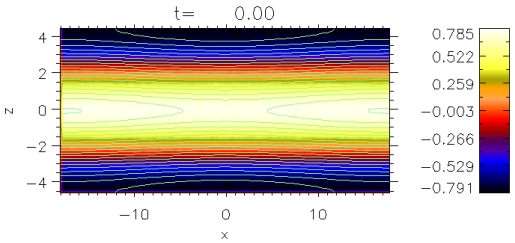

(d)

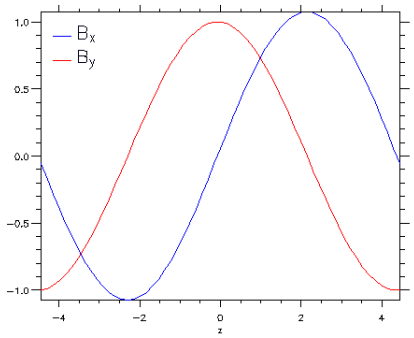

(e)

Figure 5.22: Plots showing the initial configuration for the force-free case. Figure 5.22(a) and Figure 5.22(b) show colour contour plots of B_x and B_y. Figure 5.22(c) shows a colour contour plot of the x component of the current density and Figure 5.22(d) shows a filled contour plot of the y component of the current density with magnetic field lines corresponding to contours of the flux function overplotted. Figure 5.22(e) shows a line plot of the profile of B_x and B_y along z for $x = 0$.

force-free case. For the anti-parallel case a filled contour plot of B_x is shown in Figure 5.21(a) with a line plot of the magnetic field profile plotted along z for $x = 0$ shown in Figure 5.21(b). Figure 5.21(c) is a filled contour plot of the y component of the current density with contours of the flux function overplotted showing the magnetic field lines. It is clear to see the periodic profile of B_x and also the multiple current sheet structures of j_y with X-points located at the centre and corners of the box and the 0-points located in between the X-points that are introduced by the perturbation to the equilibrium magnetic field.

For the force-free case filled contour plots of B_x and B_y are shown in Figure 5.22(a) and Figure 5.22(b) with a line plot of the magnetic field profiles plotted along z for $x = 0$ shown in Figure 5.22(e). Figure 5.22(c) shows a colour contour plot of the x component of the current density and Figure 5.22(d) is a filled contour plot of the y component of the current density with contours of the flux function overplotted showing the magnetic field lines. It is clear to see the periodic profile of B_x and B_y and also the multiple current sheet structures of j_x and j_y with X-points located at the centre and corners of the box and the 0-points located in between the X-points that are introduced by the perturbation to the equilibrium magnetic field.

Figures 5.23 - 5.26 show the evolution of the magnetic field for four different runs with the y component of the current density colour coded. Figure 5.23 shows the evolution for the anti-parallel configuration without a guide field. Figure 5.24 shows the evolution for the anti-parallel case with a guide field of value $B_{y0} = 0.5$. Figure 5.25 shows the evolution for the anti-parallel case with a guide field of value $B_{y0} = 1.0$ and Figure 5.26 shows the evolution of the force-free case. Movies of the evolution for each case can be found on the CD which is attached to this thesis (see Appendix B). It is important to note that the colour bar scale changes between each of the snapshots to range between the minimum and maximum values of the y component of the current density.

These figures show how magnetic reconnection proceeds and leads to large changes in the magnetic field structure. In the anti-parallel case with zero guide field the current density becomes reduced at the central X-point and enhanced in the regions adjacent to the diffusion region, showing a similar behaviour to the Harris sheet runs. In the cases with stronger guide field and including the force-free case the current density becomes enhanced at the X-point. In the strong guide field cases the central current layer thins and becomes more localised. At late times in the simulation runs the magnetic field structure has changed dramatically. The magnetic field configuration has gone from having a (B_x, B_y) structure to having a mainly (B_y, B_z) structure. In all the simulation runs in the majority of the simulation box the y component of the current density has been significantly reduced. In the stronger guide field cases there are also small regions where the y component of the current density is enhanced. This large scale reorganistion of the geometry of the magnetic field is due to the doubly periodic boundary conditions that are employed. In all the simulation runs the O-points above and below the central X-point have a strong effect. Once

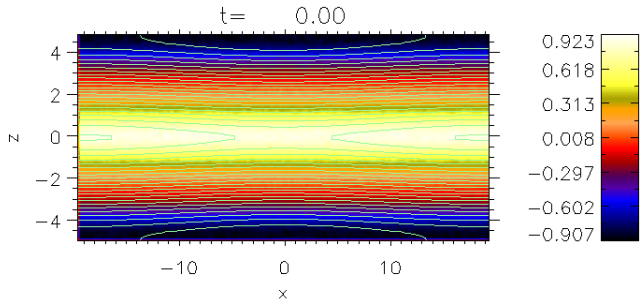

(a)

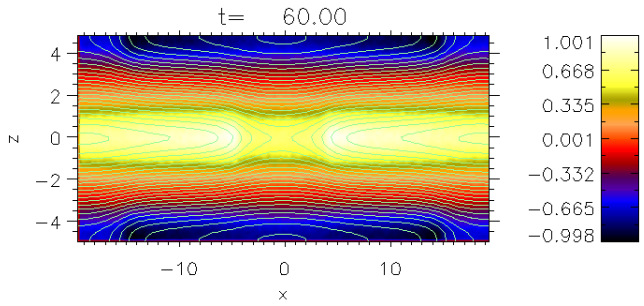

(b)

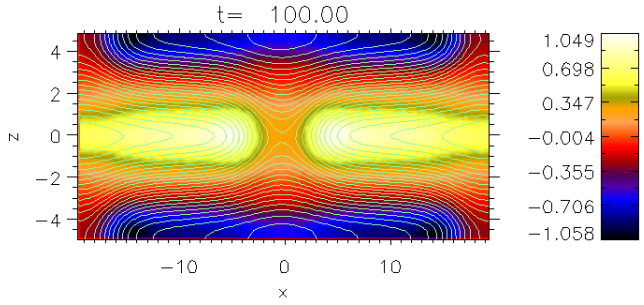

(c)

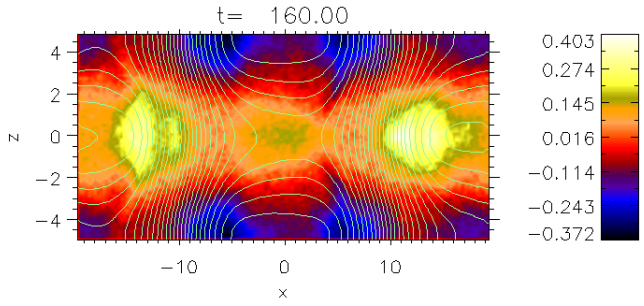

(d)

Figure 5.23: Plots of the y component of the current density with contours of the flux function overplotted for the anti-parallel case with zero guide field. The plots correspond to the different times (a) $t = 0$, (b) $t = 60$, (c) $t = 100$ and (d) $t = 160$.

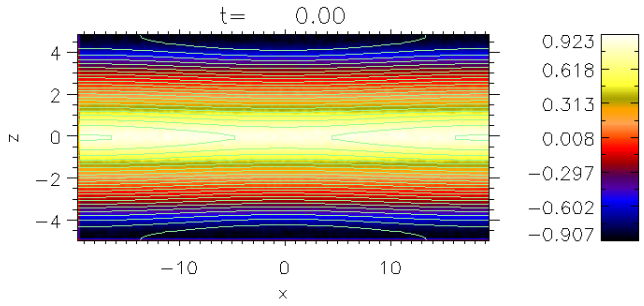

(a)

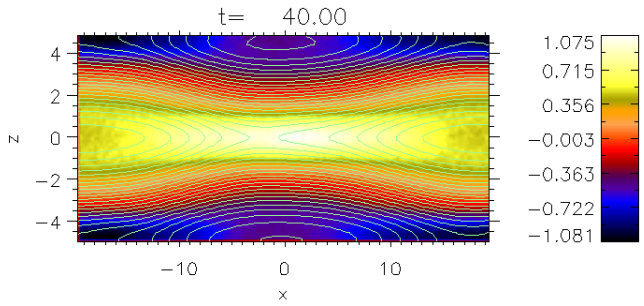

(b)

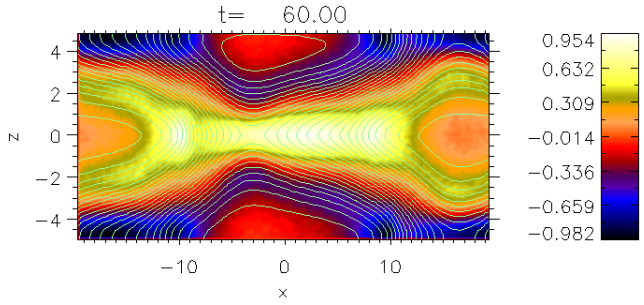

(c)

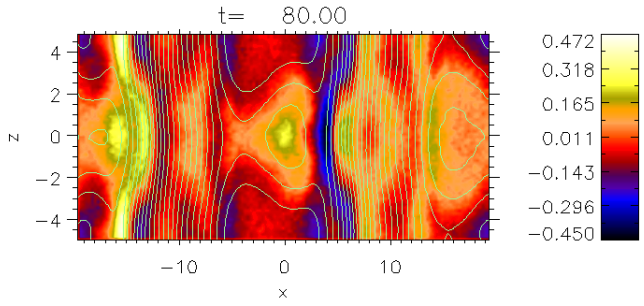

(d)

Figure 5.24: Plots of the y component of the current density with contours of the flux function overplotted for the anti-parallel case with a guide field of value $B_{y0} = 0.5$. The plots correspond to the different times (a) $t = 0$, (b) $t = 40$, (c) $t = 60$ and (d) $t = 80$.

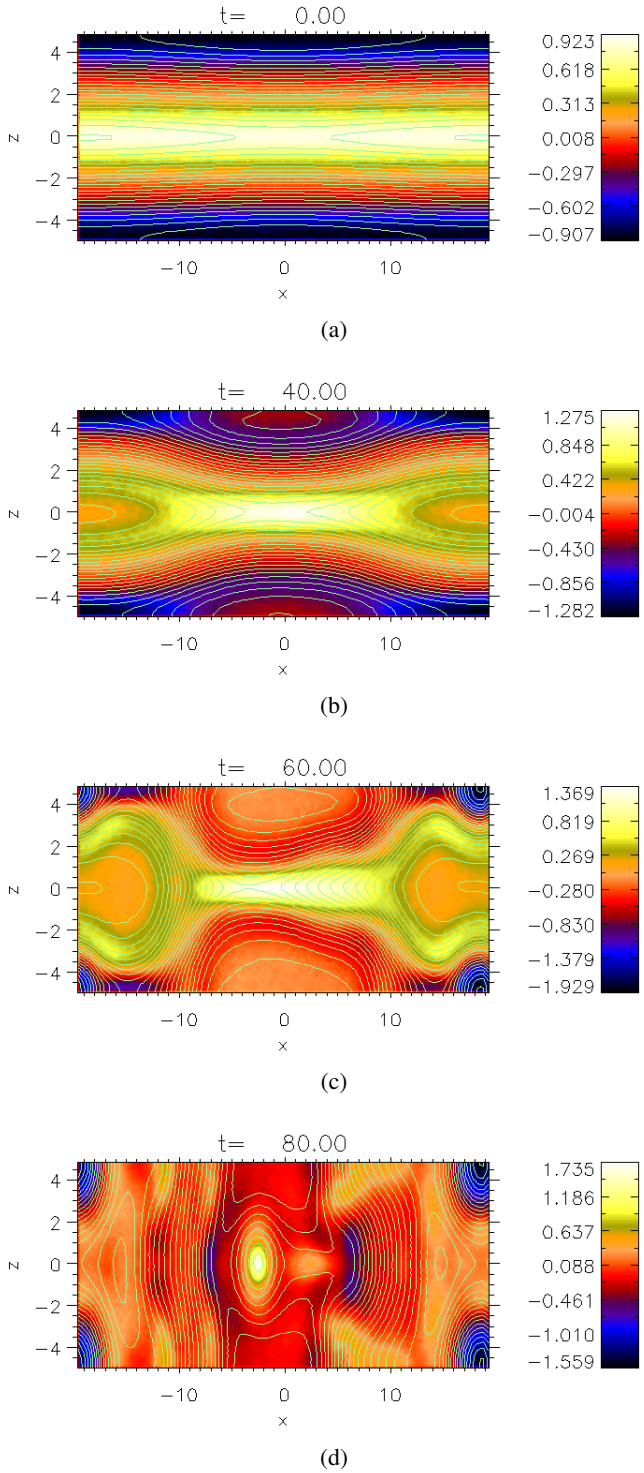

Figure 5.25: Plots of the y component of the current density with contours of the flux function overplotted for the anti-parallel case with a guide field of value $B_{y0} = 1.0$. The plots correspond to the different times (a) $t = 0$, (b) $t = 40$, (c) $t = 60$ and (d) $t = 80$.

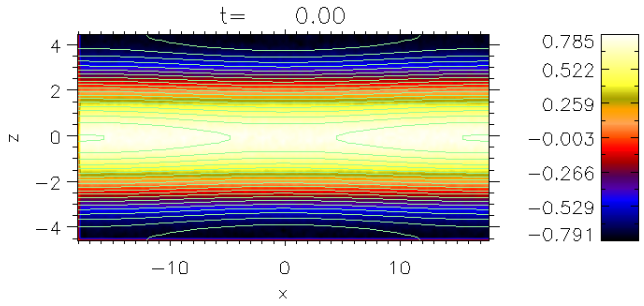

(a)

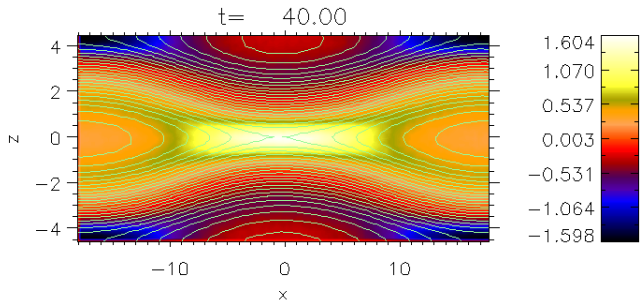

(b)

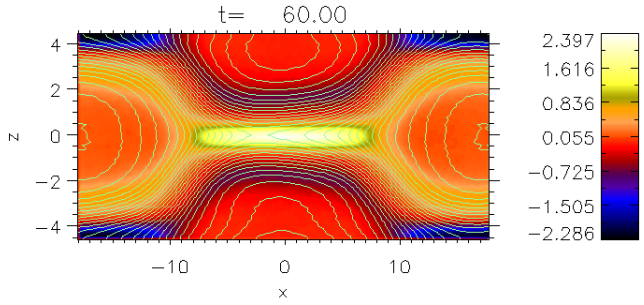

(c)

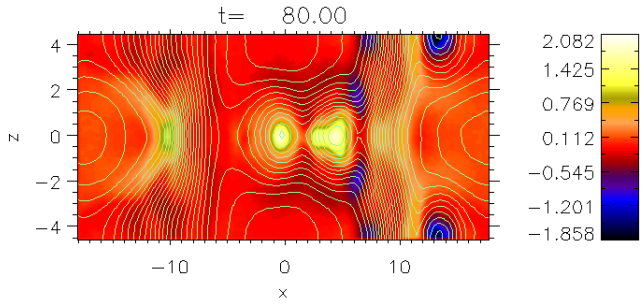

(d)

Figure 5.26: Plots of the y component of the current density with contours of the flux function overplotted for the force-free case. The plots correspond to the different times (a) $t = 0$, (b) $t = 40$, (c) $t = 60$ and (d) $t = 80$.

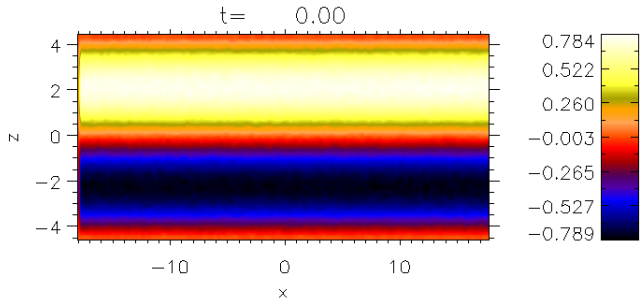

(a)

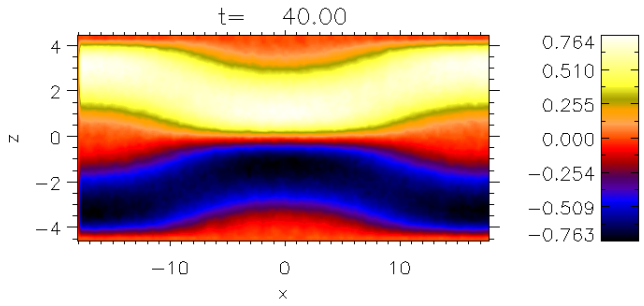

(b)

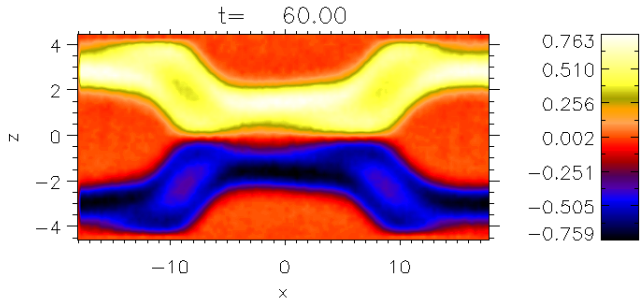

(c)

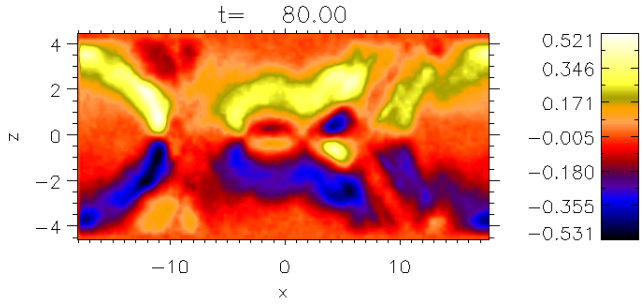

(d)

Figure 5.27: Plots of the x component of the current density for the force-free case. The plots correspond to the different times (a) $t = 0$, (b) $t = 40$, (c) $t = 60$ and (d) $t = 80$.

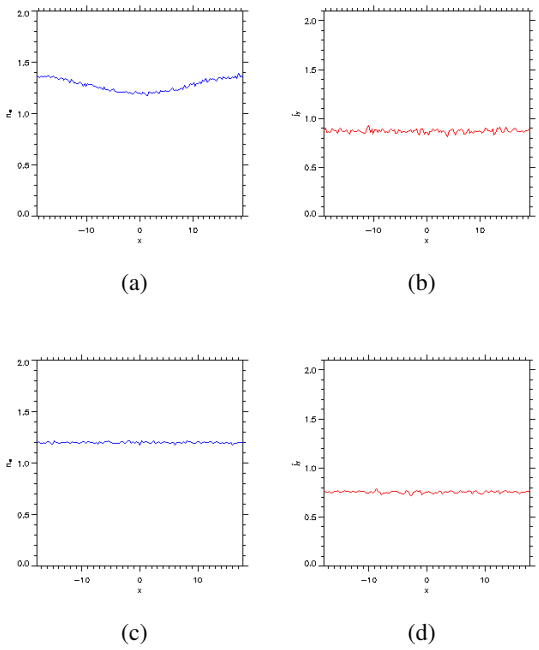

(a) (b)

(c) (d)

Figure 5.28: Line plots of the electron number density n_e (blue lines) and the y component of the current density (red lines) plotted along x for $z = 0$ at $t = 0$ for (a),(b) the anti-parallel simulation runs and also (c),(d) the linear force-free run.

the initial stages of reconnection have occurred the O-points above and below the central X-point continue to press in on the central X-point eventually leading to the large scale reorganisation that is shown.

Figure 5.29 shows line plots along x for $z = 0$ of the electron number density n_e (blue lines) and the y component of the current density (red lines) for the antiparallel cases with zero guide field, $B_{y0} = 0.5$ and $B_{y0} = 1.0$ and also the linear force-free case during reconnection. These can be compared to the initial electron number number density and y component of the current density profiles plotted along x for $z = 0$ which are shown in Figure 5.28. It is interesting to note that in the runs starting from the anti-parallel magnetic configuration, Figures 5.29(a), 5.29(c) and 5.29(e) show a density depletion around the X-point which is most significant for the zero guide field case. In the zero guide field case Figure 5.29(b) shows that the current density is also reduced at the X-point, whereas in the stronger guide field cases $B_{y0} = 0.5$ and $B_{y0} = 1.0$, Figures 5.29(d) and 5.29(f) show that the current density is actually enhanced at the X-point. In the guide field cases $B_{y0} = 0.5$ and $B_{y0} = 1.0$ the reduction of the number density at the X-point implies that the current density increase must be due to an increased drift of the electrons and ions in the vicinity of the X-point. In the linear force-free case, in contrast to the anti-parallel cases, Figure 5.29(g) shows that the number density is enhanced at the X-point. In addition to this Figure 5.29(h) shows that the current density is significantly increased at the X-point.

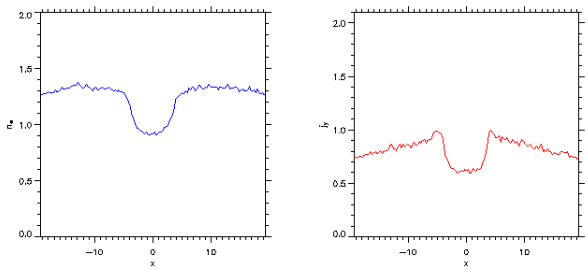

(a) (b)

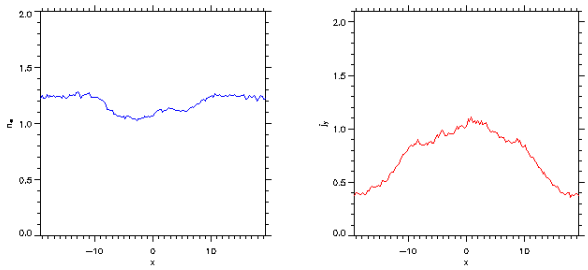

(c) (d)

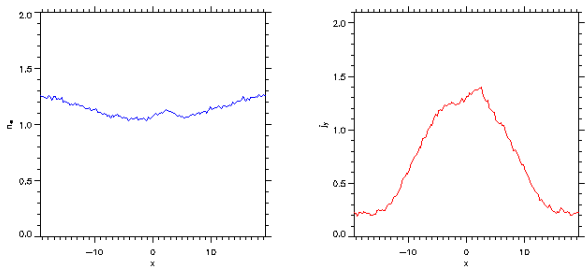

(e) (f)

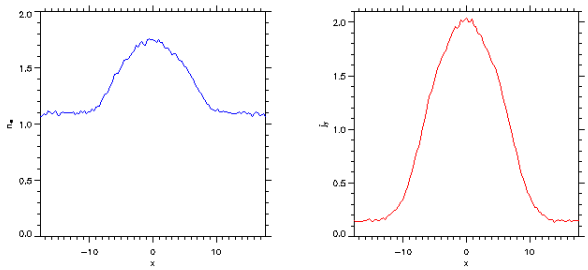

(g) (h)

Figure 5.29: Line plots of the electron number density n_e (blue lines) and the y component of the current density (red lines) plotted along x for $z = 0$ during reconnection for the anisotropic bi-Maxwellian runs for the anti-parallell case with a guide field of value (a),(b) $B_{y0} = 0.0$ ($t = 64$) (c),(d) $B_{y0} = 0.5$ ($t = 44$), (e),(f) $B_{y0} = 1.0$ ($t = 46$), and also (g),(h) linear force-free ($t = 50$).

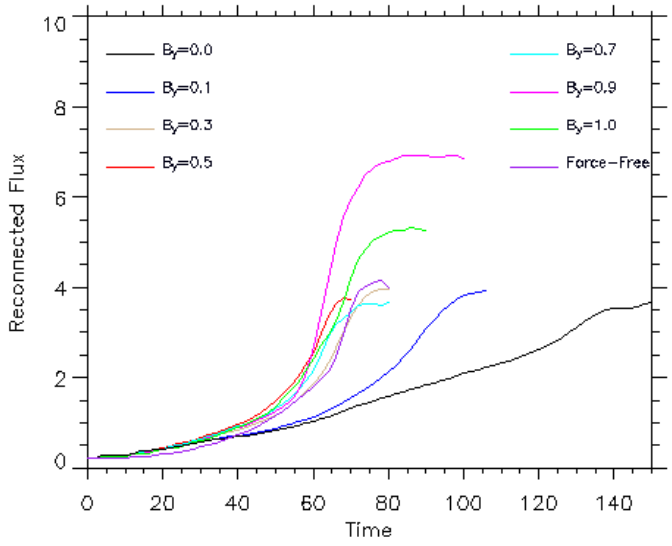

(a)

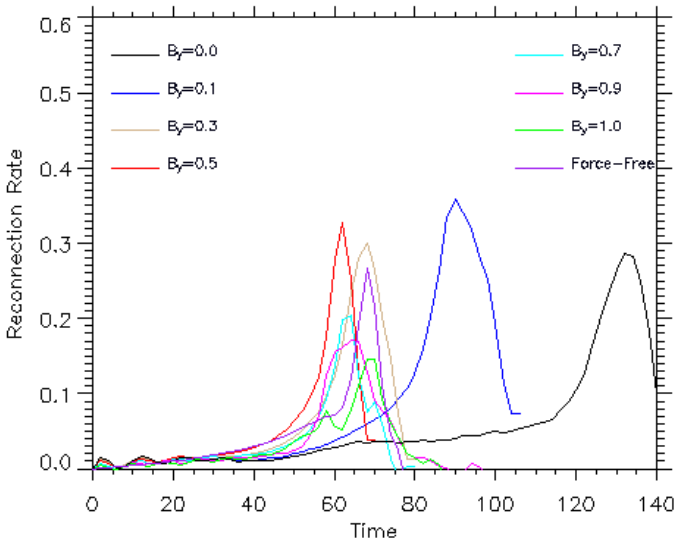

(b)

Figure 5.30: Figures showing the evolution of the simulations with varying strengths of guide field using the anti-parallel case as an initial configuration and also including the case of a linear force-free equilibrium. The reconnected flux is shown in Figure 5.30(a) and the corresponding reconnection rates in Figure 5.30(b). The colours represent the different strengths of the guide field in the initial configuration.

In comparison to the Harris sheet, the anti-parallel cases all showed a similar density depletion around the X-point. In the zero guide field case as in the Harris sheet case the current density was reduced at the X-point and enhanced in the regions adjacent to the reconnection region. In the stronger guide field cases the current density was actually enhanced at the X-points which is different to the Harris sheet cases where the current density was always reduced at the X-point. The linear force-free case is different to both the Harris sheet cases and the anti-parallel runs with there being both a significant number density and current density increase at the X-point.

Figure 5.27 shows the evolution of the x component of the current density for the linear force-free case. This shows that as reconnection proceeds the x component of the current density remains very small at and along a thin region either side of the X-point and that it is also reduced in the magnetic islands. In the final stages of the evolution the interaction of the multiple current layers leads to a breakdown of the structure of the x component of the current density.

A comparison of the evolution of the runs is given in Figure 5.30. This shows two plots, one for the reconnected flux for each case plotted using different colours to represent the strength of the guide field in each run where the reconnected flux is defined as

$$F(t) = \int_{B_z>0} dx\, B_z(z=0), \tag{5.29}$$

and the other shows the reconnection rate which is found from the gradient of the reconnected flux normalised against the maximum Alfvén speed at each timestep.

Examining the evolution from the plots of the reconnection rate shown in Figure 5.30(b), the reconnection rate in general is reduced when the guide field is of the order B_0. This is in agreement with previous studies that show that the reconnection rate is reduced once the guide field is large enough to significantly change the magnetic pressure in the system (e.g. Pritchett 2001; Ricci et al. 2004a) and is in agreement with the simulations using the Harris sheet as the initial configuration. The linear force-free case has a reconnection rate similar to that of the $B_{y0} = 0.3$ case suggesting that the shear field B_y does not strongly reduce the reconnection rate in comparison to the anti-parallel case in the way that the strong guide field does. The overall maximum reconnection rates are larger than those of the Harris sheet runs. This may be a result of the periodic boundary conditions which result in the complete reorganisation of the geometry of the magnetic field.

5.5.1 The Structure of the Diffusion Region

In this section the morphology of the off-diagonal components of the pressure tensor components are shown for the different runs. The structure of these pressure tensor components can be compared to the Harris sheet cases. It is also shown how the different contributions in Eq. (5.7)

make up the reconnection electric field in the vicinity of the X-point. This is the first time a systematic comparison of the structure of the diffusion region has been carried out which compares reconnection starting from an anti-parallel configuration with various strengths of guide field to reconnection starting from a self-consistent linear force-free equilibrium.

To investigate the structure of the off-diagonal components in the region of the central X-point it was originally intended to analyse them at the time of maximum reconnection rate which is given by the peaks of each curve in Figure 5.30(b) in the same way as the Harris sheet cases were investigated. The problem with this was though that at the time of maximum reconnection rate the pressure tensor components did not show the expected structure. This was due mainly to the interaction of the multiple current layers which led to a breakdown of the expected structure of the off-diagonal components at the central X-point which is a major difference from the Harris sheet cases. At earlier stages in the reconnection process the off-diagonal pressure tensor components do show the expected form. This can be seen in Figure 5.35 and Figure 5.36 which show the $P_{xy,e}$ and $P_{yz,e}$ components of the pressure tensor for the different strengths of guide field and including the force-free case, zoomed in around the X-point.

Figure 5.31 shows filled contour plots of y component of the current density for each case at earlier stages of reconnection when the off-diagonal components of the pressure tensor components show the expected structure. Figure 5.32 shows filled contour plots of the E_y electric field at these times. This shows that magnetic reconnection generates a strong E_y electric field in the vicinity of the X-Point. The region of enhanced E_y is larger in the strong guide field cases. The cases shown here are for the guide fields $B_{y0} = 0.0, 0.1, 0.3, 0.5, 0.7, 0.9, 1.0$ for the anti-parallel case and also the linear force-free case. In all the figures x_0 refers to the approximate position along x of the X-point. In all cases the position of the X-point along z is approximately at $z = 0$.

To demonstrate that the dominant contribution to the E_y electric field in the vicinity of the X-point is due to off-diagonal components of the electron pressure tensor Figure 5.33 and Figure 5.34 shows line plots along x and z of the contributions that make up the E_y electric field in Eq. (5.7) averaged between the times shown in Figure 5.32 for each case at which the pressure tensor components have the expected form. In each case it can be seen that the dominant contribution to the electric field close to the X-point comes from the gradients of the off-diagonal components of the electron pressure tensor (green lines).

In each of the plots shown in Figure 5.33 and Figure 5.34 the gradients of the off-diagonal components of the electron pressure tensor (green lines) dominate the electric field out to the point at which the $\mathbf{u} \times \mathbf{B}$ term (purple lines) equals the contribution from the gradients of the electron pressure tensor terms identical to the Harris sheet cases. The plots shown in Figure 5.33 show that the contribution from the gradients of the off diagonal pressure tensor components dominates to about $x \approx \pm 3c/\omega_{pi}$ either side of the X-point for the weak guide field cases but for the

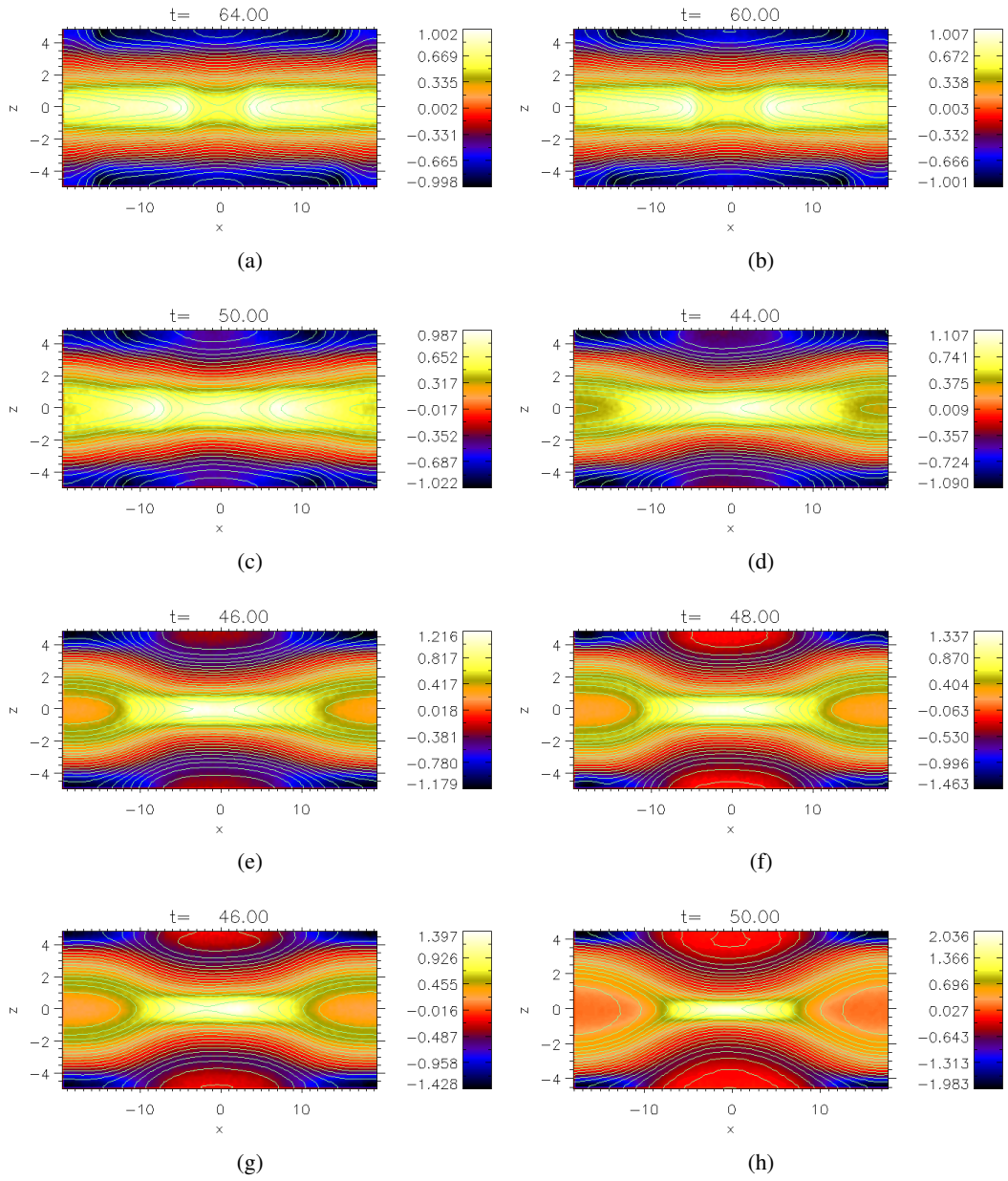

Figure 5.31: Plots of the y component of the current density with contours of the flux function overplotted for simulations with varying strengths of guide field and the force-free case at a time when the electron pressure tensor components show the expected structure. (a) $B_{y0} = 0.0$ ($x_0 = -0.28$), (b) $B_{y0} = 0.1$ ($x_0 = -0.56$), (c) $B_{y0} = 0.3$ ($x_0 = -1.68$), (d) $B_{y0} = 0.5$ ($x_0 = -2.24$), (e) $B_{y0} = 0.7$ ($x_0 = -0.56$), (f) $B_{y0} = 0.9$ ($x_0 = -2.24$), (g) $B_{y0} = 1.0$ ($x_0 = -1.68$), (h) linear force-free ($x_0 = -1.20$).

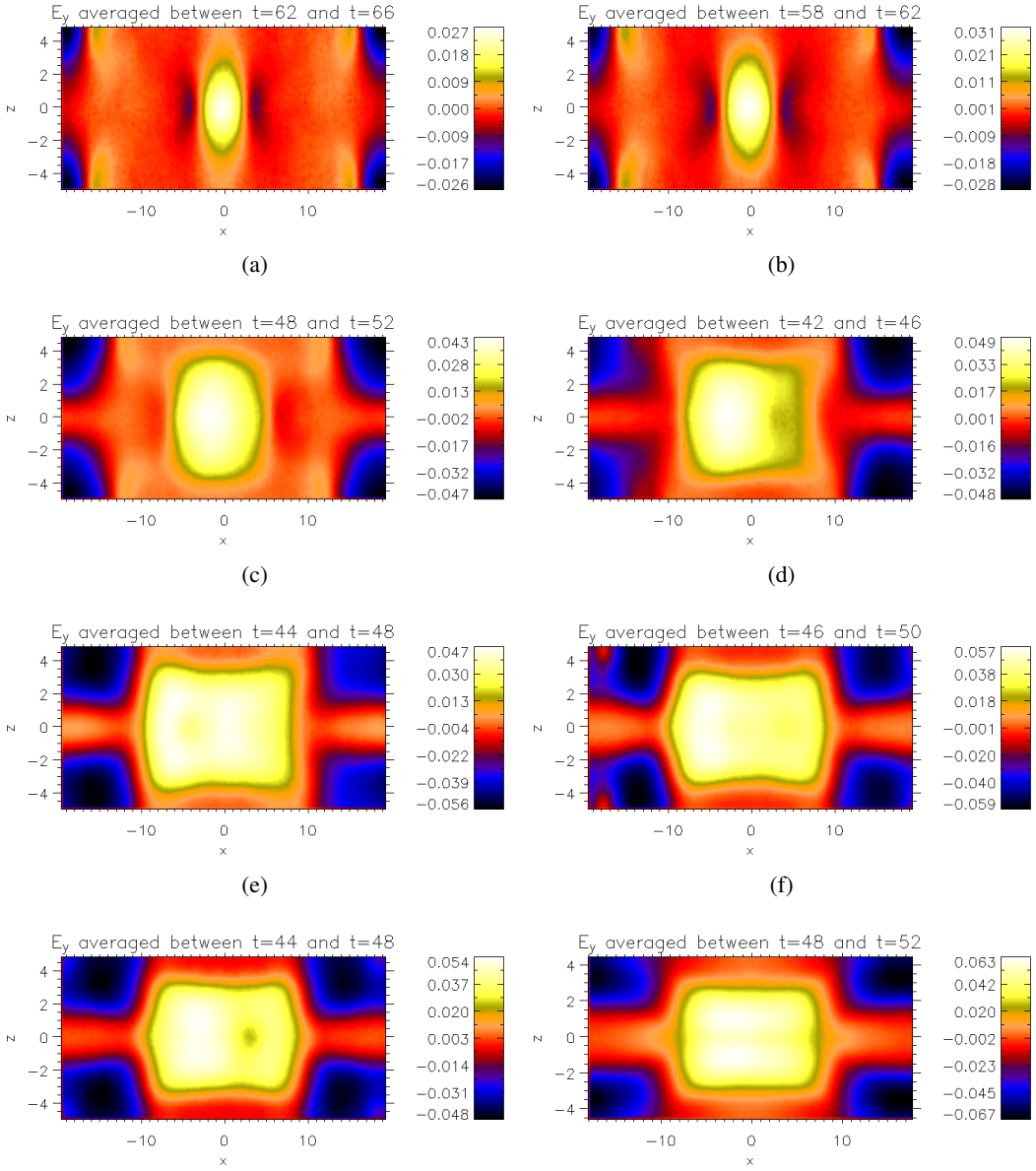

Figure 5.32: Plots of the y component of the electric field for simulations with varying strengths of guide field and the force-free case at a time when the electron pressure tensor components show the expected structure. (a) $B_{y0} = 0.0$ ($x_0 = -0.28$), (b) $B_{y0} = 0.1$ ($x_0 = -0.56$), (c) $B_{y0} = 0.3$ ($x_0 = -1.68$), (d) $B_{y0} = 0.5$ ($x_0 = -2.24$), (e) $B_{y0} = 0.7$ ($x_0 = -0.56$), (f) $B_{y0} = 0.9$ ($x_0 = -2.24$), (g) $B_{y0} = 1.0$ ($x_0 = -1.68$), (h) linear force-free ($x_0 = -1.20$).

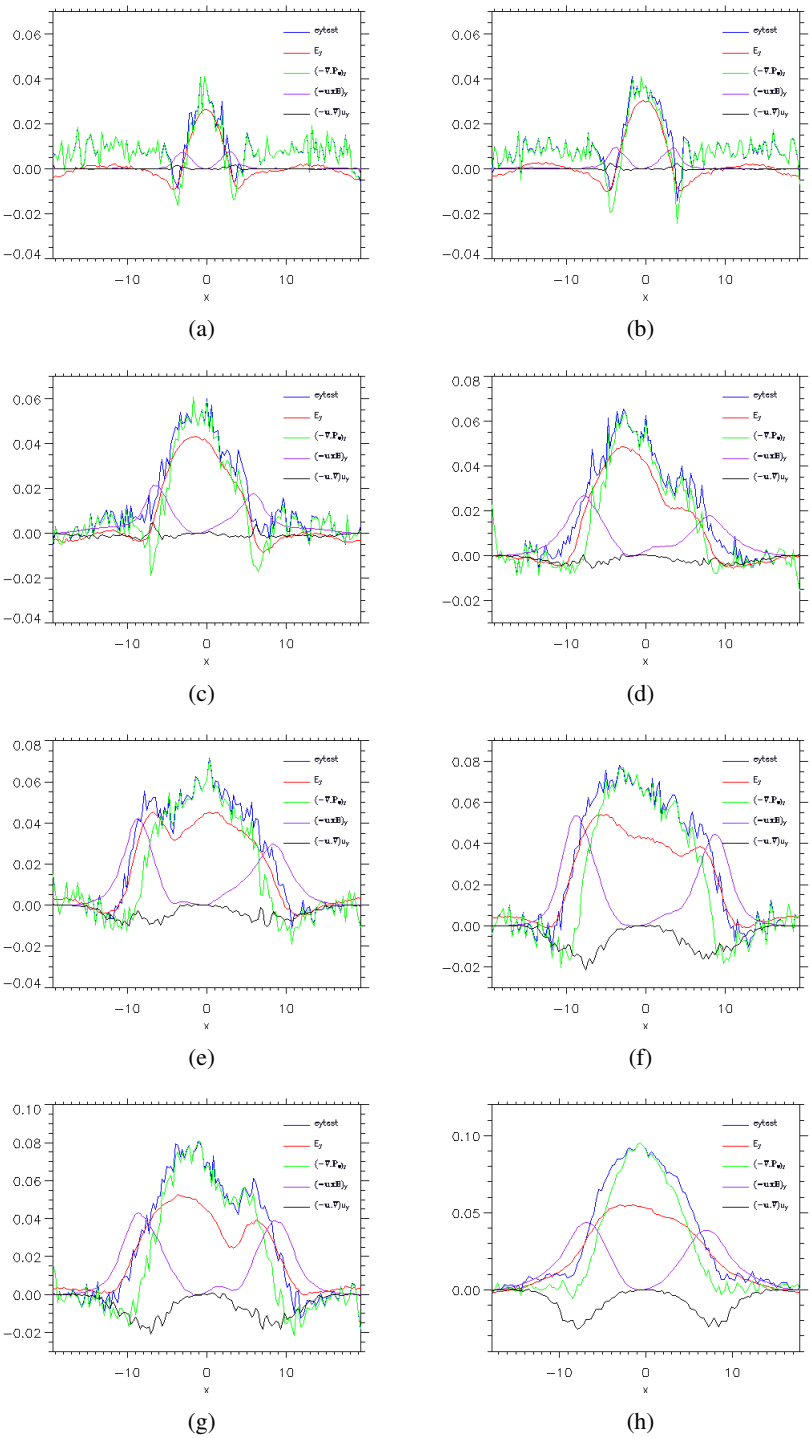

Figure 5.33: Plots along x for $z = 0$ of the contributions that make up the E_y electric field in Eq. (5.7) for simulations with varying strengths of guide field and the force-free case at a time when the electron pressure tensor components show the expected structure. (a) $B_{y0} = 0.0$ ($x_0 = -0.28$), (b) $B_{y0} = 0.1$ ($x_0 = -0.56$), (c) $B_{y0} = 0.3$ ($x_0 = -1.68$), (d) $B_{y0} = 0.5$ ($x_0 = -2.24$), (e) $B_{y0} = 0.7$ ($x_0 = -0.56$), (f) $B_{y0} = 0.9$ ($x_0 = -2.24$), (g) $B_{y0} = 1.0$ ($x_0 = -1.68$), (h) linear force-free ($x_0 = -1.20$).

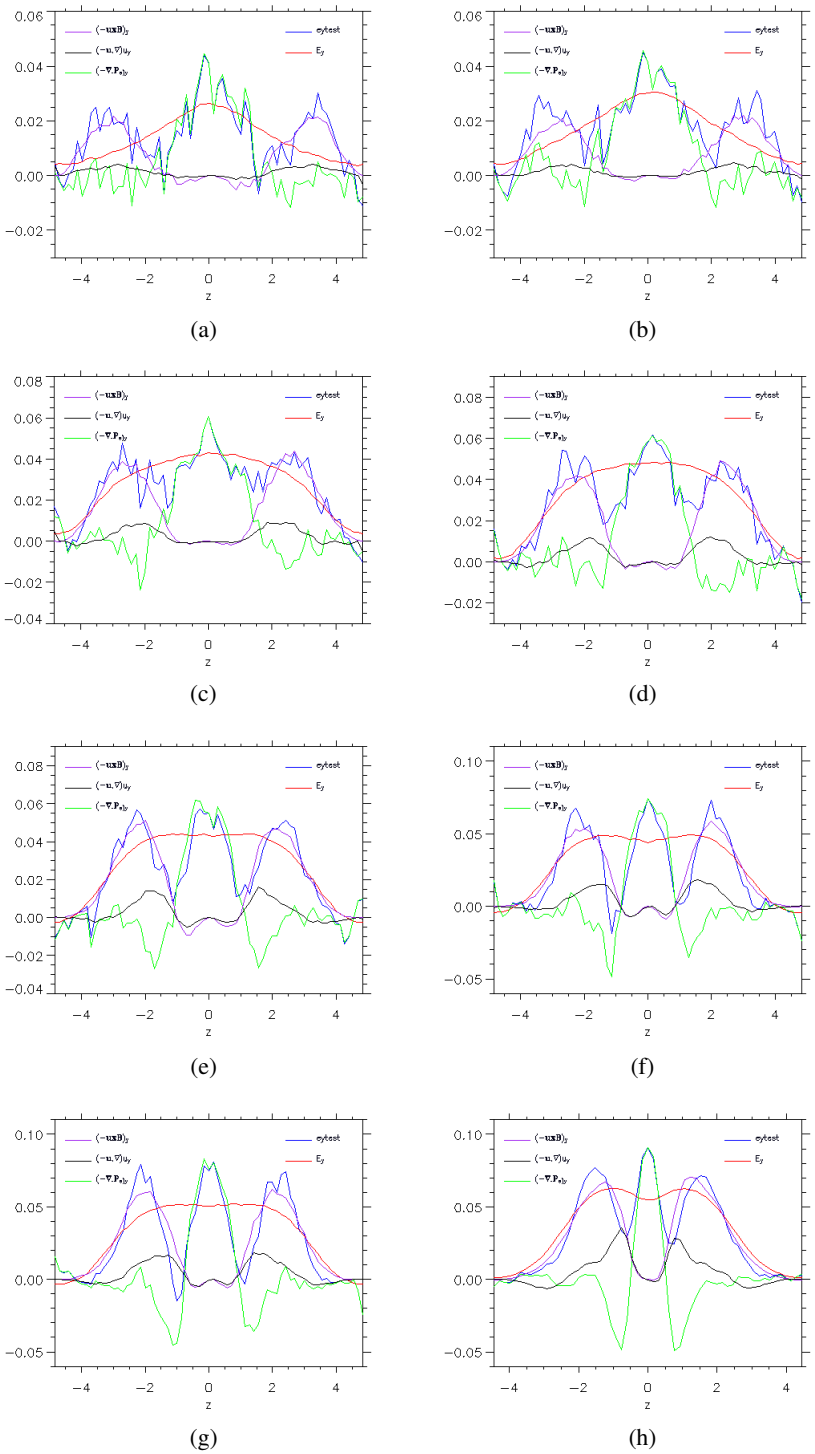

Figure 5.34: Plots along z for $x = x_0$ of the contributions that make up the E_y electric field in Eq. (5.7) for simulations with varying strengths of guide field and the force-free case at a time when the electron pressure tensor components show the expected structure. (a) $B_{y0} = 0.0$ ($x_0 = -0.28$), (b) $B_{y0} = 0.1$ ($x_0 = -0.56$), (c) $B_{y0} = 0.3$ ($x_0 = -1.68$), (d) $B_{y0} = 0.5$ ($x_0 = -2.24$), (e) $B_{y0} = 0.7$ ($x_0 = -0.56$), (f) $B_{y0} = 0.9$ ($x_0 = -2.24$), (g) $B_{y0} = 1.0$ ($x_0 = -1.68$), (h) linear force-free ($x_0 = -1.20$).

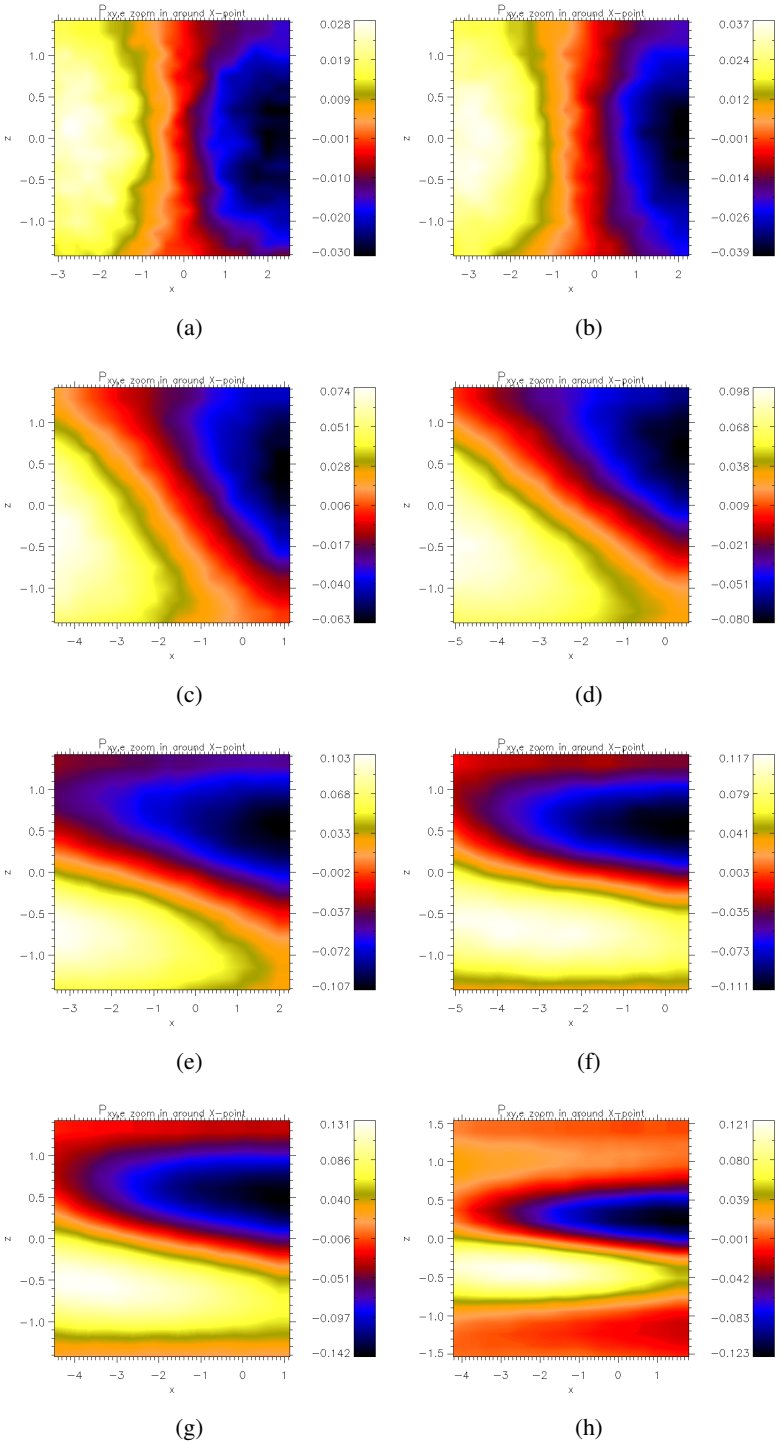

Figure 5.35: Plots of the $P_{xy,e}$ component of the electron pressure tensor for simulations with varying strengths of guide field and the force-free case at a time when the electron pressure tensor components show the expected structure. (a) $B_{y0} = 0.0$ ($x_0 = -0.28$), (b) $B_{y0} = 0.1$ ($x_0 = -0.56$), (c) $B_{y0} = 0.3$ ($x_0 = -1.68$), (d) $B_{y0} = 0.5$ ($x_0 = -2.24$), (e) $B_{y0} = 0.7$ ($x_0 = -0.56$), (f) $B_{y0} = 0.9$ ($x_0 = -2.24$), (g) $B_{y0} = 1.0$ ($x_0 = -1.68$), (h) linear force-free ($x_0 = -1.20$).

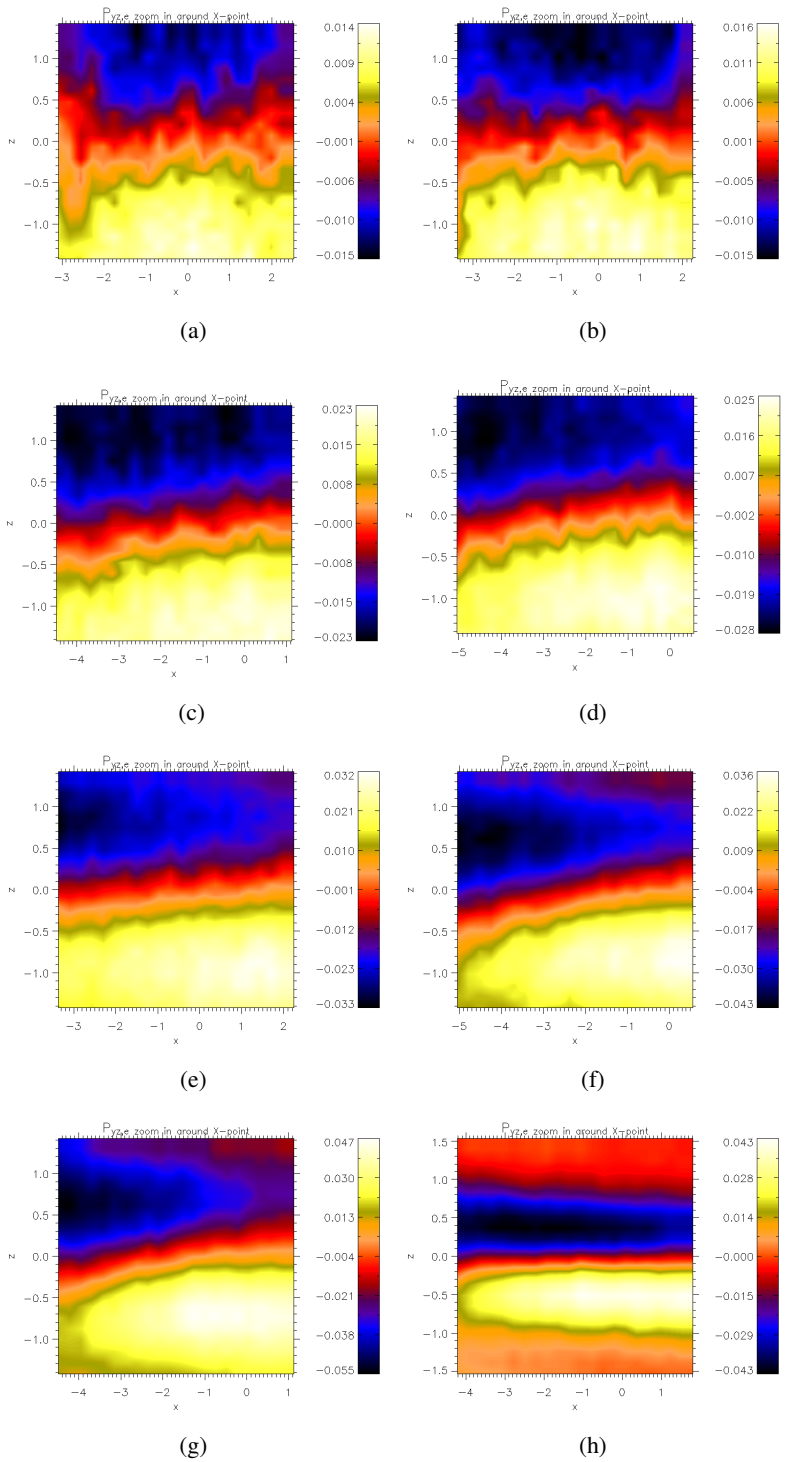

Figure 5.36: Plots of the $P_{yz,e}$ component of the electron pressure tensor for simulations with varying strengths of guide field and the force-free case at a time when the electron pressure tensor components show the expected structure. (a) $B_{y0} = 0.0$ ($x_0 = -0.28$), (b) $B_{y0} = 0.1$ ($x_0 = -0.56$), (c) $B_{y0} = 0.3$ ($x_0 = -1.68$), (d) $B_{y0} = 0.5$ ($x_0 = -2.24$), (e) $B_{y0} = 0.7$ ($x_0 = -0.56$), (f) $B_{y0} = 0.9$ ($x_0 = -2.24$), (g) $B_{y0} = 1.0$ ($x_0 = -1.68$), (h) linear force-free ($x_0 = -1.20$).

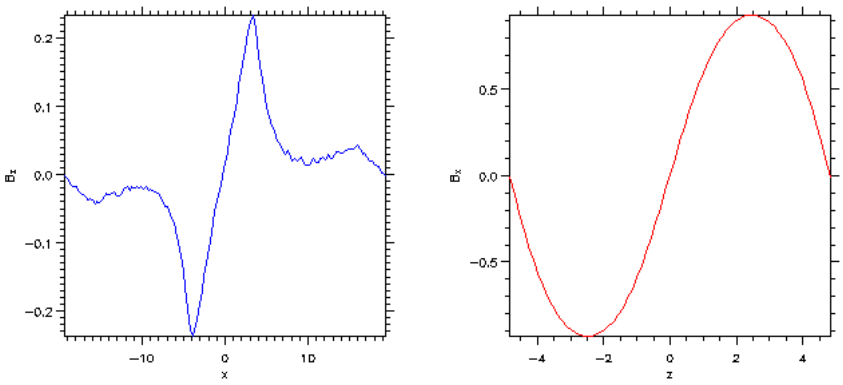

(a) (b)

Figure 5.37: Plots along x of the B_z component of the magnetic field and of the B_x component of the magnetic field along z going through the position of the X-point at a time when the off-diagonal components of the electron pressure tensor show the expected structure for the zero guide field (anti-parallel) case.

stronger guide field cases the gradients of the electron pressure tensor components dominate out to $x \approx \pm 6c/\omega_{pi}$. There is also a degree of asymmetry around the X-point. For the linear force-free case the gradients of the electron pressure tensor components dominate out to $x \approx \pm 5c/\omega_{pi}$. The plots shown in Figure 5.34 indicate that the contribution from the off diagonal pressure tensor components dominates to about $z \approx \pm 1.5c/\omega_{pi}$ either side of the X-point for the weak guide field cases whilst for the strong guide field cases they dominate up to $z \approx \pm 0.8c/\omega_{pi}$ either side of the X-point. In the force-free case the gradients of the electron pressure tensor components dominate out to only $z \approx \pm 0.5c/\omega_{pi}$ either side of the X-point.

In comparison to the Harris sheet cases these simulation runs starting from anisotropic equilibria give the same features. In all cases the mechanism that breaks the frozen in condition and dominates the contribution to the inductive electric field near to the X-point is due to gradients of the off-diagonal components of the electron pressure tensor. It must be pointed out though that for all the figures shown here, they are at an earlier time than the time of maximum reconnection rate that correspond to the peaks of the lines shown in Figure 5.30(b). This is because at the time of maximum reconnection rate, the periodic boundary conditions and the interaction of the multiple current layers in the simulation box, lead to the breakdown of the expected structure of the pressure tensor components. Examples of this are shown in Figures 5.38 - 5.45. Therefore to compare equally to the Harris sheet cases and to understand the dominant mechanism that breaks the frozen in condition, an earlier time in the reconnection process was investigated.

Although, as in the Harris sheet cases the dominant term in the vicinity of the X-point is clearly due to the gradients of the off-diagonal terms of the electron pressure tensor, there is a small

contribution to the electric field from the electron inertia term (black lines) at the edge of the diffusion regime. The electron inertia term is not significant in the weak guide field cases. It can be seen in the plots along z of the contributions to the reconnection electric field shown in Figure 5.34 that as the guide field increases in strength the contribution from the electron inertia term at the edge of the diffusion region grows. In the strong guide field cases the electron inertia term is equal to the value of the $\mathbf{u} \times \mathbf{B}$ term at the edge of the diffusion region. In fact the linear force-free case has the largest contribution to the E_y electric field from the electron inertia term at the edge of the diffusion regime. As mentioned in the discussion of the Harris sheet cases, in a recent paper by Hesse et al. (2004) it was shown that within a collisionless skin depth there was a finite contribution from the electron inertia at the edge of the localised current region. In that paper the initial condition was a Harris sheet with a guide field of $B_{y0} = 0.8$. The main contribution to the E_y electric field close to the X-point was still due to the nongyrotropic pressures. The results shown here starting from the anisotropic equilibria are again consistent with this. The significant contribution from the electron inertia term is due the small scales associated with the electron Larmor radius in the strong guide field case.

To investigate further the structure of the off-diagonal pressure tensor components, Figure 5.35 and Figure 5.36 shows filled contour plots of the $P_{xy,e}$ and $P_{yz,e}$ components of the electron pressure tensor zoomed in around the position of the central X-point. In the anti-parallel case the $P_{xy,e}$ component is approximately symmetrical about the line $x = x_0$ which goes through the X-point with a gradient in x. The $P_{yz,e}$ component of the pressure tensor is approximately symmetrical about the $z = 0$ line going through the X-point with a gradient in z. As the guide field is increased the structure of the $P_{xy,e}$ component starts to change. The symmetry along the line $x = x_0$ is broken and the structure is seen to rotate in an anti-clockwise direction until at the guide field $B_{y0} = 1.0$ the $P_{xy,e}$ component is almost symmetrical along the line $z = 0$ with a gradient in z identical to the Harris sheet cases. The central region in all of the plots can also be seen to thin. The $P_{yz,e}$ component of the electron pressure tensor is seen to rotate very slightly in the anti-clockwise direction. The significant rotation anti-clockwise and then clockwise as seen in the Harris sheet cases is not so obvious. It is also quite noisy in the weak guide field cases in particular. In the strong guide field cases there is though almost symmetry about the $z = 0$ line and once again the central region is observed to thin slightly as the guide field becomes large. The central region is thinnest in the linear force-free case. The $P_{yz,e}$ component is almost completely symmetrical about $z = 0$ line in this case with a gradient in z.

The thinning of the central region in Figure 5.35 and Figure 5.36 is due to the introduction of the guide field. In the case of the Harris sheet without a guide field the characteristic length scale of $P_{xy,e}$ and $P_{yz,e}$ has been shown to be given approximately by the electron bounce widths in a field reversal λ_x and λ_z (e.g. Hesse et al. 1999). In these simulations the electron bounce width in the x and z directions for the anti-parallel field configuration as given by Eqs. (5.3) and (5.4) at the

time shown in Figure 5.31(a) are of the order $\lambda_x \approx 3.4c/\omega_{pi}$ and $\lambda_z \approx 1.1c/\omega_{pi}$. Plots of the x and z component of the magnetic field along z and x respectively for the anti-parallel case at the time shown in Figure 5.31(a) at which the off-diagonal components of the electron pressure tensor show the correct form are shown in Figure 5.37. These are used to calculate estimates of the bounce widths λ_x and λ_z. In the strong guide field case for the Harris sheet it has been shown that the characteristic length scale changes to that of the thermal electron Larmor radius $r_L = v_{th,e}/\Omega_e$ in the guide magnetic field (Hesse et al. 2004). The electron Larmor radius for the simulation with $B_{y0} = 1.0$ at the time shown in Figure 5.31(g) is of the order $r_L \approx 0.75c/\omega_{pi}$. This characteristic change of length scale can be seen in Figure 5.35 and Figure 5.36 as the strength of the guide field is increased and is consistent with the Harris sheet cases.

The thermal electron Larmor radius for the linear force-free case at the time shown in Figure 5.31(h) based on the maximum value of the shear component of the magnetic field at the X-point ($B_y \approx 0.58$) is of the order $r_L \approx 1.0c/\omega_{pi}$. This estimate of the thermal electron Larmor radius based on the shear magnetic field at the X-point is larger than for the guide field case $B_{y0} = 1.0$ but the central regions of the plots of $P_{xy,e}$ and $P_{yz,e}$ shown in Figure 5.35 and Figure 5.36 are in fact thinner than for the equivalent plots for the guide field case $B_{y0} = 1.0$. Therefore, for the force-free case these results suggest that the characteristic length scale may be even smaller than the thermal electron gyroradius in the shear magnetic field.

To illustrate how the interaction of the multiple current layers leads to the break up of the structure of the pressure tensor components at the central X-point it is useful to look at the time evolution of the off-diagonal components of the pressure tensor components. As examples of this the evolutions for the $P_{xy,e}$ component and the $P_{yz,e}$ component for the anti-parallel cases with a guide field of $B_{y0} = 0.0, B_{y0} = 0.5, B_{y0} = 1.0$ and the linear force-free case are shown in Figures 5.38 - 5.45. The snapshots show the off-diagonal components throughout the whole simulation domain. It can be seen that at the early stages of reconnection the pressure tensor components at the central X-point have the expected structure and then as time proceeds the interaction of the boundary with the central current layer leads to the breakdown of this structure. The overall evolution is also shown in the movies that come with the thesis (see Appendix B).

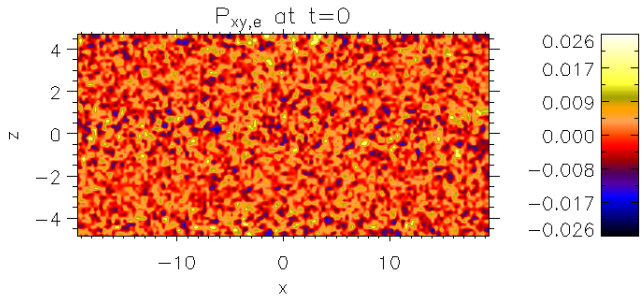

(a)

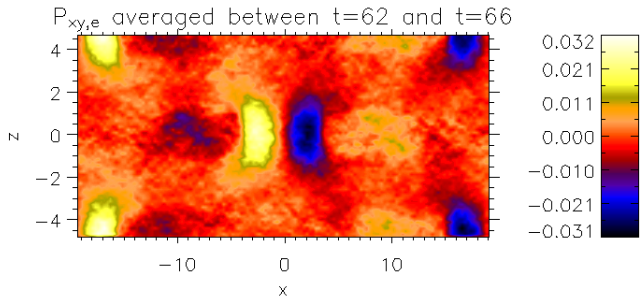

(b)

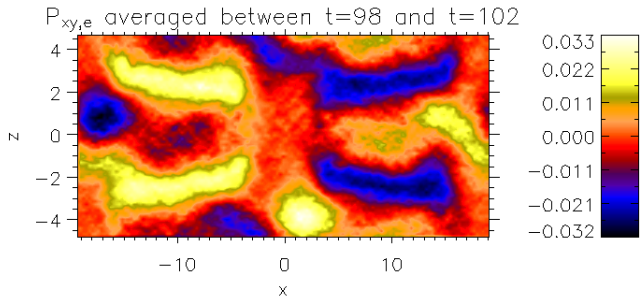

(c)

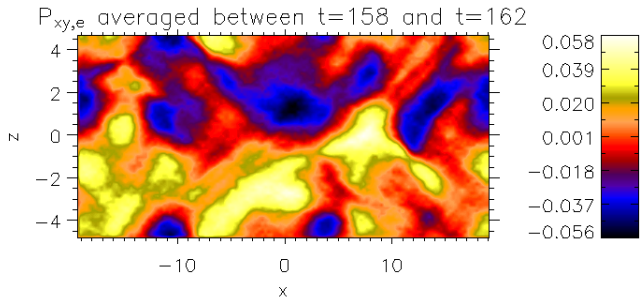

(d)

Figure 5.38: Plots of the evolution of the $P_{xy,e}$ component of the electron pressure tensor for the anti-parallel case with zero guide field. The plots correspond to the $P_{xy,e}$ component at (a) $t = 0$ and averaged around (b) $t = 64$, (c) $t = 100$ and (d) $t = 160$.

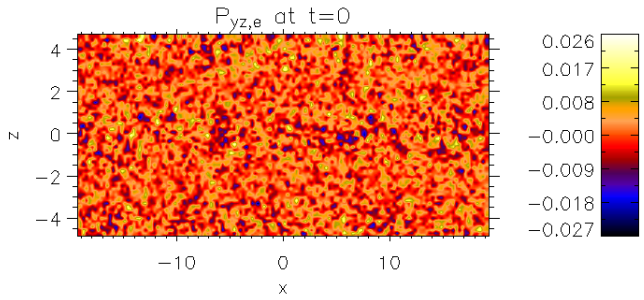

(a)

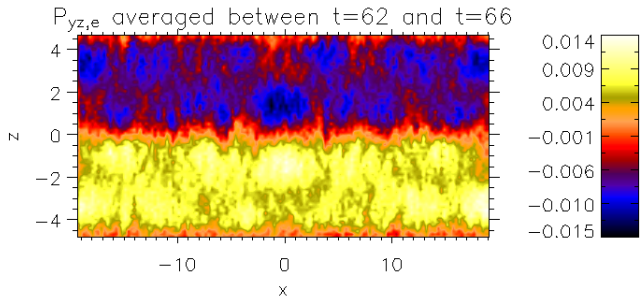

(b)

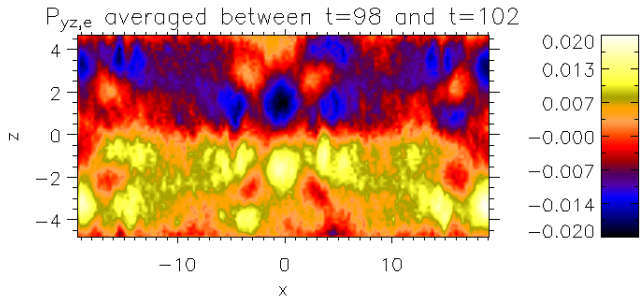

(c)

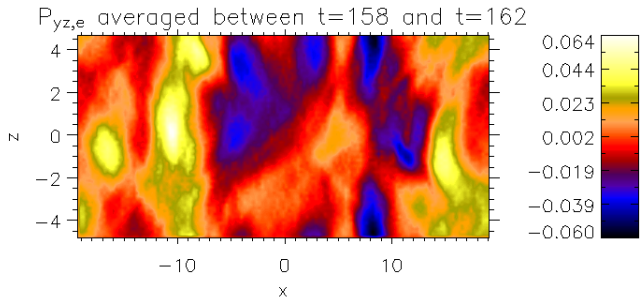

(d)

Figure 5.39: Plots of the evolution of the $P_{yz,e}$ component of the electron pressure tensor for the anti-parallel case with zero guide field. The plots correspond to the $P_{yz,e}$ component at (a) $t = 0$ and averaged around (b) $t = 64$, (c) $t = 100$ and (d) $t = 160$.

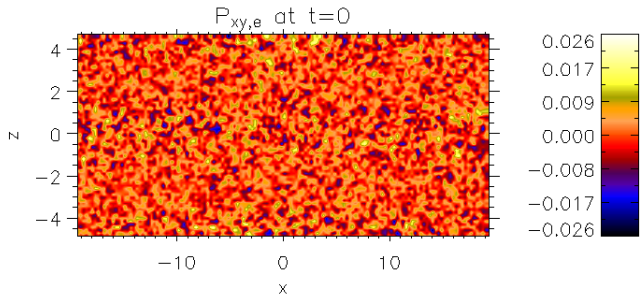

(a)

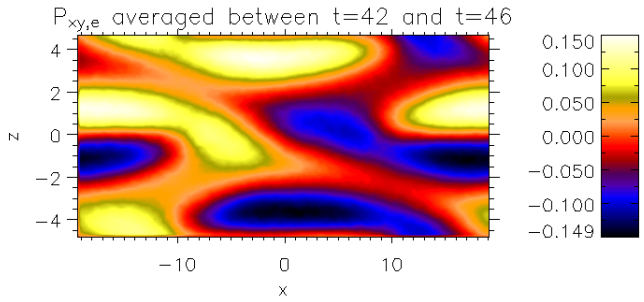

(b)

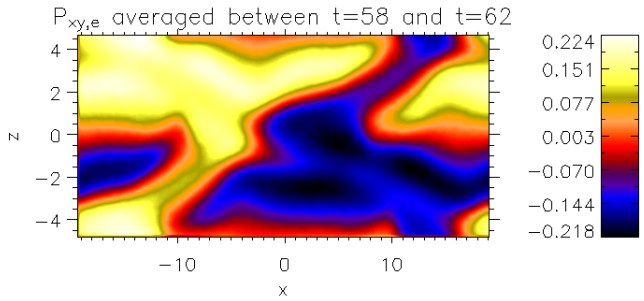

(c)

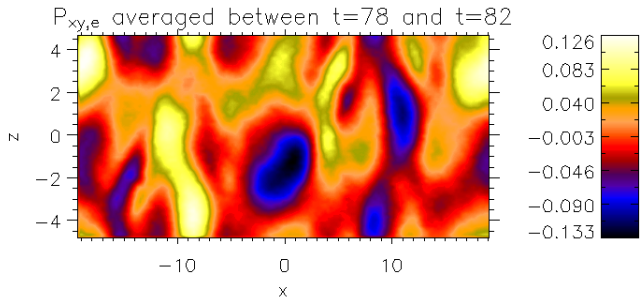

(d)

Figure 5.40: Plots of the evolution of the $P_{xy,e}$ component of the electron pressure tensor for the anti-parallel case with a guide field of $B_{y0} = 0.5$. The plots correspond to the $P_{xy,e}$ component at (a) $t = 0$ and averaged around (b) $t = 44$, (c) $t = 60$ and (d) $t = 80$.

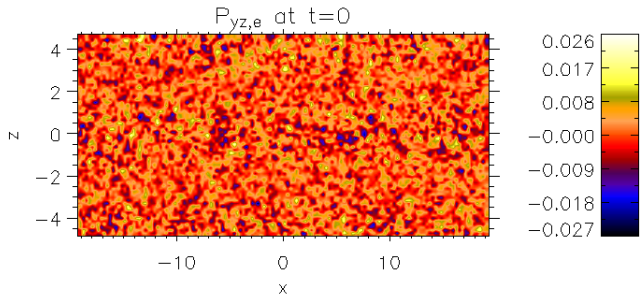

(a)

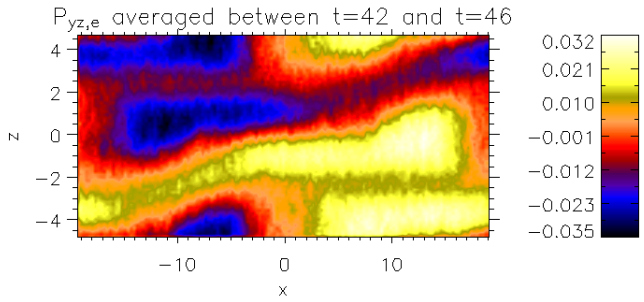

(b)

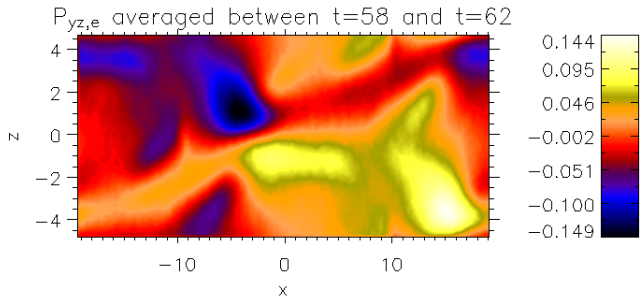

(c)

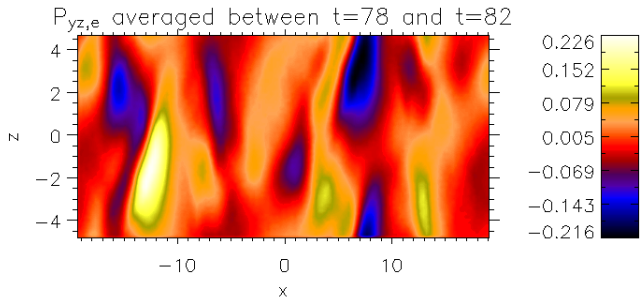

(d)

Figure 5.41: Plots of the evolution of the $P_{yz,e}$ component of the electron pressure tensor for the anti-parallel case with a guide field of $B_{y0} = 0.5$. The plots correspond to the $P_{yz,e}$ component at (a) $t = 0$ and averaged around (b) $t = 44$, (c) $t = 60$ and (d) $t = 80$.

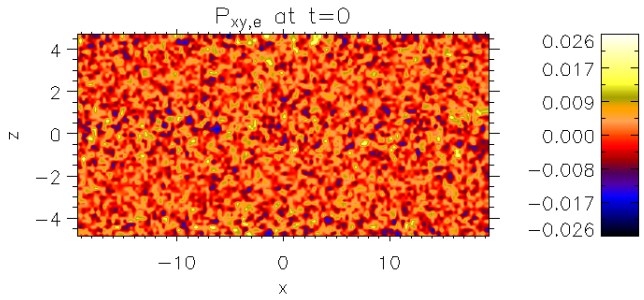

(a)

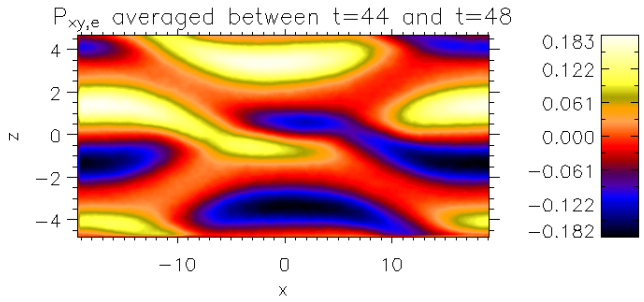

(b)

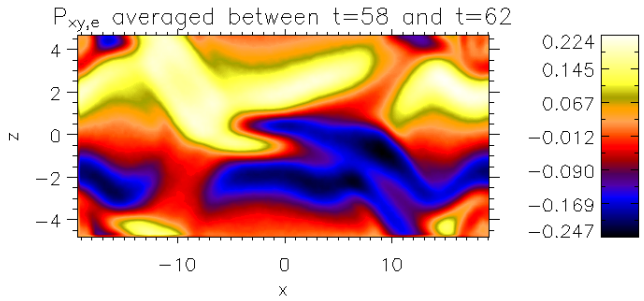

(c)

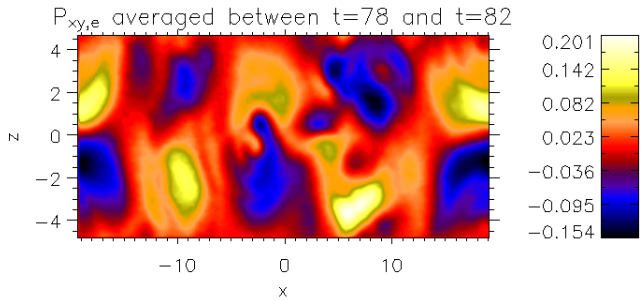

(d)

Figure 5.42: Plots of the evolution of the $P_{xy,e}$ component of the electron pressure tensor for the anti-parallel case with a guide field of $B_{y0} = 1.0$. The plots correspond to the $P_{xy,e}$ component at (a) $t = 0$ and averaged around (b) $t = 46$, (c) $t = 60$ and (d) $t = 80$.

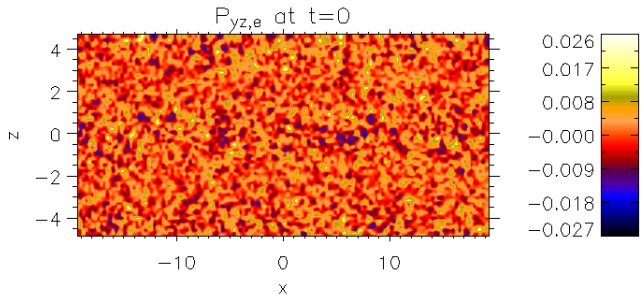

(a)

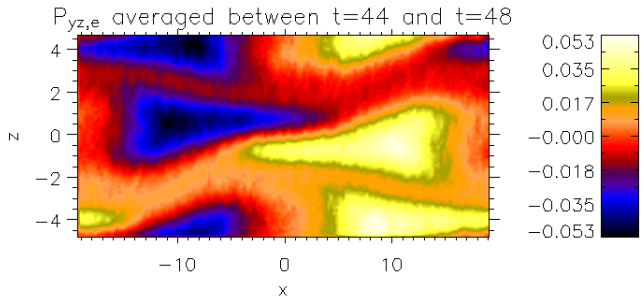

(b)

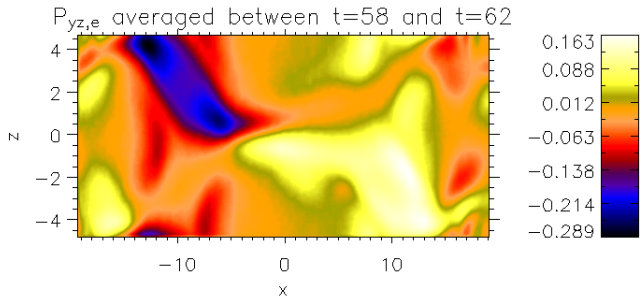

(c)

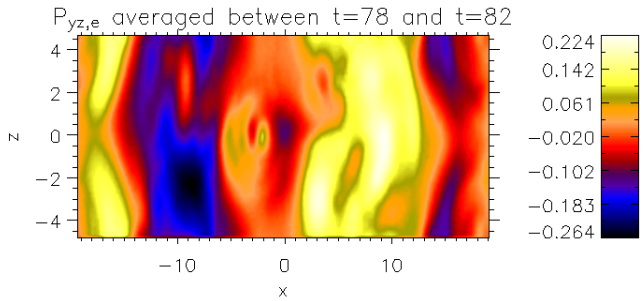

(d)

Figure 5.43: Plots of the evolution of the $P_{yz,e}$ component of the electron pressure tensor for the anti-parallel case with a guide field of $B_{y0} = 1.0$. The plots correspond to the $P_{yz,e}$ component at (a) $t = 0$ and averaged around (b) $t = 46$, (c) $t = 60$ and (d) $t = 80$.

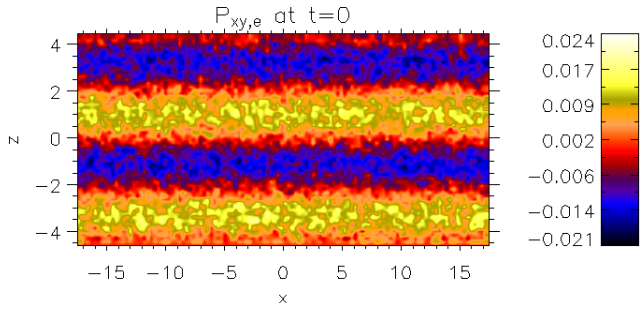

(a)

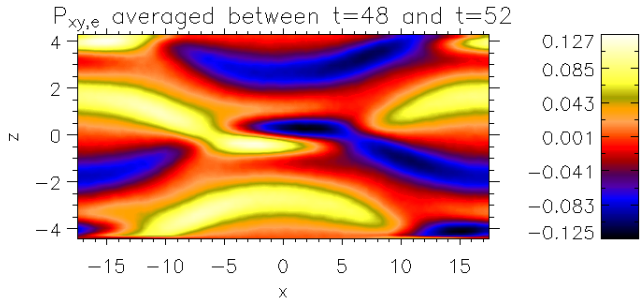

(b)

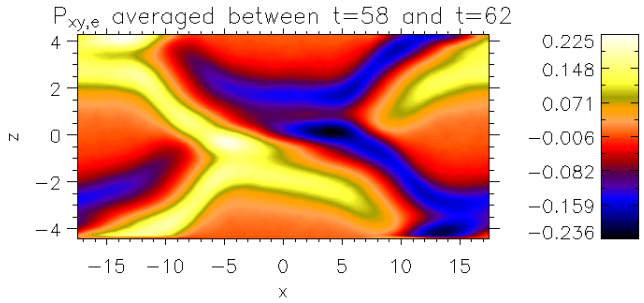

(c)

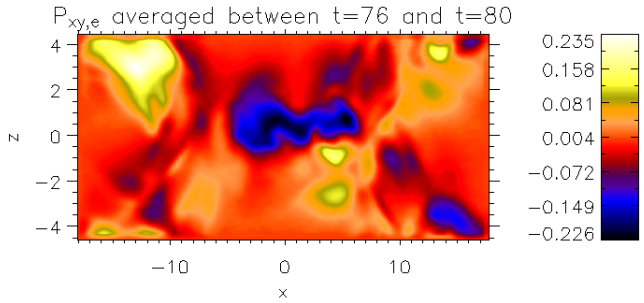

(d)

Figure 5.44: Plots of the evolution of the $P_{xy,e}$ component of the electron pressure tensor for the linear force-free case. The plots correspond to the $P_{xy,e}$ component at (a) $t = 0$ and averaged around (b) $t = 50$, (c) $t = 60$ and (d) $t = 78$.

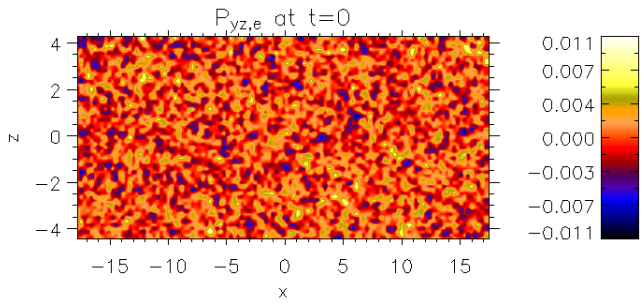

(a)

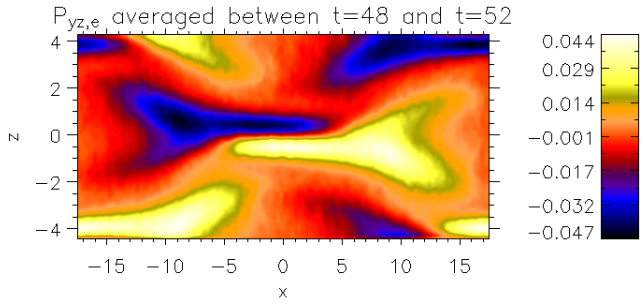

(b)

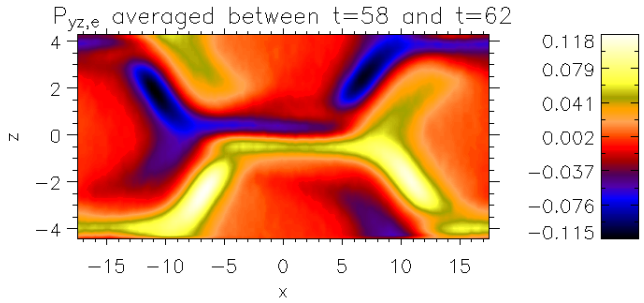

(c)

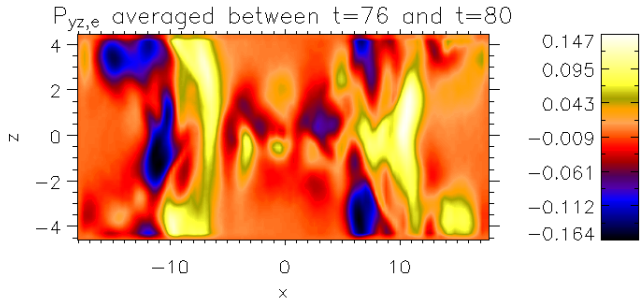

(d)

Figure 5.45: Plots of the evolution of the $P_{yz,e}$ component of the electron pressure tensor for the linear force-free case. The plots correspond to the $P_{yz,e}$ component at (a) $t = 0$ and averaged around (b) $t = 50$, (c) $t = 60$ and (d) $t = 78$.

5.6 Double Harris Sheet Simulations ($m_i/m_e = 1$)

In this section simulations starting from a double Harris sheet equilibrium with varying strengths of guide field are shown to compare to the anisotropic bi-Maxwellian simulation runs. The double Harris sheet also requires periodic boundary conditions in both x and z. This initial state was investigated to confirm that the complete re-organisation of the magnetic field and interaction of the multiple current layers which lead to the breakdown of the structure of the electron pressure tensor components is due to the doubly periodic boundary conditions that are imposed when using periodic equilibria as initial conditions. The results are also compared to the Harris sheet cases.

In the following simulation results the ion to electron mass ratio is equal to one ($m_i/m_e = 1$). Lengths are normalized to the ion inertial length c/ω_{pi} and the number density is normalised to a value n_0. Times are normalised to the inverse of the ion cyclotron frequency $\Omega_i = eB_0/m_i$. The magnetic field is normalised to the value B_0, the amplitude of the initial magnetic field. The system dimensions are $L_x = 20.0\, c/\omega_{pi}$ and $L_z = 8.0\, c/\omega_{pi}$ where L_x and L_z are the half lengths of the box in the x and z directions, with a grid that is 140×70 in the x and z directions. A time step $\omega_{pe}\Delta t = 1$ is used. The ratio ω_{pe}/Ω_e is set to a numerical value of 5.

The initial configuration is a double Harris sheet. The magnetic field is given by

$$B_x = \begin{cases} -\tanh\left(\frac{(z+L_z)}{L}\right) & -L_z \leq z \leq -L_z/2 \\ \tanh\left(\frac{z}{L}\right) & -L_z/2 \leq z \leq L_z/2 \\ -\tanh\left(\frac{(z-L_z)}{L}\right) & L_z/2 \leq z \leq L_z, \end{cases} \tag{5.30}$$

where $L = 1.2$. The electron and ion densities are given by

$$n = \begin{cases} \frac{1}{\cosh^2\left(\frac{(z+L_z)}{L}\right)} & -L_z \leq z \leq -L_z/2 \\ \frac{1}{\cosh^2\left(\frac{z}{L}\right)} & -L_z/2 \leq z \leq L_z/2 \\ \frac{1}{\cosh^2\left(\frac{(z-L_z)}{L}\right)} & L_z/2 \leq z \leq L_z. \end{cases} \tag{5.31}$$

There will be jumps in the derivatives at the boundaries between each part of the solution for B_x and n but these derivatives will be small such that they will not have any significant effect. The double Harris sheet is not a force-free equilibrium with the force balance maintained by the plasma pressure gradient.

For each simulation run a perturbation of the form

$$B_{xp} = a_0 \frac{\pi}{L_z} \sin\left(\frac{\pi z}{L_z}\right), \tag{5.32}$$

$$B_{zp} = a_0 \frac{\pi}{L_x} \sin\left(\frac{\pi x}{L_x}\right), \tag{5.33}$$

is also added where L_x and L_z are the half lengths of the box in the x and z directions. This field perturbation gives X-points at $(0,0), (L_x, L_z), (L_x, -L_z), (-L_x, L_z)$ and $(-L_x, -L_z)$. O-points are located at $(0, L_z), (0, -L_z), (-L_x, 0)$ and $(L_x, 0)$. Periodic boundary conditions are employed at $x = -L_x$ and $x = L_x$ and at $z = -L_z$ and $z = L_z$.

There are two particle populations. The foreground population consists of the first set of ions and electrons which establish the equilibrium pressures and currents. In the simulation runs temperatures are set such that $T_i + T_e = 0.5$, with $T_e/T_i = 1$. The second population consists of the second set of ions and electrons and constitutes a constant background density $n_b = 0.2$. The background temperatures are identical to the foreground population $T_e + T_i = 0.5$, with $T_e/T_i = 1.0$. The simulation run used 2×10^7 ions and electrons each for the foreground and 3×10^7 ions and electrons for the background.

The initial configuration at $t = 0$ is illustrated in Figure 5.46. A filled contour plot of B_x is shown in Figure 5.46(a) with a line plot of the magnetic field profile plotted along z for $x = 0$ shown in Figure 5.46(b). Figure 5.46(c) is a filled contour plot of the y component of the current density with contours of the flux function overplotted showing the magnetic field lines. It is clear to see the periodic profile of the x component of the magnetic field and also the current sheet structure of j_y with X-points located at the centre and corners of the box and the 0-points located in between the X-points that are introduced by the perturbation to the equilibrium magnetic field.

Figures 5.47 - 5.49 show the evolution of the magnetic field for three different runs with the y component of the current density colour coded. Figure 5.47 shows the evolution for the initial configuration with zero guide field. Figure 5.48 shows the evolution for the initial configuration with a guide field of value $B_{y0} = 0.5$ and Figure 5.49 shows the evolution for the intial configuration with a guide field of value $B_{y0} = 1.0$. Movies of the evolution for each case can be found on the CD which is attached to this thesis (see Appendix B). It is important to note that the colour bar scale changes between each of the snapshots to range between the minimum and maximum values of the y component of the current density.

These figures show how magnetic reconnection proceeds and leads to large changes in the magnetic field structure. In the case with zero guide field the current density becomes reduced at the central X-point and enhanced in the regions adjacent to the diffusion region. In the cases with stronger guide field the current density becomes enhanced at the X-point. At late times in the simulation runs the magnetic field structure has changed dramatically. The magnetic field configuration has gone from having a (B_x, B_y) structure to having a mainly (B_y, B_z) structure and exhibits the same behaviour as the anisotropic bi-Maxwellian cases in Sec. 5.5. In all the simulation runs in the majority of the simulation box the y component of the current density has

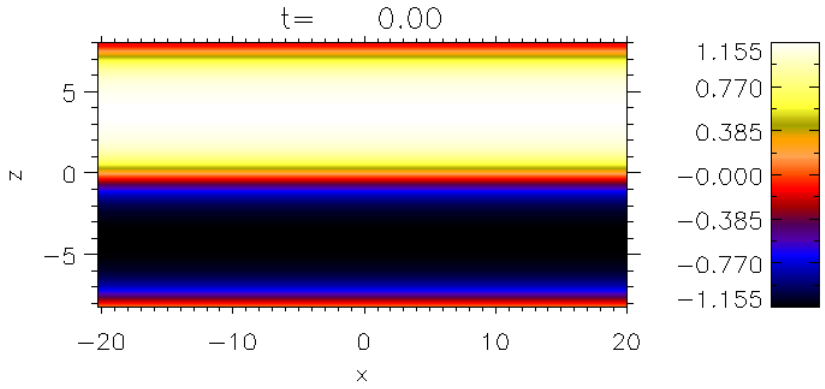

(a)

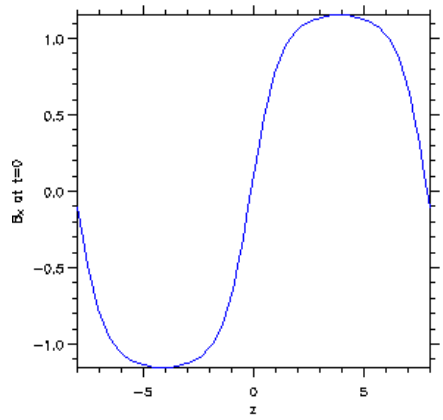

(b)

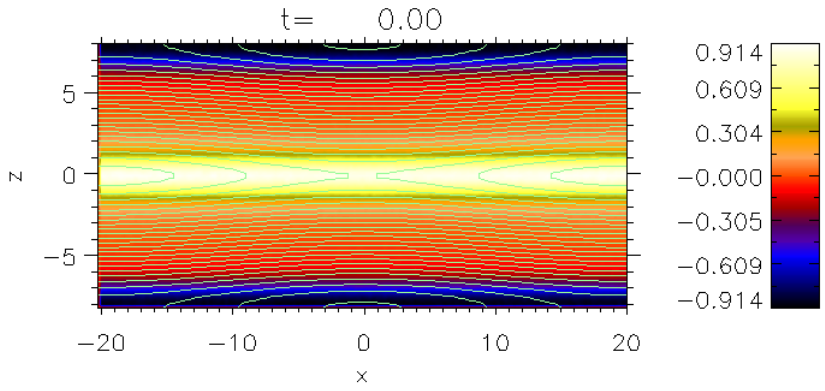

(c)

Figure 5.46: Plots showing the initial configuration for the double Harris sheet. Figure 5.46(a) shows a colour contour plot of B_x and Figure 5.46(b) shows a line plot of the profile of B_x along z for $x = 0$. Figure 5.46(c) shows a filled contour plot of the y component of the current density with magnetic field lines corresponding to contours of the flux function overplotted.

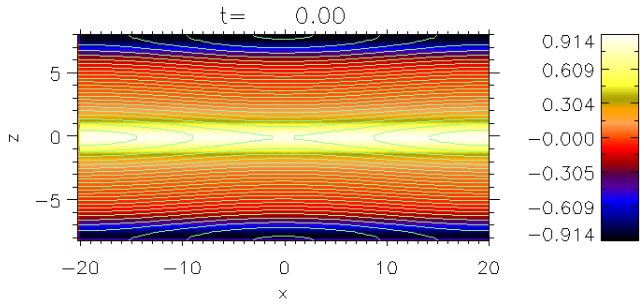

(a)

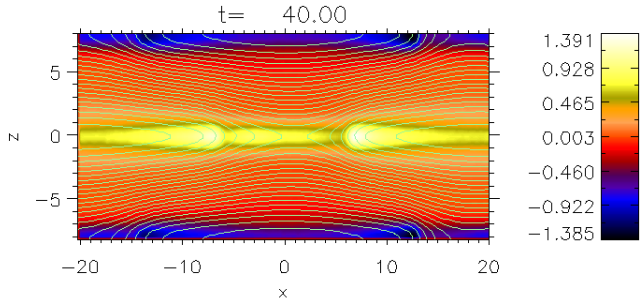

(b)

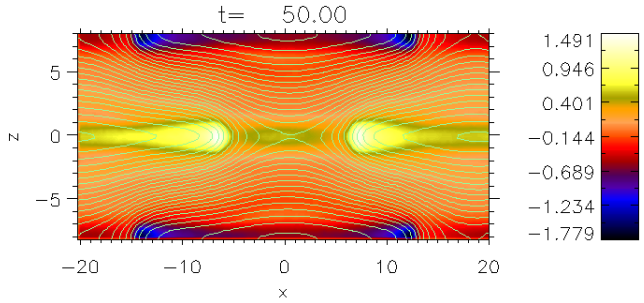

(c)

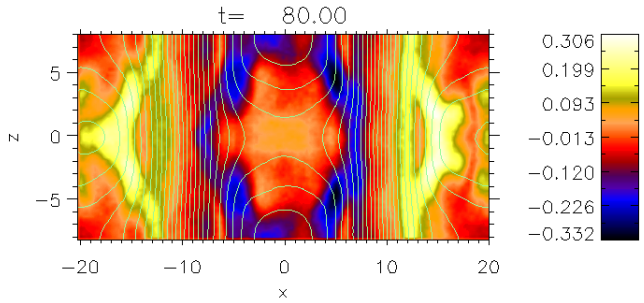

(d)

Figure 5.47: Plots of the y component of the current density with contours of the flux function overplotted for the double Harris sheet run with zero guide field. The plots correspond to the different times (a) $t = 0$, (b) $t = 40$, (c) $t = 50$ and (d) $t = 80$.

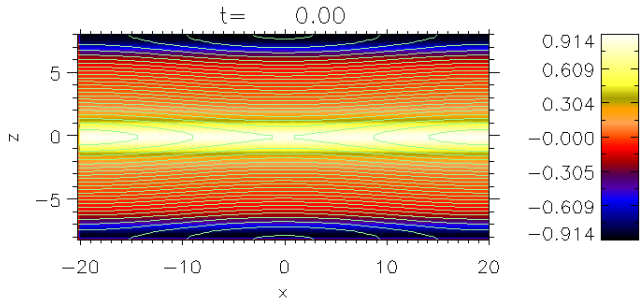

(a)

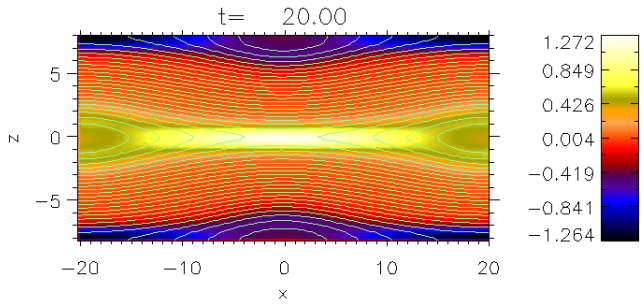

(b)

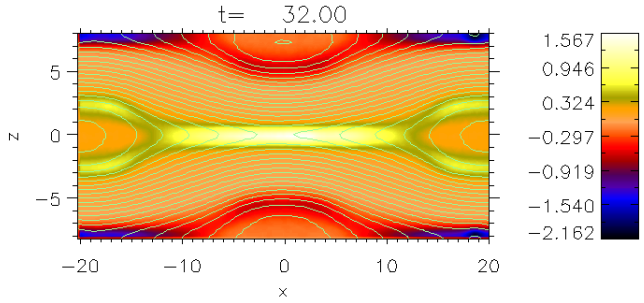

(c)

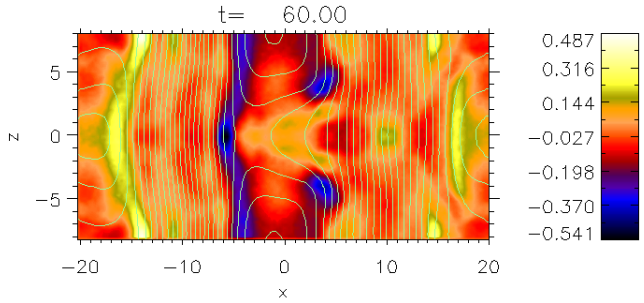

(d)

Figure 5.48: Plots of the y component of the current density with contours of the flux function overplotted for the double Harris sheet run with a guide field of value $B_{y0} = 0.5$. The plots correspond to the different times (a) $t = 0$, (b) $t = 20$, (c) $t = 32$ and (d) $t = 60$.

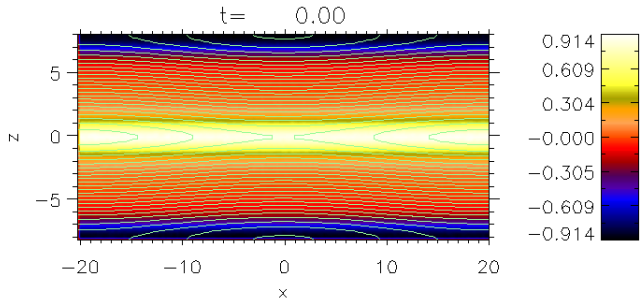

(a)

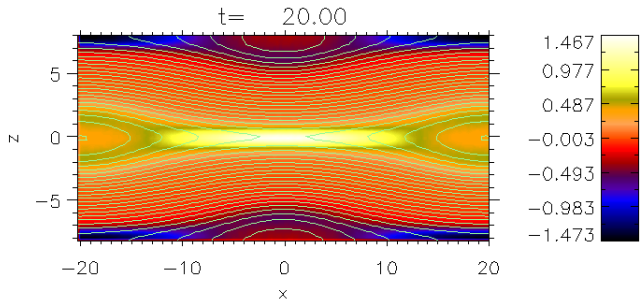

(b)

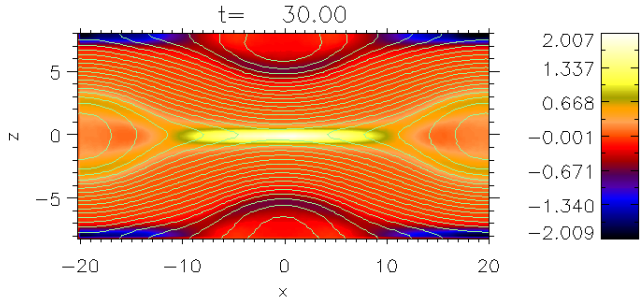

(c)

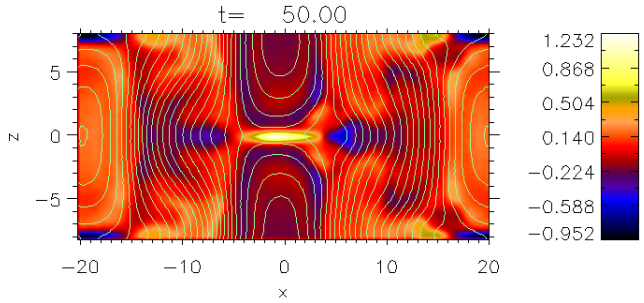

(d)

Figure 5.49: Plots of the y component of the current density with contours of the flux function overplotted for the double Harris sheet run with a guide field of value $B_{y0} = 1.0$. The plots correspond to the different times (a) $t = 0$, (b) $t = 20$, (c) $t = 30$ and (d) $t = 50$.

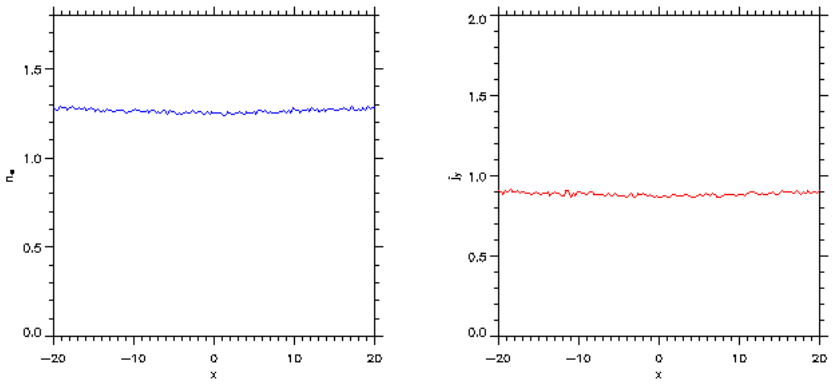

(a) (b)

Figure 5.50: Line plots of the electron number density n_e (blue line) and the y component of the current density (red line) plotted along x for $z = 0$ at $t = 0$ for the double Harris sheet runs.

been significantly reduced at the end of the simulation run. In the stronger guide field cases there are also small regions where the y component of the current density is enhanced. In the strong guide field cases the central current region thins and becomes more localised showing the same behaviour as the anisotropic bi-Maxwellian cases in Sec. 5.5. This large scale reorganistion of the geometry of the magnetic field is due to the doubly periodic boundary conditions that are used. In all the simulation runs the O-points above and below the central X-point have a strong effect. Once the initial stages of reconnection have occurred the O-points above and below the central X-point continue to press in on the central X-point eventually leading to the large scale reorganisation that is shown. This identical behaviour starting from two different initial periodic equilibria confirms that the main reason for the change in geometry of the magnetic field, once reconnection has occurred, is due to the doubly periodic boundary conditions.

Figure 5.51 shows line plots along x for $z = 0$ of the electron number density n_e (blue lines) and the y component of the current density (red lines) for the cases with zero guide field, $B_{y0} = 0.5$ and $B_{y0} = 1.0$ during reconnection. These can be compared to the electron number density and y component of the current density at $t = 0$ for each run which are shown in Figure 5.50 plotted along x for $z = 0$. In comparison to the runs discussed in Sec. 5.5 Figures 5.51(a), 5.51(c) and 5.51(e) show a similar density depletion around the X-point which is most significant for the zero guide field case. In the zero guide field case, Figure 5.51(b) shows that the current density is reduced at the X-point and enhanced in regions adjacent to it with peaks of the current density at a distance $|x| \approx 7\, c/\omega_{pi}$, whereas in the stronger guide field cases $B_{y0} = 0.5$ and $B_{y0} = 1.0$ Figures 5.51(d) and 5.51(f) show that the current density is actually enhanced at the X-point from its initial value, with the current density increase most significant for the guide field case $B_{y0} = 1.0$. In the guide field cases $B_{y0} = 0.5$ and $B_{y0} = 1.0$ the reduction of the number density at the X-point

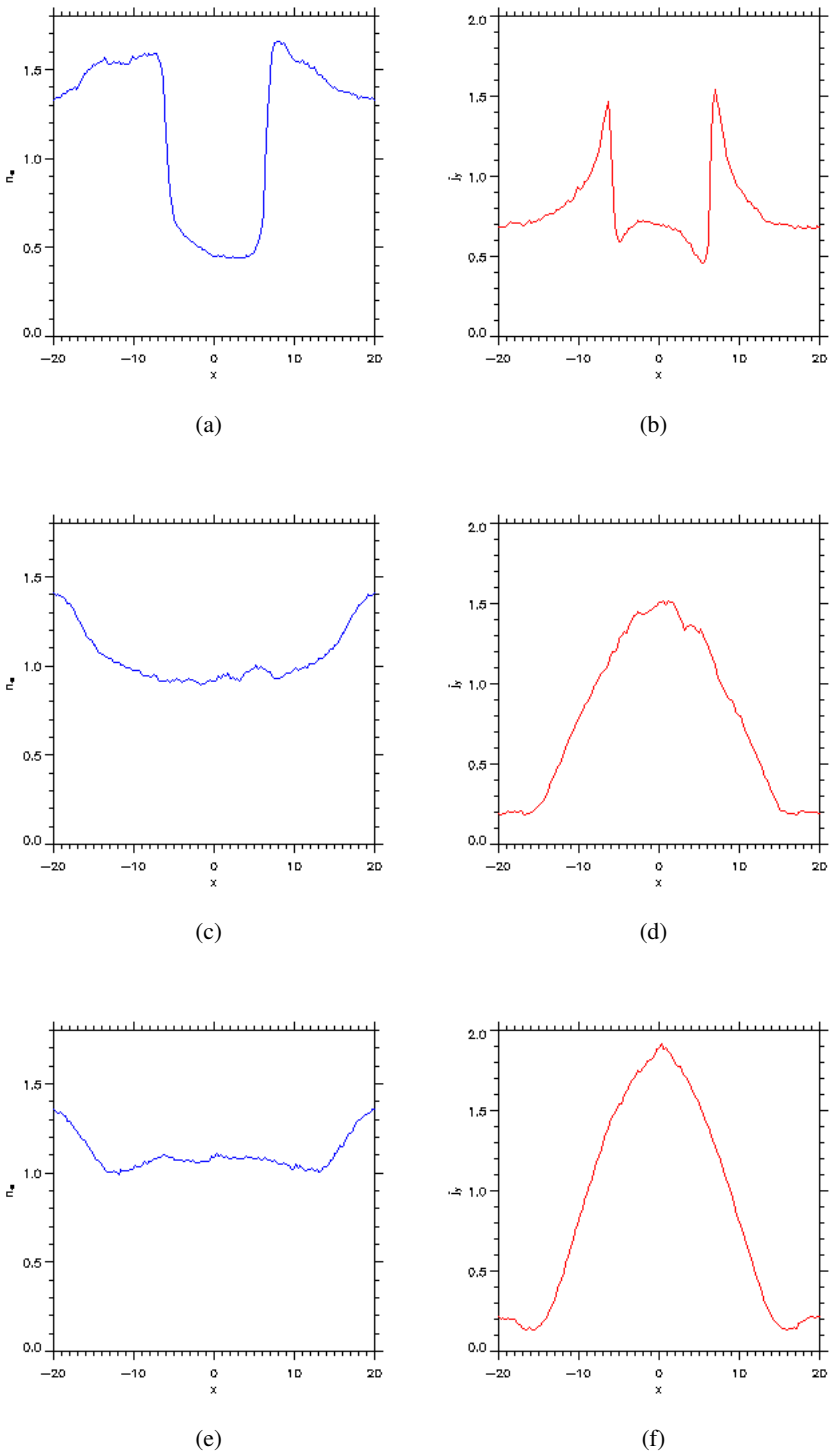

Figure 5.51: Line plots of the electron number density n_e (blue lines) and the y component of the current density (red lines) plotted along x for $z = 0$ during reconnection for the double Harris sheet runs with a guide field of value (a),(b) $B_{y0} = 0.0$ ($t = 44$) (c),(d) $B_{y0} = 0.5$ ($t = 30$), (e),(f) $B_{y0} = 1.0$ ($t = 28$).

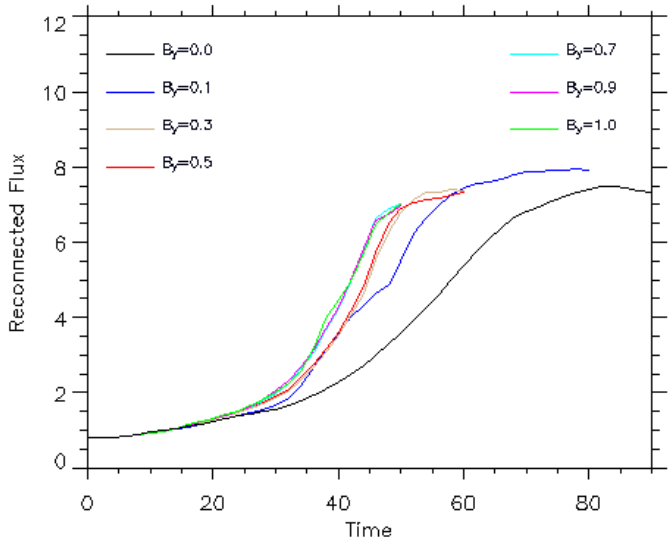

(a)

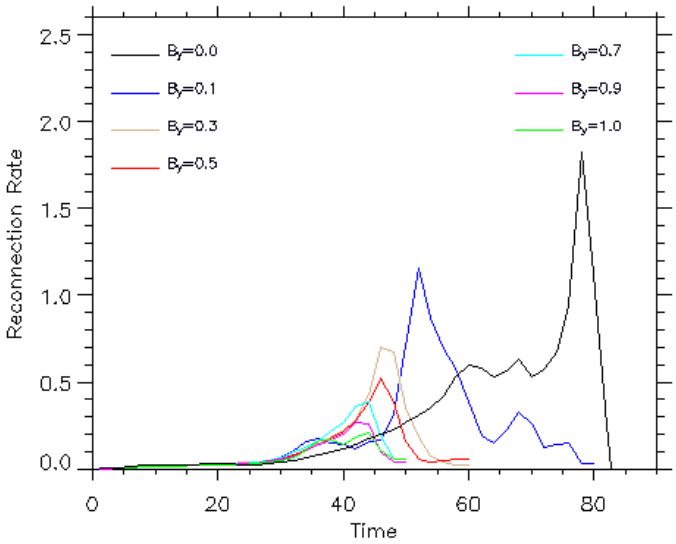

(b)

Figure 5.52: Figures showing the evolution of the simulations with varying strengths of guide field using the double Harris sheet as an initial configuration. The reconnected flux is shown in Figure 5.52(a) and the corresponding reconnection rates in Figure 5.52(b). The colours represent the different strengths of the guide field in the initial configuration.

implies that the current density increase must be due to an increased drift of the electrons and ions in the vicinity of the X-point.

In comparison to the Harris sheet, the double Harris sheet cases all showed a similar density depletion around the X-point. In the zero guide field case as in the Harris sheet case the current density was reduced at the X-point and enhanced in the regions adjacent to the reconnection region. In the stronger guide field cases the current density was actually enhanced at the X-points which is different to the Harris sheet cases where the current density was always reduced at the X-point. The behaviour of the double Harris sheet runs is overall very similar to that of the anti-parallel runs discussed in Sec. 5.5.

A comparison of the evolution of the runs is given in Figure 5.52. This shows two plots, one for the reconnected flux for each case plotted using different colours to represent the strength of the guide field in each run where the reconnected flux is defined as

$$F(t) = \int_{B_z>0} dx\, B_z(z=0), \tag{5.34}$$

and the other shows the reconnection rate where the reconnection rate is found from the gradient of the reconnected flux normalised against the maximum Alfvén speed at each timestep.

Examining the evolution of the double Harris sheet runs from the plots of the reconnection rate shown in Figure 5.52(b) they show that the reconnection rate is reduced significantly when the guide field is of the order B_0. This is in agreement with previous studies that show that the reconnection rate is reduced once the guide field is large enough to significantly change the magnetic pressure in the system (e.g. Pritchett 2001), and also agrees with simulation runs that use the Harris sheet and the anisotropic bi-Maxwellian periodic equilibria as initial conditions that have been shown in Sec. 5.4 and Sec. 5.5. The maximum reconnection rates in comparison to the previous cases show that they are in general greater for the double Harris sheet runs. This may be a consequence of the larger simulation domain for the double Harris sheet runs which results in a larger amount of free-energy in the initial setup. The doubly periodic boundary conditions may also play a role in the very high reconnection rates at later times during the simulation runs.

5.6.1 The Structure of the Diffusion Region

In this section the morphology of the off-diagonal components off the pressure tensor components are shown for the different runs. The structure of these pressure tensor components can be compared to the Harris sheet and anisotropic bi-Maxwellian cases. It is also shown how the different contributions in Eq. (5.7) make up the reconnection electric field in the vicinity of the X-point.

To investigate the structure of the off-diagonal components in the region of the central X-point

it was intended to analyse them at the time of maximum reconnection rate which is given by the peaks of each curve in Figure 5.52(b) in the same way as the Harris sheet cases were investigated. The problem with this was that at the time of maximum reconnection rate the pressure tensor components did not show the expected structure. This was due mainly to the interaction of the multiple current layers which led to a breakdown of the expected structure of the off-diagonal components at the central X-point. This process is very similar to the anisotropic bi-Maxwellian cases. It can be shown though at earlier stages in the reconnection process that the off-diagonal pressure tensor components do show the expected form. This can be seen in Figure 5.57 and Figure 5.58 which show the $P_{xy,e}$ and $P_{yz,e}$ components of the electron pressure tensor for the different strengths of guide field zoomed in around the X-point.

Figure 5.53 shows filled contour plots of the y component of the current density for each case when the off-diagonal components of the pressure tensor show the expected structure. Also shown in Figure 5.54 are filled contour plots of the E_y electric field at these times. This shows again that magnetic reconnection generates a strong y component of the electric field in the vicinity of the X-Point. The region of enhanced E_y is larger in the cases of stronger guide field. The cases shown here are for the guide fields $B_{y0} = 0.0, 0.1, 0.3, 0.5, 0.7, 0.9$ and $B_{y0} = 1.0$. In all the figures x_0 refers to the approximate position along x of the X-point. In all cases the position of the X-point along z is approximately at $z = 0$.

To demonstrate that the dominant contribution to the E_y electric field in the vicinity of the X-point is due to off-diagonal components of the electron pressure tensor Figure 5.55 and Figure 5.56 show line plots along x and z of the contributions that make up the E_y electric field in Eq. (5.7) averaged between the times shown in Figure 5.54 for each different case. In each case the dominant contribution to the electric field close to the X-point comes from the gradients of the off-diagonal components of the electron pressure tensor (green lines).

In each of the plots shown in Figure 5.55 and Figure 5.56 the gradients of the off-diagonal components of the electron pressure tensor (green lines) dominate the electric field out to the point at which the $\mathbf{u} \times \mathbf{B}$ term (purple lines) equals the contribution from the gradients of the electron pressure tensor terms identical to the Harris sheet cases. For the plots shown in Figure 5.55 they show that the contribution from the gradients of the off diagonal pressure tensor components dominate strongly to about $x \approx \pm 3 - 4c/\omega_{pi}$. There is also a degree of asymmetry of some of the contributions that make up the E_y electric field similar to the anisotropic cases. The plots shown in Figure 5.56 show that the contribution from the off diagonal pressure tensor components dominates to about $z \approx \pm 1.0c/\omega_{pi}$ either side of the X-point for the weak guide field cases whilst for the strong guide field cases they dominate up to $z \approx \pm 0.5c/\omega_{pi}$ either side of the X-point.

In comparison to the Harris sheet cases the essential features close to the X-point are the same. In all cases the mechanism that breaks the frozen in condition and dominates the contribution to the

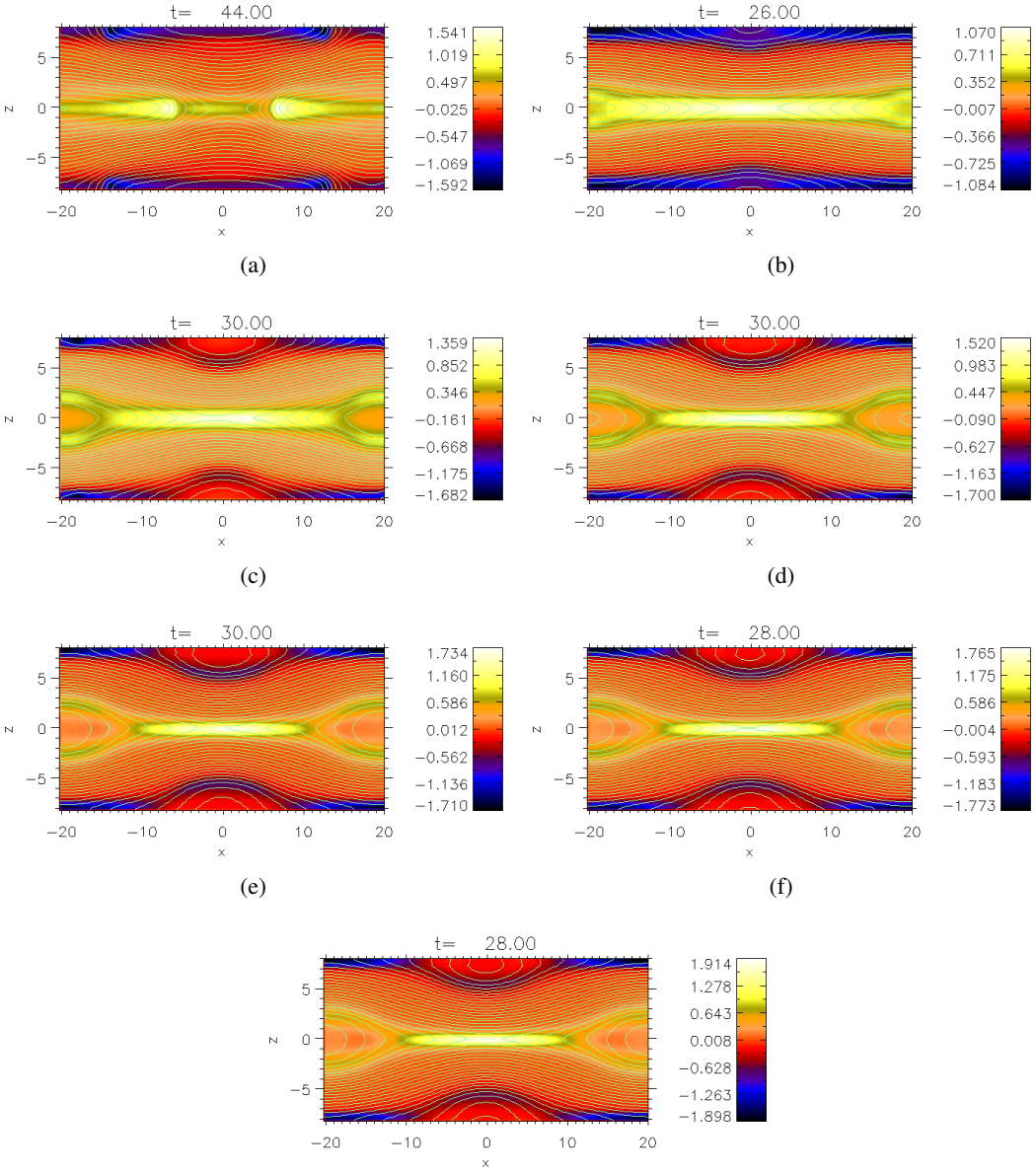

Figure 5.53: Plots of the y component of the current density with contours of the flux function overplotted for simulations with varying strengths of guide field at a time when the electron pressure tensor components show the expected structure. (a) $B_{y0} = 0.0$ ($x_0 = 0.87$), (b) $B_{y0} = 0.1$ ($x_0 = 0.58$), (c) $B_{y0} = 0.3$ ($x_0 = -0.87$), (d) $B_{y0} = 0.5$ ($x_0 = -0.87$), (e) $B_{y0} = 0.7$ ($x_0 = -1.45$), (f) $B_{y0} = 0.9$ ($x_0 = -0.58$), (g) $B_{y0} = 1.0$ ($x_0 = -0.87$).

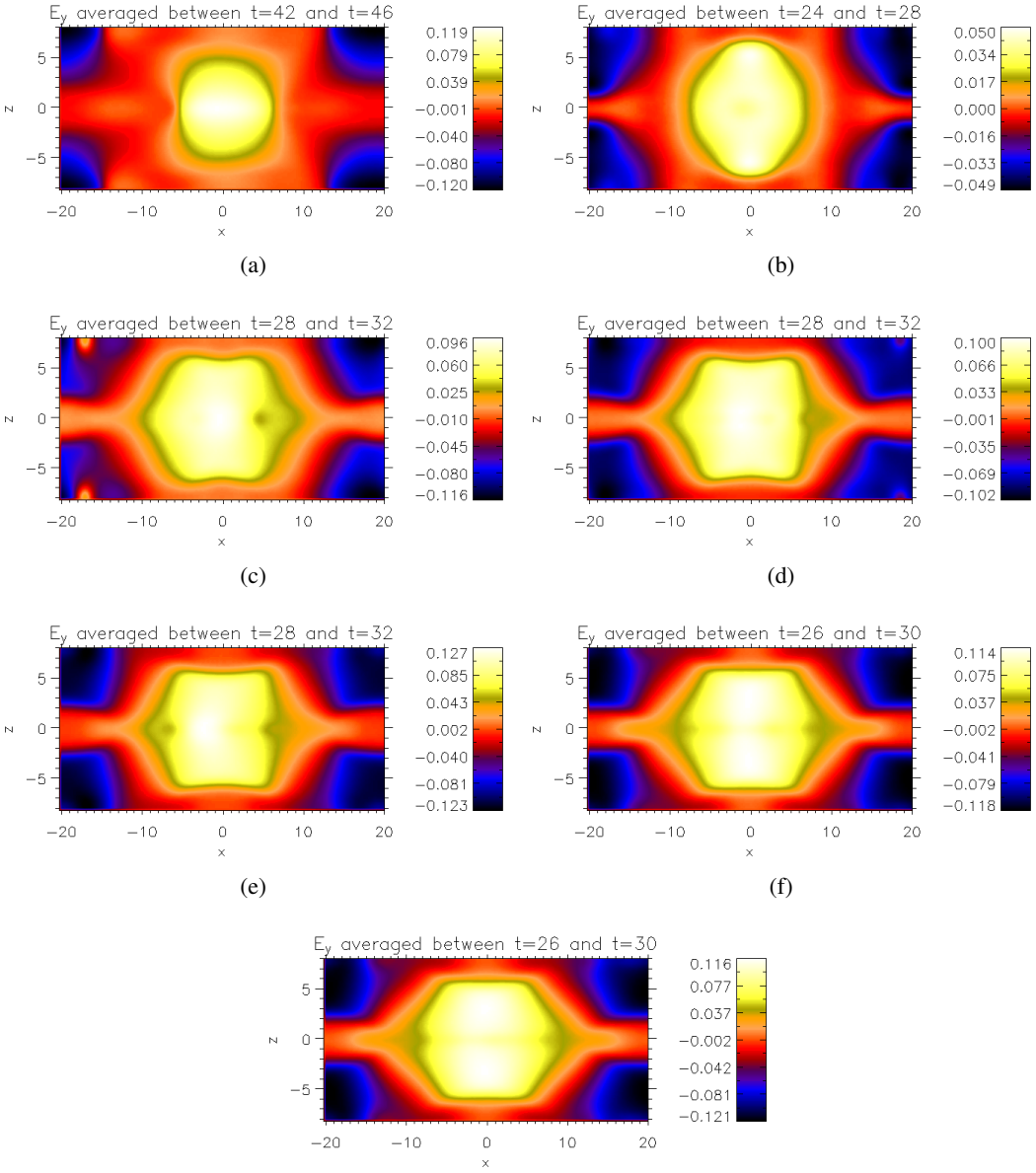

Figure 5.54: Plots of the y component of the electric field for simulations with varying strengths of guide field at a time when the electron pressure tensor components show the expected structure. (a) $B_{y0} = 0.0$ ($x_0 = 0.87$), (b) $B_{y0} = 0.1$ ($x_0 = 0.58$), (c) $B_{y0} = 0.3$ ($x_0 = -0.87$), (d) $B_{y0} = 0.5$ ($x_0 = -0.87$), (e) $B_{y0} = 0.7$ ($x_0 = -1.45$), (f) $B_{y0} = 0.9$ ($x_0 = -0.58$), (g) $B_{y0} = 1.0$ ($x_0 = -0.87$).

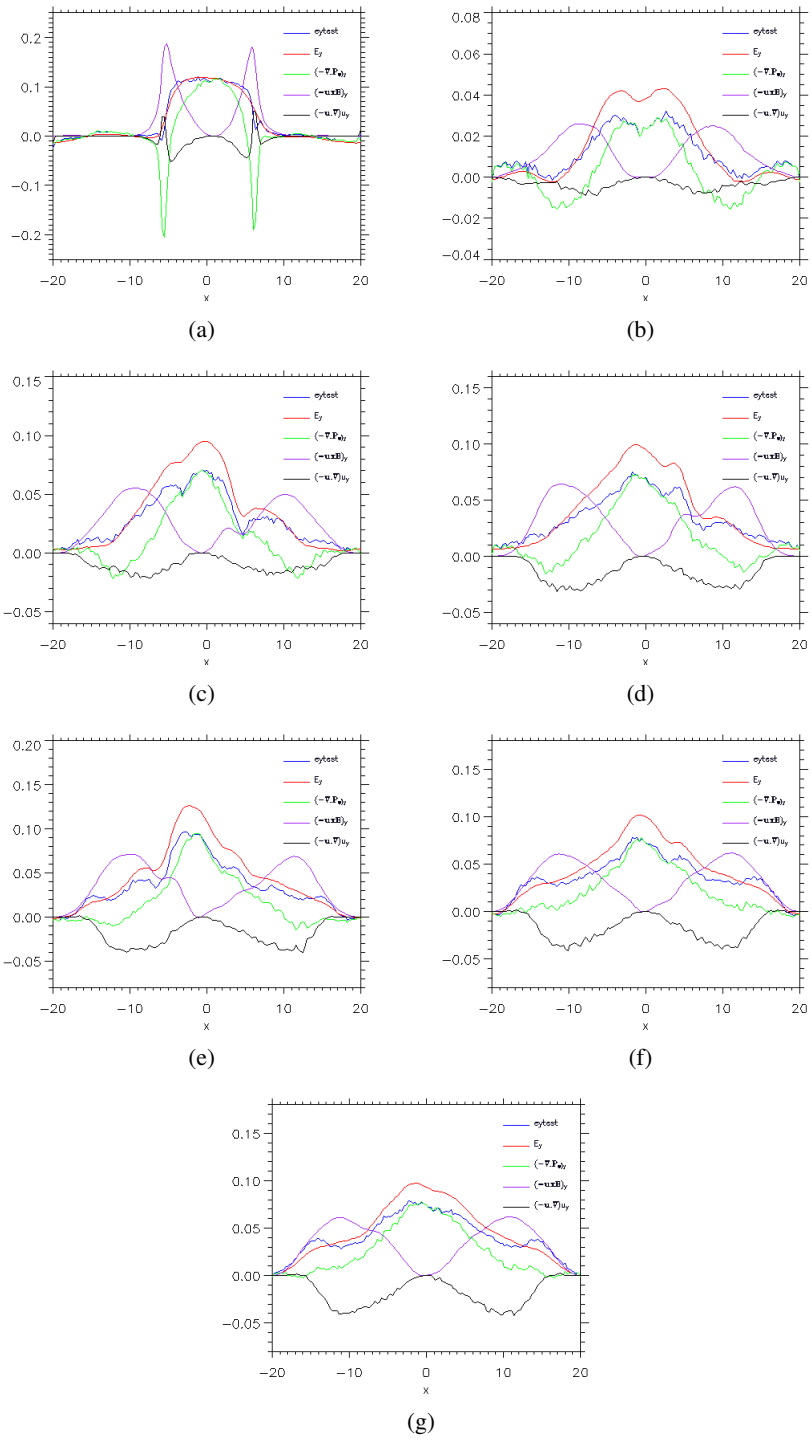

Figure 5.55: Plots along x for $z = 0$ of the contributions that make up the E_y electric field in Eq. (5.7) for simulations with varying strengths of guide field at a time when the electron pressure tensor components show the expected structure. (a) $B_{y0} = 0.0$ ($x_0 = 0.87$), (b) $B_{y0} = 0.1$ ($x_0 = 0.58$), (c) $B_{y0} = 0.3$ ($x_0 = -0.87$), (d) $B_{y0} = 0.5$ ($x_0 = -0.87$), (e) $B_{y0} = 0.7$ ($x_0 = -1.45$), (f) $B_{y0} = 0.9$ ($x_0 = -0.58$), (g) $B_{y0} = 1.0$ ($x_0 = -0.87$).

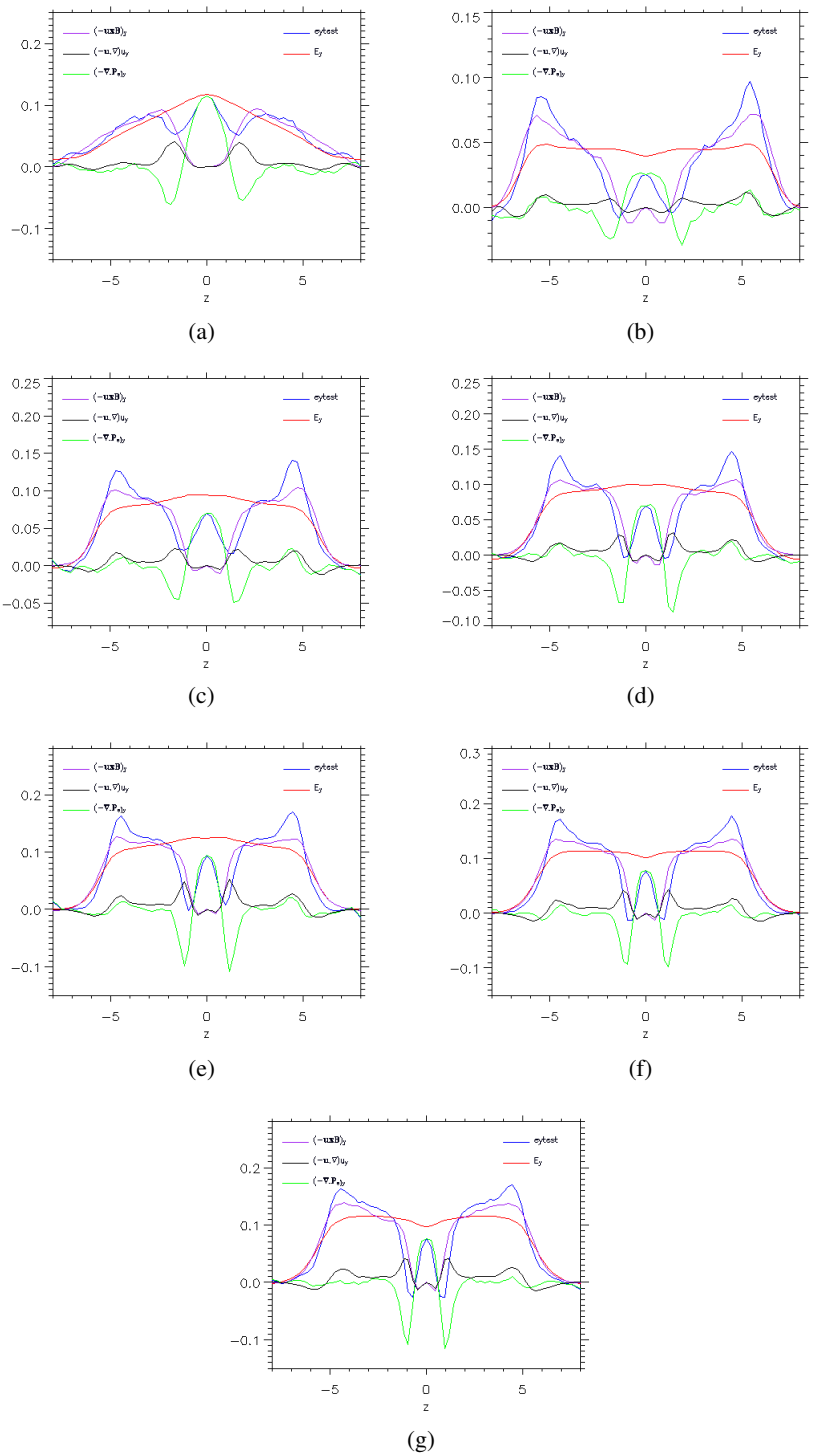

Figure 5.56: Plots along z for $x = x_0$ of the contributions that make up the E_y electric field in Eq. (5.7) for simulations with varying strengths of guide field at a time when the electron pressure tensor components show the expected structure. (a) $B_{y0} = 0.0$ ($x_0 = 0.87$), (b) $B_{y0} = 0.1$ ($x_0 = 0.58$), (c) $B_{y0} = 0.3$ ($x_0 = -0.87$), (d) $B_{y0} = 0.5$ ($x_0 = -0.87$), (e) $B_{y0} = 0.7$ ($x_0 = -1.45$), (f) $B_{y0} = 0.9$ ($x_0 = -0.58$), (g) $B_{y0} = 1.0$ ($x_0 = -0.87$).

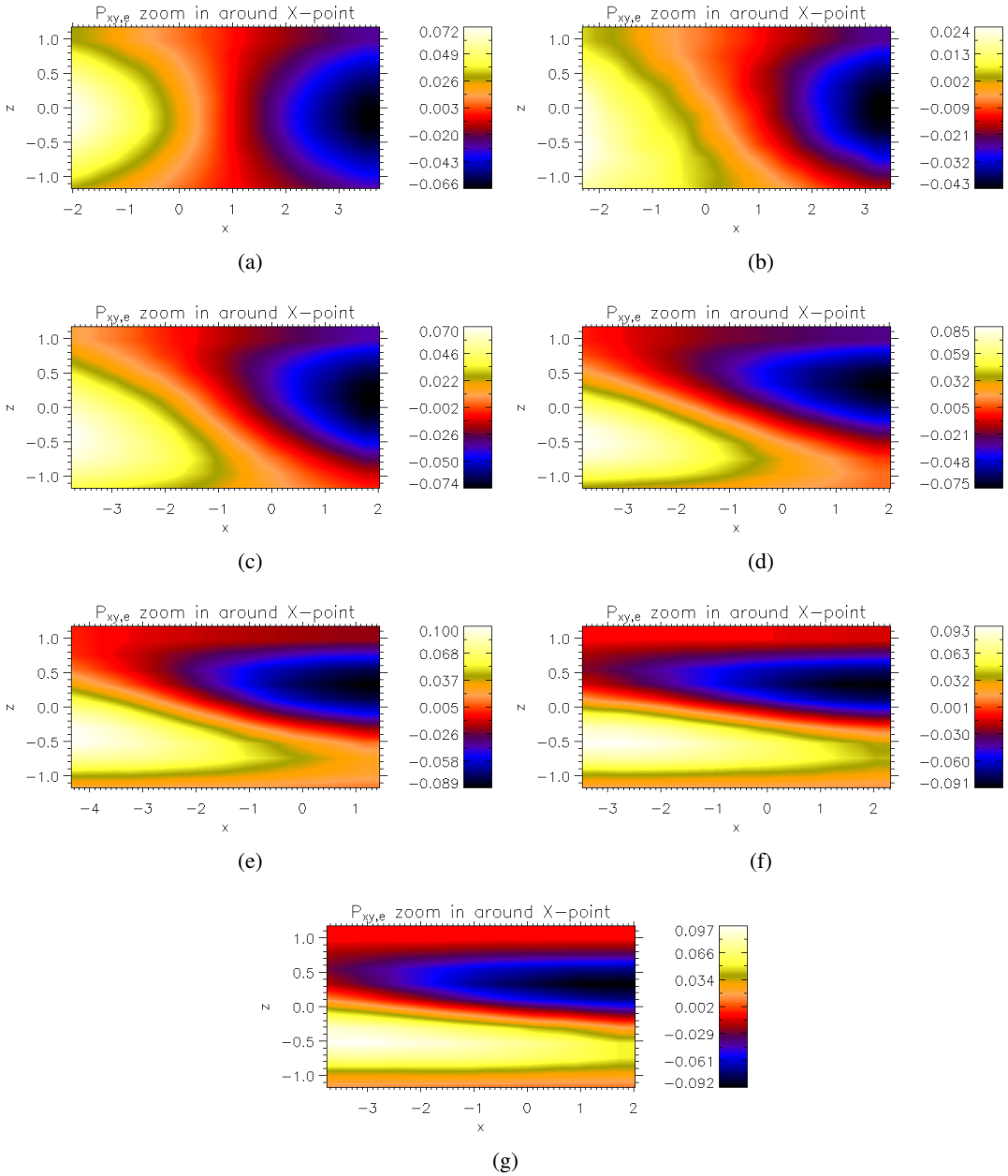

Figure 5.57: Plots of the $P_{xy,e}$ component of the electron pressure tensor for simulations with varying strengths of guide field at a time when the electron pressure tensor components show the expected structure. (a) $B_{y0} = 0.0$ ($x_0 = 0.87$), (b) $B_{y0} = 0.1$ ($x_0 = 0.58$), (c) $B_{y0} = 0.3$ ($x_0 = -0.87$), (d) $B_{y0} = 0.5$ ($x_0 = -0.87$), (e) $B_{y0} = 0.7$ ($x_0 = -1.45$), (f) $B_{y0} = 0.9$ ($x_0 = -0.58$), (g) $B_{y0} = 1.0$ ($x_0 = -0.87$).

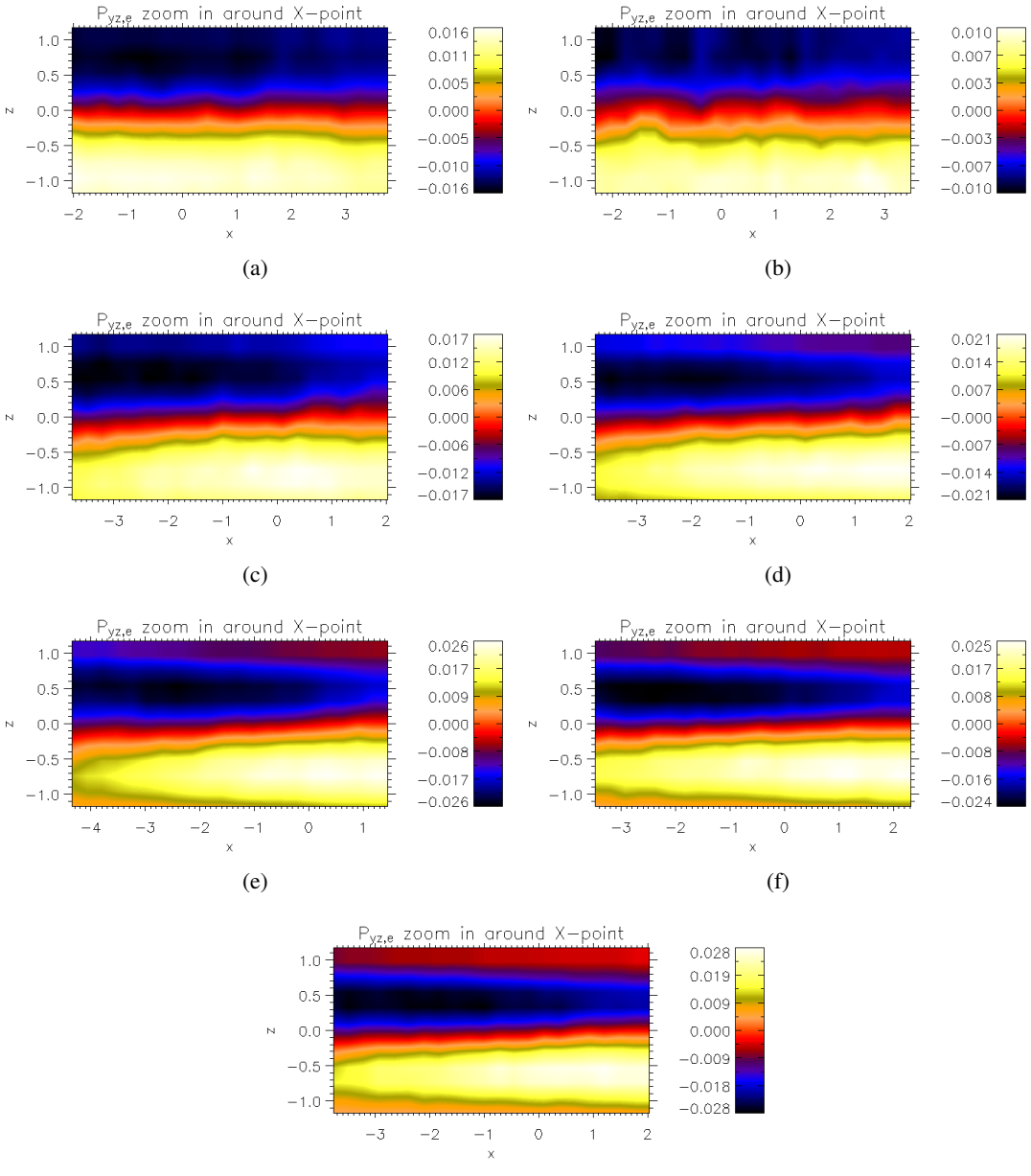

Figure 5.58: Plots of the $P_{yz,e}$ component of the electron pressure tensor for simulations with varying strengths of guide field at a time when the electron pressure tensor components show the expected structure. (a) $B_{y0} = 0.0$ ($x_0 = 0.87$), (b) $B_{y0} = 0.1$ ($x_0 = 0.58$), (c) $B_{y0} = 0.3$ ($x_0 = -0.87$), (d) $B_{y0} = 0.5$ ($x_0 = -0.87$), (e) $B_{y0} = 0.7$ ($x_0 = -1.45$), (f) $B_{y0} = 0.9$ ($x_0 = -0.58$), (g) $B_{y0} = 1.0$ ($x_0 = -0.87$).

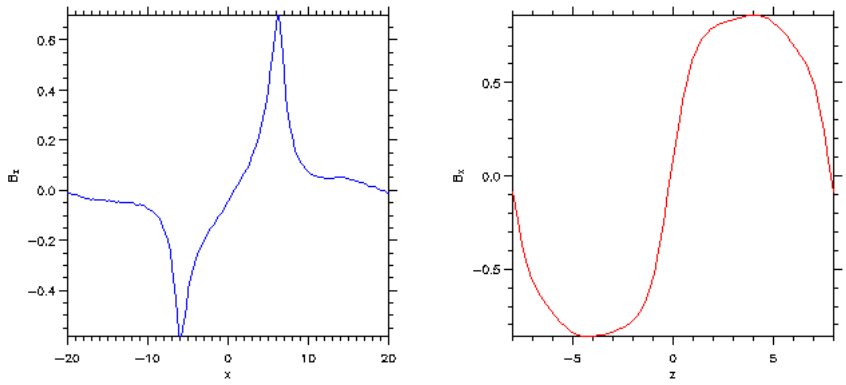

(a) (b)

Figure 5.59: Plots of the profile of B_z along x and of the profile of B_x along z going through the position of the X-point at a time when the off-diagonal components of the electron pressure tensor show the expected structure for the zero guide field (anti-parallel) case.

reconnection electric field near to the X-point is due to gradients of the off-diagonal components of the electron pressure tensor near to the X-point. It must be pointed out though that for all the figures shown here they are at an earlier time than the time of maximum reconnection rate corresponding to the peaks of the lines shown in Figure 5.52(b). This is because at the time of maximum reconnection rate, due to the periodic boundary conditions and the interaction of the multiple current layers in the simulation box as described already for the anisotropic cases, this leads to the breakdown of the expected structure of the pressure tensor components. Therefore to compare equally to the Harris sheet cases and to investigate the dominant mechanism that breaks the frozen in condition an earlier time in the reconnection process, is investigated.

Although, as in the Harris sheet cases the dominant term in the vicinity of the X-point is clearly due to the gradients of the off-diagonal terms of the electron pressure tensor, there is a small contribution to the electric field from the electron inertia term at the edge of the diffusion region. This inertia term is not significant in the weak guide field cases. It can be seen in the plots along z of the contributions to the reconnection electric field that in the strong guide field cases the electron inertia term has a significant contribution to the E_y electric field at the edge of the reconnection regime. In these cases as in the Harris sheet cases the contribution from the electron inertia at the edge of the diffusion region matches the value of the $\mathbf{u} \times \mathbf{B}$. As mentioned in the discussion of the Harris sheet cases, in a recent paper by Hesse et al. (2004) starting from a Harris sheet with a guide field of $B_{y0} = 0.8$ it was shown that within a collisionless skin depth there was a finite contribution from the electron inertia at the edge of the localised current region. The main contribution to the E_y electric field close to the X-point was still due to the nongyrotropic pressures. The results shown here starting from the double Harris sheet are consistent with this.

The significant contribution from the electron inertia term is due the small scales associated with the electron Larmor radius in the strong guide field case.

To investigate further the structure of the off-diagonal pressure tensor components, Figures 5.57 and 5.58 show filled contour plots of the $P_{xy,e}$ and $P_{yz,e}$ components of the electron pressure tensor zoomed in around the position of the central X-point. In the anti-parallel case the $P_{xy,e}$ component is approximately symmetrical about the line $x = x_0$ which goes through the X-point with a gradient in x. The $P_{yz,e}$ components of the pressure tensor is approximately symmetrical about the $z = 0$ line going through the X-point with a gradient in z. As the guide field is increased the structure of the $P_{xy,e}$ component starts to change. The symmetry along the line $x = x_0$ is broken and the structure is seen to rotate in an anti-clockwise direction until for the guide field $B_{y0} = 1.0$ case the $P_{xy,e}$ component is almost symmetrical along the line $z = 0$ with a gradient in z identical to the Harris sheet cases. The central region in all of the plots can also be seen to thin. The $P_{yz,e}$ component of the electron pressure tensor is seen to rotate very slightly in the anti-clockwise direction. The significant rotation anti-clockwise and then clockwise as seen in the Harris sheet cases is again not so obvious. In the strong guide field cases there is though almost symmetry about the $z = 0$ line. There is a thinning of the central region as the guide field becomes large but in this case the thinning is relatively slight.

The thinning of the central region in Figure 5.57 and Figure 5.58 is due to the introduction of the guide field. In the case of the Harris sheet without a guide field the characteristic length scale of $P_{xy,e}$ and $P_{yz,e}$ has been shown to be given approximately by the electron bounce widths in a field reversal λ_x and λ_z (e.g. Hesse et al. 1999). In these simulations the electron bounce width in the x and z directions for the anti-parallel field configuration as given by Eqs. (5.3) and (5.4) at the time shown in Figure 5.53(a) are of the order $\lambda_x \approx 2.7c/\omega_{pi}$ and $\lambda_z \approx 1.0c/\omega_{pi}$. Plots of the x and z components of the magnetic field along z and x respectively for the anti-parallel case at the time shown in Figure 5.53(a) at which the off-diagonal components of the electron pressure tensor show the correct form are shown in Figure 5.59. These are used to calculate estimates of the bounce widths λ_x and λ_z. In the strong guide field case for the Harris sheet it has been shown that the characteristic length scale changes to that of the thermal electron Larmor radius $r_L = v_{th,e}/\Omega_e$ in the guide magnetic field (Hesse et al. 2004). The electron Larmor radius for the simulation with $B_{y0} = 1.0$ at the time shown in Figure 5.53(g) is of the order $r_L \approx 0.6c/\omega_{pi}$. This characteristic change of length scale can be seen in Figure 5.57 and Figure 5.58 as the strength of the guide field is increased and is consistent with the Harris sheet and anisotropic bi-Maxwellian cases already shown. The very slight thinning of the central region that is seen in Figure 5.58 can be attributed to the fact that the difference between the bounce width λ_z in the zero guide field case and the thermal electron Larmor radius for the $B_{y0} = 1.0$ case is small.

To illustrate how the interaction of the multiple current layers leads to the break up of the structure of the pressure tensor components at the central X-point it is useful to look at the time evolution

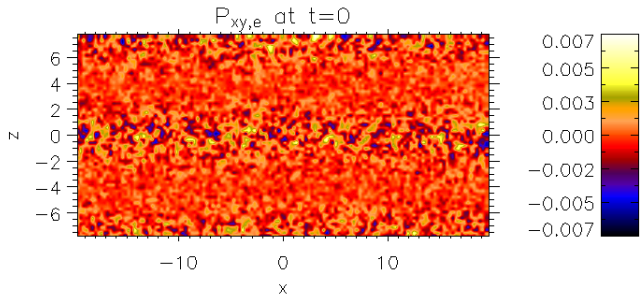

(a)

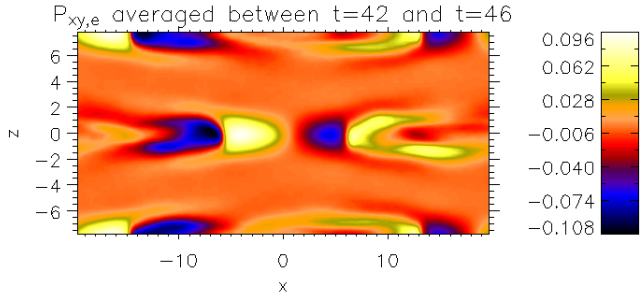

(b)

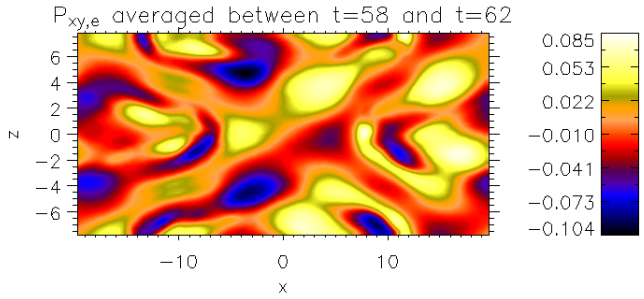

(c)

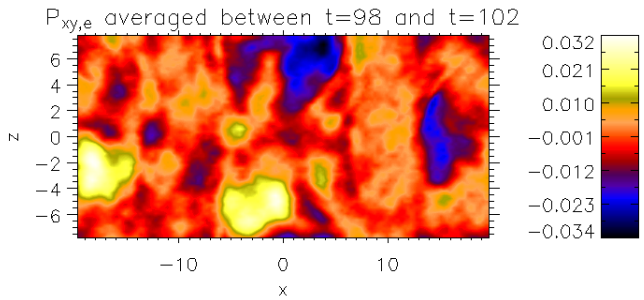

(d)

Figure 5.60: Plots of the evolution of the $P_{xy,e}$ component of the electron pressure tensor for the double Harris sheet case with zero guide field. The plots correspond to the $P_{xy,e}$ component at (a) $t = 0$ and averaged around (b) $t = 44$, (c) $t = 60$ and (d) $t = 100$.

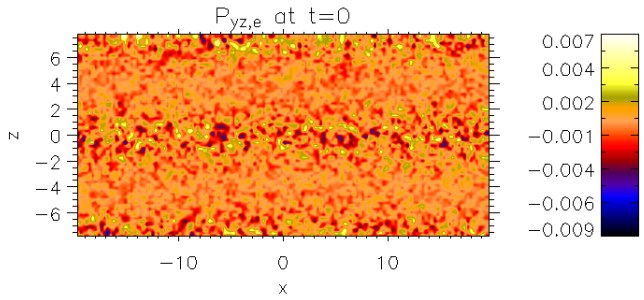

(a)

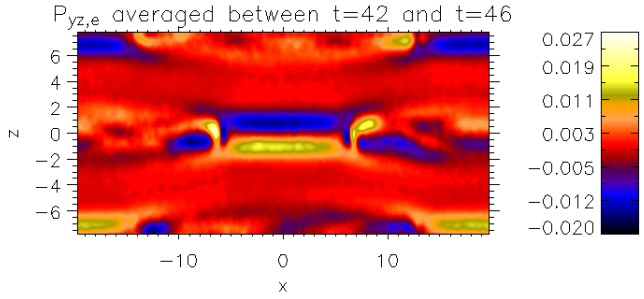

(b)

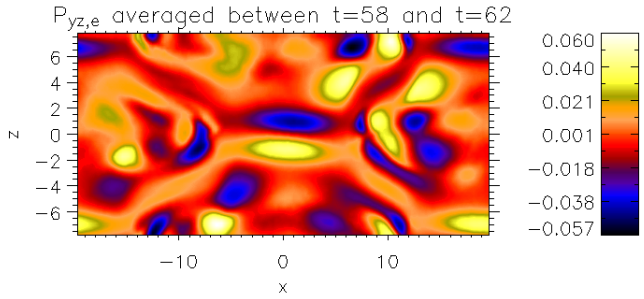

(c)

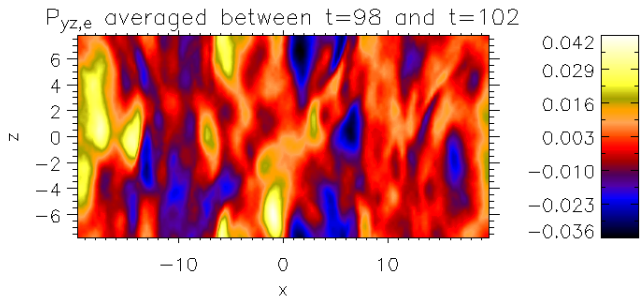

(d)

Figure 5.61: Plots of the evolution of the $P_{yz,e}$ component of the electron pressure tensor for the double Harris sheet case with zero guide field. The plots correspond to the $P_{yz,e}$ component at (a) $t = 0$ and averaged around (b) $t = 44$, (c) $t = 60$ and (d) $t = 100$.

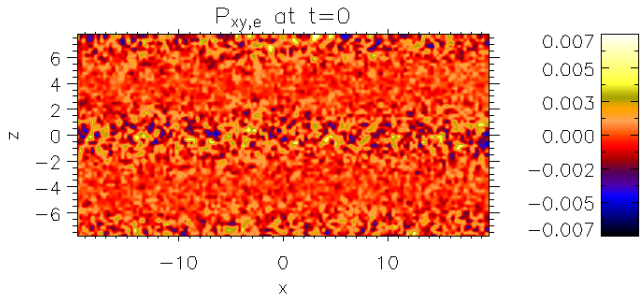

(a)

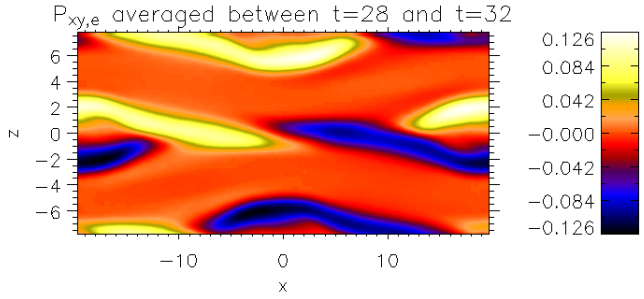

(b)

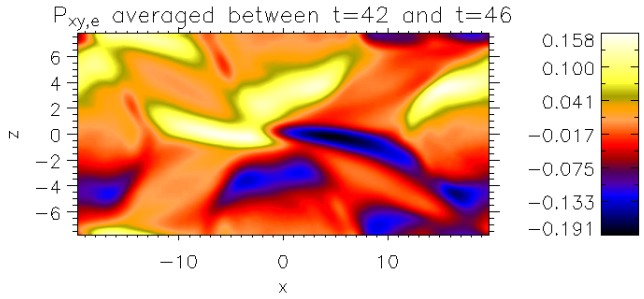

(c)

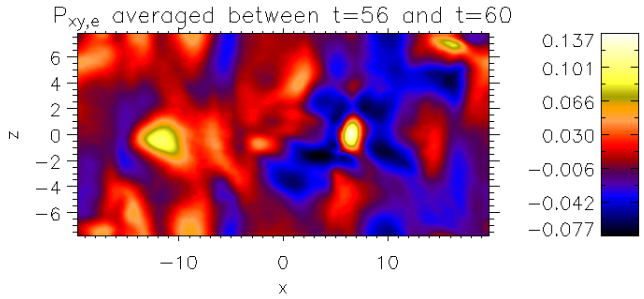

(d)

Figure 5.62: Plots of the evolution of the $P_{xy,e}$ component of the electron pressure tensor for the double Harris sheet case with a guide field of $B_{y0} = 0.5$. The plots correspond to the $P_{xy,e}$ component at (a) $t = 0$ and averaged around (b) $t = 30$, (c) $t = 44$ and (d) $t = 58$.

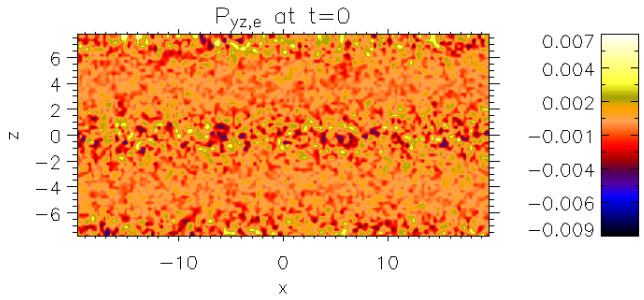

(a)

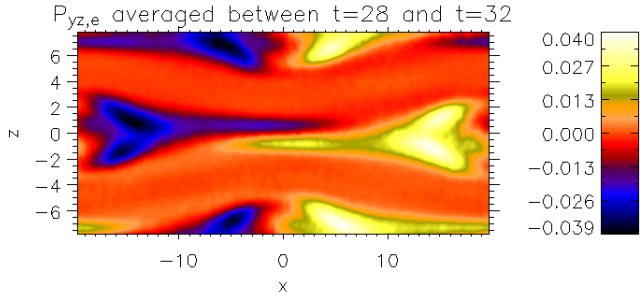

(b)

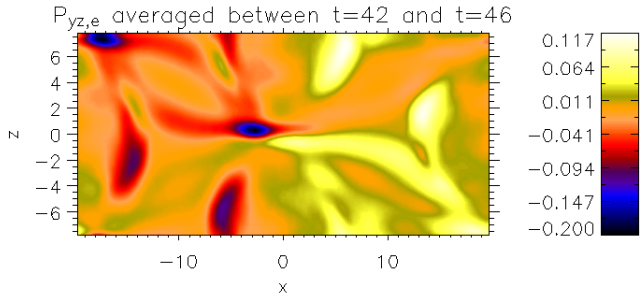

(c)

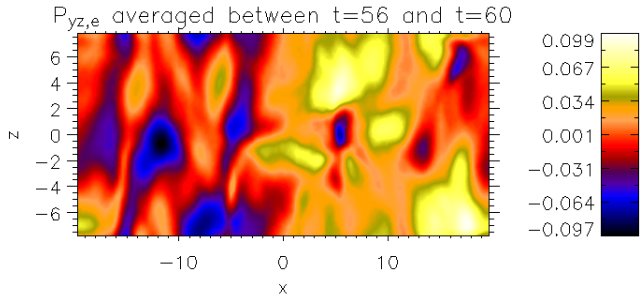

(d)

Figure 5.63: Plots of the evolution of the $P_{yz,e}$ component of the electron pressure tensor for the double Harris sheet case with a guide field of $B_{y0} = 0.5$. The plots correspond to the $P_{yz,e}$ component at (a) $t = 0$ and averaged around (b) $t = 30$, (c) $t = 44$ and (d) $t = 58$.

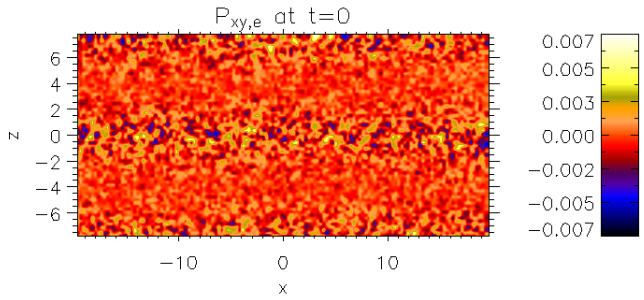

(a)

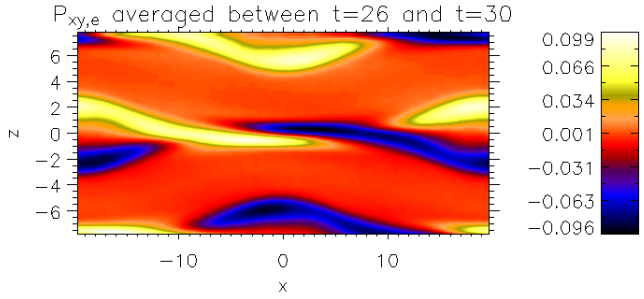

(b)

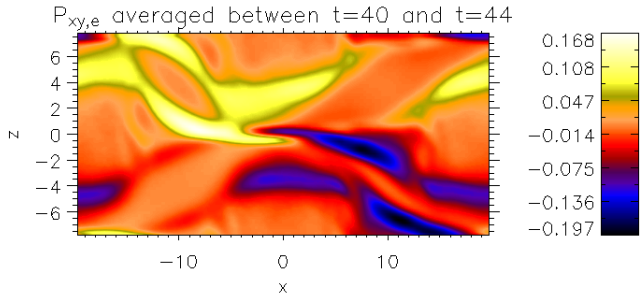

(c)

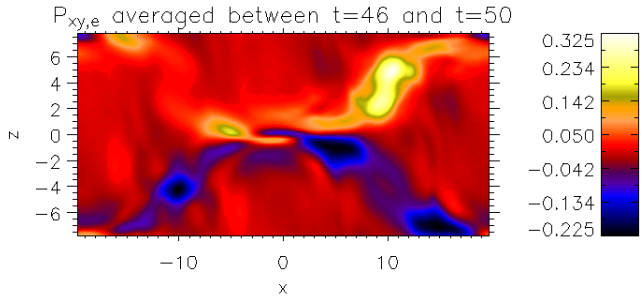

(d)

Figure 5.64: Plots of the evolution of the $P_{xy,e}$ component of the electron pressure tensor for the double Haris sheet case with a guide field of $B_{y0} = 1.0$. The plots correspond to the $P_{xy,e}$ component at (a) $t = 0$ and averaged around (b) $t = 28$, (c) $t = 42$ and (d) $t = 48$.

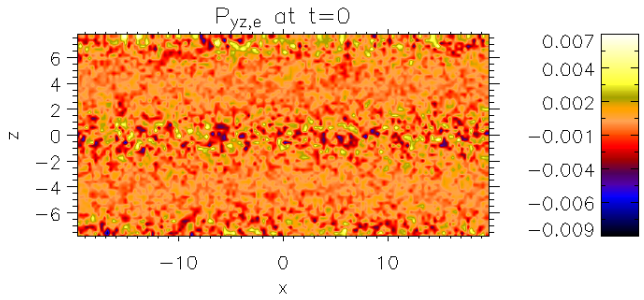

(a)

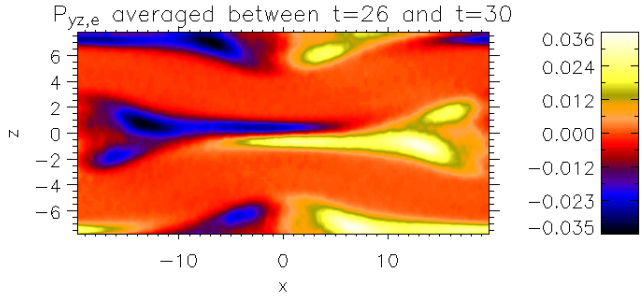

(b)

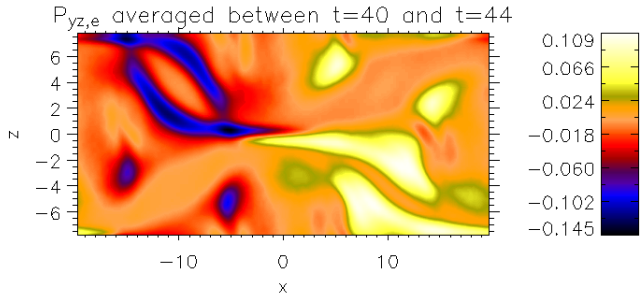

(c)

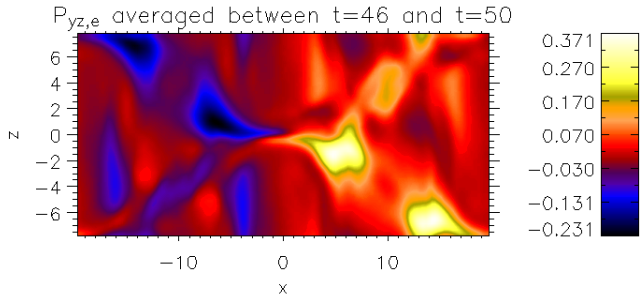

(d)

Figure 5.65: Plots of the evolution of the $P_{yz,e}$ component of the electron pressure tensor for the double Harris sheet case with a guide field of $B_{y0} = 1.0$. The plots correspond to the $P_{yz,e}$ component at (a) $t = 0$ and averaged around (b) $t = 28$, (c) $t = 42$ and (d) $t = 48$.

of the off-diagonal components of the pressure tensor components. As examples of this the evolutions for the $P_{xy,e}$ component and the $P_{yz,e}$ component for the double Harris sheet cases with a guide field of $B_{y0} = 0.0, B_{y0} = 0.5, B_{y0} = 1.0$ are shown in Figures 5.60 - 5.65. The snapshots show the off-diagonal components throughout the whole simulation domain. It can be seen that at the early stages of reconnection the pressure tensor components at the central X-point have the expected structure and then as time proceeds the interaction of the boundary with the central current layer leads to the breakdown of this structure. The overall evolution is also shown in the movies that come with the thesis (see Appendix B).

5.7 Anisotropic Bi-Maxwellian Simulations ($m_i/m_e = 25$)

In this section simulations starting from the anisotropic bi-Maxwellian cases already shown for $m_i/m_e = 1$ in Sec. 5.5 are extended to show cases using a mass ratio of $m_i/m_e = 25$. Results using an anti-parallel configuration as the initial configuration with varying strengths of guide field are shown and compared to a simulation run where a self consistent linear force-free equilibrium is used as the initial condition to see what differences there are when the characteristic time and lengths scales for the electrons and ions are different. This is the first time a detailed comparison of the structure of the diffusion region has been carried out for $m_i/m_e > 1$ that compares simulations starting from an an anti-parallel configuration with different strengths of guide field to simulations starting from a self-consistent linear force-free field.

In the following simulation results ions are considered to be protons. Lengths are normalized to the ion inertial length c/ω_{pi} and the number density is normalised to a value n_0. Times are normalised to the inverse of the ion cyclotron frequency $\Omega_i = eB_0/m_i$. The magnetic field is normalised to the value B_0, the amplitude of the initial magnetic field.

In the anti-parallel case the system dimensions are $L_x = 3.22\, c/\omega_{pi}$ and $L_z = 1.61\, c/\omega_{pi}$ where L_x and L_z are the half lengths of the box in the x and z directions, with a grid that is 100×50 in the x and z directions. The linear force-free case has system dimensions $L_x = 2.96\, c/\omega_{pi} = 2\pi/\alpha$ and $L_z = 1.48\, c/\omega_{pi} = \pi/\alpha$ where L_x and L_z are the half lengths of the box in the x and z directions with a grid that is 100×50 in the x and z directions and $\alpha = 2.12\omega_{pi}/c$. A time step $\omega_{pe}\Delta t = 1$ is used. The ratio ω_{pe}/Ω_e is set to a numerical value of 5 in both cases. It should be noted that the simulation box is very small in both cases. This is due to the fact that the magnetic field components are periodic and the total simulation box length in the z direction must correspond to one full period of the magnetic field. In the force-free case this length is given by $2\pi/\alpha$. The period in the z direction is determined by the choice of parameters for each equilibrium (see Sec. 3.3.3 in Chap. 3 for an example) and therefore the length of the box in the z direction is always restricted by this constraint. The small size of the box consequently means that the amount

of magnetic flux in the simulation box is small. The typical width of the current sheet in all cases is relatively large. These two factors combined could result in the possibility that the initial state is stable due to the relatively small amount of free-energy available.

For each simulation run a perturbation of the form

$$B_{xp} = a_0 \frac{\pi}{L_z} \sin\left(\frac{\pi z}{L_z}\right), \tag{5.35}$$

$$B_{zp} = a_0 \frac{\pi}{L_x} \sin\left(\frac{\pi x}{L_x}\right), \tag{5.36}$$

is also added where L_x and L_z are the half lengths of the box in the x and z directions. This field perturbation gives X-points at $(0,0), (L_x, L_z), (L_x, -L_z), (-L_x, L_z)$ and $(-L_x, -L_z)$. O-Points are located at $(0, L_z), (0, -L_z), (-L_x, 0)$ and $(L_x, 0)$. In all cases periodic boundary conditions are employed at $x = -L_x$ and $x = L_x$ and $z = -L_z$ and $z = L_z$. The electron-ion temperature ratios are chosen as $T_{e\perp}/T_{i\perp} = 5.0$ and $T_{e\parallel}/T_{i\parallel} = 23/7$. The mass ratio for the simulation runs is $m_i/m_e = 25$.

There are two particle populations in all simulation runs. The foreground population consists of the first set of ions and electrons which establish the equilibrium pressures and currents in all cases. In the anti-parallel runs there is both an electron and ion temperature anisotropy. The distribution of the ions and electrons is therefore specified by (5.13). To ensure that the electric field is zero a frame of reference is chosen in which the condition

$$\frac{V^e_{dy}}{V^e_{dy}} = -\frac{T_{e\perp}}{T_{i\perp}} \tag{5.37}$$

is satisfied. The same overall temperatures as in the previous simulation runs are used i.e. $T_{e\perp} + T_{i\perp} = 1.0, T_{e\parallel} + T_{i\parallel} = 1.25$ and the ratio of the quantities $\Delta T_e/\Delta T_i = 1$ where $\Delta T_e = T_{e\parallel} - T_{e\perp}$ and $\Delta T_i = T_{i\parallel} - T_{i\perp}$. This therefore sets the temperature anisotropy such that $T_{e\perp}/T_{e\parallel} = 20/23$ and $T_{i\perp}/T_{i\parallel} = 4/7$. The second population consists of the second set of ions and electrons which constitute a constant background density $n_b = 0.2$. The background temperatures are identical to the foreground population, $T_{e\perp} + T_{i\perp} = 1.0, T_{e\parallel} + T_{i\parallel} = 1.25$. The simluation run used 4×10^7 ions and electrons each for the foreground and 1×10^7 ions and electrons for the background.

In the force-free run there is both an electron and ion temperature anisotropy. The distribution of the ions and electrons is therefore specified by (5.18). A frame of reference is chosen in which the conditions that

$$\frac{V^e_{dx}}{V^i_{dx}} = -\frac{T_{e\perp}}{T_{i\perp}}, \tag{5.38}$$

$$\frac{V^e_{dy}}{V^i_{dy}} = -\frac{T_{e\perp}}{T_{i\perp}}, \tag{5.39}$$

are satisfied. The same overall temperatures as in the previous simulation runs are used i.e. $T_{e\perp} + T_{i\perp} = 0.4, T_{e\|} + T_{i\|} = 0.5$ and the ratio of the quantities $\Delta T_e/\Delta T_i = 1$ where $\Delta T_e = T_{e\|} - T_{e\perp}$ and $\Delta T_i = T_{i\|} - T_{i\perp}$. This therefore sets the temperature anisotropy such that $T_{e\perp}/T_{e\|} = 20/23$ and $T_{i\perp}/T_{i\|} = 4/7$. The second population again consists of the second set of ions and electrons which constitute a constant background density $n_b = 0.2$. The background temperatures are identical to the foreground population, $T_{e\perp} + T_{i\perp} = 0.4, T_{e\|} + T_{i\|} = 0.5$. The simluation run used 4×10^7 ions and electrons each for the foreground and 1×10^7 ions and electrons for the background. This is the first study for $m_i/m_e \gg 1$ to start from the self-consistent linear force-free equilibria as discussed by Sestero (1967); Bobrova and Syrovatskiĭ (1979); Correa-Restrepo and Pfirsch (1993); Bobrova et al. (2001) where both the electrons and the ions carry the initial current.

For the anti-parallel configuration the strength of the constant guide field $B_y = B_{y0}$ is varied to consider the cases $B_{y0} = 0.0, B_{y0} = 0.5$ and $B_{y0} = 1.0$. These results are compared to the force-free case.

In the figures shown below the initial configurations for the anti-parallel cases and the force-free case are shown. For the anti-parallel case a filled contour plot of B_x is shown in Figure 5.66(a) with a line plot of the magnetic field profile plotted along z for $x = 0$ shown in Figure 5.66(b). Also shown in Figure 5.66(c) is a filled contour plot of the y component of the current density with contours of the flux function overplotted showing the magnetic field lines. For the force-free case filled contour plots of B_x and B_y are shown in Figure 5.67(a) and Figure 5.67(b). Figure 5.67(c) is a filled contour plot of the x component of the curent density and Figure 5.67(d) is a filled contour plot of the y component of the current density with contours of the flux function overplotted showing the magnetic field lines. Finally a line plot of the magnetic field profiles plotted along z for $x = 0$ is shown in Figure 5.67(e). In both cases it is clear to see the periodic profile of the magnetic field components and also the multiple current sheet structures of j_x and j_y with X-points located at the centre and corners of the box and the 0-points located in between the X-points that are introduced by the perturbation to the equilibrium magnetic field.

Figures 5.68 - 5.70 show the evolution of the magnetic field for different runs with the y component of the current density colour coded. Figure 5.68 shows the evolution for the anti-parallel case with a guide field of value $B_{y0} = 0.5$. Figure 5.69 shows the evolution for the anti-parallel case with a guide field of value $B_{y0} = 1.0$ and Figure 5.70 shows the evolution of the force-free case. Movies of the evolution for each case can be found on the CD which is attached to this thesis (see Appendix B). In the anti-parallel case the initial configuration seems to be stable to the tearing mode. The simulation was run for an extended period of time and the system remains relatively unchanged. This stability may be a consequence of the small initial magnetic flux in the system which is a consequence of the periodic boundary conditions. In the cases with a guide field of $B_{y0} = 0.5$, $B_{y0} = 1.0$ and the force-free case the system reconnects and releases the stored energy in the

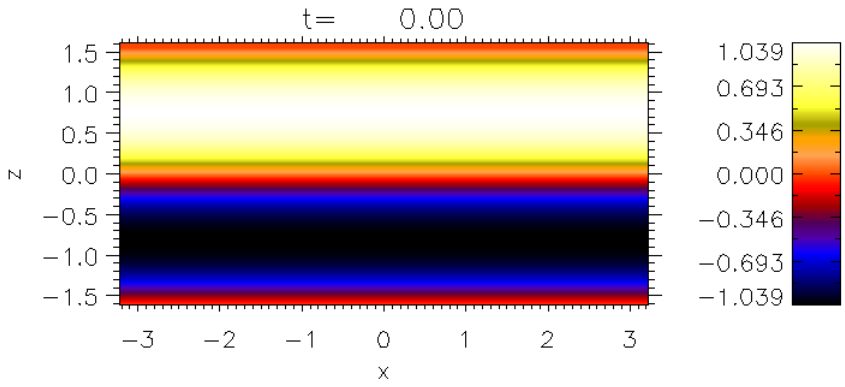

(a)

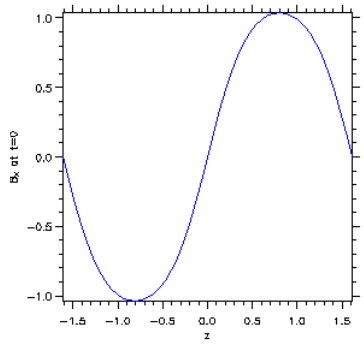

(b)

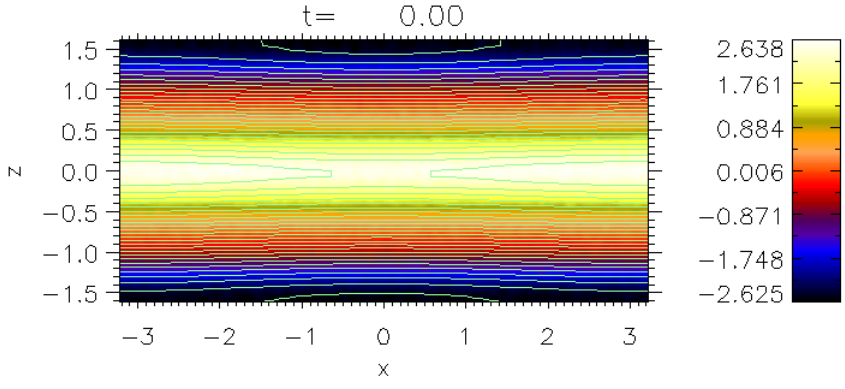

(c)

Figure 5.66: Plots showing the initial configuration for the anti-parallel case. Figure 5.66(a) shows a colour contour plot of B_x and Figure 5.66(b) shows a line plot of the profile of B_x along z for $x = 0$. Figure 5.66(c) shows a filled contour plot of the y component of the current density with magnetic field lines corresponding to contours of the flux function overplotted.

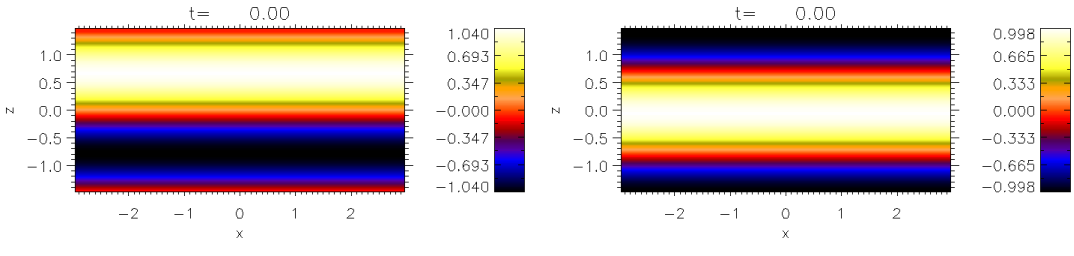

(a)

(b)

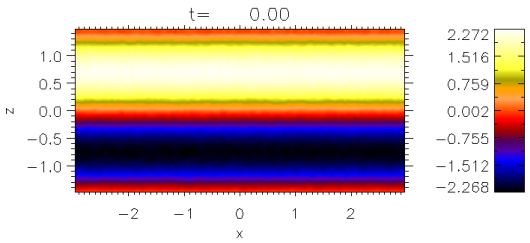

(c)

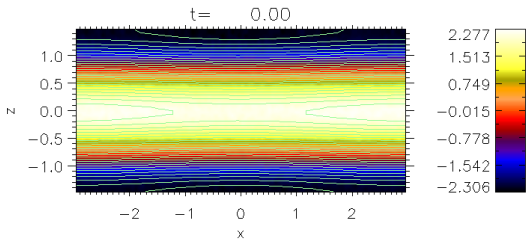

(d)

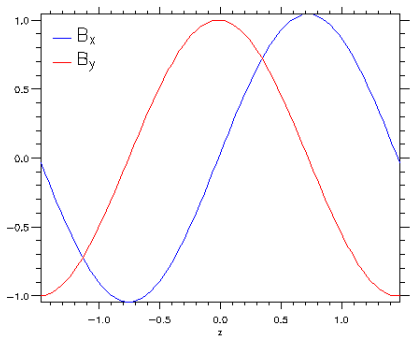

(e)

Figure 5.67: Plots showing the initial configuration for the force-free case. Figure 5.67(a) and Figure 5.67(b) show colour contour plots of B_x and B_y. Figure 5.67(c) shows a filled contour plot of the x component of the current density and Figure 5.67(d) shows a filled contour plot of the y component of the current density with magnetic field lines corresponding to contours of the flux function overplotted. Figure 5.67(e) shows a line plot of the profile of B_x and B_y along z for $x = 0$.

magnetic field. Therefore it would seem that the guide field plays a role in the stability properties of the anti-parallel equilibrium. As of yet a full linear stability analysis has not been carried out but it would be interesting in the future to try and understand the role of the guide field.

Figures 5.68 - 5.70 show how magnetic reconnection proceeds and leads to large changes in the magnetic field structure. In the guide field case $B_{y0} = 0.5$ the current density is reduced at the X-point from its initial value and enhanced in regions adjacent to it. In the guide field case $B_{y0} = 1.0$ the magnitude of the current density at the X-point is only slightly reduced from its initial value. In the force-free case the current density is enhanced at the X-point. At late times in the simulation runs the magnetic field structure has changed dramatically. The magnetic field configuration has gone from having a (B_x, B_y) structure to having a mainly (B_y, B_z) structure which is identical to the behaviour for the equal mass ratio simulations. It is also clear that in all the simulation runs in the majority of the simulation box the y component of the current density has been significantly reduced. This large scale reorganistion of the geometry of the magnetic field is again due to the doubly periodic boundary conditions that are used. It is clear to see that in all the simulation runs that the O-points above and below the central X-point have a strong effect. Once the initial stages of reconnection have occurred the O-points above and below the central X-point continue to press in on the central X-point eventually leading to the large scale reorganisation that is shown.

Figure 5.73 shows line plots along x for $z = 0$ of the electron number density n_e (blue lines) and the y component of the current density (red lines) for the antiparallel cases with guide field, $B_{y0} = 0.5$ and $B_{y0} = 1.0$ and also the linear force-free case during reconnection. These can be compared to the initial electron number number density and y component of the current density profiles plotted along x for $z = 0$ which are shown in Figure 5.72. In comparison to the equal mass ratio runs in Sec. 5.5, Figures 5.73(a) and 5.73(b) show that the runs starting from the anti-parallel magnetic configuration show a similar density depletion around the X-point. In the guide field cases $B_{y0} = 0.5$ and $B_{y0} = 1.0$, Figures 5.73(b) and 5.73(d) show that the current density is strongest in regions adjacent to the X-point with peaks either side of the X-point at $|x| \approx 1.2\, c/\omega_{pi}$ for the case $B_{y0} = 0.5$ and $|x| \approx 1.3\, c/\omega_{pi}$ for the case with $B_{y0} = 1.0$. Figure 5.73(b) shows that for the guide field case $B_{y0} = 0.5$ the current density is significantly reduced from its initial value at the X-point. In the stronger guide field case $B_{y0} = 1.0$ the current density is only slightly reduced at the X-point from its initial value and is stronger than that of the guide field $B_{y0} = 0.5$ case. In the linear force-free case, in contrast to the anti-parallel cases, Figure 5.73(e) shows that the number density is enhanced at the X-point. In addition to this Figure 5.73(f) shows that the current density is significantly increased at the X-point. This behaviour is identical to the equal mass ratio case discussed in Sec. 5.5.

Figure 5.71 shows the evolution of the x component of the current density for the linear force-free case. This shows that as reconnection proceeds the x component of the current density remains very small at and along a thin region either side of the X-point and that it is also reduced in the

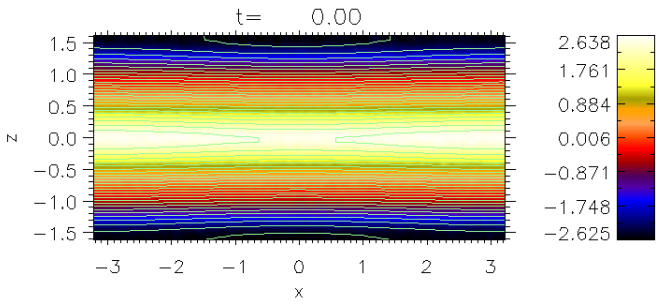

(a)

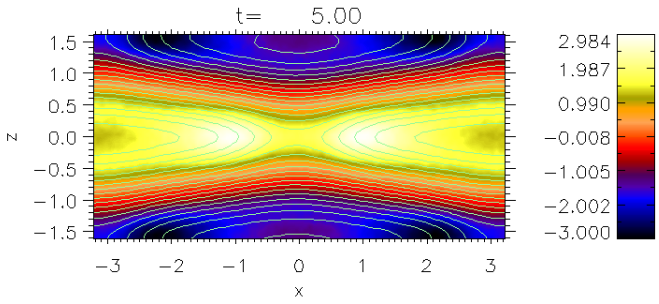

(b)

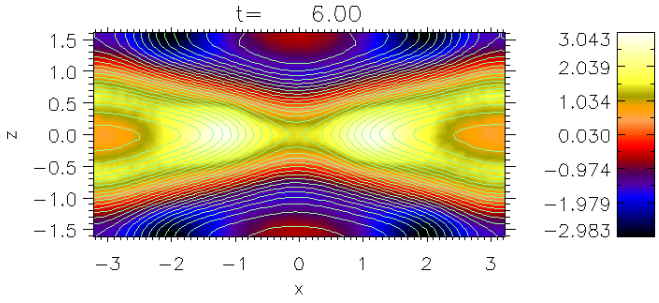

(c)

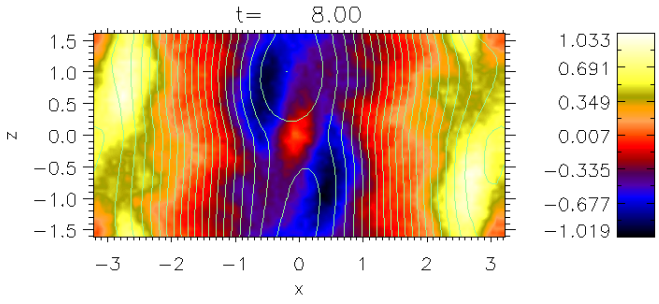

(d)

Figure 5.68: Plots of the y component of the current density with contours of the flux function overplotted for the anti-parallel case with a guide field of value $B_{y0} = 0.5$. The plots correspond to the different times (a) $t = 0$, (b) $t = 5$, (c) $t = 6$ and (d) $t = 8$.

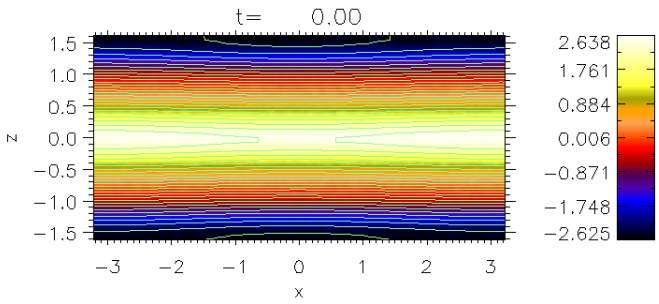

(a)

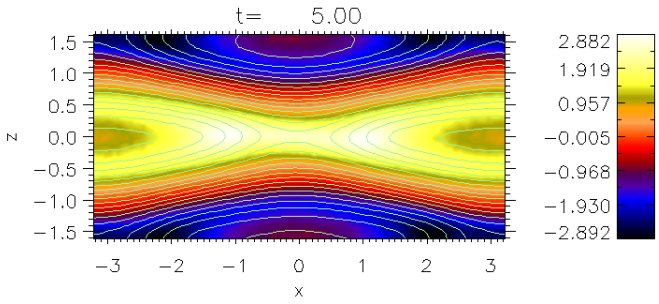

(b)

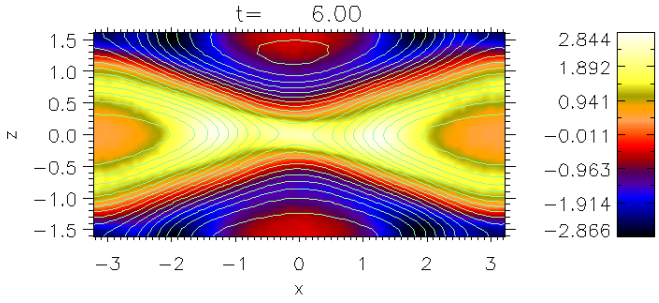

(c)

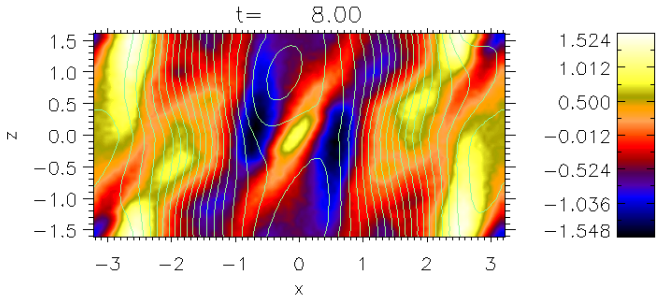

(d)

Figure 5.69: Plots of the y component of the current density with contours of the flux function overplotted for the anti-parallel case with a guide field of value $B_{y0} = 1.0$. The plots correspond to the different times (a) $t = 0$, (b) $t = 5$, (c) $t = 6$ and (d) $t = 8$.

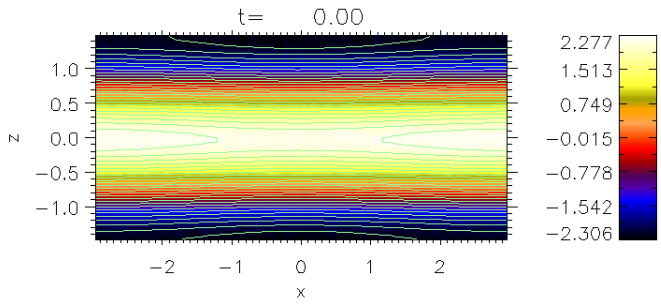

(a)

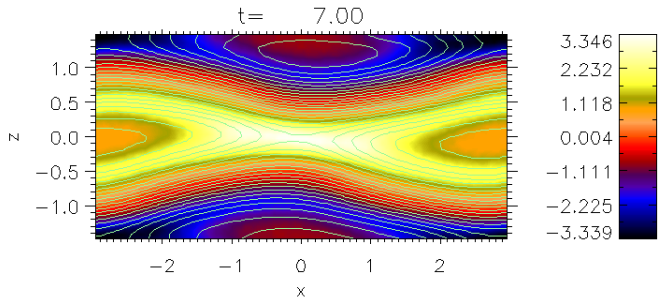

(b)

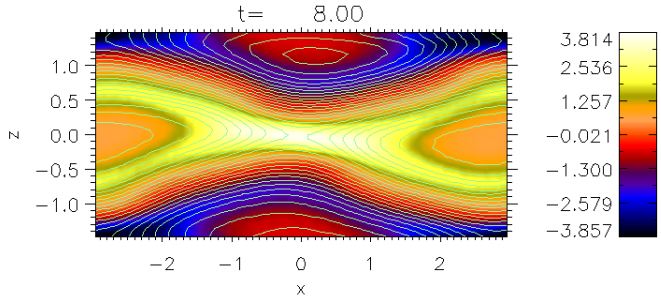

(c)

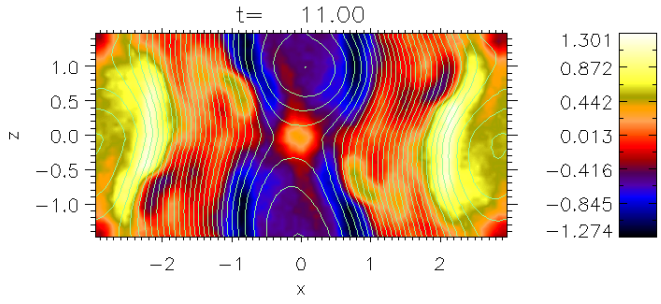

(d)

Figure 5.70: Plots of the y component of the current density with contours of the flux function overplotted for the force-free case. The plots correspond to the different times (a) $t = 0$, (b) $t = 7$, (c) $t = 8$ and (d) $t = 11$.

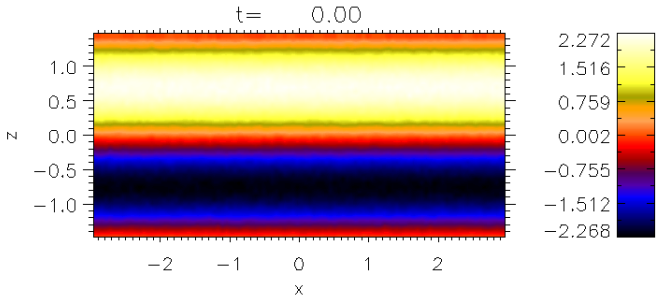

(a)

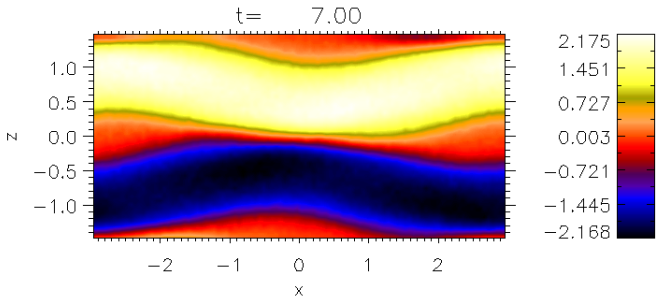

(b)

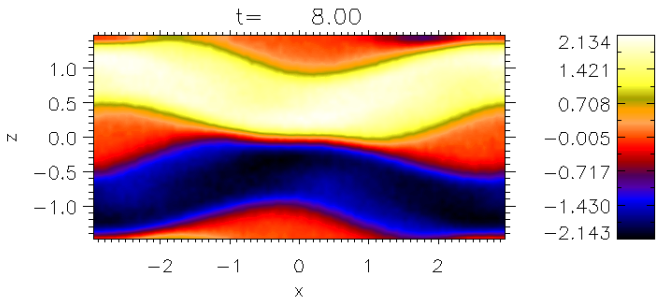

(c)

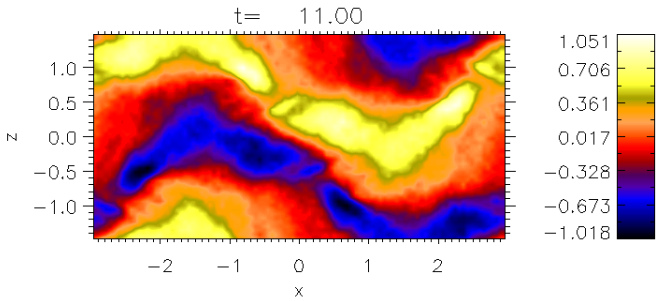

(d)

Figure 5.71: Filled contour plots of the x component of the current density for the force-free case. The plots correspond to the different times (a) $t = 0$, (b) $t = 7$, (c) $t = 8$ and (d) $t = 11$.

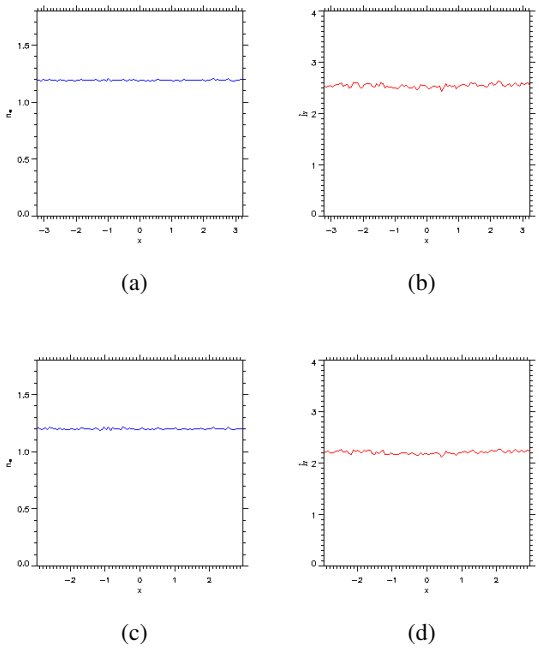

(a) (b)

(c) (d)

Figure 5.72: Line plots of the electron number density n_e (blue lines) and the y component of the current density (red lines) plotted along x for $z = 0$ at $t = 0$ for (a),(b) the anti-parallel simulation runs and also (c),(d) the linear force-free run.

magnetic islands. The thin central region is also inclined to the x axis. In the final stages of the evolution the interaction of the multiple current layers leads to a breakdown of the structure of the x component of the current density.

In the strong guide field case and in the force-free case for the y component of the current density you can also see the characteristic inclination of the central current sheet with respect to the x axis. In the zero guide field case it would have been expected that the electrons and the ions drift towards the X-point due to the $\mathbf{E} \times \mathbf{B}$ drift. In the reconnection region they would become demagnetised and accelerated in the y direction by the reconnection electric field. They would also be expelled from the reconnection region with super Alfvénic velocities along x. The electron and ion flows would be expected to be symmetric. The introduction of the guide field changes the dynamics. In particular in the strong guide field case, where the inclination of the current sheet is most prominent the guide field modifies the $\mathbf{E} \times \mathbf{B}$ drift and causes the ions and electrons to drift in directions not possible in the zero guide field case. The electrons in the strong guide field case have strong flows along the separatrices. The electron flow parallel to the magnetic field is shown for the guide field case $B_{y0} = 1.0$ and for the force-free case in Figure 5.74. There is clearly a large electron flow along the separatrices in the strong guide field and force-free cases. The strongest flows in both cases are along the upper left and bottom right separatrices.

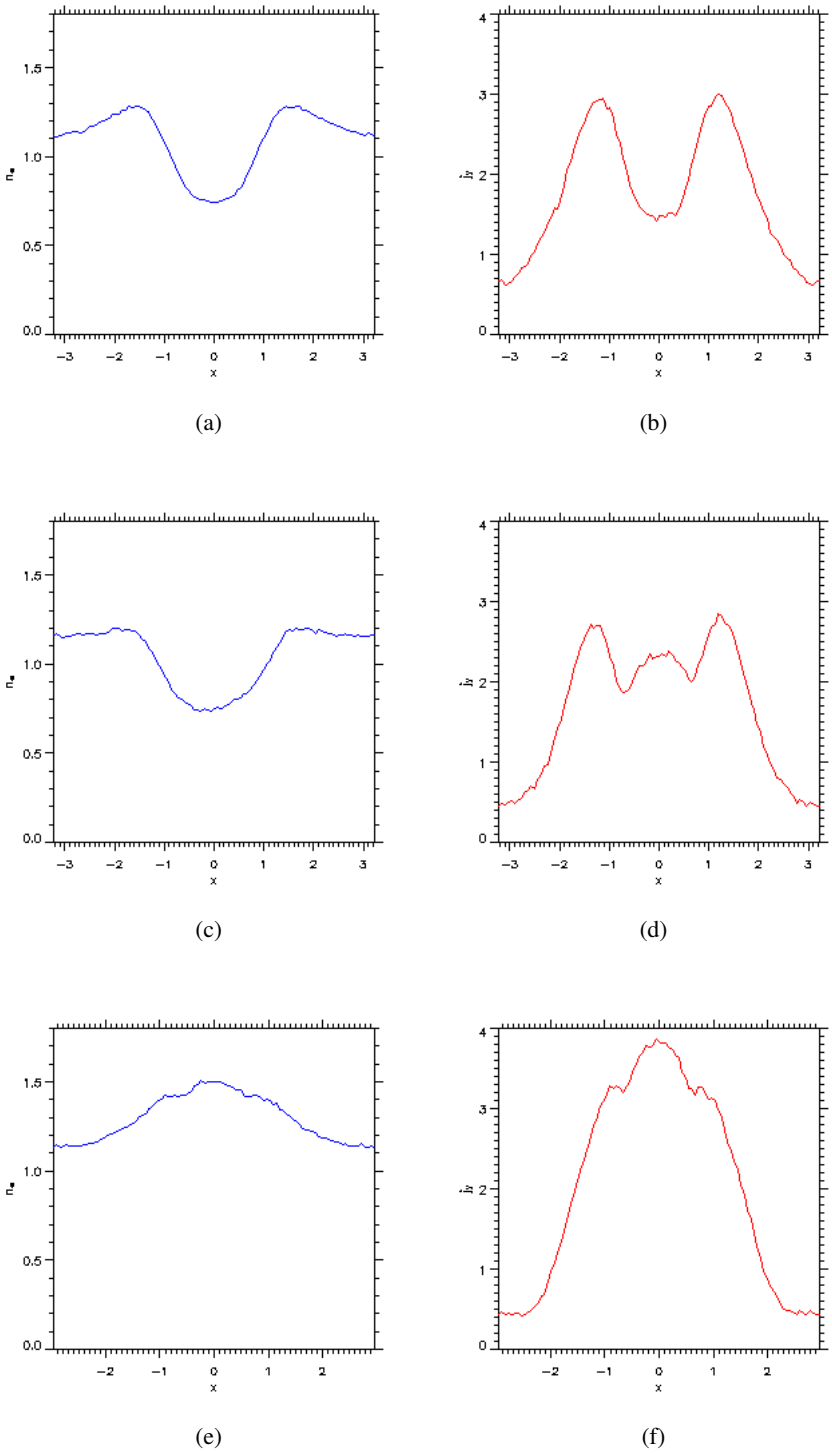

Figure 5.73: Line plots of the electron number density n_e (blue lines) and the y component of the current density (red lines) plotted along x for $z = 0$ during reconnection for the anisotropic bi-Maxwellian runs for the anti-parallell case with a guide field of value (a),(b) $B_{y0} = 0.5$ ($t = 6$) (c),(d) $B_{y0} = 1.0$ ($t = 6$), and also (e),(f) linear force-free ($t = 9$).

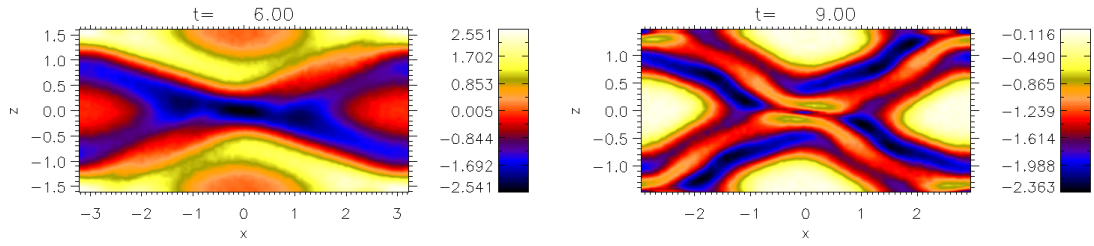

(a) (b)

Figure 5.74: Figures showing the electron flow along the magnetic field during reconnection for the guide field case $B_{y0} = 1.0$ and the force-free case. In these cases the electrons have large flows along the separatrices.

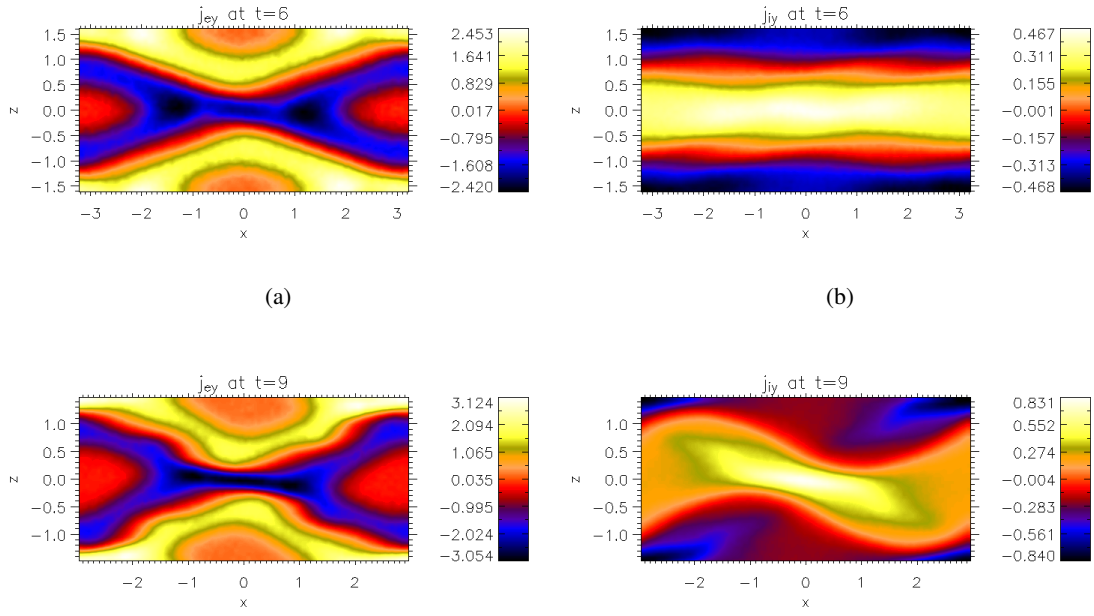

(a) (b)

(c) (d)

Figure 5.75: Plots of the electron and ion contributions to the y component of the current density for different cases during reconnection. (a),(b) $B_{y0} = 1.0$ ($x_0 = -0.07$), (c),(d) linear force-free ($x_0 = -0.06$).

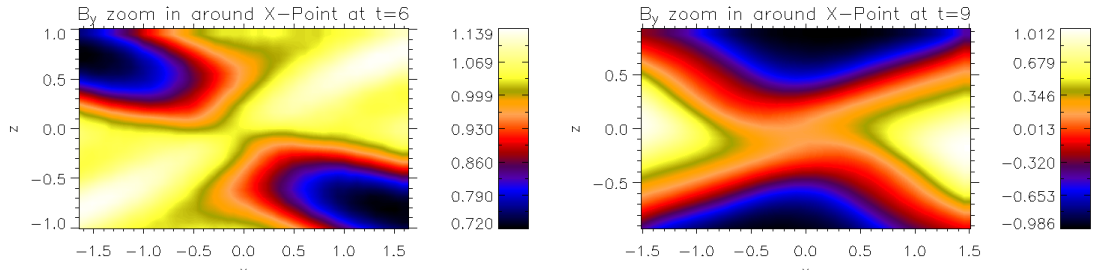

(a) (b)

Figure 5.76: Figures showing the y component of the magnetic field during the reconnection process. (a) In the guide field case $B_{y0} = 1$ the quadrupolar structure is overlaid on top of the guide field. (b) In the force-free case the quadrupolar B_y magnetic field is similar to the anti-parallel case although slightly distorted from the expected symmetry.

Figure 5.75 shows the electron and ion contributions to the y component of the current density during the reconnection process for the guide field $B_{y0} = 1.0$ and force-free case. In each example it is clear that in the vicinity of the central X-point the electron current layer is much thinner than the ion current layer in the z direction which is charactersitic of the change of scaling that the higher mass ratio introduces. The electrons are demagnetized for a smaller region than the ions. In the guide field $B_{y0} = 1.0$ case the ion current layer is relatively unchanged from the initial state. The electron current layer in the force-free case and the guide field $B_{y0} = 1.0$ cases are very similar. In both cases it is clear that the y component of the current density is dominated by the electrons. This is again a characteristic feature of collisionless reconnection. The region in which the ions are demagnetized is known as the Hall zone. This characteristic property of collisionless reconnection leads to the formation of a quadrupolar out of the plane magnetic field in the case of zero guide field. In the strong guide field case you also get the formation of a quadrupolar out of the plane magnetic field, but overlaid on the guide magnetic field and this is shown in Figure 5.76(a). In the force-free case there is the formation of a quadrupolar out of the plane magnetic field that is similar to the anti-parallel case but it is distorted from the symmetry that would be expected in the anti-parallel case. This is shown in Figure 5.76(b).

A comparison of the evolution of the runs is given in Figure 5.77. This shows two plots, one for the reconnected flux for each case plotted using different colours to represent the strength of the guide field in each run where the reconnected flux is defined as

$$F(t) = \int_{B_z>0} dx\, B_z(z=0), \tag{5.40}$$

and the other shows the reconnection rate which is found from the gradient of the reconnected flux normalised against the maximum Alfvén speed at each timestep.

Examining the evolution of these runs one can clearly see from the plots of the reconnection rate

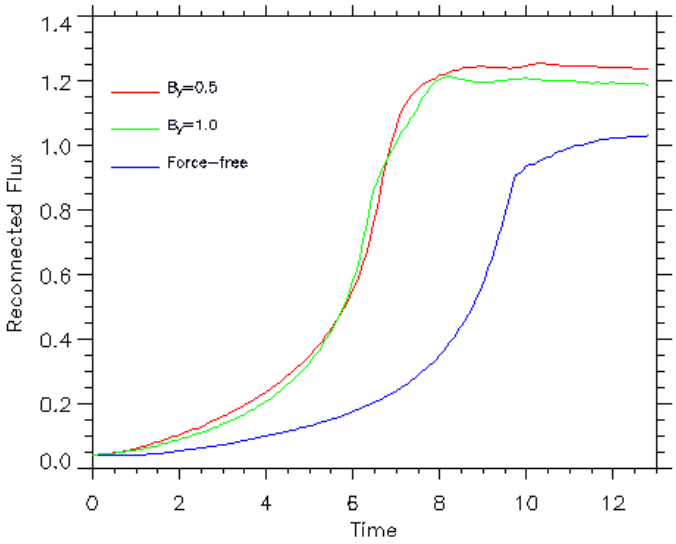

(a)

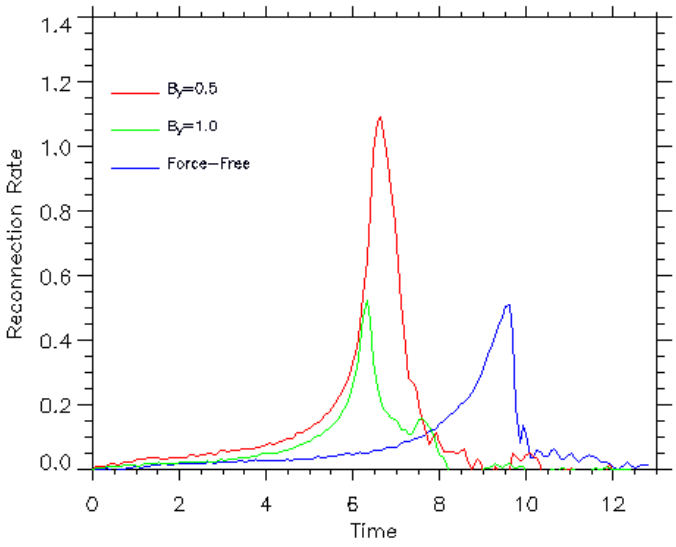

(b)

Figure 5.77: Figures showing the evolution of the simulations with varying strengths of guide field using the anti-parallel case as an initial configuration and also including the case of a linear force-free equilibrium for $m_i/m_e = 25$ simulation runs. The reconnected flux is shown in Figure 5.77(a) and the corresponding reconnection rates in Figure 5.77(b). The colours represent the different strengths of the guide field in the initial configuration.

shown in Figure 5.77(b) that the reconnection rate in general is reduced when the guide field is of the order B_0. This is in agreement with previous studies that show that the reconnection rate is reduced once the guide field is large enough to significantly change the magnetic pressure in the system (e.g. Pritchett 2001). It is also in agreement with all the previous results shown for initial conditions with equal mass ratio. The linear force-free case has a maximum reconnection rate that is approximately equivalent to the $B_{y0} = 1.0$ case which suggests that the shear magnetic field component B_y also has the effect of reducing the reconnection rate compared to the anti-parallel case.

5.7.1 The Structure of the Diffusion Region

In this section the morphology of the off-diagonal components off the electron pressure tensor components are shown for the different runs. The structure of these pressure tensor components can be compared to the previous examples for the equal masss ratio runs. It is also shown how the different contributions in Eq. (5.7) make up the reconnection electric field in the vicinity of the X-point.

To investigate the structure of the off-diagonal components in the region of the central X-point it was intended to analyse them at the time of maximum reconnection rate which is given by the peaks of each curve in Figure 5.77(b) in the same way as the Harris sheet cases. As in the equal mass ratio cases the problem with this was that at the time of maximum reconnection rate the pressure tensor components did not show the expected structure. This is again due to the interaction of the multiple current layers which leads to a breakdown of the expected structure of the off-diagonal components at the central X-point. It can be shown though at earlier stages in the reconnection process that the off-diagonal pressure tensor components do show the expected form. This can be seen in Figure 5.82 and Figure 5.83 which show the $P_{xy,e}$ and $P_{yz,e}$ components of the electron pressure tensor for the different strengths of guide field and including the force-free case.

Figure 5.78 shows filled contour plots of the y component of the current density for each case at earlier stages of reconnection where the off-diagonal components of the electron pressure tensor show the expected structure. Also shown in Figure 5.79 are filled contour plots of the y component of the electric field at these times. This clearly shows how magnetic reconnection generates a strong E_y electric field in the vicinity of the X-Point. The cases shown here are for the guide fields $B_{y0} = 0.5, 1.0$ for the anti-parallel case and also the linear force-free case. In all the figures x_0 refers to the approximate position along x of the X-point. In all cases the position of the X-point along z is approximately at $z = 0$.

To demonstrate that the dominant contribution to the E_y electric field in the vicinity of the X-

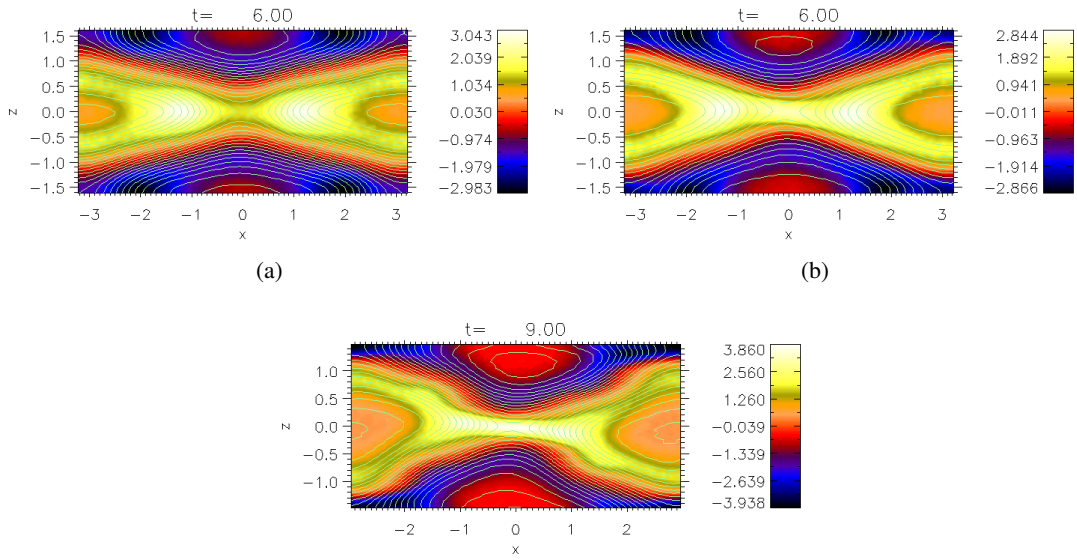

(a) (b)

(c)

Figure 5.78: Plots of the y component of the current density with contours of the flux function overplotted for simulations with varying strengths of guide field and the force-free case at a time when the electron pressure tensor components show the expected structure. (a) $B_{y0} = 0.5$ ($x_0 = -0.07$), (b) $B_{y0} = 1.0$ ($x_0 = -0.07$), (c) linear force-free ($x_0 = -0.06$).

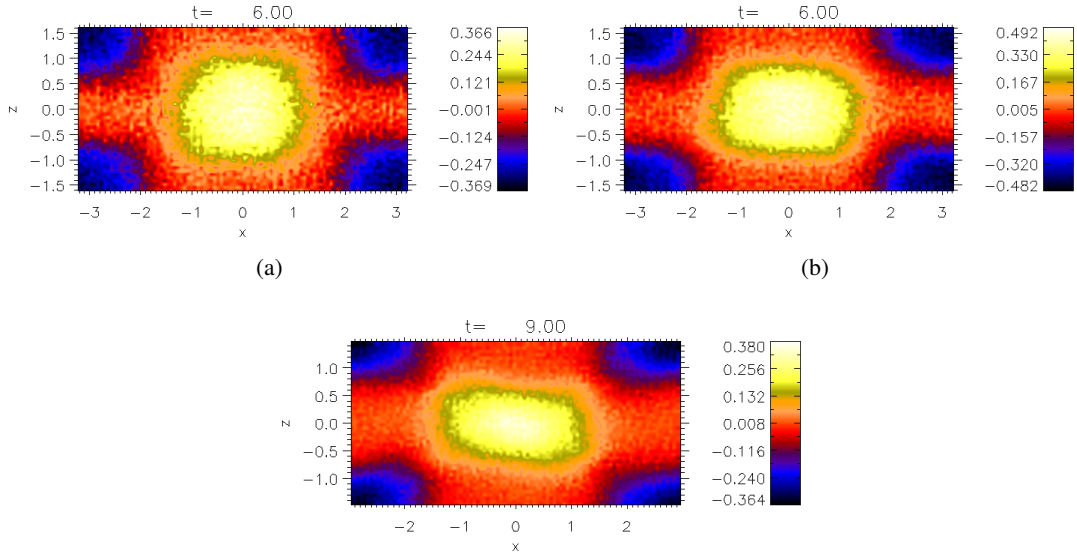

(a) (b)

(c)

Figure 5.79: Plots of the y component of the electric field for simulations with varying strengths of guide field and the force-free case at a time when the electron pressure tensor components show the expected structure. (a) $B_{y0} = 0.5$ ($x_0 = -0.07$), (b) $B_{y0} = 1.0$ ($x_0 = -0.07$), (c) linear force-free ($x_0 = -0.06$).

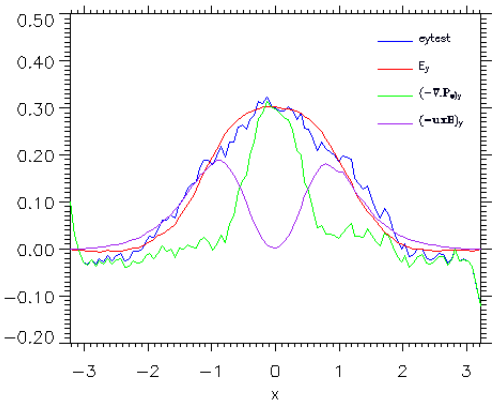

(a)

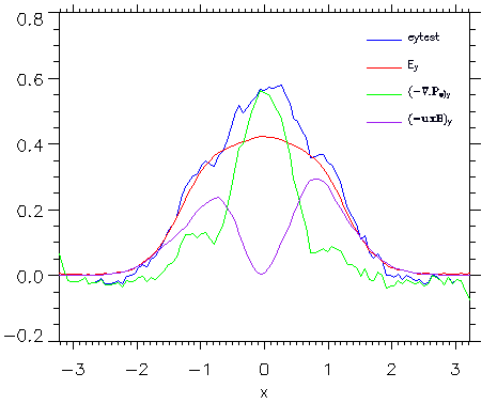

(b)

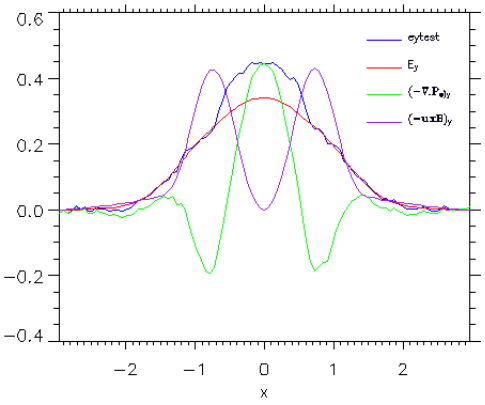

(c)

Figure 5.80: Plots along x for $z = 0$ of the contributions that make up the E_y electric field in Eq. (5.7) for simulations with varying strengths of guide field and the force-free case at a time when the electron pressure tensor components show the expected structure. (a) $B_{y0} = 0.5$ ($x_0 = -0.07$), (b) $B_{y0} = 1.0$ ($x_0 = -0.07$), (c) linear force-free ($x_0 = -0.06$).

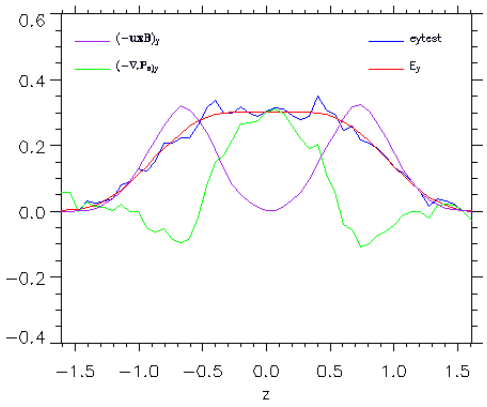

(a)

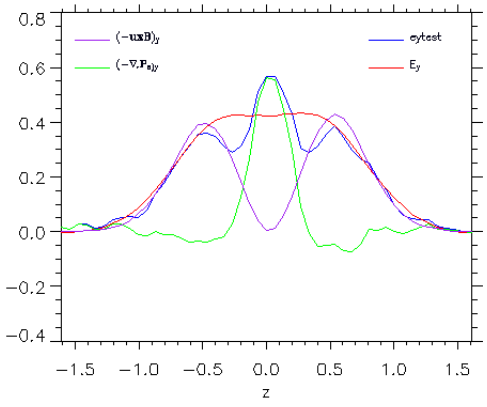

(b)

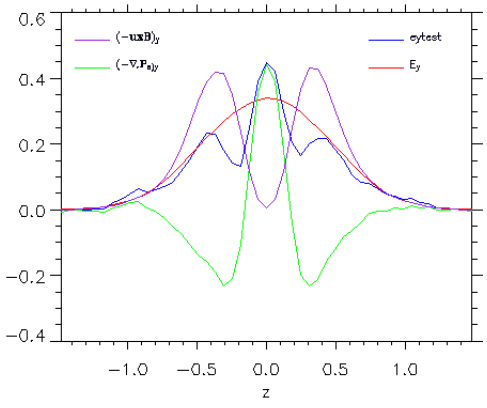

(c)

Figure 5.81: Plots along z for $x = x_0$ of the contributions that make up the E_y electric field in Eq. (5.7) for simulations with varying strengths of guide field and the force-free case at a time when the electron pressure tensor components show the expected structure. (a) $B_{y0} = 0.5$ ($x_0 = -0.07$), (b) $B_{y0} = 1.0$ ($x_0 = -0.07$), (c) linear force-free ($x_0 = -0.06$).

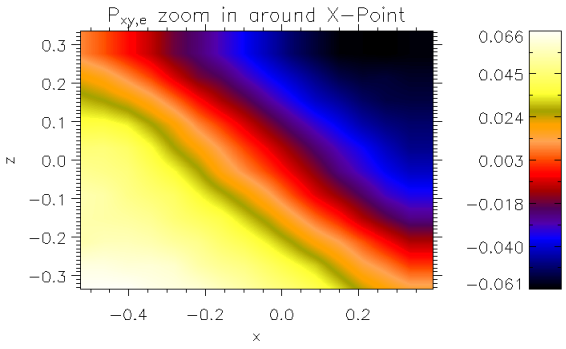

(a)

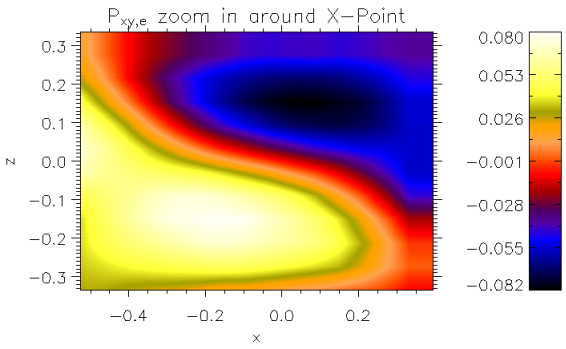

(b)

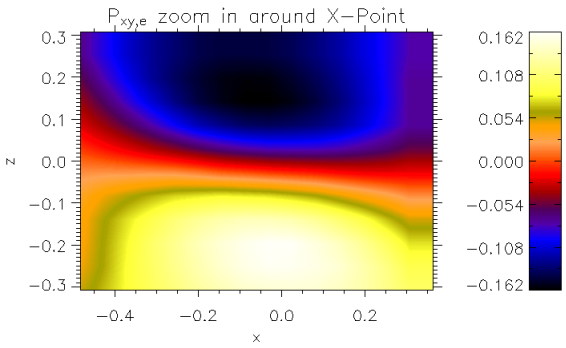

(c)

Figure 5.82: Plots of the $P_{xy,e}$ component of the electron pressure tensor for simulations with varying strengths of guide field and the force-free case at a time when the electron pressure tensor components show the expected structure. (a) $B_{y0} = 0.5$ ($x_0 = -0.07$), (b) $B_{y0} = 1.0$ ($x_0 = -0.07$), (c) linear force-free ($x_0 = -0.06$).

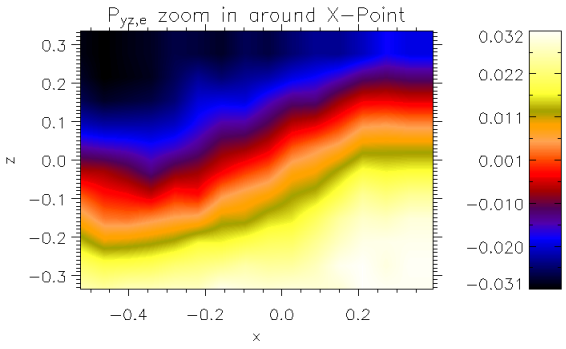

(a)

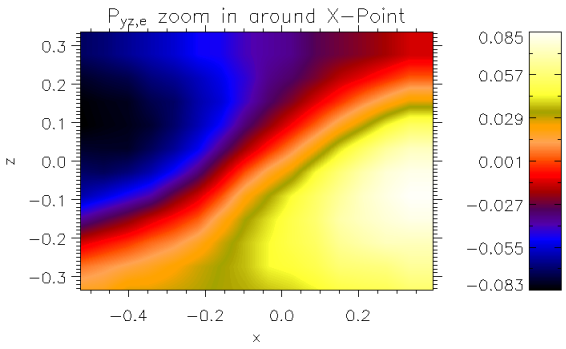

(b)

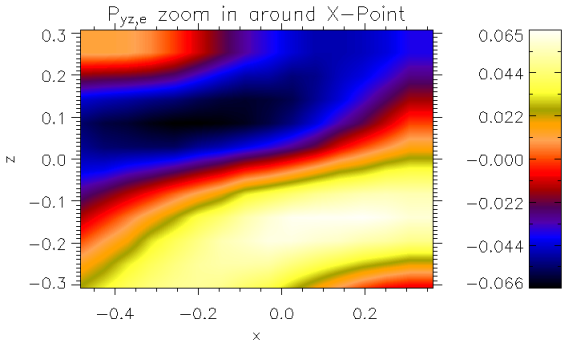

(c)

Figure 5.83: Plots of the $P_{yz,e}$ component of the electron pressure tensor for simulations with varying strengths of guide field and the force-free case at a time when the electron pressure tensor components show the expected structure. (a) $B_{y0} = 0.5$ ($x_0 = -0.06$), (b) $B_{y0} = 1.0$ ($x_0 = -0.06$), (c) linear force-free ($x_0 = -0.07$).

point is due to off-diagonal components of the electron pressure tensor Figure 5.80 and Figure 5.81 shows line plots along x and z of the contributions that make up the E_y electric field in Eq. (5.7) averaged for $0.08\Omega_i^{-1}$ either side of the times the E_y electric field is shown at in Figure 5.79 for each different case. In each case the red line corresponds to the E_y component of the electric field. It can be seen that the dominant contribution to the electric field close to the X-point comes from the gradients of the off-diagonal components of the electron pressure tensor as at this point the magnitude of the contribution from the gradients of the off-diagonal components of the electron pressure tensor (green line) match the magnitude of the y component of the electric field.

In each of the plots shown in Figure 5.80 and Figure 5.81 the gradients of the off-diagonal components of the electron pressure tensor dominate the electric field out to the point at which the $\mathbf{u} \times \mathbf{B}$ term equals the contribution from the gradients of the electron pressure tensor terms identical to the Harris sheet cases and the previous results for equal mass ratio. The plots shown in Figure 5.80 show that the contribution from the gradients of the off diagonal pressure tensor components dominates to about $x \approx \pm 0.5c/\omega_{pi}$ either side of the X-point for the guide field cases and the force-free case. The plots shown in Figure 5.81 indicate that the contribution from the off diagonal pressure tensor components dominates to about $z \approx \pm 0.4c/\omega_{pi}$ either side of the X-point for the $B_{y0} = 0.5$ case whilst for $B_{y0} = 1.0$ case they dominate up to $z \approx \pm 0.2c/\omega_{pi}$ either side of the X-point. In the force-free case the gradients of the electron pressure tensor components dominate out to only $z \approx \pm 0.1c/\omega_{pi}$ either side of the X-point.

In comparison to the previous cases for equal mass ratio these simulation runs starting from anisotropic equilibria give the same features. In all cases the mechanism that breaks the frozen in condition and dominates the contribution to the inductive electric field near to the X-point is due to gradients of the off-diagonal components of the electron pressure tensor near to the X-point. It must be pointed out though that for all the figures shown here, they are at an earlier time than the time of maximum reconnection rate that correspond to the peaks of the lines shown in Figure 5.77(b). This is because at the time of maximum reconnection rate, due to the periodic boundary conditions and the interaction of the multiple current layers in the simulation box, this leads to the breakdown of the expected structure of the pressure tensor components. Therefore to compare equally to the Harris sheet cases and to investigate the dominant mechanism that breaks the frozen in condition, an earlier time in the reconnection process has been investigated.

To investigate further the structure of the off-diagonal pressure tensor components, Figures 5.82 and 5.83 show filled contour plots of the $P_{xy,e}$ and $P_{yz,e}$ components of the electron pressure tensor zoomed in around the position of the central X-point. It would be expected that in the anti-parallel case the $P_{xy,e}$ component would be approximately symmetrical about the line $x = x_0$ which goes through the X-point with a gradient in x and the $P_{yz,e}$ component of the pressure tensor would be approximately symmetrical about the $z = 0$ line going through the X-point with a gradient in z. This expected structure has been shown already for the Harris sheet, anisotropic

bi-Maxwellian case and the double Harris sheet with equal mass ratio in Sec. 5.4 - 5.6. As the guide field is increased the structure of the $P_{xy,e}$ component starts to change. The symmetry along the line $x = x_0$ is broken and the structure is seen to rotate in an anti-clockwise direction until for the guide field $B_{y0} = 1.0$ the $P_{xy,e}$ component is almost symmetrical along the line $z = 0$ with a gradient in z identical to the equal mass ratio cases. The central region in all of the plots can also be seen to thin. The $P_{yz,e}$ component of the electron pressure tensor is seen to rotate slightly in the anti-clockwise direction. The significant rotation anti-clockwise and then clockwise as seen in the Harris sheet cases with equal mass ratio is not so obvious. In the strong guide field case the structure of the $P_{yz,e}$ component is still inclined to the $z = 0$ line, which is different to the equal mass ratio cases but once again the central region is observed to thin as the guide field becomes large. In the force-free case the inclination to the line $z = 0$ for the $P_{yz,e}$ component of the pressure tensor is less than the strong guide field case. The central region is thinnest in the linear force-free case.

The thinning of the central region in Figure 5.82 and Figure 5.83 is due to the introduction of the guide field. In the case of the Harris sheet without a guide field the characteristic length scale of $P_{xy,e}$ and $P_{yz,e}$ has been shown to be given approximately by the electron bounce widths in a field reversal λ_x and λ_z (e.g. Hesse et al. 1999). In the strong guide field case for the Harris sheet it has been shown that the characteristic length scale changes to that of the thermal electron Larmor radius $r_L = v_{th,e}/\Omega_e$ in the guide magnetic field (Hesse et al. 2004). The thermal electron Larmor radius for the simulation with $B_{y0} = 1.0$ at the time shown in Figure 5.78(b) is of the order $r_L \approx 0.18c/\omega_{pi}$. The width of the central region in Figure 5.82(b) and 5.83(b) is consistent with this estimate suggesting that the scale length of $P_{xy,e}$ and $P_{yz,e}$ is of the order of the thermal electron Larmor radius.

The thermal electron Larmor radius for the linear force-free case at the time shown in Figure 5.78(c) based on the maximum value of the shear component of the magnetic field at the X-point ($B_y \approx 0.16$) is of the order $r_L \approx 0.82c/\omega_{pi}$. This estimate of the thermal electron Larmor radius based on the shear magnetic field at the X-point is larger than for the guide field case $B_{y0} = 1.0$ but the central regions of the plots of $P_{xy,e}$ and $P_{yz,e}$ shown in Figure 5.82(c) and Figure 5.83(c) are of a similar width to the equivalent plots for the guide field case $B_{y0} = 1.0$. Therefore, for the force-free case these results suggest that the characteristic length scale may be even smaller than the thermal electron gyroradius in the shear magnetic field.

To illustrate how the interaction of the multiple current layers leads to the break up of the structure of the pressure tensor components at the central X-point it is useful to look at the time evolution of the off-diagonal components of the pressure tensor components. As examples of this the evolutions for the $P_{xy,e}$ component and the $P_{yz,e}$ component for the anti-parallel cases with a guide field of $B_{y0} = 0.5, B_{y0} = 1.0$ and the linear force-free case are shown in Figures 5.84 - 5.89. The snapshots show the off-diagonal components throughout the whole simulation domain. It can be

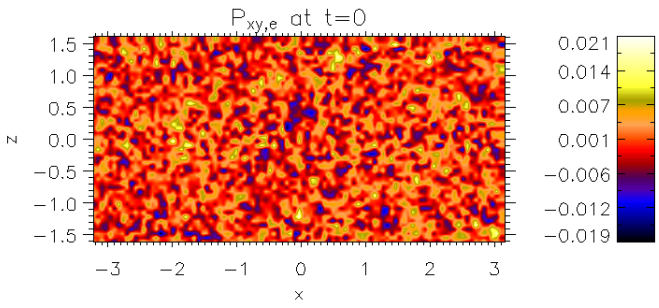

(a)

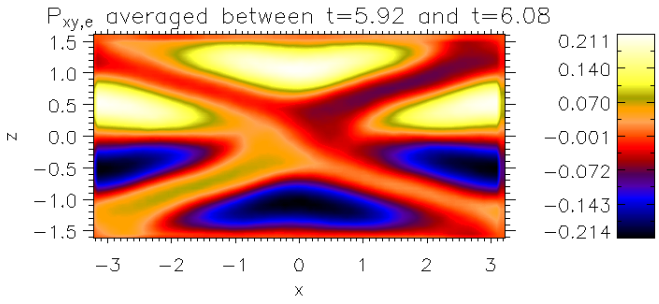

(b)

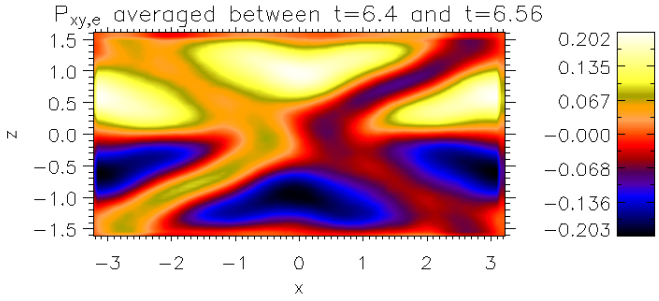

(c)

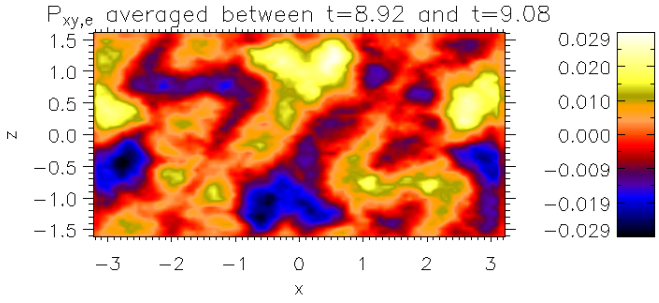

(d)

Figure 5.84: Plots of the evolution of the $P_{xy,e}$ component of the electron pressure tensor for the anti-parallel case with a guide field of $B_{y0} = 0.5$. The plots correspond to the $P_{xy,e}$ component at (a) $t = 0$ and averaged around (b) $t = 6$, (c) $t = 6.48$ and (d) $t = 9$.

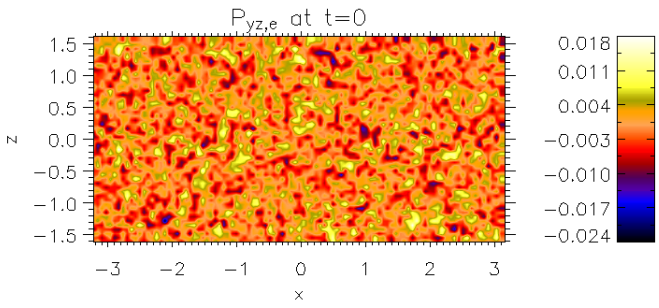

(a)

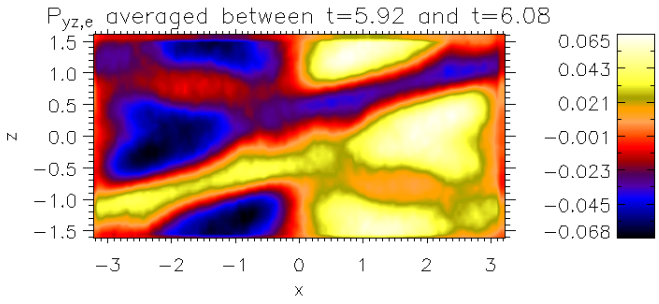

(b)

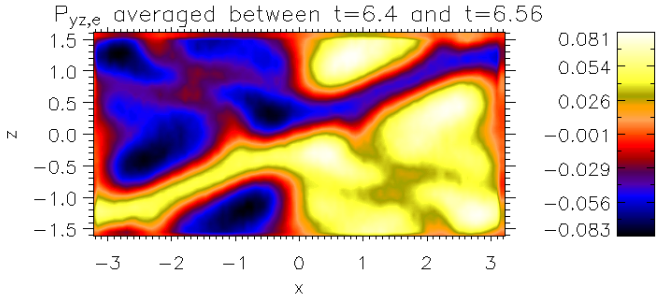

(c)

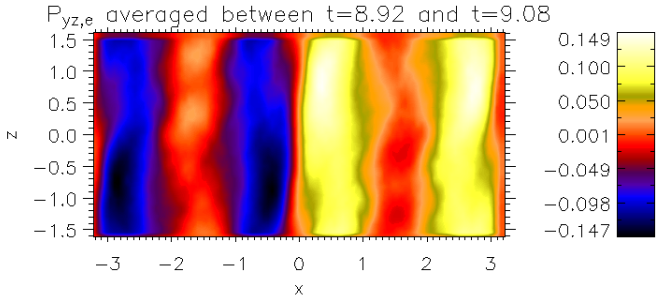

(d)

Figure 5.85: Plots of the evolution of the $P_{yz,e}$ component of the electron pressure tensor for the anti-parallel case with a guide field of $B_{y0} = 0.5$. The plots correspond to the $P_{yz,e}$ component at (a) $t = 0$ and averaged around (b) $t = 6$, (c) $t = 6.48$ and (d) $t = 9$.

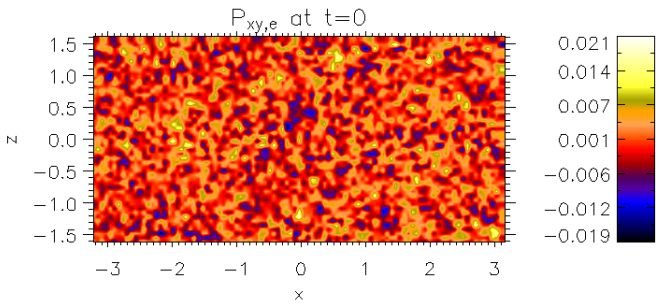

(a)

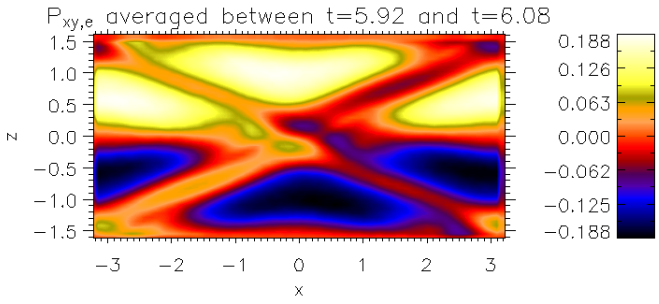

(b)

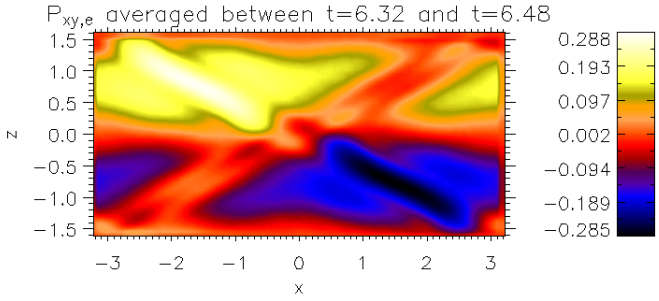

(c)

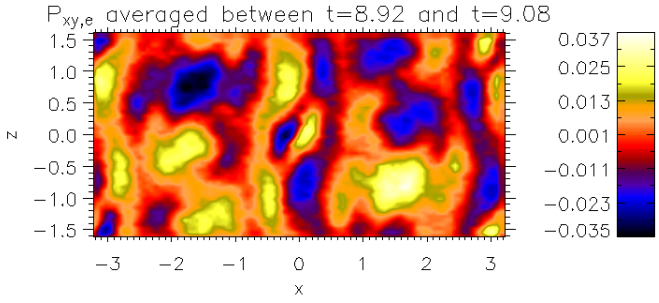

(d)

Figure 5.86: Plots of the evolution of the $P_{xy,e}$ component of the electron pressure tensor for the anti-parallel case with a guide field of $B_{y0} = 1.0$. The plots correspond to the $P_{xy,e}$ component at (a) $t = 0$ and averaged around (b) $t = 6$, (c) $t = 6.4$ and (d) $t = 9$.

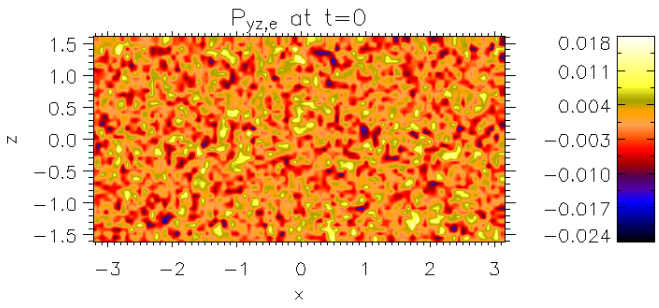

(a)

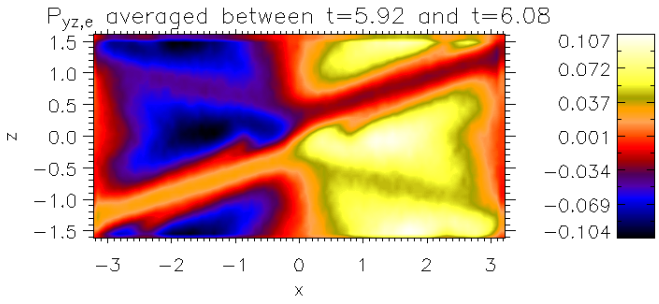

(b)

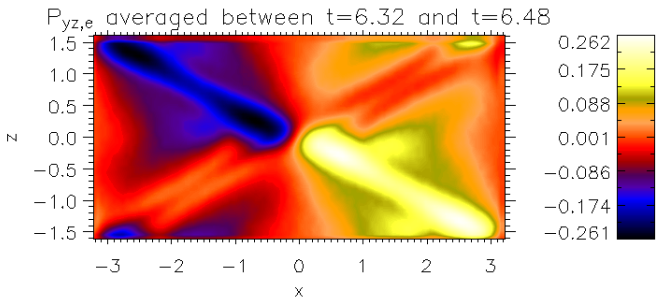

(c)

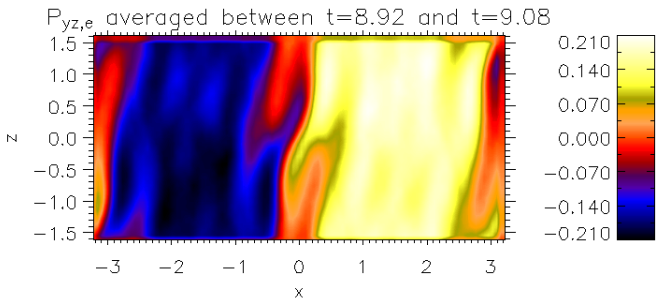

(d)

Figure 5.87: Plots of the evolution of the $P_{yz,e}$ component of the electron pressure tensor for the anti-parallel case with a guide field of $B_{y0} = 1.0$. The plots correspond to the $P_{yz,e}$ component at (a) $t = 0$ averaged around (b) $t = 6$, (c) $t = 6.4$ and (d) $t = 9$.

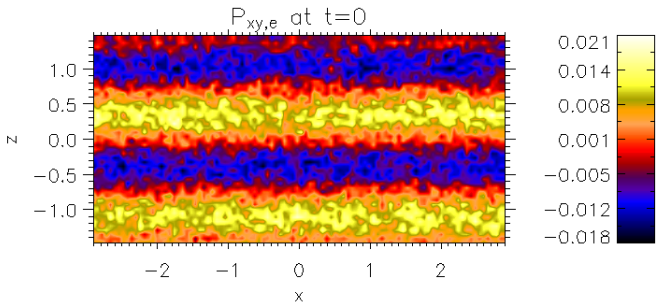

(a)

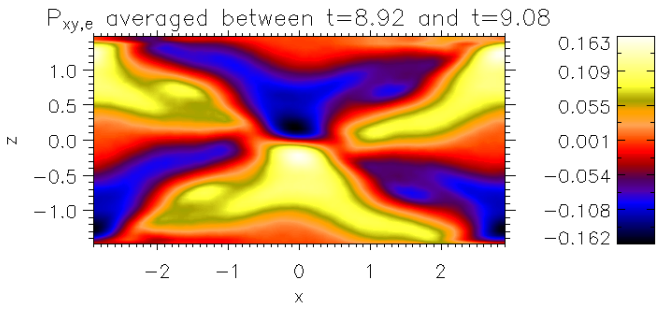

(b)

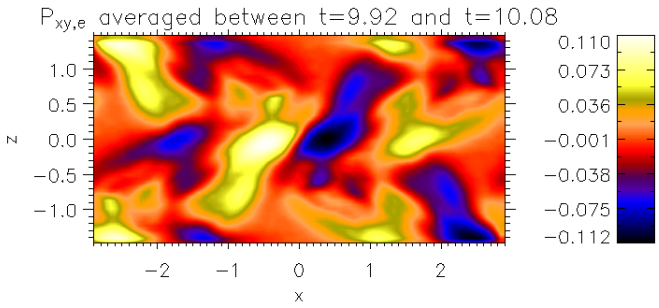

(c)

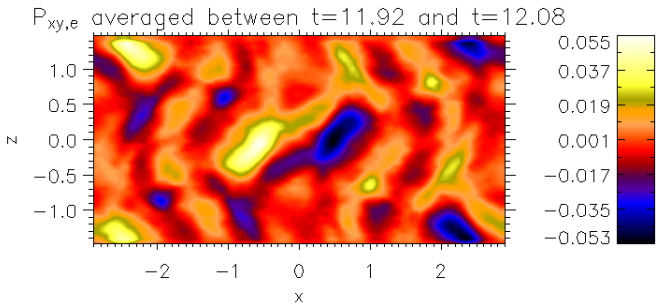

(d)

Figure 5.88: Plots of the evolution of the $P_{xy,e}$ component of the electron pressure tensor for the linear force-free case. The plots correspond to the $P_{xy,e}$ component at (a) $t = 0$ and averaged around (b) $t = 9$, (c) $t = 10$ and (d) $t = 12$.

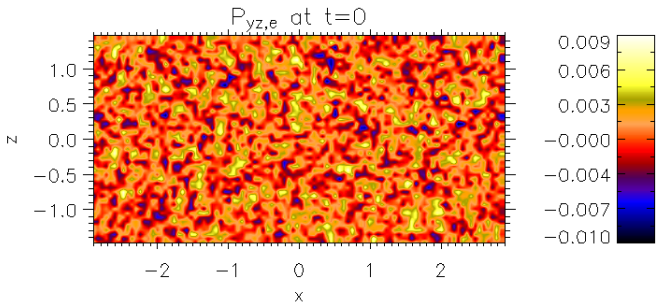

(a)

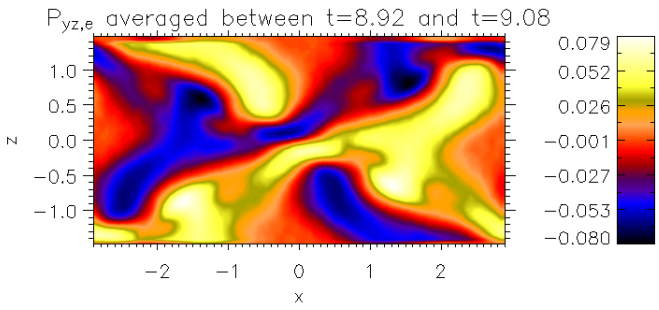

(b)

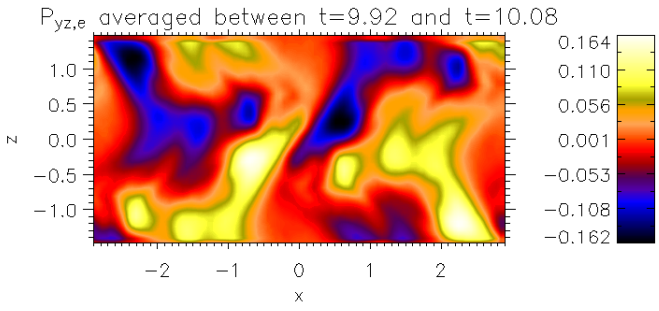

(c)

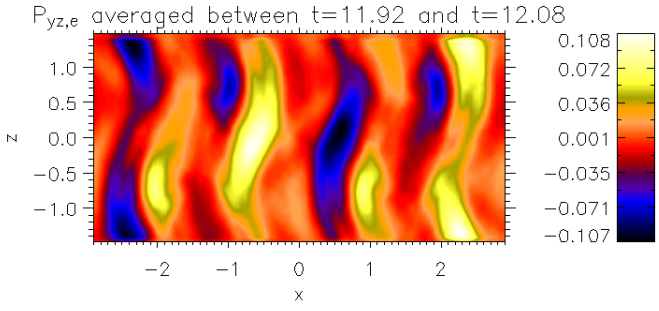

(d)

Figure 5.89: Plots of the evolution of the $P_{yz,e}$ component of the electron pressure tensor for the linear force-free case. The plots correspond to the $P_{yz,e}$ component at (a) $t = 0$ and averaged around (b) $t = 9$, (c) $t = 10$ and (d) $t = 12$.

seen that at the early stages of reconnection the pressure tensor components at the central X-point have the expected structure and then as time proceeds the interaction of the boundary with the central current layer leads to the breakdown of this structure. The overall evolution is also shown in the movies that come with the thesis (see Appendix B).

5.8 Force-Free Harris Sheet Simulations

The major aim of this work was to investigate the structure of the diffusion region for different initial conditions and to compare how the structure of the off-diagonal components of the electron pressure tensor changes. In this section reconnection simulations starting from a self-consistent force-free Harris sheet are investigated. This is the first ever study of collisionless reconnection to use an exact self-consistent non-linear force-free equilibrium as an initial condition. These are compared to the Harris sheet simulations, in particular to the strong guide field cases which have commonly been used to model low-β plasmas.

The reconnection rates of each simulation run are also investigated. It is a well know trend that for the Harris sheet case the effect of increasing the strength of the constant guide field reduces the reconnection rate. It is interesting to compare the reconnection rates for simulations starting from a self-consistent non-linear force-free field to see if in the force-free case the effect of the shear B_y magnetic field is to reduce or increase the reconnection rate.

In the first simulation the ion to electron mass ratio is set equal to one $(m_i/m_e = 1)$. In the second simulation the mass ratio is set to $m_i/m_e = 9$. Lengths are normalized to the ion inertial length c/ω_{pi} and the number density is normalised to a value n_0. Times are normalised to the inverse of the ion cyclotron frequency $\Omega_i = eB_0/m_i$. The magnetic field is normalised to the value B_0, the amplitude of the initial magnetic field. In the equal mass ratio simulation the system dimensions are $L_x = 20.0\, c/\omega_{pi}$ and $L_z = 10.0\, c/\omega_{pi}$ and in the $m_i/m_e = 9$ the system dimensions are $L_x = 13.3\, c/\omega_{pi}$ and $L_z = 6.7\, c/\omega_{pi}$ where L_x and L_z are the half lengths of the box in the x and z directions. In the equal mass ratio simulation the grid is 200×100 and in the $m_i/m_e = 9$ case the grid is 260×130 in the x and z directions. A time step $\omega_{pe}\Delta t = 1$ is used. The ratio ω_{pe}/Ω_e is set to a numerical value of 5.

The initial configuration is a force-free Harris sheet. The magnetic field is given by

$$B_x = \tanh\left(\frac{z}{L}\right), \tag{5.41}$$

$$B_y = \frac{B_0}{\cosh\left(\frac{z}{L}\right)}, \tag{5.42}$$

where $L = 1.0$. The electron and ion densities are constant. For each simulation run a perturbation

of the form

$$B_{xp} = -a_0 x_m \frac{\pi}{2L_z} \exp\left(-\frac{x^2}{2x_m^2} + 0.5\right) \sin\left(\frac{\pi z}{2L_z}\right), \tag{5.43}$$

$$B_{zp} = a_0 \frac{x}{x_m} \exp\left(-\frac{x^2}{2x_m^2} + 0.5\right) \cos\left(\frac{\pi z}{2L_z}\right), \tag{5.44}$$

is also added where $a_0 = 0.1$ and $x_m = L_z/2$. This gives an X-point type reconnection site at the centre of the box.

The velocity distribution of each particle species is set up according to the distribution function (3.203) described in Chap. 3. There are two particle populations which set up the equilibrium pressures and currents. The first population consists of a set of ions and electrons which establish the equilibrium pressures and currents for the Harris sheet part of the distribution function. The second population consists of a second set of ions and electrons which set up the additional pressure and currents that correspond to the shear B_y magnetic field. In the simulation runs temperatures are set such that $T_i + T_e = 0.5$, with $T_e/T_i = 1$. The equal mass ratio simluation run used 2×10^7 ions and electrons each for the first population and 3×10^7 ions and electrons for the second population. The $m_i/m_e = 9$ simulation run used 1.0×10^8 ions and electrons for the first population and 1.0×10^8 ions and electrons for the second population. Periodic boundary conditions are employed at $x = -L_x$ and $x = L_x$. Particles are specularly reflected at $z = -L_z$ and $z = L_z$. One of the advantages of the force-free Harris sheet is that unlike the linear force-free case it is not necessary to use periodic boundary conditions in the z direction and therefore the box size is free to be chosen, provided that you satisfy the condition (4.6) given in Chap. 4.

Figures 5.90 and 5.91 show the initial configuration at $t = 0$ for the equal mass ratio and $m_i/m_e = 9$ cases. Filled contour plots of the magnetic field components B_x and B_y for the two cases are shown in Figures 5.90(a), 5.90(b), 5.91(a) and 5.91(b). Figures 5.90(e) and 5.91(e) show line plots of the magnetic field profiles and current density profiles plotted along z for $x = 0$ (i.e. through the X-point). It is important to note the slight modification of the hyperbolic tangent profile of the x component of the magnetic field and the respective y component of the current density along z in both cases which is introduced by the perturbation to the magnetic field. Figures 5.90(c) and 5.91(c) show filled contour plots of the x component of the current density and Figures 5.90(d) and 5.91(d) are filled contour plots of the y component of the current density with contours of the flux function overplotted showing the magnetic field lines. It is clear to see in both cases the current sheet structure of the x and y components of the current density with the X-point structure introduced by the perturbation to the equilibrium magnetic field.

Figures 5.92 and 5.93 show the evolution of the magnetic field for the equal mass ratio and $m_i/m_e = 9$ runs with the y component of the current density colour coded. Movies of the evolution for each case can be found on the CD which is attached to this thesis (see Appendix B).

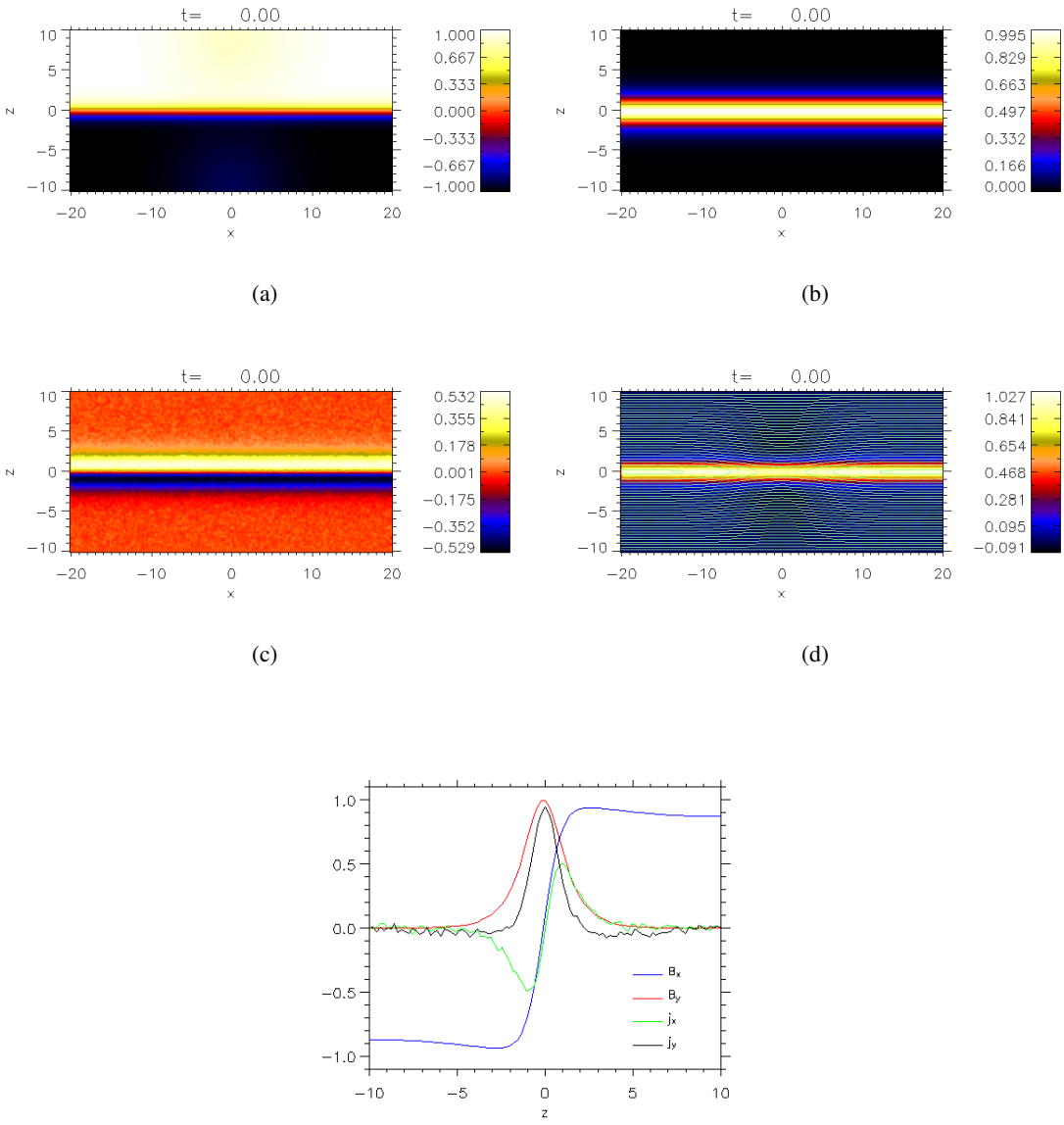

Figure 5.90: Plots showing the initial configuration for the force-free Harris sheet with equal mass ratio. Figures 5.90(a) and 5.90(b) shows colour contour plots of B_x and B_y. Figure 5.90(c) shows a filled contour plot of the x component of the current density and Figure 5.90(d) shows a filled contour plot of the y component of the current density with magnetic field lines corresponding to contours of the flux function overplotted. Figure 5.90(e) shows line plots of the profiles of B_x, B_y, j_x and j_y along z for $x = 0$.

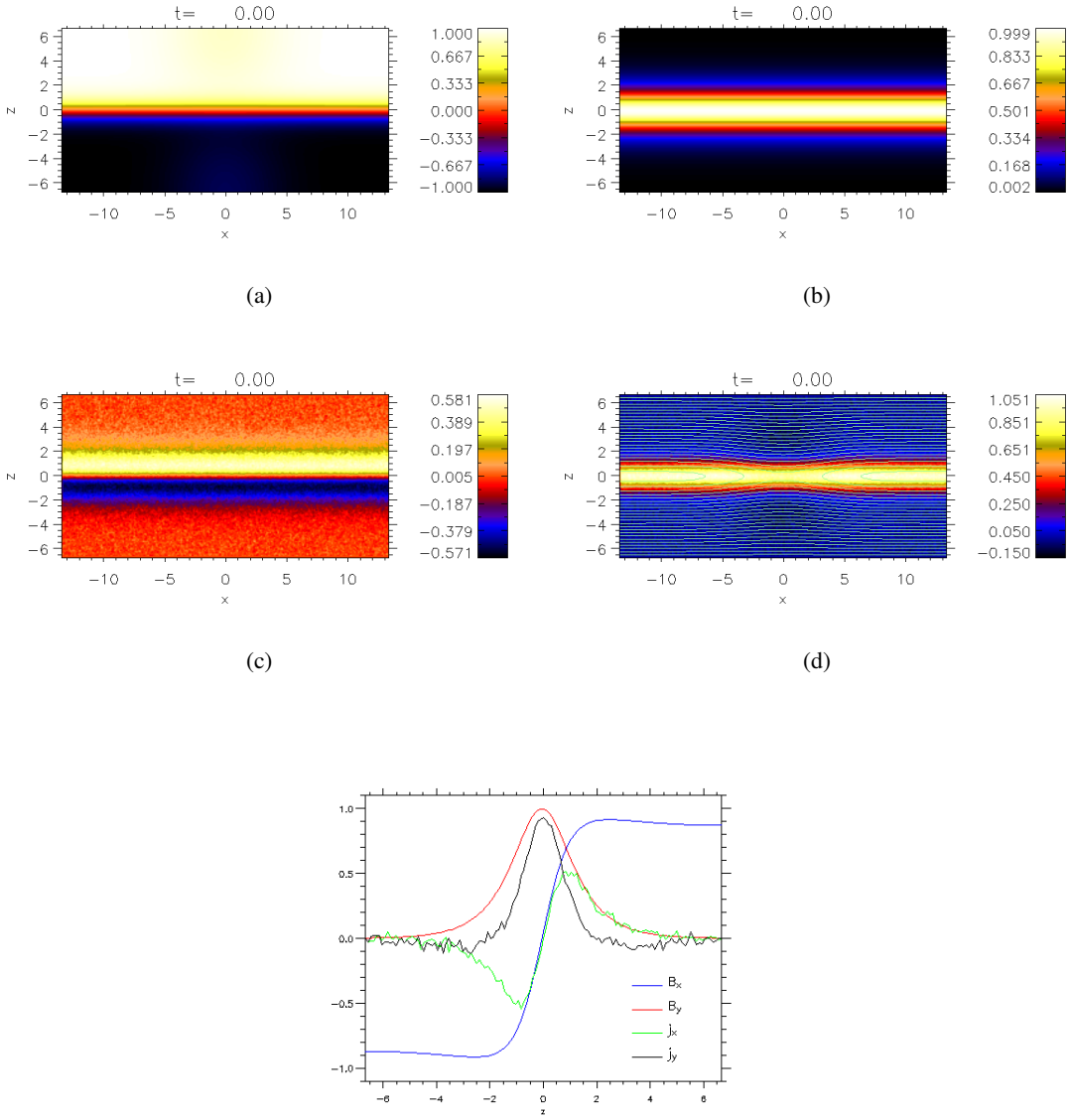

Figure 5.91: Plots showing the initial configuration for the force-free Harris sheet with mass ratio $m_i/m_e = 9$. Figures 5.91(a) and 5.91(b) shows colour contour plots of B_x and B_y. Figure 5.91(c) shows a filled contour plot of the x component of the current density and Figure 5.91(d) shows a filled contour plot of the y component of the current density with magnetic field lines corresponding to contours of the flux function overplotted. Figure 5.91(e) shows line plots of the profile of B_x and B_y along z for $x = 0$.

These figures show how magnetic reconnection proceeds and leads to large changes in the magnetic field structure. In the central X-point region in both cases the current density is enhanced and particle densities are increased during the first phase of the evolution. This is different to the Harris sheet cases as in all those cases the current density and particle densities are reduced at the central X-point. In the equal mass ratio case there is symmetry of the central current sheet about the X-point. In the mass ratio $m_i/m_e = 9$ case as the evolution proceeds there is a rotation of the central current sheet with respect to the x axis where the electrons are the dominant current carriers. The rotation with respect to the x axis is a characteristic feature of guide field reconnection and is related to the shear y component of the magnetic field at the X-point. In the late stages of the evolution in both cases the current density reduces at the X-point and the y component of the magnetic field is almost zero at the X-point which corresponds to a transition to anti-parallel reconnection. The evolution of B_y for the two cases is shown in Figures 5.96 and 5.97. Eventually in both cases reconnection slows due to the build up of magnetic flux in the magnetic islands which causes a magnetic pressure gradient which reduces the pulling of the magnetic field lines away from the reconnection site.

Figure 5.99 shows line plots along x for $z = 0$ of the electron number density n_e (blue lines) and the y component of the current density (red lines) for the force-free Harris sheet runs with mass ratio $m_i/m_e = 1$ amd $m_i/m_e = 9$ at the time of maximum reconnection rate. These can be compared to the electron number density (blue lines) and the y component of the current density at $t = 0$ for each case which is shown in Figure 5.98. Figures 5.99(a) and 5.99(b) show that for the equal mass ratio run at the time of maximum reconnection rate the number density and current density are increased at the X-point. This feature has also been shown for the linear force-free runs in Sec. 5.5 and 5.7. The increase in the current density and number density at the time of maximum reconnection rate is different to a Harris sheet run with zero guide field where the current density and number density are depleted at the X-point during reconnection. In the mass ratio $m_i/m_e = 9$ case the time of maximum reconnection rate occurs at a later time in the evolution. At this time the evolution is closer to anti-parallel reconnection with a weak guide field and therefore Figures 5.99(c) and 5.99(d) show a density depletion and current density decrease at the X-point similar to reconnection starting from a Harris sheet with weak guide field. Figure 5.99(d) also shows increases of the y component of the current density at peaks located at $|x| \approx 9 - 10\, c/\omega_{pi}$ either side of the X-point. This is also a typical feature of anti-parallel reconnection.

Figures 5.94 and 5.95 show the evolution of the x component of the current density for the equal mass ratio and $m_i/m_e = 9$ cases. This shows that as reconnection proceeds the x component of the current density is reduced in regions close to the X-point and in the magnetic islands with wing-like structures at the edges of the magnetic islands where the x component of the current density is enhanced. The enhanced wing-like structures correspond to gradients of the y component of

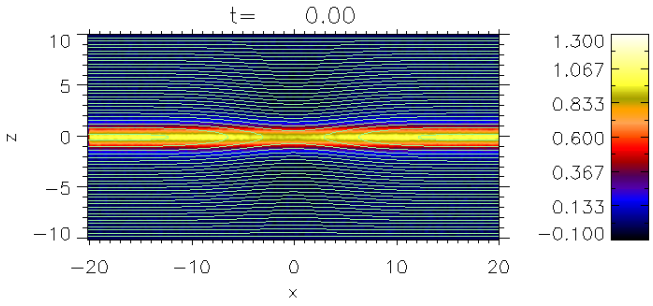

(a)

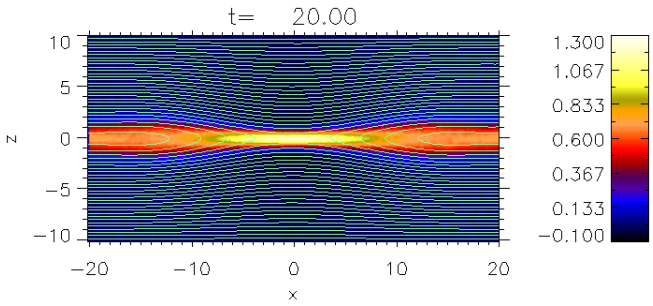

(b)

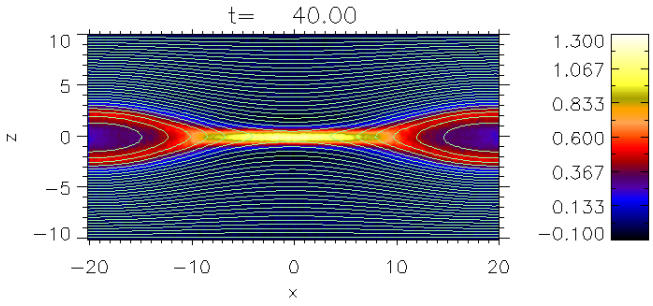

(c)

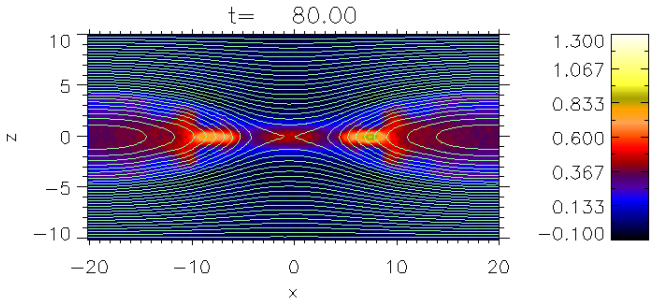

(d)

Figure 5.92: Plots of the y component of the current density with contours of the flux function overplotted for the force-free Harris sheet run with equal mass ratio. The plots correspond to the different times (a) $t = 0$, (b) $t = 20$, (c) $t = 40$ and (d) $t = 80$.

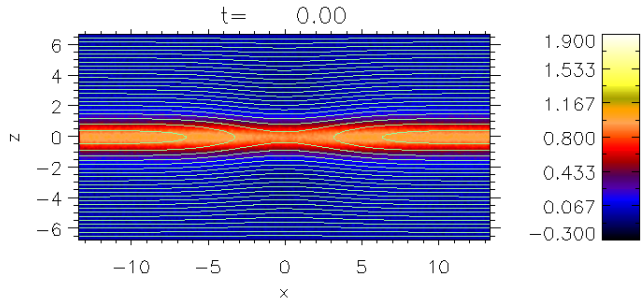

(a)

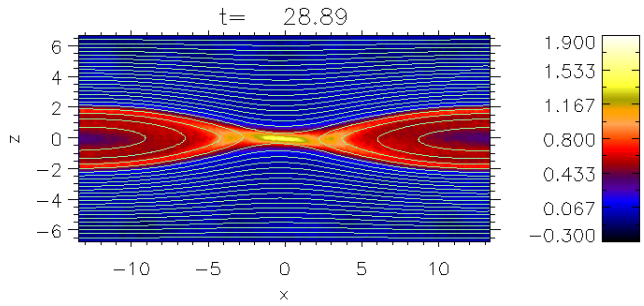

(b)

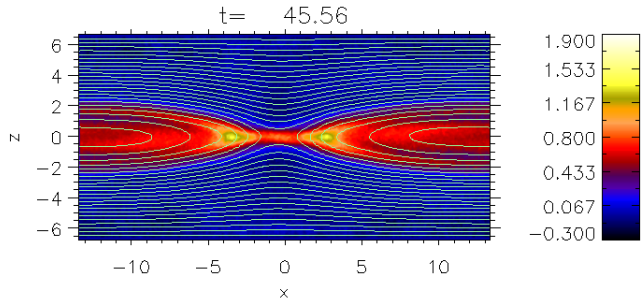

(c)

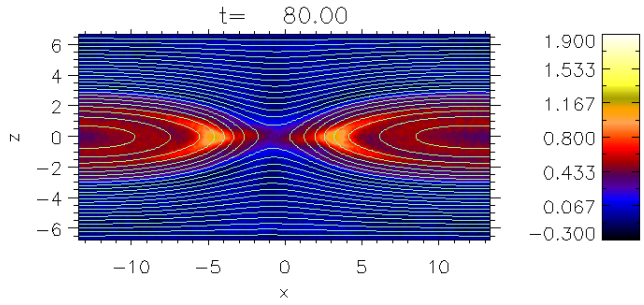

(d)

Figure 5.93: Plots of the y component of the current density with contours of the flux function overplotted for the force-free Harris sheet run with a mass ratio $m_i/m_e = 9$. The plots correspond to the different times (a) $t = 0$, (b) $t = 28.89$, (c) $t = 45.56$ and (d) $t = 80$.

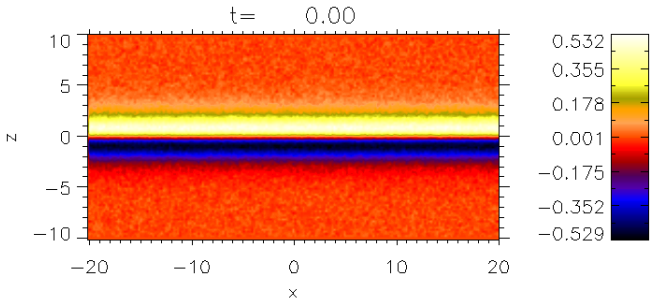

(a)

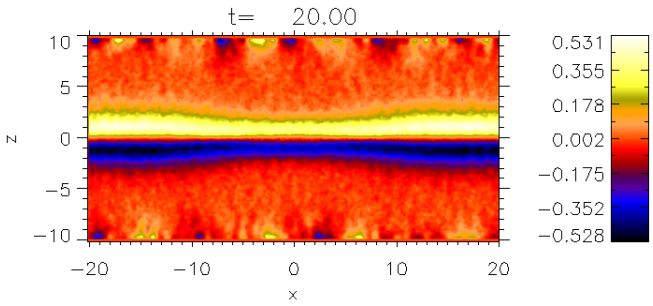

(b)

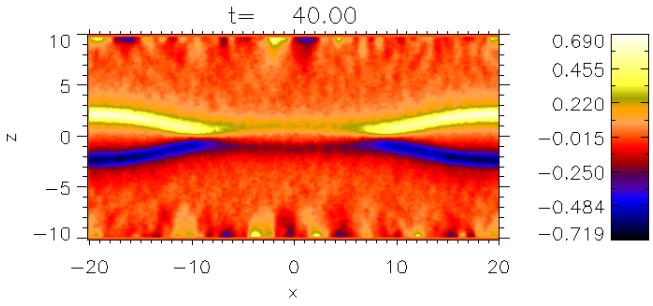

(c)

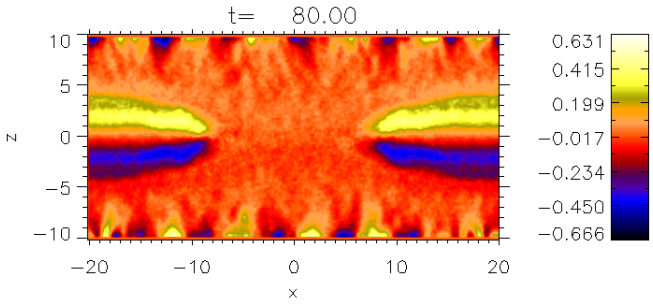

(d)

Figure 5.94: Plots of the x component of the current density for the force-free Harris sheet run with equal mass ratio. The plots correspond to the different times (a) $t = 0$, (b) $t = 20$, (c) $t = 40$ and (d) $t = 80$.

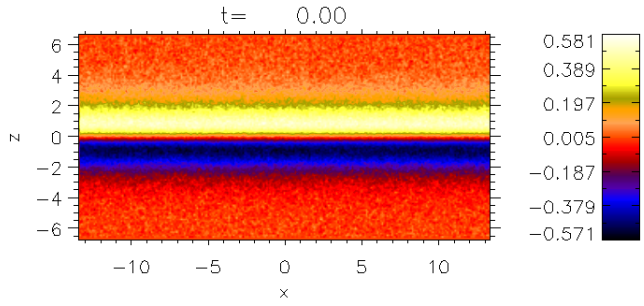

(a)

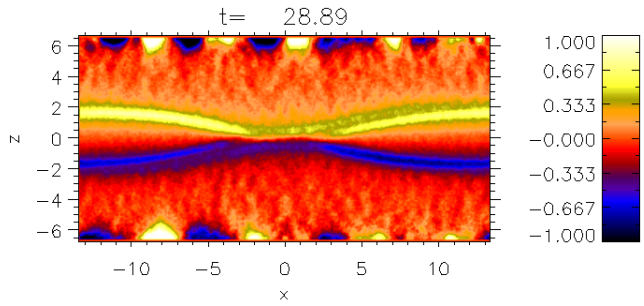

(b)

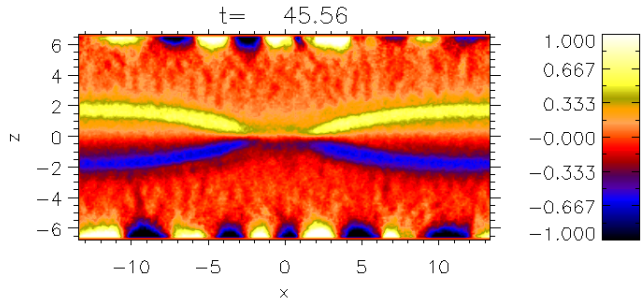

(c)

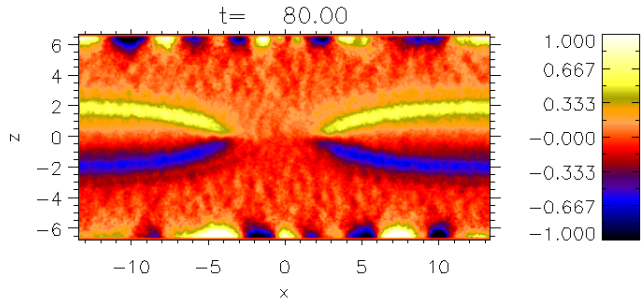

(d)

Figure 5.95: Plots of the x component of the current density for the force-free Harris sheet run with a mass ratio $m_i/m_e = 9$. The plots correspond to the different times (a) $t = 0$, (b) $t = 28.89$, (c) $t = 45.56$ and (d) $t = 80$.

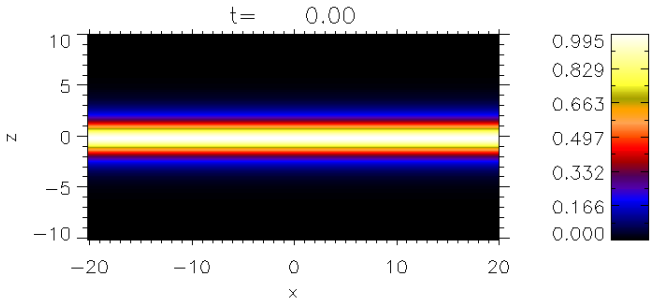

(a)

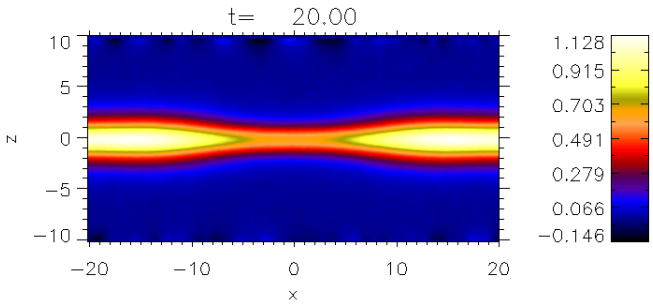

(b)

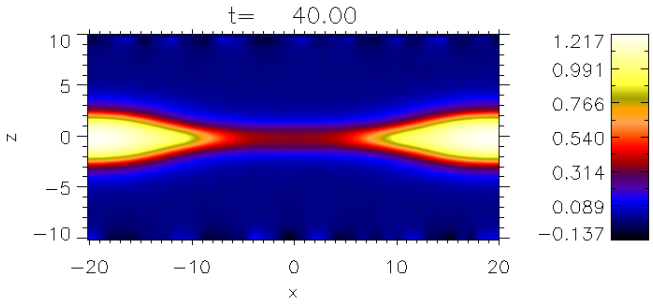

(c)

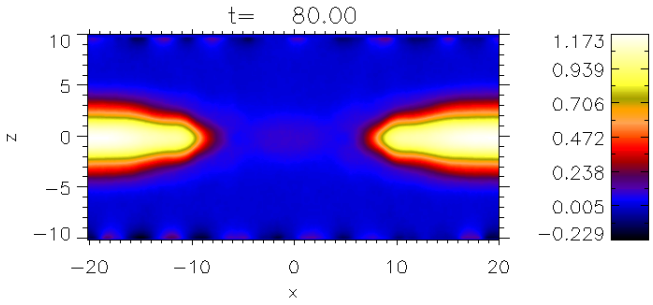

(d)

Figure 5.96: Plots of the y component of the magnetic field for the force-free Harris sheet run with equal mass ratio. The plots correspond to the different times (a) $t = 0$, (b) $t = 20$, (c) $t = 40$ and (d) $t = 80$.

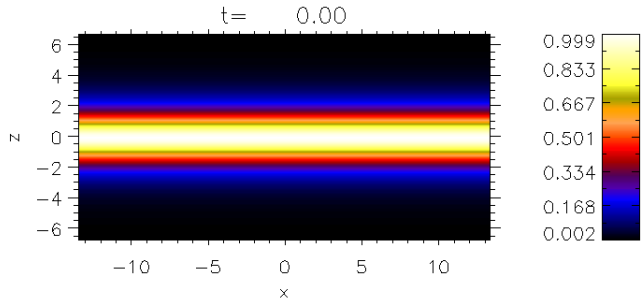

(a)

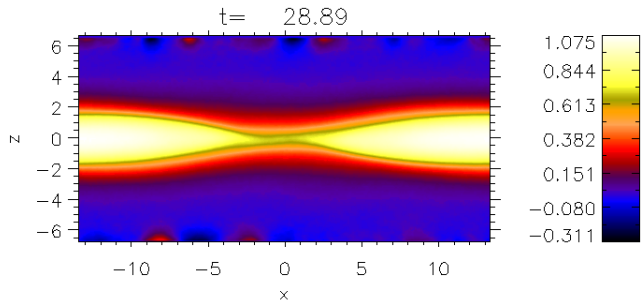

(b)

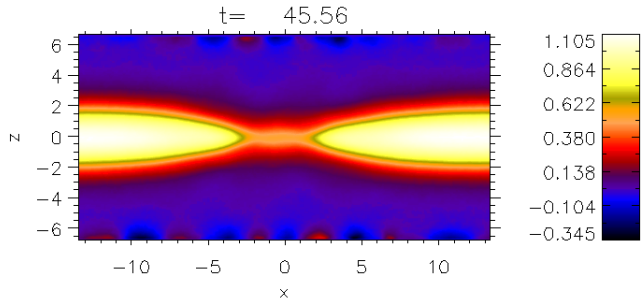

(c)

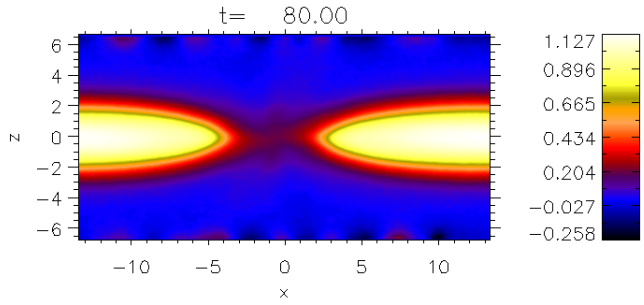

(d)

Figure 5.97: Plots of the y component of the magnetic field for the force-free Harris sheet run with a mass ratio $m_i/m_e = 9$. The plots correspond to the different times (a) $t = 0$, (b) $t = 28.89$, (c) $t = 45.56$ and (d) $t = 80$.

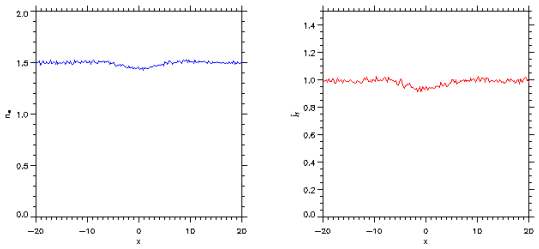

(a) (b)

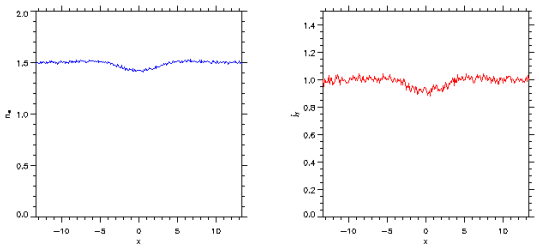

(c) (d)

Figure 5.98: Line plots of the electron number density n_e (blue lines) and the y component of the current density (red lines) plotted along x for $z = 0$ at $t = 0$ for the force-free Harris sheet runs with a mass ratio of (a),(b) $m_i/m_e = 1$ and (c),(d) $m_i/m_e = 9$.

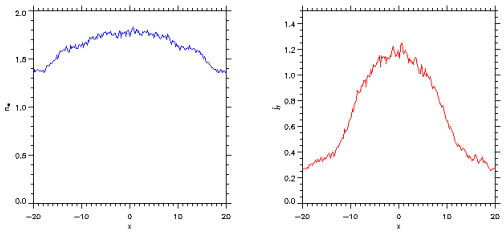

(a) (b)

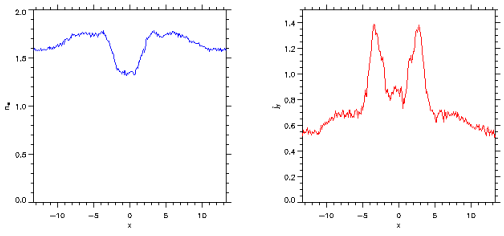

(c) (d)

Figure 5.99: Line plots of the electron number density n_e (blue lines) and the y component of the current density (red lines) plotted along x for $z = 0$ at the time of maximum reconnection rate for the force-free Harris sheet runs with a mass ratio of (a),(b) $m_i/m_e = 1$ ($t = 38$) and (c),(d) $m_i/m_e = 9$ ($t = 45.56$).

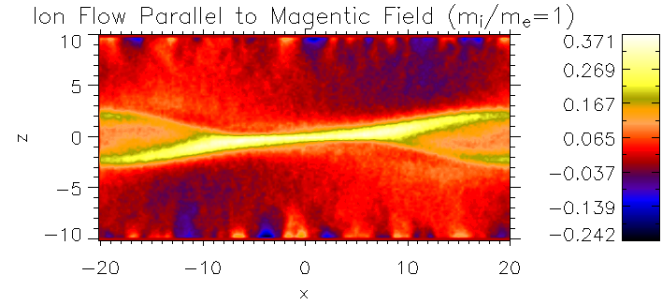

(a)

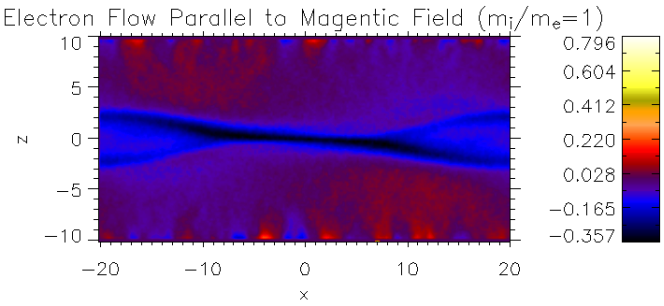

(b)

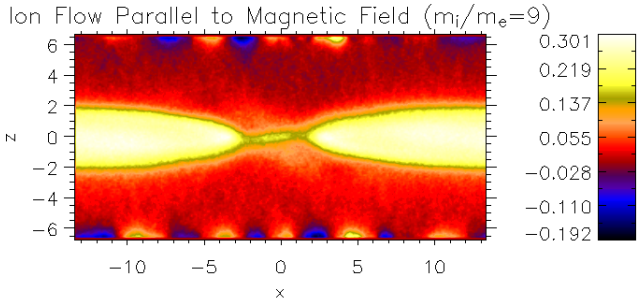

(c)

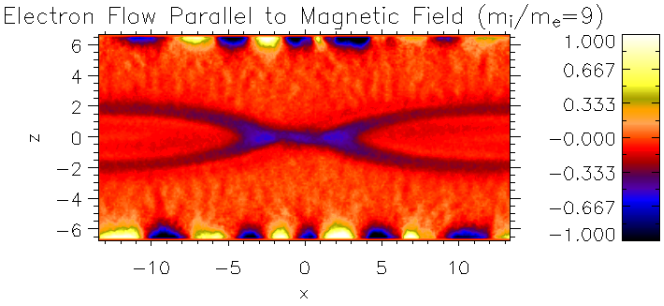

(d)

Figure 5.100: Filled contour plots of the ion and electron flows parallel to the magnetic field for (a),(b) the equal mass ratio case ($t = 38$) and (c),(d) the mass ratio $m_i/m_e = 9$ case ($t = 45.56$) at the time of maximum reconnection rate.

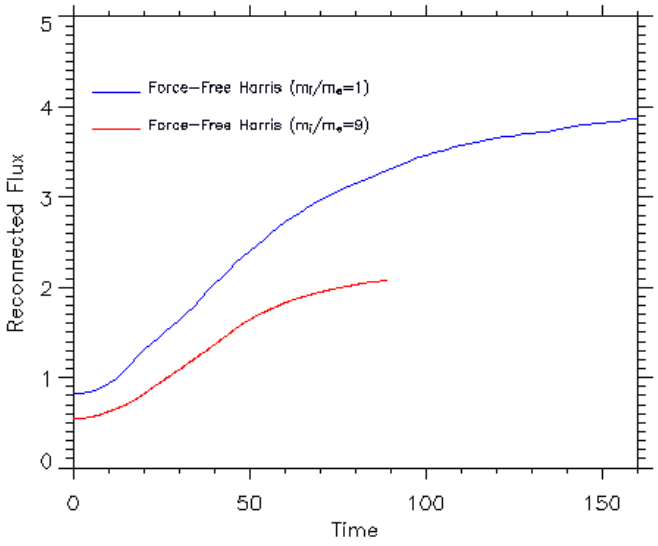

(a)

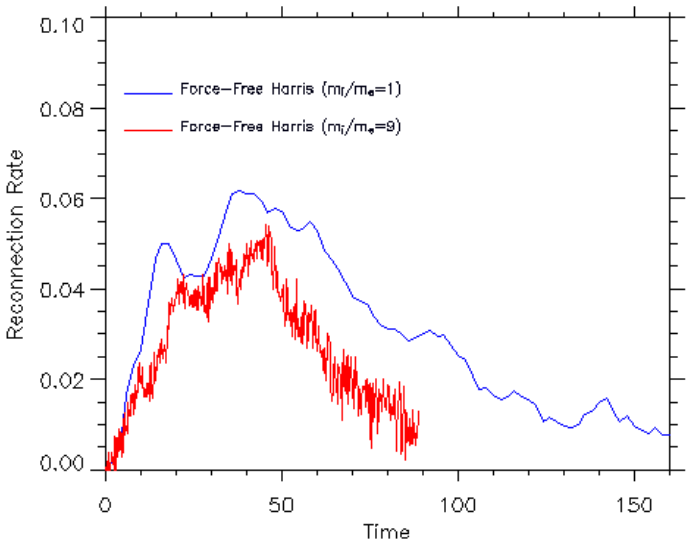

(b)

Figure 5.101: Figures comparing the evolution of the simulations using the force-free Harris sheet as an initial configuration with equal mass ratio and mass ratio $m_i/m_e = 9$. The reconnected flux is shown in Figure 5.101(a) and the corresponding reconnection rates in Figure 5.101(b).

the magnetic field at the edges of the magnetic islands which can be seen in Figure 5.96 and 5.97 for the two cases. This behaviour is similar to the linear force-free cases already discussed in Secs. 5.5 and 5.7. In Figures 5.94 - 5.97 there are some boundary effects which do not change the overall evolution of j_x and B_y but in the future need to be investigated to understand why they occur.

Figure 5.100 shows the ion and electron flows parallel to the magnetic field for the equal mass ratio and mass ratio $m_i/m_e = 9$ cases at the time of maximum reconnection rate. In the equal mass ratio case the ions have the strongest flows along the bottom left and upper right separatrices. The electron flows have the opposite symmetry with the strongest flows along the upper left and bottom right separatrices. The magnitude of the flows are equal in this case but the electrons flow are in the opposite direction along the magnetic field to the ions. The mass ratio $m_i/m_e = 9$ case shows that the strongest electron flows are still along the separatrices. The electron flows are also larger than the ion flows and flow in the opposite direction to the ions. The largest ion flows are in the magnetic islands. The central region is rotated clockwise with respect to the x axis for the electrons whereas for the ions the central region is rotated anti-clockwise.

A comparison of the evolution of the runs is given in figure 5.101. This shows two plots, one for the reconnected flux for each case plotted using different colours to represent the equal mass ratio and $m_i/m_e = 9$ runs where the reconnected flux is defined as

$$F(t) = \int_{B_z>0} dx\, B_z(z=0), \tag{5.45}$$

and the other shows the reconnection rate where the reconnection rate is found by taking the derivative of the reconnected flux and normalising it against the maximum Alfvén speed at each timestep. In the equal mass ratio case the peak of the reconnection rate has a value of ≈ 0.06 and in the mass ratio of $m_i/m_e = 9$ a rate of ≈ 0.055. Comparing the reconnection rates to the Harris sheet simulations in Sec. 5.4, the peak of the reconnection rate for the force-free Harris sheet cases have a value of a similar magnitude to an intermediate guide field case. Therefore it seems that the shear magnetic field B_y in the vicinity of the X-point which is still present, although reduced from its intial value at the time of maximum reconnection rate still has the effect of reducing the reconnection rate.

5.8.1 The Structure of the Diffusion Region

In this section the structure of the off-diagonal components of the electron pressure tensor components are shown for the force-free Harris sheet cases with equal mass ratio and mass ratio $m_i/m_e = 9$ at the time of maximum reconnection rate. It is also shown how the different contributions in Eq. (5.7) make up the reconnection electric field in the vicinity of the X-point.

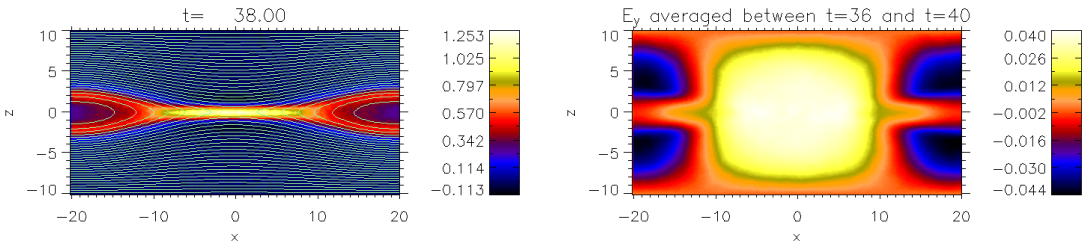

(a)

(b)

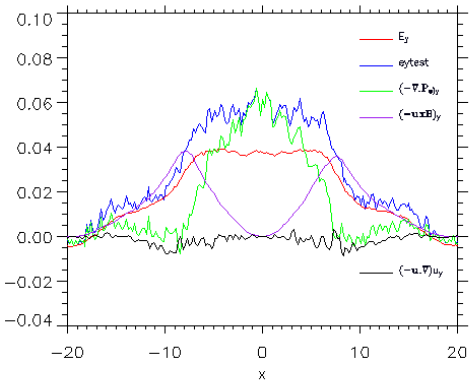

(c)

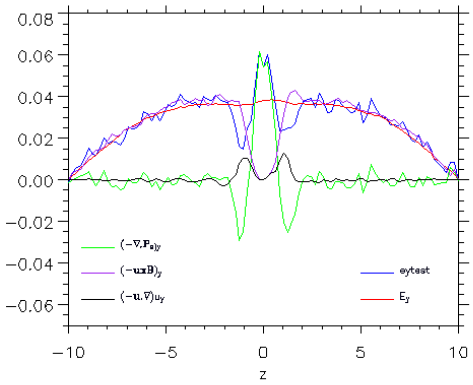

(d)

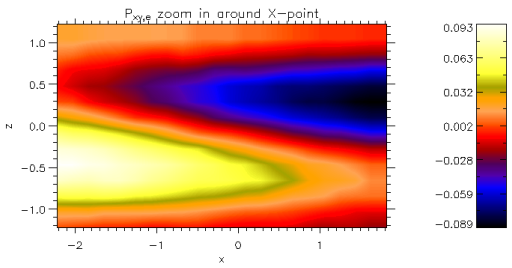

(e)

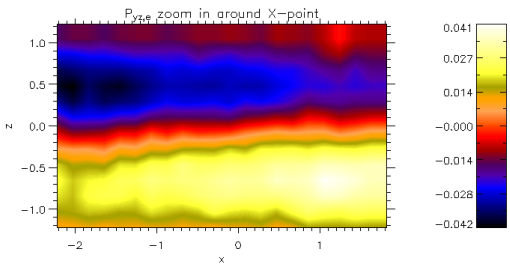

(f)

Figure 5.102: Plots of Force-Free Harris sheet with $m_e = m_i$, $L = 1.0$, $T_e = T_i$ at the time of maximum reconnection rate: (a) y component of the current density with the magnetic field, (b) E_y electric field, (c)(d) lineplots along x and z through the X-point of different contributions to E_y electric field, (e)(f) zoom-ins of $P_{xy,e}$ and $P_{yz,e}$ components of electron pressure tensor.

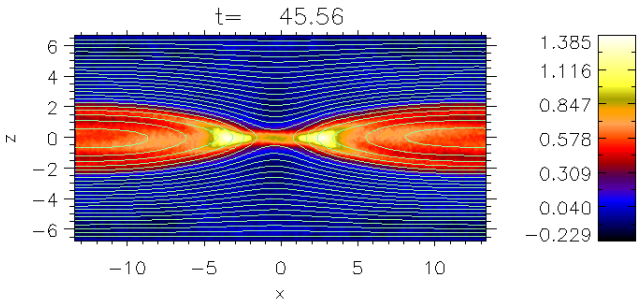

(a)

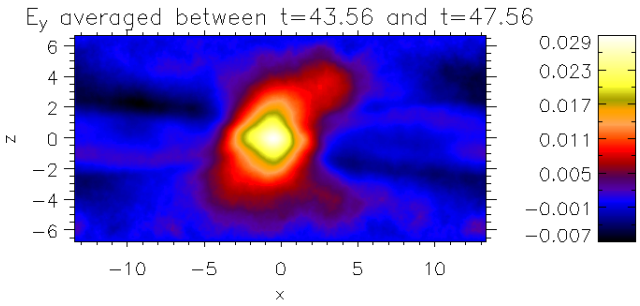

(b)

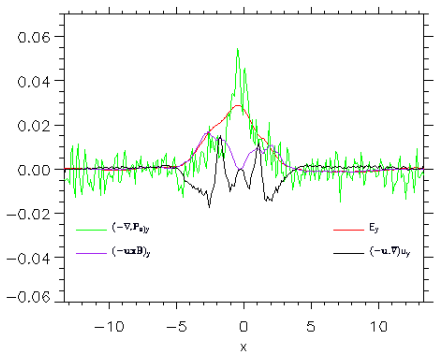

(c)

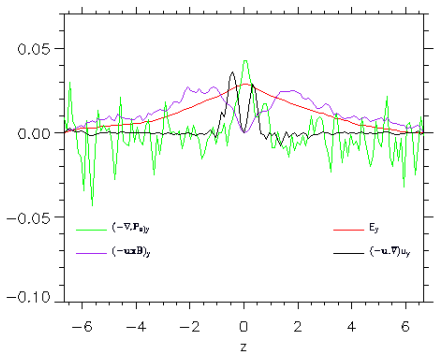

(d)

Figure 5.103: Plots of Force-Free Harris sheet with $m_i/m_e = 9$, $L = 1.0$, $T_e = T_i$ at the time of maximum reconnection rate: (a) y component of the current density with the magnetic field lines overplotted, (b) E_y electric field, (c)(d) lineplots along x and z through the X-point of different contributions to E_y electric field.

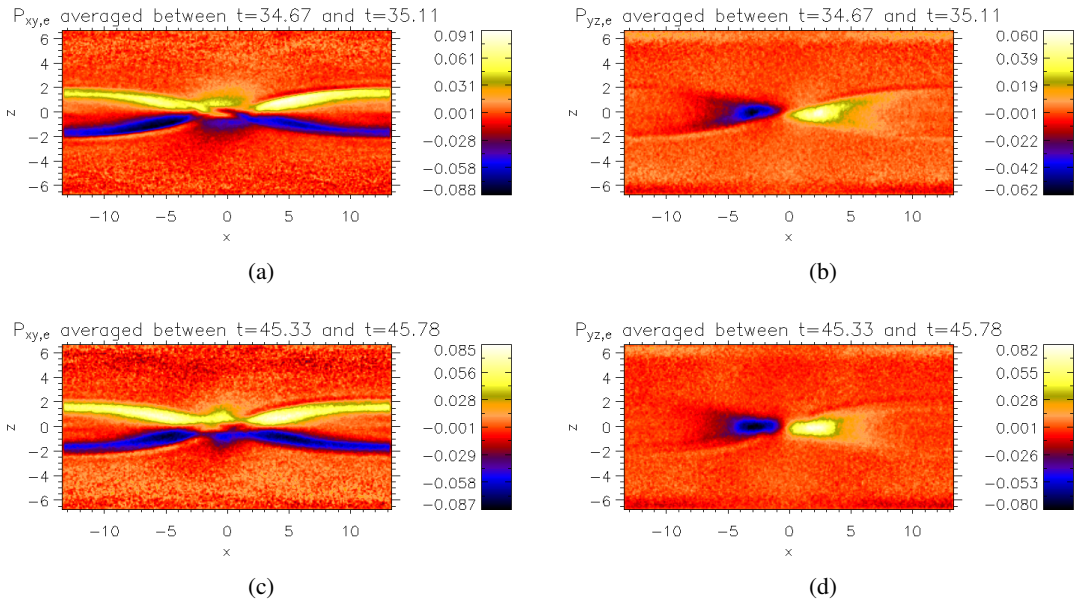

Figure 5.104: Plots showing the off diagonal components of the electron pressure tensor $P_{xy,e}$ and $P_{yz,e}$ for the $m_i/m_e = 9$ case during (a),(b) the early stages of reconnection and (c),(d) at the time of maximum reconnection rate.

Figure 5.102 shows a comparison for the force-free Harris sheet with equal mass ratio at the time of maximum reconnection rate. Figure 5.102(a) shows a filled contour plot of the y component of the current density at the time of maximum reconnection rate which corresponds to the peak of the graph for the equal mass ratio case shown in Figure 5.101(b). Figure 5.102(b) is a filled contour plot of the E_y electric field at the time of maximum reconnection rate. The electric field has been averaged for $2\Omega_i^{-1}$ either side of the time of maximum reconnection rate. This shows how magnetic reconnection generates a strong E_y electric field in the vicinity of the X-point. In the figures the X-point is located approximately at $x = -0.20$ and $z = 0$. Figure 5.102(c) and 5.102(d) show line plots along x and z respectively through the X-point of the E_y electric field and the contributions that make up the reconnection electric field in Eq. (5.7). It is clear that the dominant contribution to the E_y electric field in the vicinity of the X-point is due to the off-diagonal components of the electron pressure tensor (green lines).

A similar analysis is shown in Figure 5.103 for the $m_i/m_e = 9$ case. Figure 5.103(a) shows a filled contour plot of the y component of the current density at the time of maximum reconnection rate which corresponds to the peak of the graph for the mass ratio $m_i/m_e = 9$ case shown in Figure 5.101(b). Figure 5.103(b) is a filled contour plot of the E_y electric field at the time of maximum reconnection rate. The electric field has been averaged for $2\Omega_i^{-1}$ either side of the time of maximum reconnection rate. This shows how magnetic reconnection generates a strong E_y electric field in the vicinity of the X-point. In the figures the X-point is located approximately at $x = -0.4$ and $z = 0$. Figure 5.103(c) and 5.103(d) show line plots along x and z respectively

through the X-point of the E_y electric field and the contributions that make up the reconnection electric field in Eq. (5.7). The dominant contribution to the E_y electric field very close to the X-point is due to the off-diagonal components of the electron pressure tensor (green lines). It is noticable outside the diffusion region that there are large changes in the gradients of the electron pressure tensor components. This suggests that the pressure tensor components may still be strongly time dependent and is a question for future investigations.

Although the dominant term in the vicinity of the X-point is due to the gradients of the off-diagonal terms of the electron pressure tensor, Figure 5.102(d) and Figure 5.103(d) show there is in both the equal mass ratio and $m_i/m_e = 9$ cases a contribution to the electric field from the electron inertia term at the edge of the diffusion regime along z. In the equal mass ratio case this is relatively small compared to the peak of the gradients of the electron pressure terms at the X-point and is of equal magnitude to the $\mathbf{u} \times \mathbf{B}$ term at the edge of the diffusion region. In the mass ratio $m_i/m_e = 9$ case the contribution from the electron inertia at the edge of the diffusion region is significantly large relative to the peak of the gradients of the electron pressure terms at the X-point and is greater than the magnitude of the $\mathbf{u} \times \mathbf{B}$ term at the edge of the diffusion region. In the future it would be necessary to carry out a more detailed investigation of the role of the electron inertia in this case. It has been shown though in a recent paper by Hesse et al. (2004) for a simulation starting from a Harris sheet with a guide field of $B_{y0} = 0.8$, that within a collisionless skin depth there was a finite contribution from the electron inertia at the edge of the localised current region. The main contribution to the E_y electric field close to the X-point was still due to the nongyrotropic pressures. The results shown here for the force-free Harris sheet also show this feature.

Figures 5.102(e) and 5.102(f) show zoom-ins of the off-diagonal components of the electron pressure tensor around the X-point showing their structure for the equal mass ratio case at the time of maximum reconnection rate. The structure of the $P_{xy,e}$ component of the pressure tensor, in comparison to the Harris sheet cases looks similar to an intermediate guide field case which is consistent with the fact that the y component of the magnetic field has a value of approximately $B_y \approx 0.35$ in the vicinity of the X-point. The $P_{yz,e}$ component of the electron pressure tensor has a strong gradient along z.

Figure 5.104 show the off-diagonal components of the electron pressure tensor for the $m_i/m_e = 9$ case in the early phase of reconnection and also at the time of maximum reconnection rate. It is clear to see that at the earlier time the structures of $P_{xy,e}$ and $P_{yz,e}$ are similar to an intermediate guide field case when compared to simulations starting from the Harris sheet. This result is consistent with the y component of the magnetic field having a value of $B_y = 0.66$ at the X-point. At the time of maximum reconnection rate it would be expected, considering that the value of the y component of the magnetic field has reduced to $B_y = 0.51$ at the X-point that the structure of $P_{xy,e}$ and $P_{yz,e}$ would start to exhibit a transition to a structure similar to a simulation starting from a Harris sheet with a weak guide field. Examination of Figure 5.104(c) does not show a clear

structure for $P_{xy,e}$ and Figure 5.104(d) shows that the structure of $P_{yz,e}$ close to the X-point has symmetry along $x = 0$ which is not seen in the Harris sheet cases. It has been shown in Sec. 5.4 that in a weak guide field case the $P_{yz,e}$ component of the pressure tensor is approximately symmetrical about $z = 0$. Clearly further, more detailed studies would be needed in the future to fully understand the evolution of the structure of $P_{xy,e}$ and $P_{yz,e}$ for this case.

In the case with zero guide field the characteristic length scale of $P_{xy,e}$ and $P_{yz,e}$ is given approximately by the electron bounce widths in a field reversal λ_x and λ_z (e.g. Hesse et al. 1999). In the strong guide field case the characteristic length scale changes to that of the thermal electron Larmor radius $r_L = v_{th,e}/\Omega_e$ in the guide magnetic field (Hesse et al. 2004). The thermal electron Larmor radius for the force-free Harris sheet case with equal mass ratio at the time of maximum reconnection rate based on the maximum value of the shear component of the magnetic field at the X-point ($B_y \approx 0.35$) is of the order $r_L \approx 1.4c/\omega_{pi}$. The central region in Figures 5.102(e) and 5.102(f) are thinner than this estimate of the electron Larmor radius. This suggests that the characteristic length scale of $P_{xy,e}$ and $P_{yz,e}$ may be even smaller than the thermal electron Larmor radius in the shear magnetic field B_y which is consistent with the linear force-free simulation runs. In the mass ratio $m_i/m_e = 9$ case it would be necessary in the future to carry out a more detailed study of the evolution of the structure of the off-diagonal components of the electron pressure tensor before the characteristic length scales can be accurately determined.

5.9 Summary

In this chapter examples of the equilibria that are discussed in Chap. 3 were used as initial conditions in particle in cell (PIC) simulations of magnetic reconnection. It is been shown by several authors (e.g. Hesse et al. 1999, 2004; Pritchett 2001) that the dominant contribution to the reconnection electric field component E_y for a collisionless plasma is due to the off-diagonal components of the electron pressure tensor where the initial condition consisted of a Harris sheet with varying strengths of guide field. In the weak guide field case the characteristic scale length for the off diagonal components of the electron pressure tensor in the vicinity of the X-point is the electron bounce width. In the strong guide field cases the charactersitic length scale is the thermal electron Larmor radius in the guide field.

Comparisons of the structure of the diffusion region starting from initial configurations which were not the Harris sheet have been shown and compared to simulations starting from a Harris sheet with different strengths of guide field. Initially these investigations were carried out for equal mass ratio. Section 5.5 used the anti-parallel periodic anisotropic bi-Maxwellian equilibria with varying strengths of guide field as initial conditions and compared this to a simulation starting from a self-consistent linear force-free equilibrium that were discussed in Sec. 3.3.3 and Sec. 3.4 of Chap.

3. The evolution of these equilibria showed that the use of doubly periodic boundary conditions has a significant effect. As a result of the multiple current layers the O-points above and below the central X-point push in on the central X-point eventually causing a complete re-organisation of magnetic field geometry from that of a (B_x, B_y) configuration to a mainly (B_y, B_z) magnetic field configuration. It was found that the reconnection rates were reduced as the guide field was increased. In the linear force-free case the effect of the shear magnetic field B_y was also to reduce the reconnection rate with the maximum reconnection rate similar to that of the $B_{y0} = 0.3$ guide field case.

Due to the interaction of the multiple current layers as a consequence of the doubly periodic boundary conditions, this led to a breakdown of the structure of the off-diagonal electron pressure tensor components at the time of maximum reconnection rate. This is a major difference to the Harris sheet cases. Therefore the off-diagonal components of the electron pressure tensor were investigated at an earlier time than the time of maximum reconnection rate. Examination of the structure of the diffusion region led to the conclusion that the dominant contribution to the reconnection electric field in the vicinity of the X-point is due to the gradients of the off-diagonal components of the electron pressure tensor. As in the Harris sheet cases the characteristic length scale was the electron bounce width in the weak guide field cases and the thermal electron Larmor radius in the strong guide field cases. In the force-free case it was suggested that the characteristic length scales of $P_{xy,e}$ and $P_{yz,e}$ may be even smaller than the thermal electron Larmor radius based on the value of the shear magnetic field B_y at the X point.

Reconnection simulations starting from a double Harris sheet with equal mass ratio have also been shown with varying strengths of guide field added. The evolution was similar to the anisotropic bi-Maxwellian cases. The effect of the doubly periodic boundary conditions was that at the end of the reconnection process the geometry of the magnetic field had been completely re-organised from a (B_x, B_y) structure to a mainly (B_y, B_z) structure. Once again it was shown that one of the effects of the guide field was to reduce the reconnection rate. As in the anisotropic bi-Maxwellian cases the interaction of the multiple current layers led to the breakdown of the structure of the off-diagonal components of the electron pressure tensor and therefore they were investigated at an earlier time than the time of maximum reconnection rate. Examination of the structure of the diffusion region during reconnection confirmed that the dominant contribution to the reconnection electric field was due to the gradients of the off-diagonal components of the electron pressure tensor. The characteristic length scales of $P_{xy,e}$ and $P_{yz,e}$ was the electron bounce width in the weak guide field cases and the thermal electron Larmor radius in the strong guide field cases.

In both the anisotropic bi-Maxwellian simulations and the double Harris sheet simulations it was shown that in the strong guide field cases there was a significant contribution to the reconnection electric field along z at the edge of the diffusion region from the electron inertia term. In the linear force-free case there was also a significant contribution from the electron inertia term at the edge

of the diffusion region.

The study using the anisotropic bi-Maxwellian equilibria as initial conditions was extended to investigate a mass ratio $m_i/m_e = 25$. The effect of introducing the unequal mass ratio was to introduce the characteristic change in length and time scales between the electrons and ions. Four different simulation runs were carried out. The first three runs were for an anti-parallel equilibrium with constant guide fields $B_{y0} = 0.0, 0.5, 1.0$ and these were compared to a simulation starting from a linear force-free equilibrium. It was found that the anti-parallel case with zero guide field was stable to the tearing mode. This may have been due to the small amount of free energy due to the relatively large width of the current layer and small size of the simulation box. The cases with guide field $B_{y0} = 0.5$, $B_{y0} = 1.0$ and linear force-free case were unstable to the tearing mode. It seems that the guide field plays some role in the stability properties in equilibria of this type. A complete linear stability anlysis of these anisotropic bi-Maxwellian equilibria has not yet been carried out but it may be interesting to do in the future so that the role of the guide field on stability can be fully understood.

In the guide field case $B_{y0} = 1.0$ and the force-free case the characteristic inclination of the current sheet is shown. The current density is dominated by the electrons, with the electron current density region in the vicinity of the X-point in the z direction being much thinner than that of the ion current density. The electrons are demagnetized for a much smaller region than the ions which is a charactersitic feature of collisionless magnetic reconnection with an unequal mass ratio. In the strong guide field case and force-free case the electrons have strong flows along the separatrices. Finally in all cases there is the formation of the typical quadrupolar y component of the magnetic field, although in the strong guide field case overlaid on top of the guide magnetic field. The quadrupolar B_y magnetic field for the linear force-free case is distorted from the symmmetry that would be expected in the case with zero guide field. Comparisons of the evolution of the different runs shows that the linear force-free case and guide field case $B_{y0} = 1.0$ have maximum reconnection rates of similar value which is slower than the $B_{y0} = 0.5$ case. This illustrates that the effects of increasing the guide field and of the shear magnetic field B_y in the force-free case is to reduce the reconnection rate. The effect of the doubly periodic boundary conditions once again led to the complete re-organisation of the magnetic field geometry from the initial (B_x, B_y) structure to a mainly (B_y, B_z) structure at the end of the reconnection process.

Due to the interaction of the multiple current layers leading to the breakdown of the structure of the off-diagonal components of the electron pressure tensor components at the time of maximum reconnection rate they were investigated at an earlier time in the reconnection process. It was shown that the dominant contribution to the electric field was again due to the gradients of the off-diagonal components of the electron pressure tensor components close to the X-point. The typical rotation of the structure of the $P_{xy,e}$ component of the pressure tensor from symmetry about the line $x = x_0$ for the zero guide field case where x_0 refers to the position of the X-

point to symmetry about the line $z = 0$ through the X-point in the strong guide field case and force-free case is evident. The structure of the $P_{yz,e}$ component of the pressure tensor for the strong guide field case was different to the Harris sheet cases as it was still fairly inclined to the $z = 0$ line whereas in the Harris sheet case the $P_{yz,e}$ component of the pressure tensor was almost symmetrical about the $z = 0$ line. The $P_{yz,e}$ component of the pressure tensor for the linear force-free case was almost symmetrical along $z = 0$. The characteristic length scales of $P_{xy,e}$ and $P_{yz,e}$ for the $B_{y0} = 1.0$ case was of the order of the thermal electron Larmor radius in the guide field. In the force-free case it was suggested that the characteristic length scales of $P_{xy,e}$ and $P_{yz,e}$ may be even smaller than the thermal electron Larmor radius based on the value of the shear magnetic field B_y at the X point.

Finally a comparison of two different runs for the force-free Harris sheet were compared. A run with equal mass ratio and mass ratio $m_i/m_e = 9$ was carried out. It was shown in both cases that in the initial stages of the evolution the current density is enhanced at the X-point. In the equal mass ratio the particle density is also enhanced at the X-point. In the late stages of the evolution the y component of the magnetic field is reduced almost to zero at the X-point corresponding to a change from guide field reconnection to anti-parallel reconnection. The x component of the current density in each case is enhanced in wing-like structures that enclose the magnetic islands and correspond to gradients of the y component of the magnetic field. In both cases it was shown that at the time of maximum reconnection rate the gradients of the off-diagonal components of the electron pressure tensors were the dominant terms that give rise to the reconnection electric field. In both cases there was also a contribution from the electron inertia at the edge of the diffusion region along z, which was most significant in the $m_i/m_e = 9$ case. The structure of the off-diagonal components of the electron pressure tensor were investigated. In the equal mass ratio case it was shown that the structure of the pressure tensor components were similar to an intermediate guide field case. It was suggested that the characteristic scale length of the pressure tensor components may be even smaller than the electron Larmor radius in the shear magnetic field. In the $m_i/m_e = 9$ case in the early stages of reconnection the pressure tensor components were again equivalent to an intermediate guide field case. At the time of maximum reconnection rate the structure of the pressure tensor components did not show the expected form and in the future a more detailed investigation of the pressure tensor components is necessary.

Chapter 6

Summary and Further Work

6.1 Summary

In this thesis a general discussion of some well known 1D MHD equilibria is given in Chap. 2. These included the Harris sheet (Harris 1962), force-free Harris sheet and the combined cases. The Harris sheet equilibrium is well known in both MHD and Vlasov theory with a one-to-one correspondence. The aim of the thesis was to find analogous equilibria in the framework of Vlasov-Maxwell theory for the combined case and force-free Harris sheet case. Therefore it was necessary to understand the properties of these equilibria in MHD which must also be present in Vlasov-Maxwell theory. Also shown was a discussion of 1D multi-fluid theory. This showed that under certain assumptions that the overall equilibria are identical to the Harris sheet, force-free Harris sheet and combined cases. A two-fluid example was considered. In this case it was possible to determine some of the bulk properties of each individual fluid. It was shown that an important property of the Harris sheet is that the average drift velocity is constant and only in the y direction and that the number density is spatially varying whereas in the force-free case the number density is constant and there is an average drift velocity in both the x and y directions which are spatially varying. These two properties are important when investigating the possibility of force-free Vlasov-Maxwell equilibria.

A general theory of 1D Vlasov-Maxwell equilibria has been given where the distribution functions depend on the three constants of motion which correspond to the particle energy (the Hamiltonian) and the two canonical momenta. The important results of this general theory is that it can be shown that the charge density and current densities can all be determined from a general potential P where P is in fact the P_{zz} component of the pressure tensor. In the quasineutral case P is a function of A_x and A_y alone and is denoted by P_{qn}. Furthermore Ampère's law, in terms of the potential P_{qn} reduces to Hamilton's equations for a particle with coordinates (A_x, A_y) moving

in a conservative 2D potential $\mu_0 P_{qn}$. The potential P_{qn} is epecially useful in cases where an analytical solution to the magnetic field configuration cannot be easily found as gradients of the potential surface correspond to gradients of the magnetic field components so that large gradients of the potential surface indicates large current densities in the solution. Several examples of how this particle analogy can be used to determine the nature of the solution has been given in Sec. 3.3 in Chap. 3.

In terms of the aims of this thesis, perhaps the most important application of this theory was to determine general conditions for force-free Vlasov-Maxwell equilibria. It has been shown that to obtain a pseudo-particle trajectory corresponding to a force-free magnetic field, a pseudo-potential (P_{zz}) which has at least one equipotential line (contour) that is also a particle trajectory is needed. This is a necessary condition for the existence of a 1D force-free VM equilibrium.

A well-known family of pseudo-potentials that satisfies the condition of allowing trajectories which are identical to contours of the pseudo-potential are attractive central potentials. These have to be restricted to nonsingular pseudo-potentials because the equivalent pressure must be positive and nonsingular. This rules out, for example, all potentials which are negative powers of the radial coordinate. For central pseudo-potentials there is not only pseudo-energy conservation, but also pseudo-angular momentum conservation. Examples of distribution functions resulting in a central attractive potential has already been given by Sestero (1967); Bobrova and Syrovatskiĭ (1979); Correa-Restrepo and Pfirsch (1993); Bobrova et al. (2001) and are discussed in Sec. 3.3.3 and Sec. 3.6 in Chap. 3. The distribution function given by (Bobrova et al. 2001) was extended to incude an additional dimensionless parameter b_s in front of the x component of the canonical momenta. This distribution function allowed a family of periodic solutions to be constructed which show a transition from an anti-parallel ($b_s = 0$) magnetic field configuration through to a linear force-free field configuration ($b_s = 1$). As the transition is made the dominant contribution to the force balance comes from the gradient of the shear field rather than the plasma pressure gradient, where in the force-free case the plasma pressure across the sheet is constant. The shearing and twisting of the field increases as B_y increases relative to B_x. In terms of the particle trajectories the solutions are in general oscillatory, with the trajectories approaching closer to that of a circle for the force-free solution.

A distribution function which has the force-free Harris sheet as a solution has been shown (Harrison and Neukirch 2009a). This is the first ever non-linear self-consistent force-free 1D Vlasov Maxwell solution known. The distribution function was found by first finding the quasi-neutral pressure function that corresponds to the force-free Harris sheet magnetic field configuration. This pressure function was then used to write down an integral equation for the $g_s(p_{xs}, p_{ys})$ function which was solved via a Fourier transform method, where it was assumed that there must be a choice of parameters for which the quasineutral electric potential ϕ_{qn} can be set to zero. The resulting $g_s(p_{xs}, p_{ys})$ function was found to be a sum of two contributions. The first contibution

has a cosine dependence on p_{xs} and the second contribution an exponential dependence on p_{ys} which is equivalent to the Harris sheet case. To check the validity of the distribution function it was used as the starting point from which the moment equations were calculated. It was shown that there is a choice of parameters which set the quasineutral electric potential ϕ_{qn} to zero. The differential equations resulting from Ampère's law were then solved to give the force-free Harris sheet magnetic field solution. This distribution function was also extended to show that for the correct choice of parameters a family of equilibria can be constructed that describe the transition from the Harris sheet through to the force-free Harris sheet.

This new family of VM equilibria will generate new possibilities for studies of linear and nonlinear instabilities of force-free current sheets. The stability of the VM equilibria presented here have yet to be investigated. It must be pointed out that the p_{xs}-dependent part of the distribution function (3.203) may have multiple peaks in the v_x-direction and this may give rise to instabilities. It is also remarked that although the $B_x(z)$ and $j_y(z)$-profiles are identical to the Harris sheet, $j_x(z)$ is anti-symmetric with respect to $z = 0$. This is closely linked to the fact that in the Harris sheet solution the spatial structure of the current density is determined by the density structure with the average velocity of each particle species being constant, whereas in the force-free solution presented here the particle density is constant and the spatial structure of the current density is determined by the spatial structure of the average velocity. Further investigations will be needed to clarify exactly what the implications are for the stability of the new solution, but on the basis of the physical differences just mentioned one would expect the stability properties of the force-free solution to differ considerably from those of the Harris sheet. Apart from studying the stability properties of the solution class presented here, it will be also be very interesting to investigate whether the general method employed here can be used to find other non-linear force-free solutions and is an aim for future work.

In Chap. 5 examples of the equilibria that are discussed in Chap. 3 were used as initial conditions in particle in cell (PIC) simulations of magnetic reconnection. It is been shown by several authors (e.g. Hesse et al. 1999, 2004; Pritchett 2001) that the dominant contribution to the reconnection electric field component E_y for a collisionless plasma is due to the off-diagonal components of the electron pressure tensor where the initial condition consisted of a Harris sheet with varying strengths of guide field. In the weak guide field case the characteristic scale length for the off diagonal components of the electron pressure tensor in the vicinity of the X-point is the electron bounce width. In the strong guide field cases the charactersitic length scale is the thermal electron Larmor radius in the guide field.

Chapter 5 shows comparisons of the structure of the diffusion region starting from initial configurations which were not the Harris sheet. Initially these investigations were carried out for equal mass ratio. This is the first time a systematic comparison of the reconnection process and the structure of the diffusion region has been carried out which compares results from simulations starting

from an anti-parallel configuration with a guide field to a simulation starting from a self-consistent linear force-free equilibrium. Section 5.5 of Chap. 5 used the anti-parallel periodic anisotropic bi-Maxwellian equilibria with varying strengths of guide field as initial conditions and compared this to a simulation starting from a self-consistent linear force-free equilibrium that were discussed in Sec. 3.4 and 3.3.3 of Chap. 3. The evolution of these equilibria showed that the use of doubly periodic boundary conditions has a significant effect. As a result of the multiple current layers the O-points above and below the central X-point push in on the central X-point eventually causing a complete re-organisation of magnetic field geometry from that of a (B_x, B_y) configuration to a (B_y, B_z) magnetic field configuration. It was found that the reconnection rates were reduced as the guide field was increased. In the linear force-free case the effect of the shear magnetic field B_y was also to reduce the reconnection rate with the maximum reconnection rate similar to that of the $B_{y0} = 0.3$ guide field case.

Due to the interaction of the multiple current layers as a consequence of the doubly periodic boundary conditions, this led to a breakdown of the structure of the off-diagonal electron pressure tensor components at the time of maximum reconnection rate. Therefore the off-diagonal components of the electron pressure tensor were investigated at an earlier time than the time of maximum reconnection rate. Examination of the structure of the diffusion region led to the conclusion that the dominant contribution to the reconnection electric field in the vicinity of the X-point is due to the gradients of the off-diagonal components of the electron pressure tensor. As in the Harris sheet cases the characteristic length scale was the electron bounce width in the weak guide field cases and the thermal electron Larmor radius in the strong guide field cases. In the force-free case it was suggested that the characteristic length scales of $P_{xy,e}$ and $P_{yz,e}$ may be even smaller than the thermal electron Larmor radius based on the value of the shear magnetic field B_y at the X point.

Reconnection simulations starting from a double Harris sheet were also shown with varying strengths of guide field added. The evolution was similar to the anisotropic bi-Maxwellian cases. The effect of the doubly periodic boundary conditions was that at the end of the reconnection process the geometry of the magnetic field had been completely re-organised from a (B_x, B_y) structure to a mainly (B_y, B_z) structure. Once again it was shown that one of the effects of the guide field was to reduce the reconnection rate. As in the anisotropic Bi-Maxwellian cases the interaction of the multiple current layers led to the breakdown of the structure of the off-diagonal components of the electron pressure tensor and therefore they were investigated at an earlier time than the time of maximum reconnection rate. Examination of the structure of the diffusion region during reconnection confirmed that the dominant contribution to the reconnection electric field was due to the gradients of the off-diagonal components of the electron pressure tensor. The characteristic length scales of $P_{xy,e}$ and $P_{yz,e}$ was the electron bounce width in the weak guide field cases and the thermal electron Larmor radius in the strong guide field cases.

In both the anisotropic bi-Maxwellian simulations and the double Harris sheet simulations it was

shown that in the strong guide field cases there was a significant contribution to the reconnection electric field along z at the edge of the diffusion region from the electron inertia term. In the linear force-free case there was also a significant contribution from the electron inertia term at the edge of the diffusion region.

The study using the anisotropic bi-Maxwellian equilibria as initial conditions was extended to investigate the case of using a mass ratio $m_i/m_e = 25$. The effect of introducing the unequal mass ratio was to introduce the characteristic change in length and time scales between the electrons and ions. Four different simulation runs were carried out. The first three runs were for an anti-parallel equilibrium with constant guide fields $B_{y0} = 0.0, 0.5, 1.0$ and these were compared to a simulation starting from a self-consistent linear force-free equilibrium. It was found that the anti-parallel case with zero guide field was stable to the tearing mode. This may have been due to the small amount of free energy due to the relatively large width of the current layer and small size of the simulation box. The cases with guide field $B_{y0} = 0.5$, $B_{y0} = 1.0$ and linear force-free case were unstable to the tearing mode. It seems that the guide field plays some role in the stability properties in equilibria of this type. A complete linear stability anlysis of these anisotropic bi-Maxwellian equilibria has not yet been carried out but it may be interesting to do in the future so that the role of the guide field on the stability can be fully understood.

In the guide field case $B_{y0} = 1.0$ and the force-free case the characteristic inclination of the current sheet is shown. The current density is dominated by the electrons, with the electron current density region in the vicinity of the X-point in the z direction being much thinner than that of the ion current density. The electrons are demagnetized for a much smaller region than the ions which is a charactersitic feature of collisionless magnetic reconnection with an unequal mass ratio. In the strong guide field case and force-free case the electrons have strong flows along the separatrices. Finally in all cases there is the formation of the typical quadrupolar B_y magnetic field configuration, although in the in the strong guide field case overlaid on top of the guide magnetic field. The quadrupolar B_y magnetic field for the linear force-free case is also distorted from the symmmetry that would be expected in the case with zero guide field. Comparisons of the evolution of the different runs shows that the linear force-free case and guide field case $B_{y0} = 1.0$ have maximum reconnection rates of similar value which is slower than the $B_{y0} = 0.5$ case. This illustrates that the effects of increasing the guide field and of the shear magnetic field B_y in the force-free case is to reduce the reconnection rate. The effect of the doubly periodic boundary conditions once again led to the complete re-organisation of the magnetic field geometry from the initial (B_x, B_y) structure to a mainly (B_y, B_z) structure at the end of the reconnection process.

Due to the interaction of the multiple current layers leading to the breakdown of the off-diagonal components of the electron pressure tensor components at the time of maximum reconnection rate they were investigated at an earlier time in the reconnection process. It was shown that the dominant contribution to the electric field was again due to the gradients of the off-diagonal

components of the electron pressure tensor components close to the X-point. The typical rotation of the structure of the $P_{xy,e}$ component of the pressure tensor from symmetry about the line $x = x_0$ for the zero guide field case where x_0 refers to the position of the X-point to symmetry about the line $z = 0$ through the X-point in the strong guide field case and force-free case is evident. The structure of the $P_{yz,e}$ component of the pressure tensor for the strong guide field case was different to the Harris sheet cases as it was still fairly inclined to the $z = 0$ line whereas in the Harris sheet case the $P_{yz,e}$ component of the pressure tensor was almost symmetrical about the $z = 0$ line. The $P_{yz,e}$ component of the pressure tensor for the linear force-free case was almost symmetrical along $z = 0$. The characteristic length scales of $P_{xy,e}$ and $P_{yz,e}$ for the $B_{y0} = 1.0$ case was of the order of the thermal electron Larmor radius in the guide field. In the force-free case it was suggested that the characteristic length scales of $P_{xy,e}$ and $P_{yz,e}$ may be even smaller than the thermal electron Larmor radius based on the value of the shear magnetic field B_y at the X point.

Finally a comparison of two different runs for the force-free Harris sheet were compared. This is the first ever study of collisionless reconnection to use an exact self-consistent non-linear force-free equilibrium as an initial condition. A run with equal mass ratio and mass ratio $m_i/m_e = 9$ was carried out. It was shown in both cases that in the initial stages of the evolution the current density is enhanced at the X-point. In the equal mass ratio the particle density is also enhanced at the X-point. In the late stages of the evolution the y component of the magnetic field is reduced almost to zero at the X-point corresponding to a change from guide field reconnection to anti-parallel reconnection. The x component of the current density in each case is enhanced in wing-like structures that enclose the magnetic islands and correspond to gradients of the y component of the magnetic field. In both cases it was shown that at the time of maximum reconnection rate the gradients of the off-diagonal components of the electron pressure tensors were the dominant terms that give rise to the reconnection electric field. In both cases there was also a contribution from the electron inertia at the edge of the diffusion region along z, which was most significant in the $m_i/m_e = 9$ case which is similar to guide field reconnection. The structure of the off-diagonal components of the electron pressure tensor were investigated. In the equal mass ratio case it was shown that the structure of the pressure tensor components were similar to an intermediate guide field case. It was suggested that the characteristic scale length of the pressure tensor components may be even smaller than the electron Larmor radius in the shear magnetic field. In the $m_i/m_e = 9$ case in the early stages of reconnection the pressure tensor components were again equivalent to an intermediate guide field case. At the time of maximum reconnection rate the structure of the pressure tensor components did not show the expected form and in the future a more detailed investigation of the pressure tensor components is necessary.

In the future a major aim would be to use the general theory for the Vlasov-Maxwell equilibria and the conditions for force-free equilibria to investigate the possibility of additional analytical force-free equilibria. Even if the differential equations resulting from Ampère's law were not

analytically solvable it might be possible to apply numerical methods to find additional force-free equilibria (e.g. Mynick et al. 1979). It may be possible to apply the general method of finding the corresponding quasineutral pressure functions P_{qn} and inverting this to find the distribution function to other simple 1D force-free magnetic field configurations.

This thesis only shows two different 2.5D PIC simulations starting from the same force-free Harris sheet equilibrium for equal mass ratios and mass ratio $m_i/m_e = 9$. It would be interesting to investigate this equilibrium for even larger mass ratio. The length scale of the equilibrium could also be varied to see what effect this has. Also it would be interesting to add different constant guide fields on top of the spatially varying shear field to see what difference that makes. In addition to this reconnection simulations starting from a combined Harris sheet case could be carried out.

A major aim for the future would be to extend this work to run full 3D PIC simulations. It would be extremely interesting to investigate how the reconnection process might change starting from a self-consistent non-linear force-free magnetic field, for example how microinstabilities found for systems with plasma density gradients change for force-free equilibria.

Appendix A: The Pressure Potential

Following Schindler et al. (1973); Schindler (2007) the relation (3.15) can be derived directly by use of the chain rule and by noticing that

$$\int \left(\frac{\partial f_s}{\partial v_x}\right)_{v_y,v_z} d^3v = 0, \tag{A1}$$

using integration by parts. This integral vanishes because f_s has to vanish for large $|\mathbf{v}|$. Also

$$\left(\frac{\partial f_s}{\partial v_x}\right)_{v_y,v_z} = m_s \left[v_x \left(\frac{\partial f_s}{\partial H_s}\right)_{p_{xs},p_{ys}} + \left(\frac{\partial f_s}{\partial p_{xs}}\right)_{H_s,p_{ys}} \right], \tag{A2}$$

using $H_s = m_s v^2/2 + q_s\phi$ and $p_{xs} = m_s v_x + q_s A_x$. We obtain

$$\begin{aligned}
\frac{\partial \sigma}{\partial A_x} + \frac{\partial j_x}{\partial \phi} &= \sum_s q_s \left(\frac{\partial}{\partial A_x} \int f_s d^3v + \frac{\partial}{\partial \phi} \int v_x f_s d^3v \right) \\
&= \sum_s q_s^2 \int \left[\left(\frac{\partial f_s}{\partial p_{xs}}\right)_{H_s,p_{ys}} + v_x \left(\frac{\partial f_s}{\partial H_s}\right)_{p_{xs},p_{ys}} \right] d^3v \\
&= \sum_s \frac{q_s^2}{m_s} \int \left(\frac{\partial f_s}{\partial v_x}\right)_{v_y,v_z} d^3v = 0,
\end{aligned}$$

which leads to Eq. (3.15). Equation (3.16) can be derived in exactly the same way by replacing v_x with v_y and A_x by A_y.

Equation (3.17) can be verified by direct differentiation of Eqs. (3.13) and (3.14). It can be seen that

$$\begin{aligned}
\frac{\partial j_x}{\partial A_y} &= \sum_s q_s^2 \int v_x \left(\frac{\partial f_s}{\partial p_{ys}}\right)_{H_s,p_{xs}} d^3v \\
&= \sum_s q_s^2 \int \left[\frac{1}{m_s} \left(\frac{\partial (v_x f_s)}{\partial v_y}\right)_{v_x,v_z} - v_x v_y \left(\frac{\partial f_s}{\partial H_s}\right)_{p_{xs},p_{ys}} \right] d^3v \\
&= -\sum_s q_s^2 \int v_x v_y \left(\frac{\partial f_s}{\partial H_s}\right)_{p_{xs},p_{ys}} d^3v,
\end{aligned}$$

where again the chain rule has been used in the first step and integration by parts in the second step. The first term vanishes during integration by parts as any admissible f_s has to go to zero as $|\mathbf{v}| \to \infty$ faster than any power of $\mathbf{v}$. Replacing A_y by A_x, p_{ys} by p_{xs} and exchanging v_x and v_y it is found with a similar calculation that

$$\frac{\partial j_y}{\partial A_x} = -\sum_s q_s^2 \int v_x v_y \left(\frac{\partial f_s}{\partial H_s}\right)_{p_{xs},p_{ys}} d^3v,$$

which shows the general validity of Eq. (3.17).

Equation (3.19) can also be directly derived by differentiation of the pressure tensor in the following way:

$$\begin{aligned}\frac{\partial P}{\partial \phi} &= \sum_s m_s q_s \int v_z^2 \left(\frac{\partial f_s}{\partial H_s}\right)_{p_{xs},p_{ys}} d^3v \\ &= \sum_s q_s \int v_z \left(\frac{\partial f_s}{\partial v_z}\right)_{v_x,v_y} d^3v \\ &= -\sum_s q_s \int f_s d^3v = -\sigma,\end{aligned}$$

where integration by parts has been used in the last step and

$$\left(\frac{\partial f_s}{\partial v_z}\right)_{v_x,v_y} = m_s v_z \left(\frac{\partial f_s}{\partial H_s}\right)_{p_{xs},p_{ys}} \tag{A3}$$

in the previous step.

Equations (3.20) and (3.21) are similar in structure and thus the derivation is explicitly shown only for one of them. Differentiating the zz-component of the pressure tensor with respect to A_x we get

$$\frac{\partial P}{\partial A_x} = \sum_s q_s m_s \int v_z^2 \left(\frac{\partial f_s}{\partial p_{xs}}\right)_{H_s,p_{ys}} d^3v.$$

Equation (A2) can be used to express the partial derivative of f_s as

$$m_s \left(\frac{\partial f_s}{\partial p_{xs}}\right)_{H_s,p_{ys}} = \left(\frac{\partial f_s}{\partial v_x}\right)_{v_y,v_z} - m_s v_x \left(\frac{\partial f_s}{\partial H_s}\right)_{p_{xs},p_{ys}}$$

and Eq. (A3) to replace $m_s v_z \left(\partial f_s/\partial H_s\right)_{p_{xs},p_{ys}}$ to obtain

$$\frac{\partial P}{\partial A_x} = \sum_s q_s \int \left[v_z^2 \left(\frac{\partial f_s}{\partial v_x}\right)_{v_y,v_z} - v_x v_z \left(\frac{\partial f_s}{\partial v_z}\right)_{v_x,v_y}\right] d^3v$$

$$= \sum_s q_s \int v_x f_s d^3v = j_x.$$

Integration by parts has been used again in the final step and only the non-vanishing terms have been retained. Equation (3.21) follows in exactly the same way by replacing v_x by v_y and A_x by A_y.

Appendix B: Movies

This is a directory for the movies that are on the CD which accompany this thesis.

Harris Sheet Cases

Zero Guide Field

- **harriscxz.mpg**: Evolution of the magnetic field lines with the y component of the current density colour coded.
- **harrispxye.mp4**: Evolution of the $P_{xy,e}$ component of the electron pressure tensor zoomed in around the X-point.
- **harrispyze.mp4**: Evolution of the $P_{yz,e}$ component of the electron pressure tensor zoomed in around the X-point.

Guide Field $B_{y0} = 0.5$

- **harrisby05cxz.mpg**: Evolution of the magnetic field lines with the y component of the current density colour coded.
- **harrisby05pxye.mp4**: Evolution of the $P_{xy,e}$ component of the electron pressure tensor zoomed in around the X-point.
- **harrisby05pyze.mp4**: Evolution of the $P_{yz,e}$ component of the electron pressure tensor zoomed in around the X-point.

Guide Field $B_{y0} = 1.0$

- **harrisby1cxz.mpg**: Evolution of the magnetic field lines with the y component of the current density colour coded.

- **harrisby1pxye.mp4**: Evolution of the $P_{xy,e}$ component of the electron pressure tensor zoomed in around the X-point.
- **harrisby1pyze.mp4**: Evolution of the $P_{yz,e}$ component of the electron pressure tensor zoomed in around the X-point.

Anisotropic bi-Maxwellian $(m_i/m_e = 1)$

Zero Guide Field

- **cxzaniso.mpg**: Evolution of the magnetic field lines with the y component of the current density colour coded.
- **anisopxye.mp4**: Evolution of the $P_{xy,e}$ component of the electron pressure tensor.
- **anisopyze.mp4**: Evolution of the $P_{yz,e}$ component of the electron pressure tensor.

Guide Field $B_{y0} = 0.5$

- **cxzanisoby05.mpg**: Evolution of the magnetic field lines with the y component of the current density colour coded.
- **anisopxyeby05.mp4**: Evolution of the $P_{xy,e}$ component of the electron pressure tensor.
- **anisopyzeby05.mp4**: Evolution of the $P_{yz,e}$ component of the electron pressure tensor.

Guide Field $B_{y0} = 1.0$

- **cxzanisoby1.mpg**: Evolution of the magnetic field lines with the y component of the current density colour coded.
- **anisopxyeby1.mp4**: Evolution of the $P_{xy,e}$ component of the electron pressure tensor.
- **anisopyzeby1.mp4**: Evolution of the $P_{yz,e}$ component of the electron pressure tensor.

Linear Force-Free

- **cxzff.mpg**: Evolution of the magnetic field lines with the y component of the current density colour coded.
- **anisopxyeff.mp4**: Evolution of the $P_{xy,e}$ component of the electron pressure tensor.

- **anisopyzeff.mp4**: Evolution of the $P_{yz,e}$ component of the electron pressure tensor.
- **jxff.mp4**: Evolution of the x component of the current density.

Double Harris Sheet

Zero Guide Field

- **cxzdblh.mpg**: Evolution of the magnetic field lines with the y component of the current density colour coded.
- **dblhpxye.mp4**: Evolution of the $P_{xy,e}$ component of the electron pressure tensor.
- **dblhpyze.mp4**: Evolution of the $P_{yz,e}$ component of the electron pressure tensor.

Guide Field $B_{y0} = 0.5$

- **cxzdblhby05.mp4**: Evolution of the magnetic field lines with the y component of the current density colour coded.
- **dblhpxyeby05.mp4**: Evolution of the $P_{xy,e}$ component of the electron pressure tensor.
- **dblhpyzeby05.mp4**: Evolution of the $P_{yz,e}$ component of the electron pressure tensor.

Guide Field $B_{y0} = 1.0$

- **cxzdblhby1.mp4**: Evolution of the magnetic field lines with the y component of the current density colour coded.
- **dblhpxyeby1.mp4**: Evolution of the $P_{xy,e}$ component of the electron pressure tensor.
- **dblhpyzeby1.mp4**: Evolution of the $P_{yz,e}$ component of the electron pressure tensor.

Anisotropic bi-Maxwellian $(m_i/m_e = 25)$

Guide Field $B_{y0} = 0.5$

- **cxzanisomime25by05.mp4**: Evolution of the magnetic field lines with the y component of the current density colour coded.

- **anisomime25pxyeby05.mp4**: Evolution of the $P_{xy,e}$ component of the electron pressure tensor.
- **anisomime25pyzeby05.mp4**: Evolution of the $P_{yz,e}$ component of the electron pressure tensor.

Guide Field $B_{y0} = 1.0$

- **cxzanisomime25by1.mp4**: Evolution of the magnetic field lines with the y component of the current density colour coded.
- **anisomime25pxyeby1.mp4**: Evolution of the $P_{xy,e}$ component of the electron pressure tensor.
- **anisomime25pyzeby1.mp4**: Evolution of the $P_{yz,e}$ component of the electron pressure tensor.

Linear Force-Free

- **cxzffmime25.mp4**: Evolution of the magnetic field lines with the y component of the current density colour coded.
- **ffmime25pxye.mp4**: Evolution of the $P_{xy,e}$ component of the electron pressure tensor.
- **ffmime25pyze.mp4**: Evolution of the $P_{yz,e}$ component of the electron pressure tensor.
- **jxffmime25.mp4**: Evolution of the x component of the current density.

Force-Free Harris Sheet

Simulation Run with $m_i/m_e = 1$

- **cxzffharris.mp4**: Evolution of the magnetic field lines with the y component of the current density colour coded.
- **jxffharris.mp4**: Evolution of the $P_{xy,e}$ component of the electron pressure tensor.
- **pxyeffharris.mp4**: Evolution of the $P_{yz,e}$ component of the electron pressure tensor.
- **pyzeffharris.mp4**: Evolution of the x component of the current density.

Simulation Run with $m_i/m_e = 9$

- **cxzffharrismime9.mp4**: Evolution of the magnetic field lines with the y component of the current density colour coded.

Bibliography

Alpers, W. (1969). Steady State Charge Neutral Models of the Magnetopause. *Astrophysics and Space Science*, 5:425–437.

Attico, N. and Pegoraro, F. (1999). Periodic equilibria of the Vlasov-Maxwell system. *Physics of Plasmas*, 6:767–770.

Bertotti, B. (1963). Fine structure in current sheaths. *Annals of Physics*, 25:271–289.

Birdsall, C. K. and Langdon, A. B. (1985). *Plasma Physics via Computer Simulation*. McGraw-Hill.

Birn, J., Drake, J. F., Shay, M. A., Rogers, B. N., Denton, R. E., Hesse, M., Kuznetsova, M., Ma, Z. W., Bhattacharjee, A., Otto, A., and Pritchett, P. L. (2001). Geospace Environmental Modeling (GEM) magnetic reconnection challenge. *J. Geophys. Res.*, 106:3715–3720.

Birn, J. and Hesse, M. (2001). Geospace Environment Modeling (GEM) magnetic reconnection challenge: Resistive tearing, anisotropic pressure and hall effects. *J. Geophys. Res.*, 106:3737–3750.

Biskamp, D. (2000). *Magnetic Reconnection in Plasmas*. Magnetic reconnection in plasmas, Cambridge, UK: Cambridge University Press, 2000 xiv, 387 p. Cambridge monographs on plasma physics, vol. 3, ISBN 0521582881.

Bobrova, N. A., Bulanov, S. V., Sakai, J. I., and Sugiyama, D. (2001). Force-free equilibria and reconnection of the magnetic field lines in collisionless plasma configurations. *Physics of Plasmas*, 8:759–768.

Bobrova, N. A. and Syrovatskiĭ, S. I. (1979). Violent instability of one-dimensional forceless magnetic field in a rarefied plasma. *Soviet Journal of Experimental and Theoretical Physics Letters*, 30:535–+.

Bowers, K. and Li, H. (2007). Spectral Energy Transfer and Dissipation of Magnetic Energy from Fluid to Kinetic Scales. *Physical Review Letters*, 98(3):035002–+.

Boyd, T. J. M. and Sanderson, J. J. (2003). *Magnetic Reconnection*. Cambridge University Press.

Büchner, J. and Kuska, J.-P. (1999). Sausage mode instability of thin current sheets as a cause of magnetospheric substorms. *Annales Geophysicae*, 17:604–612.

Channell, P. J. (1976). Exact Vlasov-Maxwell equilibria with sheared magnetic fields. *Physics of*

Fluids, 19:1541–1545.

Correa-Restrepo, D. and Pfirsch, D. (1993). Negative-energy waves in an inhomogeneous force-free Vlasov plasma with sheared magnetic field. *Physical Review E*, 47:545–563.

Daughton, W. (1999). The unstable eigenmodes of a neutral sheet. *Physics of Plasmas*, 6:1329–1343.

Daughton, W., Lapenta, G., and Ricci, P. (2004). Nonlinear Evolution of the Lower-Hybrid Drift Instability in a Current Sheet. *Physical Review Letters*, 93(10):105004–+.

Davies, C. M. (1968). The boundary layer between a cold plasma and a confined magnetic field when the plasma is not normally incident on the boundary. *Planetary and Space Science*, 16:1249–+.

Davies, C. M. (1969). The structure of the magnetopause. *Planetary and Space Science*, 17:333–+.

Fu, W.-Z. and Hau, L.-N. (2005). Vlasov-Maxwell equilibrium solutions for Harris sheet magnetic field with Kappa velocity distribution. *Physics of Plasmas*, 12(7):070701–+.

Furth, H. P., Killeen, J., and Rosenbluth, M. N. (1963). Finite-Resistivity Instabilities of a Sheet Pinch. *Physics of Fluids*, 6:459–484.

Grad, H. (1961). Boundary Layer between a Plasma and a Magnetic Field. *Physics of Fluids*, 4:1366–1375.

Greene, J. M. (1993). One-dimensional Vlasov-Maxwell equilibria. *Physics of Fluids B*, 5:1715–1722.

Harris, E. G. (1962). On a plasma sheath separating regions of oppositely directed magnetic field. *Nuovo Cimento*, 23:115.

Harrison, M. G. and Neukirch, T. (2009a). One-Dimensional Vlasov-Maxwell Equilibrium for the Force-Free Harris Sheet. *Physical Review Letters*, 102(13):135003–+.

Harrison, M. G. and Neukirch, T. (2009b). Some remarks on one-dimensional force-free Vlasov-Maxwell equilibria. *Physics of Plasmas*, 16(2):022106–+.

Hesse, M., Birn, J., and Kuznetsova, M. (2001a). Collisionless magnetic reconnection: Electron processes and transport modeling. *J. Geophys. Res.*, 106:3721–3736.

Hesse, M., Kuznetsova, M., and Birn, J. (2001b). Particle-in-cell simulations of three-dimensional collisionless magnetic reconnection. *Journal of Geophysical Research*, 106:29831–29842.

Hesse, M., Kuznetsova, M., and Birn, J. (2004). The role of electron heat flux in guide-field magnetic reconnection. *Physics of Plasmas*, 11:5387–5397.

Hesse, M., Kuznetsova, M., and Hoshino, M. (2002). The structure of the dissipation region for component reconnection: Particle simulations. *Geophys. Res. Lett.*, 29(12):120000–1.

Hesse, M., Kuznetsova, M., Schindler, K., and Birn, J. (2005). Three-dimensional modeling of electron quasiviscous dissipation in guide-field magnetic reconnection. *Physics of Plasmas*, 12(10):100704–+.

Hesse, M., Schindler, K., Birn, J., and Kuznetsova, M. (1999). The diffusion region in collisionless magnetic reconnection. *Physics of Plasmas*, 6:1781–1795.

Hockney, R. W. and Eastwood, J. W. (1988). *Computer Simulation usng Particles*. Adam Hilger.

Hurley, J. (1963). Analysis of the Transition Region between a Uniform Plasma and its Confining Magnetic Field. II. *Physics of Fluids*, 6:83–88.

Kan, J. R. (1972). Equilibrium configurations of Vlasov plasmas carrying a current component along an external magnetic field. *Journal of Plasma Physics*, 7:445–+.

Karimabadi, H., Daughton, W., and Quest, K. B. (2004). Role of electron temperature anisotropy in the onset of magnetic reconnection. *Geophysical Research Letters*, 31:18801–+.

Krall, N. A. and Trivelpiece, A. W. (1973). *Principles of plasma physics*. International Student Edition - International Series in Pure and Applied Physics, Tokyo: McGraw-Hill Kogakusha, 1973.

Kuznetsova, M. M., Hesse, M., and Winske, D. (1998). Kinetic quasi-viscous and bulk flow inertia effects in collisionless magnetotail reconnection. *J. Geophys. Res.*, 103:199–214.

Kuznetsova, M. M., Hesse, M., and Winske, D. (2000). Toward a transport model of collisionless magnetic reconnection. *J. Geophys. Res.*, 105:7601–7616.

Kuznetsova, M. M., Hesse, M., and Winske, D. (2001). Collisionless reconnection supported by nongyrotropic pressure effects in hybrid and particle simulations. *Journal of Geophysical Research*, 106:3799–3810.

Lam, S. H. (1967). One-Dimensional Static Pinch Solutions. *Physics of Fluids*, 10:2454–2457.

Langdon, A. B. (1992). On enforcing Gauss' law in electromagnetic particle-in-cell codes. *Computer Physics Communications*, 70:447–450.

Lapenta, G. (2003). A new paradigm for 3D Collisionless Magnetic Reconnection. *Space Science Reviews*, 107:167–174.

Laval, G., Pellat, R., and Vuillemin, M. (1966). Instabilités électromagnétiques des plasmas sans collisions (CN-21/71). In *Plasma Physics and Controlled Nuclear Fusion Research, Volume II*, pages 259–+.

Lee, L. C. and Kan, J. R. (1979a). A unified kinetic model of the tangential magnetopause structure. *Journal of Geophysical Research (Space Physics)*, 84:6417–6426.

Lee, L. C. and Kan, J. R. (1979b). Transition layer between two magnetized plasmas. *Journal of Plasma Physics*, 22:515–524.

Lemaire, J. and Burlaga, L. F. (1976). Diamagnetic boundary layers - A kinetic theory. *Astrophysics and Space Science*, 45:303–325.

Lerche, I. (1967). On the Boundary Layer between a Warm, Streaming Plasma and a Confined Magnetic Field. *Journal of Geophysical Research (Space Physics)*, 72:5295–+.

Li, H., Nishimura, K., Barnes, D. C., Gary, S. P., and Colgate, S. A. (2003). Magnetic dissipation in a force-free plasma with a sheet-pinch configuration. *Physics of Plasmas*, 10:2763–2771.

Ma, Z. W. and Bhattacharjee, A. (2001). Hall magnetohydrodynamic reconnection: The Geospace Environment Modeling challenge. *J. Geophys. Res.*, 106:3773–3782.

Marder, B. (1987). A Method for Incorporating Gauss' Law into Electromagnetic PIC Codes. *Journal of Computational Physics*, 68:48–+.

Mottez, F. (2003). Exact nonlinear analytic Vlasov-Maxwell tangential equilibria with arbitrary density and temperature profiles. *Physics of Plasmas*, 10:2501–2508.

Mottez, F. (2004). The pressure tensor in tangential equilibria. *Annales Geophysicae*, 22:3033–3037.

Mynick, H. E., Sharp, W. M., and Kaufman, A. N. (1979). Realistic Vlasov slab equilibria with magnetic shear. *Physics of Fluids*, 22:1478–1484.

Neukirch, T. (1993). Deformation of a magnetic dipole field by trapped particles. *Journal of Geophysical Research*, 98:3753–3765.

Neukirch, T. (1998). Introduction to the Theory of MHD Equilibria. http://www-solar.mcs.st-andrews.ac.uk/ thomas.

Nicholson, R. B. (1963). Solution of the Vlasov Equations for a Plasma in an Externally Uniform Magnetic Field. *Physics of Fluids*, 6:1581–1586.

Nishimura, K., Gary, S. P., Li, H., and Colgate, S. A. (2003). Magnetic reconnection in a force-free plasma: Simulations of micro- and macroinstabilities. *Physics of Plasmas*, 10:347–356.

Otto, A. (2001). Geospace Environment Modeling (GEM) magnetic reconnection challenge: MHD and Hall MHD-constant and current dependent resistivity models. *J. Geophys. Res.*, 106:3751–3758.

Parker, E. N. (1957). Sweet's Mechanism for Merging Magnetic Fields in Conducting Fluids. *J. Geophys. Res.*, 62:509–520.

Parker, E. N. (1963). The Solar-Flare Phenomenon and the Theory of Reconnection and Annihiliation of Magnetic Fields. *Astropjys. J. Supp.*, 8:177–+.

Parker, E. N. (1967). Confinement of a Magnetic Field by a Beam of Ions. *Journal of Geophysical Research (Space Physics)*, 72:2315–+.

Petschek, H. E. (1964). Magnetic Field Annihilation. In Hess, W. N., editor, *The Physics of Solar Flares*, pages 425–+.

Press, W. H., Teukolsky, S. A., Vetterling, W. T., and Flannery, B. P. (1992). *Numerical recipes in FORTRAN. The art of scientific computing*. Cambridge: University Press, —c1992, 2nd ed.

Priest, E. (1984). *Solar Magnetohydrodynamics*. Reidel.

Priest, E. and Forbes, T. (2000). *Magnetic Reconnection*. Magnetic Reconnection, by Eric Priest and Terry Forbes, pp. 612. ISBN 0521481791. Cambridge, UK: Cambridge University Press, June 2000.

Pritchett, P. L. (2001). Geospace Environment Modeling magnetic reconnection challenge: Simulations with a full particle electromagnetic code. *J. Geophys. Res.*, 106:3783–3798.

Pritchett, P. L. (2005). Onset and saturation of guide-field magnetic reconnection. *Physics of Plasmas*, 12(6):062301–+.

Pritchett, P. L. and Coroniti, F. V. (2004). Three-dimensional collisionless magnetic reconnection in the presence of a guide field. *Journal of Geophysical Research (Space Physics)*, 109(A18):1220–+.

Ricci, P., Brackbill, J. U., Daughton, W., and Lapenta, G. (2004a). Collisionless magnetic reconnection in the presence of a guide field. *Physics of Plasmas*, 11:4102–4114.

Ricci, P., Brackbill, J. U., Daughton, W., and Lapenta, G. (2004b). Influence of the lower hybrid drift instability on the onset of magnetic reconnection. *Physics of Plasmas*, 11:4489–4500.

Ricci, P., Brackbill, J. U., Daughton, W., and Lapenta, G. (2005). New role of the lower-hybrid drift instability in the magnetic reconnection. *Physics of Plasmas*, 12(5):055901–+.

Rogers, B. N., Denton, R. E., and Drake, J. F. (2003). Signatures of collisionless magnetic reconnection. *Journal of Geophysical Research (Space Physics)*, 108:6–1.

Roth, M. (1976). The plasmapause as a plasma sheath: a minimum thickness. *Journal of Atmospheric and Terrestrial Physics*, 38:1065–1070.

Roth, M., de Keyser, J., and Kuznetsova, M. M. (1996). Vlasov Theory of the Equilibrium Structure of Tangential Discontinuities in Space Plasmas. *Space Science Reviews*, 76:251–317.

Sakai, J.-I. and Matsuo, A. (2004). Three-dimensional dynamics of relativistic flows in pair plasmas with force-free magnetic configuration. *Physics of Plasmas*, 11:3251–3258.

Schindler, K. (2007). *Physics of Space Plasma Activity*. Cambridge.

Schindler, K. and Birn, J. (2002). Models of two-dimensional embedded thin current sheets from Vlasov theory. *Journal of Geophysical Research (Space Physics)*, 107:20–1.

Schindler, K., Pfirsch, D., and Wobig, H. (1973). *Plasma Physics*, 15:1165.

Scholer, M., Sidorenko, I., Jaroschek, C. H., Treumann, R. A., and Zeiler, A. (2003). Onset of collisionless magnetic reconnection in thin current sheets: Three-dimensional particle simulations. *Physics of Plasmas*, 10:3521–+.

Sestero, A. (1964). Structure of Plasma Sheaths. *Physics of Fluids*, 7:44–51.

Sestero, A. (1966). Vlasov Equation Study of Plasma Motion across Magnetic Fields. *Physics of Fluids*, 9:2006–2013.

Sestero, A. (1967). Self-Consistent Description of a Warm Stationary Plasma in a Uniformly Sheared Magnetic Field. *Physics of Fluids*, 10:193–197.

Sestero, A. and Zannetti, M. (1967). Self-consistent astron e layer with spread in energy and angular momentum. *Phys. Rev. Lett.*, 19(24):1377–1379.

Shay, M. A., Drake, J. F., Denton, R. E., and Biskamp, D. (1998). Structure of the dissipation region during collisionless magnetic reconnection. *J. Geophys. Res.*, 103:9165–9176.

Shay, M. A., Drake, J. F., Rogers, B. N., and Denton, R. E. (2001). Alfvénic collisionless magnetic reconnection and the Hall term. *J. Geophys. Res.*, 106:3759–3772.

Silin, I. and Büchner, J. (2003). Nonlinear instability of thin current sheets in antiparallel and guided magnetic fields. *Physics of Plasmas*, 10:3561–3570.

Silin, I. and Büchner, J. (2005). Small-scale reconnection due to lower-hybrid drift instability in current sheets with sheared fields. *Physics of Plasmas*, 12:2320–+.

Su, S.-Y. and Sonnerup, B. U. Ö. (1971). On the equilibrium of the magnetopause current layer. *Journal of Geophysical Research (Space Physics)*, 76:5181–5188.

Sweet, P. A. (1958a). The Neutral Point Theory of Solar Flares. In Lehnert, B., editor, *Electromagnetic Phenomena in Cosmical Physics*, volume 6 of *IAU Symposium*, pages 123–+.

Sweet, P. A. (1958b). The Production of High-Energy Particles in Solar Flares. *Nuovo Cimento Suppl.*, 8:188–196.

Tassi, E., Pegoraro, F., and Cicogna, G. (2008). Solutions and symmetries of force-free magnetic fields. *Physics of Plasmas*, 15(9):092113–+.

Tonks, L. (1959). Trajectory-Wise Analysis of Cylindrical and Plane Plasmas in a Magnetic Field and Without Collisions. *Physical Review*, 113:400–407.

Villasenor, J. and Buneman, O. (1992). Rigorous charge conservation for local electromagnetic field solvers. *Computer Physics Communications*, 69:306–316.

Yoon, P. H., Lui, A. T. Y., and Sheldon, R. B. (2006). On the current sheet model with κ distribution. *Physics of Plasmas*, 13(10):102108–+.